

https://dspace.org/

A fundamental investigation of the hydrothermal dissolution and oxidation of manganese metal.

Glück, Thomas

2001
https://hdl.handle.net/10539/27901

Downloaded from a DSpace repository. https://dspace.org/

A FUNDAMENTAL INVESTIGATION OF THE HYDROTHERMAL DISSOLUTION AND OXIDATION OF MANGANESE METAL

By

THOMAS GLÜCK

A thesis submitted to the Faculty of Engineering, University of the Witwatersrand, Johannesburg, in fulfilment of the requirements for the degree of Doctor of Philosophy

Johannesburg, 2001

DECLARATION

I declare that this thesis is my own, unaided work. It is being submitted for the Degree of Doctor of Philosophy to the University of the Witwatersrand, Johannesburg. It has not been submitted before for any degree or examination in any other University.

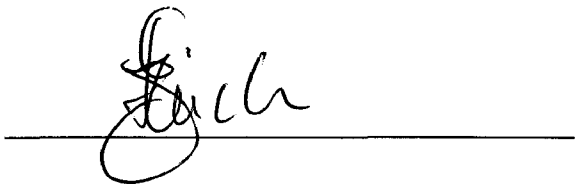

Thomas Glück

4th day of May 2001

ABSTRACT

The oxides of manganese display a number of allotropic structures, a number of which have significant industrial importance. In particular, mangano-manganic oxide (Mn_3O_4), is used as a raw material for the manufacture of soft ferrites. The preparation of Mn_3O_4 by hydrothermal dissolution and oxidation of manganese metal at elevated temperature and pressure yields a raw material that has unique chemical, morphological and structural characteristics. In this work experimental and theoretical investigations were conducted to determine the mechanisms of the dissolution and oxidation reactions as well as the influence that processing conditions have on the morphological and structural properties of the oxidation products.

Simplified Pourbaix diagrams were generated to map the stability domains of relevant manganese oxides for hydrothermal processing conditions. These show that the domain of stability of manganous hydroxide, $Mn(OH)_{2(aq)}$ may be larger than currently reported in literature. Hydrothermal dissolution experiments were conducted to investigate the influence of hydrogen partial pressure on reaction kinetics. An experimental and mathematical methodology was developed to facilitate the analysis of the non-isothermal dissolution kinetics with polydisperse shrinking particles of Mn metal. The rate of the dissolution reaction was found to be controlled by a heterogeneous chemical reaction occurring on the surface of the manganese metal particles but was not influenced by hydrogen partial pressure. The rate of oxidation of solid $Mn(OH)_2$ formed after the dissolution of manganese metal by oxygen in a mechanically agitated, gas-sparged reactor was found to follow linear kinetics. Dissolution and reprecipitation processes were found to occur during the oxidation of $Mn(OH)_2$ particles that results in the formation of a daughter population of particles. The hydrothermal oxidation of $Mn(OH)_2$ occurs via a homogeneous oxidation mechanism. Mass transfer of oxygen from the gas phase to the liquid was found to be the rate-controlling step of the oxidation process.

The changes in morphology and crystal structure of the hydroxide/oxide intermediates and products during hydrothermal oxidation were investigated using a number of different characterisation techniques. Mn_3O_4 made under hydrothermal conditions can be oxidised by heating in air in contrast to naturally occurring minerals or synthetic Mn_3O_4 made via high temperature processes. In addition, this material shows larger deviations from stoichiometry than materials prepared by high temperature synthesis. The crystal defect structures of oxidation intermediates and products were analysed using Rietveld structural refinement techniques and compared to a number of theoretical structural models. The reactivity of hydrothermal Mn_3O_4 is attributed to the cationic vacancies in tetrahedral and octahedral lattice sites.

This thesis is dedicated to my parents,
Franz and Herta Glück,
who made it possible for me to complete this work.

In memory of J.Painter (1962-1995)

ACKNOWLEDGEMENTS

The author gratefully acknowledges the assistance and guidance of Professor A.W. Bryson during the preparation of this thesis. Dr M. Thackeray, Dr A. Kleyenstuber, Dr P.J. Harris, A. de Kock, M. Rossouw, and S. Swart are thanked for their work on the sample preparation procedures and X-Ray Diffraction analysis of manganese oxides and hydroxides. The contributions of Dr M. Thackeray of the Argonne National Laboratory in the USA and the assistance of Professor G. Kruger of the Rand Afrikaans University in Johannesburg in conducting the structural refinement modelling of the hausmannite structures is gratefully acknowledged. C. Penberthy of Mintek and E. Lourens of Billiton Process Research are thanked for the scanning electron images and M. Schoeman of Delta EMD kindly made a Malvern Mastersizer available for particle size analysis.

Manganese Metal Company is thanked for the generous sponsorship and the opportunity to complete this work. The support, encouragement and assistance of my colleagues at MMC, in particular, J. Eigenhuis, is gratefully acknowledged. D. Kauffman, with indomitable spirit, constructed the testwork equipment and performed a substantial portion of the small reactor testwork. M. Pieterse is thanked for the assistance with the small reactor testwork and morphological investigations. D. Kok and his team kindly collected contributed data from a large reactor.

M. Rossouw, S. Glück, Dr P. Holmes and M. Pieterse endured the arduous task of proof-reading the drafts that were the precursors of this manuscript.

The encouragement and support of my family and friends made completion of this thesis possible. My wife, Sharon, and our children, Jocelyn and Khendyl, had to endure many hours of my absence. Their loving patience contributed as much to the completion of this work as did the hours of study.

CONTENTS PAGE

DECLARATION ii

ABSTRACT iii

DEDICATION iv

ACKNOWLEDGEMENTS v

CONTENTS vi

1 INTRODUCTION 8

1.1 THESIS ORGANISATION 10

1.2 LITERATURE SURVEY 10
1.2.1 Dissolution of Manganese and Other Metals 10
1.2.2 Electrochemical Effects during Oxide Dissolution 15
1.2.3 Surface Processes on Metals and Oxides 17
1.2.4 Oxidation of Metals in the Gas Phase 19
1.2.5 Aqueous Oxidation of Transition Metals and Equilibrium Diagrams 23
1.2.6 Heterogeneous Oxidation of Manganous Hydroxide 34
1.2.7 Structural Aspects of Oxidation 37
1.2.8 Summary of Literature Review and Conclusions 45
1.2.9 Specific Objectives and Contributions 48

2 HYDROTHERMAL MANGANESE METAL DISSOLUTION EXPERIMENTS 51

2.1 INTRODUCTION 51

2.2 EXPERIMENTAL DESIGN AND MECHANISTIC CONSIDERATIONS 51

2.3 Mn DISSOLUTION EXPERIMENTS 55
2.3.1 Literature Data 56
2.3.2 Isothermal Laboratory Experiments at 95°C 62
2.3.3 Non-Isothermal Large Scale Reactor Experiment 64
2.3.4 Non-isothermal Reactor Experiments 74

2.4 Summary of Results from Dissolution Experiments 87

3 EQUILIBRIUM AND KINETIC ASPECTS OF MANGANESE METAL DISSOLUTION 90

3.1 INTRODUCTION 90

3.2 EQUILIBRIUM MODELLING ANALYSIS 90
3.2.1 Oxidation Reduction Equilibria 91
3.2.2 Manganese Hydrolysis 92
3.2.3 Electrochemical Equilibria 97
3.2.4 Conclusions 101

3.3 MODELLING OF HYDROTHERMAL MANGANESE METAL DISSOLUTION KINETICS **103**
3.3.1 Isothermal shrinking particle kinetic models 103
3.3.2 Non-isothermal polydisperse model 108
3.3.3 Conclusions 119

3.4 Summary of Results from Kinetic and Equilibrium Modelling **121**

4 HYDROTHERMAL $MN(OH)_2$ OXIDATION EXPERIMENTS **123**

4.1 INTRODUCTION **123**

4.2 SOLID CHARACTERISATION AND KINETIC INVESTIGATIONS **127**
4.2.1 Analyses of Particle Morphology 127
4.2.2 Thermogravimetric and kinetic investigations 134
4.2.3 Structural Investigations 143
4.2.4 Summary of experimental results 153

5 KINETIC AND STRUCTURAL ASPECTS OF THE HYDROTHERMAL OXIDATION OF MANGANOUS HYDROXIDE **156**

5.1 Kinetic and Mechanistic Modelling **156**
5.1.1 Conclusions 159

5.2 Mass Transfer Modelling **160**
5.2.1 Conclusions 162

5.3 Modelling of Particle Morphology **163**
5.3.1 Conclusions 168

5.4 Characterisation and Modelling of Solid State Structures **169**
5.4.1 Thermogravimetric analysis of dried reactor samples 169
5.4.2 Conclusions 174
5.4.3 Structural Modelling of Manganese Oxides 174
5.4.4 Conclusions 180

5.5 Summary of overall conclusions **181**

6 DENOUEMENT **184**

6.1 RECOMMENDATIONS FOR FUTURE RESEARCH **187**

APPENDICES **189**

BIBLIOGRAPHY **265**

1 INTRODUCTION

The higher oxides of manganese, Mn_3O_4, Mn_2O_3 and MnO_2, display a number of allotropic structures. These materials are applied in diverse industrial and technological applications, for example, certain forms of MnO_2 are the active components in secondary batteries. Spinel structured manganese oxides (e.g. α-Mn_3O_4 and λ-MnO_2) and mixed metal oxides are used in the manufacture of soft magnets, rechargeable batteries, thermistors and oxygen evolving electrode materials. Manganese-zinc soft ferrites are used extensively in electronic applications such as switched mode power supplies, fly-back transformers, deflection yokes for television sets and ballast transformers for fluorescent lighting. $LiMn_xO_y$ spinels are used in cathode materials of rechargeable, portable battery systems. Ni-doped Mn_3O_4 spinel is used for the manufacture of thermally sensitive ceramic resistors which have decreasing resistance with increasing temperature. Rare earth manganates, e.g. $LaMnO_3$, have potential applications as oxygen electrodes in fuel cells. Manganese oxides are also found in molecular sieves and catalysts for organic synthesis.

Manufacturing processes for synthetic manganese oxide materials that are based on the hydrothermal oxidation of manganese metal can yield high purity, spinel-structured, mangano-manganic oxides (Mn_3O_4). These are suitable starting materials for electronic component manufacture, in particular soft ferrites. One method for preparing high purity Mn_3O_4 from manganese metal utilises two reactions occurring sequentially at elevated temperature (>100°C) and pressure (>400kPa) in a mechanically agitated vessel. The first reaction includes the hydrothermal dissolution of solid manganese metal particles with evolution of hydrogen gas, hydrolysis of dissolved manganese ions and simultaneous precipitation of manganous hydroxide $Mn(OH)_2$. The overall reaction may be written as:

$$Mn_{(s)} + 2H_2O_{(aq)} \rightarrow Mn(OH)_{2(s)} + H_{2\,(g)}$$

The second reaction is the oxidation of the manganous hydroxide in a slurry form by oxygen or air to mangano-manganic oxide (Mn_3O_4):

$$6Mn(OH)_{2(s)} + O_{2(g)} \rightarrow 2Mn_3O_{4(s)} + 6H_2O_{(aq)}$$

For simultaneous dissolution and oxidation, the above reactions can be combined and represented as:

$$6Mn_{(s)} + 6H_2O_{(aq)} + O_{2(g)} \rightarrow 2Mn_3O_{4(s)} + 6H_{2(g)}$$

One of the important advantages of hydrothermal processing is that the rate of oxidation of manganese metal is substantially increased at elevated temperature so that relatively small and compact plants can be utilised for the commercial manufacture of Mn_3O_4. In addition, the process can be conducted without additives such as catalysts or complexing ligands. This simplifies the plant design and the operating procedures by eliminating the need to recover these additives or to control their concentrations. This feature reduces operating costs and results in a product with low concentrations of impurities such as Cl, SO_4 and the light metals i.e. Na, Ca, K.

The design and operation of such a production facility requires knowledge of the mechanisms and rates of the different conversion reactions. The influence that the processing conditions have on the physical, chemical and structural properties of the manganese oxide products must also be determined so that the physico-chemical properties of these materials can be tailored to specific requirements. Combining this knowledge with ferrite preparation technology is essential for the optimal use of the manganese oxides and their extended utilisation in related materials processing applications. This understanding should ideally be captured in the form of simple, relevant physical and mathematical models that can be used to optimise product quality, plant design and manufacturing procedures. All aspects of this knowledge must be validated relative to existing scientific knowledge so it can be applied in this and similar reaction systems. The investigations and analyses described in this thesis address these technological aspects for the hydrothermal oxidation of manganese.

The oxidation of manganese ions and manganese oxyhydroxides at ambient temperature is a field of study that has been extensively researched. The technique of hydrothermal oxidation of manganese metal or hydroxide has been described and investigated by Simon (1943), Bricker (1965), Nørland-Christensen & Ollivier (1972) and Ohta *et al.* (1990). The thermodynamics of the above reactions can also be derived from Pourbaix type diagrams. However, investigations of the rates and mechanisms of the hydrothermal oxidation of manganese metal in the absence of complexing ligands with appropriate characterisation of the products have not been reported in the literature. In addition, a number of shortcomings were identified in the published literature in terms of providing explanations to results obtained and to observations made during the experimental and theoretical investigations. These shortcomings are identified more specifically in the literature survey presented in section 1.2. As a result of these shortcomings, three areas of research were selected for investigation, these are:

- High temperature equilibrium of the manganese-oxygen-water system.
- Kinetics and mechanisms of the manganese metal dissolution reaction.
- Kinetics, morphology and mechanisms of the manganous hydroxide oxidation reaction

More specific details of the experimental and theoretical work conducted and the purpose for this work in each of the above areas of investigation is described in the paragraph 1.2.8 following the literature survey.

1.1 THESIS ORGANISATION

Each of the chapters in this thesis is structured differently. A literature review on manganese metal dissolution, equilibrium modelling and manganese oxidation is presented as part of this chapter. Chapter 2 presents experimental results for the hydrothermal dissolution of manganese metal particles. These results are analysed in Chapter 3 together with the equilibrium modelling. Experimental results for the oxidation of manganous hydroxide suspensions are reported in Chapter 4 and are discussed in Chapter 5. The structural aspects of the oxidation of manganous hydroxide to spinel-structure Mn_3O_4 are included in Chapter 5 as well as the identification of the rate controlling mechanism of this reaction. Chapter 6 is a concluding chapter that combines the summaries from each subsection of the thesis. The Appendices contain detailed derivations and results that support the main chapters. A separate nomenclature schedule has not been included as detailed explanation of symbols is made where these are introduced.

1.2 LITERATURE SURVEY

The dissolution and oxidation of base metals and their oxides have been and continue to be studied extensively in the literature. The following literature survey first reviews the dissolution of manganese metal and its oxides in terms of electrokinetic considerations. The formation of surface layers of oxides and hydroxides which is a feature of a number of metal dissolution and oxidation reactions is then considered. These layers may form in both gas and liquid phase systems and affect reaction mechanisms as well as significantly altering the physical and chemical properties of the metals. The equilibrium stability domains of these species can be mapped by a number of different methods that are reviewed following the dissolution discussion. The surface films can be oxidised further or grow due to the action of the oxidising agent to form bulk oxides. The mechanisms of formation and characteristics of these materials are reviewed subsequently in the context of solid state structural chemistry.

1.2.1 Dissolution of Manganese and Other Metals

The dissolution of manganese metal may be viewed electrochemically as the anodic dissolution of manganese metal and the cathodic evolution of hydrogen gas according to the half reactions:

$$Mn_{(s)} \rightarrow Mn^{2+}_{(aq)} + 2e^-$$
$$2H^+_{(aq)} + 2e^- \rightarrow H_{2(g)}$$

The dissolved manganous ions subsequently hydrolyse and precipitate. The mechanisms of dissolution and the plating of manganese metal have been investigated by Hurlen (1962), who found that Fe, Cr, Zn and Mn all have similar behaviour as polarised electrodes. Surface conditions for anodic and cathodic behaviour were similar and the dissolution rate was proportional to the square root of the metal ion activity. This type of kinetic behaviour was explained by means of an activated controlled model that has a kinetic equation based on the reaction of two metal atoms. The reaction mechanism was postulated to include a process of electrochemical initiation that forms kinks at surface steps. The steps act as chain carriers for subsequent direct electrochemical propagation reactions at the kinks. The dissolution rate and deposition rate were found to depend on pH in a manner corresponding to a first order catalytic interaction of hydroxyl ions:

$$2Mn_{(s)} + OH^-_{(aq)} \rightarrow 2Mn^{2+}_{(aq)} + OH^-_{(aq)} + 4e^-$$

Hurlen (1962) did not present quantitative elucidation of his model and its verification is required for the manganese system. These processes have however been incorporated into the general theories of crystallisation and electrocrystallisation, e.g. Mullin (1993) and Budevski *et al.* (1996).

The dissolution of manganese in a number of different acids at room was investigated by Hurlen & Valand (1964a). The corrosion rate of manganese in acids is controlled by the diffusion of hydrogen ions from the solution to the metal surface. The corrosion point on a Tafel diagram (potential vs. corrosion rate) was given by the intercept of two lines representing the above half reactions (1) and (2). The hydrogen evolution reaction had a pH and stirring dependent limiting line while the line for the metal dissolution reaction was pH dependent and stirring independent. The corrosion potential was typically –1,12V to –1,20V for pH 1 and 2,6 respectively. The corrosion rate increased from 10^{-3} to 10^{-1} $A.cm^{-2}$ for corrosion potentials of –1,20V to –1,12V respectively. Blocking effects due to the precipitation of solid corrosion products at higher corrosion rates caused deviations from linearity in some of the Tafel plots.

Comprehensive reviews have been made of the electrochemistry of manganese by Liang (1973) and Gmelins (1973). Gmelins' review of the mechanism of dissolution in alkaline conditions for anodically polarised Mn addresses the formation of manganate ($MnO_4^=$) and permanganate ions (MnO_4^-). An inspection of the Pourbaix Eh-pH diagram for manganese reveals that the thermodynamic stability regions of manganese metal and the

soluble high valence oxide ions are separated by the regions of stability for the solid phases $Mn(OH)_2$, MnOOH, Mn_3O_4, Mn_2O_3 and MnO_2.

Figure 1.1 Simplified Eh-pH diagram for Mn-O-H_2O at 25°C

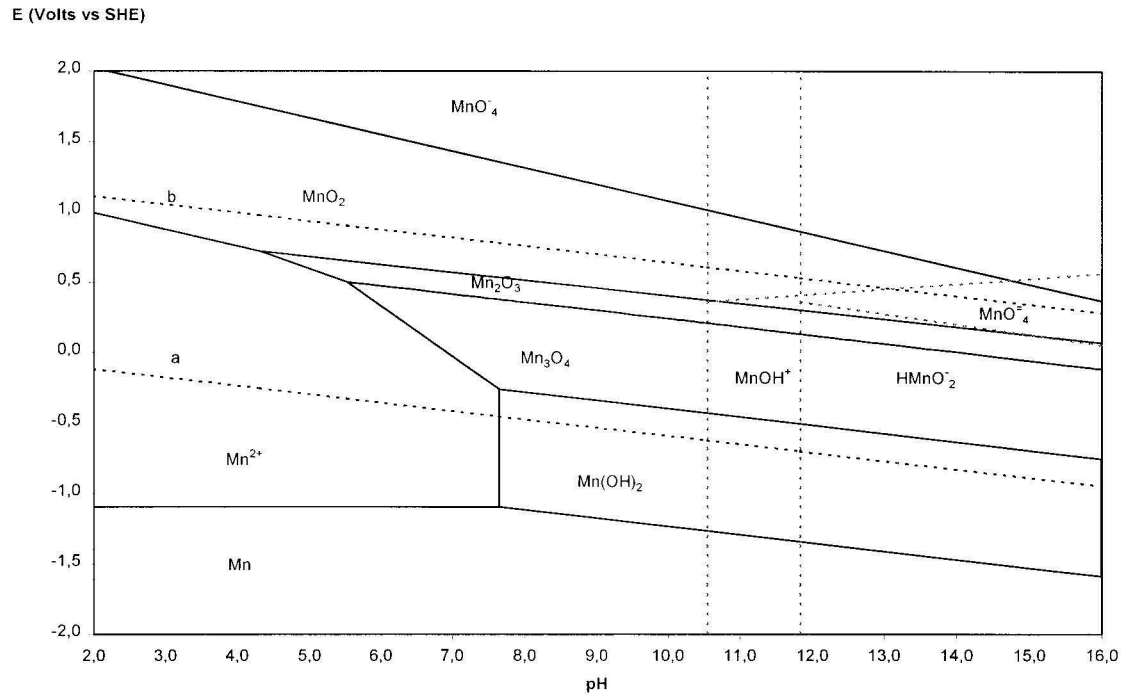

Note: Diagram generated accorded to equilibrium modelling method described in paragraph 3.2.

The potentials for the formation of Mn_3O_4 are positive (0 to –0,2V) with respect to the expected corrosion point. Thus, the formation of oxidation states for manganese of higher than two can only occur if localised sites of high potential are created on the surface of the metal during the dissolution process. The review by Gmelins claims that manganese with oxide layering can be dissolved in alkali media with the formation of MnO_4^-. Polarised dissolution under these conditions is accompanied by oxygen evolution. The Mn^{2+} ion concentration in the pores of the oxide layer increases during dissolution which raises the electrode potential. This favours MnO_4^- formation that eventually becomes the dominant process. The concurrent formation of MnO_4^{2-} at higher OH^- concentrations and temperatures is attributed to the reduction of MnO_4^- ions by hydrogen evolved through the cathodic half-reaction. The soluble and gaseous products therefore clearly influence dissolution pathways and mechanisms. This occurs in a similar manner in the iron corrosion system as discussed by Pourbaix (1974).

The corrosion potential of iron at pH 0 occurs at -0,250V while the equilibrium potential of the electrode is -0,500V. This large deviation is not apparent in the zinc system (-0,755 c.f. -0,822V) or the manganese system (-1,08 c.f. -1,179V). Corrosion in the manganese

system is therefore expected to occur at low overpotentials. The anodic polishing of manganese is possible in ClO_4^- containing baths. Here the formation of a water-free layer on the metal surface leads to conditions where the metal can dissolve directly to metal ions.

Hurlen & Valand (1964c) conducted slow galvanostatic experiments in HCl and H_2SO_4 solutions. The dissolution and deposition processes gave Tafel plots that had slope and intercept essentially independent of bulk pH (pH 1 - 3) with the H_2 evolution slope of 117 $mV.decade^{-1}$. The second order mechanisms proposed by Hurlen (1962) were confirmed with no hydroxyl ion interactions observed. Hydrogen evolution at the corrosion potential was H^+ diffusion controlled. Higher overpotentials resulted in direct reduction of water.

Hurlen & Valand (1964b) used an activated complex model to explain the effects of temperature on the manganese electrode. The activation energies measured were numerically equivalent to the heats of reaction and the determination of absolute electrode potentials was proposed. The transition state entropy of Mn and Cu was found to lie midway between a metallic and ionic end-state entropy whereas Fe and Zn lie near the metallic end-state. The concepts of entropic contribution to a Born-Haber cycle type of calculation were used by Cavollotti *et al.* (1987) to classify metals into normal, intermediate and inert groups. Mn belongs to the intermediate group that has slightly reversible behaviour, Tafel law kinetics and strongly textured deposits.

Heusler & Bergmann (1970) conducted potentiodynamic experiments on a number of metals in neutral and weak acid solutions of $(NH_4)_2SO_4$ and NH_4Cl. Stationary anodic polarisation curves could not be obtained for manganese. The cathodic process of deposition and hydrogen evolution was modelled by a half crystal site adsorption model with the activity of the surface concentration dependent on overpotential only. The Toshkarev coupling of manganese deposition and hydrogen evolution was not confirmed. The observation that the surface concentration of metal ions was independent of solution concentration showed that the crystal sites do not equilibrate with solution. This was in contrast to Fe, Ni and Co. The slope of the cathodic process of H_2 evolution gave 120 $mV.decade^{-1}$ (log $A.cm^{-2}$) in the pH range 2 - 6.5. The rate of H_2 evolution in chloride media was twice as fast as in sulphate media. H_2O reacted to form hydroxides that cause irreversible changes to the Mn surface and catalyse H_2 evolution. The hydroxides could have been the reason for non-stationary anodic polarisation curves.

Gmelins (1973) reviewed work by Antropov & Gorachevskaya on the dissolution of manganese in 20% $MgCl_2$ solutions at 20°C. Cathodic polarisation curves showed three linear regions in the Tafel plane which were ascribed to:

a) Manganese dissolution, O_2 ionisation and direct loading of H^+

b) Mn dissolution and H^+ reduction

c) Pure H_2 evolution.

Similar behaviour was observed in synthetic seawater in the pH range 1 - 2,8. The dissolution of manganese under cathodic polarisation conditions was confirmed by Hurlen & Valand (1964c). The theory of delayed charging applied in steps (b) and (c) above and cathodic protection started at (c) only. Proton donation was via the water molecule and not via the hydronium ion. Studies in $(NH_4)_2SO_4$ solutions in the pH range 6 -10 showed that adsorption of NH_4^+ occurs with the subsequent reaction

$$NH_4^+{}_{(aq)} + e^- \Leftrightarrow NH_{3(aq)} + H_{ads}$$

The NH_3 complexes Mn-hydroxides formed on the surface and raises the solubility of the dissolved manganese. The overpotential of H_2 evolution on Mn in sulphate solutions was also influenced by cations in solution. The overpotential drops in the series Na^+, K^+, Li^+, Rb^+, Cs^+. The presence of NH_4^+ acts as a depolariser. The H_2 overpotential in H_2 saturated $(NH_4)_2SO_4$ solutions is independent of the $(NH_4)_2SO_4$ concentration. The presence of air lowers the overpotential with increasing concentration of $(NH_4)_2SO_4$ (0,25 - 0,52M $(NH_4)_2SO_4$), which is presumably due to the solubility of O_2 decreasing with increasing $(NH_4)_2SO_4$ concentration.

The hydrogen evolution process on manganese in alkali media (6M NaOH) at 25°C gives linear regression values of a = 0,90V, b = 0,12V ($\eta = a + b \log i$, η= overpotential, i = current density) in a Tafel plot with exchange current $j_o = 3x10^{-8} A.cm^{-2}$ and transfer coefficient α = 0,5. Gamma manganese has smaller a values and larger slopes indicating that alpha manganese is more easily deposited from aqueous solutions. A more recent study by Ilea *et al.* (1997) found that the Tafel parameters of the hydrogen evolution reaction on a manganese metal surface at pH 7,8 in $(NH)_4SO_4$ and Na_2SO_4 solutions were dependent on the current density used in galvanostatic rotating disc electrode experiments. This was explained by a Heyrovsky type discharge mechanism at current densities of less than 200mA. cm^{-2} and a Tafel mechanism at higher current densities according to the following general mechanistic framework:

$H_2O + e^- \rightarrow H_{ad} + OH^-$ (Volmer mechanism)

$H_{ad} + H_2O + e^- \rightarrow H_2 + OH^-$ (Heyrofsky mechanism)

$2H_{ad} \rightarrow H_2$ (Tafel mechanism)

Manganese is an active metal with passivation possible only under strongly oxidising conditions, e.g. anodic polarisation. Melendez & Brenet (1971) and Heusler (1963) studied passivation phenomena on manganese electrodes. Melendez & Brenet (1963) measured anodic polarisation curves in 0,5M phosphate solutions and found that the passivation was controlled by the diffusion of $Mn_3(PO_4)_2$. The corrosion process is spontaneous and may be depicted by a curve that lies between the hydrogen evolution and Mn^{2+}/Mn lines on an Eh-pH plot. Melendez & Brenet (1963) used concepts similar to those proposed in the Franck-Fitzhugh model (1961) to explain inflections observed on the polarisation curves. A porous phosphate layer caused an increase in the slope of the hydrogen evolution reaction. Melendez & Brenet (1963) used the dependence of the surface solution equilibrium on pH to identify the Mn phosphate diffusion mechanism and to explain the drop in corrosion current with increasing pH. The experiments were conducted at large overpotentials that were sufficient to oxidise the surface to Mn_2O_3-H_2O, MnO_2 and MnO_4^-. No passivation phenomena were found in sulphate media.

The anodic behaviour of the Mn electrode thus depends on the pH of the electrolyte. In acidic and neutral electrolytes, dissolution to Mn^{2+} occurs. Alkali solutions result in the formation of $Mn(OH)_2$, which at higher anodic overpotentials, is oxidised to mixed Mn^{2+}-Mn^{4+} oxides or oxy-hydroxides. The equilibrium curve in the pH range 7 to 16 lies in the potential region 0,1 to -0,5V (SHE). These potentials are considerably more anodic than the free corrosion potential at -1,0 to -1,1V and unpolarised corrosion processes are not expected to form higher Mn oxides.

The above works show that the formation of oxy-hydroxide layers can occur on the surface of a manganese metal particle during the dissolution of manganese under a wide range of experimental conditions. A systematic study of these processes has however not been reported for the manganese metal under hydrothermal dissolution conditions. Here the hydroxide that is precipitated at elevated temperature forms a second phase of discrete particles. In addition, the hydrogen evolved during hydrothermal dissolution of manganese could act as a reducing agent in closed or pressurised systems. A systematic study of the influence of hydrogen pressure on manganese dissolution kinetics was not found during the compilation of this literature review.

1.2.2 Electrochemical Effects during Oxide Dissolution

Further consideration is given to oxide dissolution mechanisms as it was found that the manganese metal used for the dissolution experiments contained surface oxide layers. These layers may therefore alter the reaction kinetics and the dissolution mechanisms of of the metal. The study of oxide dissolution encompasses metal oxide leaching technology and numerous works exist which address the electrochemical aspects of

these systems. Engel (1956) pointed out the major difference between metal and metal oxide dissolution. Metals must have charge transfer whereas oxides can dissolve without change in valence. Large differences in surface potential and electrochemical effects also need to be taken into account (*vide supra* Table 1.2). Osseo-Assare (1984) discussed the ion-transfer model of non-oxidation dissolution that stipulates the dissolution process is controlled by the double layer potential. The corrosion rate and freely dissolving potential in this model are given by the condition when the rates of electrochemical cation and anionic transfer are equivalent. The acid base equilibria of the surface hydroxyl groups determine the leaching characteristics of simple oxides as proposed by the general leaching model of Warren & Devuyst (1973).

Burton *et al.* (1951) addressed the fundamental aspects of crystal growth theory. The reverse processes were used by Valverde & Wagner (1976) to discuss metal oxide dissolution reactions. Valverde (1976) studied dissolution of various metal oxides, though this work has been shown not to shed any light on the redox processes involved by later works on the nickel oxide system by Lussiez *et al.* (1981) and Jones *et al.* (1977, 1978a, 1978b). These works have a high experimental content and do not present a generalised model for the effects observed in the dissolution systems studied. The general model of leaching proposed by Warren & DeVuyst (1973) has addressed this shortcoming.

Studies in the dissolution of the uranium oxides by Nicol *et al.* (1975) and Laxen (1972) presented an electrochemical model that could be used quantitatively to predict the behaviour of the leaching processes. The effect of solution redox behaviour on the oxide could be duplicated by anodic polarisation as long as the potentials were similar. Vermilyea (1966) analysed the electrostatic effects of surface charge on dissolution rate. Segal & Sellers (1984) presented a more qualitative description of the solid-liquid interface processes and contrasted reductive and oxidative dissolution amongst others.

Jones *et al.* (1990) studied the dissolution kinetics of MnO, Mn_3O_4 and Mn_2O_3 at pH 2,0-2,5 and 25°C in perchloric and nitric acid solutions. A feature of this work was to determine the influence that the method of preparation of the oxides had on the dissolution rate. It was found that the nature of MnO dissolution is similar to CoO which is a p-type, semiconducting oxide. The rates of MnO dissolution ($4x10^{-5}$ $mol.s^{-1}m^{-2}$) were however two orders of magnitude higher than for CoO. The presence of oxidising agents in solution had a minor effect on reaction rates. Dissolved oxygen was found to increase the reaction rate by 20%. Reducing agents had a strong influence on kinetics particularly for higher defect structured MnO prepared at lower temperatures. This was ascribed to the presence of non-reactive Mn^{3+} in the surface structure. Dissolution rates for Mn_3O_4 and Mn_2O_3 were two to three orders of magnitude lower than for MnO that was again explained by the presence of more Mn^{3+} in the surface and bulk structure. The kinetics

measured were found to be consistent with the Vermilyea protonation mechanism described by :

$$[O^{2-}]_{(ss)} + H^{+}_{(aq)} \rightarrow [OH^{-}]_{(ads)}$$
$$[OH^{-}]_{(ads)} + H^{+}_{(aq)} \rightarrow H_2O_{(aq)}$$
$$[O^{2-}]_{(ss)} + 2H^{+}_{(aq)} \rightarrow H_2O_{(aq)}$$

These mechanisms were found to apply to the initial fast stages of oxide dissolution in acid solutions where surface dynamics are far from equilibrium. The rates of reaction were slower in the advanced, reaction rate controlled regime where charge transfer processes through the charge depletion layer at the surface of the solid are critical.

1.2.3 Surface Processes on Metals and Oxides

A review is given here of the surface processes that are characteristic of manganese metal. Under oxidising conditions, surface oxides are formed on the surface of the metal that can influence reaction kinetics. The characterisation of the oxides can be achieved by a number of different analytical techniques.

Gaseous and aqueous oxidation reactions can involve a chemisorption step as part of the overall reaction. Anderson (1971) and Tompkins (1978) give comprehensive treatises of chemisorption. The specific characteristics of chemisorption on manganese metal have been studied by a number of investigators. Hu & Rabalais (1981) conducted X-ray Photoelectron Spectroscopy (XPS), Ultraviolet Photoelectron Spectroscopy (UPS) and active ion bombardment experiments on clean manganese. O_2 is dissociatively absorbed with the formation of a monoxide. The dissociation is non-activated and the adsorbed species is immobile on the surface. CO adsorbs in both molecular and dissociated forms that coexist on the surface at sufficiently high coverage. N_2 reacts only after an activation barrier has been overcome. Glück (1994) confirmed some of these findings at elevated temperatures (>700°C) and showed that mixed dual site adsorption and solid diffusion controls the rate of nitrogen absorption into manganese metal. Sarma & Sen (1983) used Auger Electron Spectroscopy (AES) and XPS to study the surface oxidation of manganese metal and found that manganese exhibited an unusually rapid oxidation rate compared to other transition metals. The surface oxide formed was MnO and defects in the oxide determined kinetics.

Borges-Soares *et al.* (1983) studied the reactions of electrolytic manganese metal flake with oxygen and water vapour using XPS. The smooth side of a piece of electrolytic flake contained layers of MnO, Mn_3O_4 and Mn_2O_3. Their experiments showed that pure, oxide-free, surface films of manganese could only be obtained by ionic sputtering. The

reactions of the metal with oxygen were rapid, topochemical and progressed through the product series:

$$Mn \rightarrow MnO \rightarrow Mn_3O_4 \rightarrow Mn_2O_3$$

The stability regimes of the different oxides of manganese according to the equilibrium diagram of Mah (1960) were confirmed except for MnO_2. MnO_2 could not be formed due to slow kinetics. Room temperature reactions with water vapour and water contaminated ultravacuum atmospheres gave similar reaction products. It was suspected that $Mn(OH)_2$ was detected in these experiments due to water vapour contamination. The ultravacuum experiment showed two kinetic regimes that could be identified from the time dependent shift in the XPS binding energy peaks:

(1) - a rapid period encompassing adsorption, redistribution of water molecules on the surface, formation of oxide islands and then a complete layer,
(2) - a slow period during which OH^- ions diffuse through the surface layer.

The product of reaction was $Mn(OH)_2$ which could be converted to MnO. A splitting of the $O1s^{1/2}$ XPS peak was consistent with the formation of hydroxide and adsorbed water layers. Reactions of the hydroxide with water vapour at elevated temperature (625K) in ultravacuum gave Mn_3O_4. The authors do not describe how the oxygen partial pressure in the water vapour was controlled which could explain the formation of the higher oxide. Exposing metal to higher partial pressures of water (10^{-2} c.f. 10^{-8} torr) without vacuum yielded MnO.

Foord *et al.* (1984) investigated the oxidation of manganese by O_2 using XPS and showed that the reaction proceeded by the sequence:

$$Mn \rightarrow MnO \rightarrow Mn_2O_3 \rightarrow MnO_2$$

The resolution of Mn_3O_4 was difficult under the specific experimental conditions. Oku *et al.* (1975) conducted XPS on various manganese oxides and found it difficult to determine the oxidation states of manganese in Mn_3O_4. Narbutt (1988) used XPS to show that the oxidation states of surface manganese atoms in a number of manganese minerals could be correlated with the shift in the position of the $MnK\beta_1$ line relative to the Mn metal peak. Ardizzone *et al.* (1998) also analysed Mn_3O_4 and γ-MnOOH using XPS and XRD and claimed that the stoichiometry of Mn_3O_4 is $Mn_2^{2+}Mn^{4+}O_4$ rather than $Mn^{2+}Mn_2^{3+}O_4$ It is interesting to note that the shift obtained for hausmannite in Narbutt's work corresponding to an oxidation state intermediate between 4+ or 3+, which tends to

support Ardizzones' postulate. The valency of Mn_3O_4 is still being debated in the literature.

Cohen *et al.* (1988) measured the reactivity of freshly deposited MnFe films toward O_2, H_2O and N_2 using a number of different experimental techniques. The adsorption of H_2O was slow in comparison to O_2 and a Mn oxide/hydroxide film formed on the surface. Mn was preferentially oxidised at low coverage forming MnO. The adsorption of N_2 was not observed at room temperature.

Brennan *et al.* (1960) estimated that the surface of body centred Mn has an active site concentration of 1,40 x 10^{15} atom Mn / cm^2. Mn had anomalous hydrogen adsorption behaviour with respect to other transition metals. The observations made for O_2 adsorption on Mn in the above studies were confirmed though Brennan *et al.* (1960) found that the stable oxide formed in the experiment was Mn_2O_3 at high O_2 exposures. The heat of oxygen adsorption for the transition metals increased linearly with increasing metal atom size (viz. Mn>Fe>Ni>Co). Manganese also showed an unusual ability to regenerate sites for oxygen adsorption suggesting considerable oxygen mobility at the surface.

The above studies show that the topochemistry of a manganese metal surface progresses through a distinctive sequence of oxidation products. It is shown below that this is similar to the oxidation sequence of the bulk phase and that this progression is common to gaseous and aqueous reaction systems. The metal surface is active and surface reactions in the presence of water will form $Mn(OH)_2$. The chemisorption and dissociation parameters of water on manganese metal in the gas or liquid phase have not been reported in the literature. The mechanism of this reaction in aqueous systems has been studied as the hydrogen evolution reaction using electrochemical experimental techniques. The chemisorption parameters will therefore be embedded in the electrokinetic parameters that could be extracted from the results of appropriately designed experiments.

1.2.4 Oxidation of Metals in the Gas Phase

The manganese metal used for the hydrothermal dissolution experiments was found to contain oxide layers. A review is therefore given below of the characteristics and formation mechanisms of these layers. These are relevant in that references are made to activation energies for a number of manganese oxidation reactions. These activation energies are compared to experimental results obtained under hydrothermal oxidation conditions later in this thesis. The oxidation of metals by gaseous oxygen at elevated temperatures (>200°C) and the formation of oxide surface layers has been extensively

researched. Texts such as Hauffe (1965) and Birks & Meier (1983) present the technology of these processes.

Sully (1955) reported that the rate of manganese oxidation in the temperature range 400-1100°C follows parabolic kinetics. Smallman & Bishop's (1995) review of metal oxidation shows that parabolic kinetics correspond to a reaction mechanism where the rate is controlled by solid state diffusion processes involving point defects within the oxide layers. Breakaway kinetics, where the oxide film fractures or spalls with a resulting increase in reaction rate, have been reported in the manganese system (*vide infra* Gesmundo *et al.*(1975)) and it is possible that these apply to metal dust explosions. Echeverria & Paidassi (1959) measured gaseous parabolic oxidation kinetics for electrolytic manganese flake in the temperature range 400 to 1200°C. The activation energies measured increased from 29,2kcal/mol in the temperature range 400-900°C to 79,8kcal/mol between 1000 and 1200°C. The increase in activation energy could have been due to the allotropic transformation of alpha to beta manganese at roughly 720°C though the authors discount this as they mistakenly understood the allotropic transformation to occur at higher temperatures (1060-1100°C).

Fuecki & Wagner (1965) studied electrolytic manganese oxidation in CO_2-CO mixtures in the temperature range 800-1200°C and reported parabolic oxidation kinetics with activation energies that were dependant on gas composition in the range 40,5 to 45,6 kcal/mol. The oxidation process was shown to be controlled the diffusion of interstitial Mn^{2+} ions that are formed by Frankel or Schottky defect mechanisms. No breaks were obtained in the Arrhenius plots, which is consistent with the experimental temperature regime being above the temperature for allotropic transformation of α-Mn. Gesmundo *et al.* (1975) measured oxidation kinetics on electrolytic manganese chips in a pure oxygen environment in the temperature range 550-650°C (i.e. below the allotropic transition of α-Mn). Parabolic kinetics were again obtained in two regions of the weight-time curves. A two layer scale formation process explained this feature. The spalling and blistering of the outside layer allowed higher rates of diffusion. Two well-defined oxide layers were observable under a microscope. The thinner inner layer looked adherent, compact and had a bright green colour. The outer layer was reddish-brown, porous and exhibited blistering and spalling. XRD confirmed the presence of MnO and Mn_3O_4 in the respective layers (no Mn_2O_3 was found). Increasing the total oxygen pressure increased the rate of reaction at a given temperature as long as the thin inner layer was not controlling the rate of reaction. Once the thicker outer layer controlled the rate of reaction the process became dependent on oxygen pressure. Heusler *et al.* (1990) investigated the mechanisms of Fe_3O_4 layer growth on a pure iron rod at elevated temperature in borate buffered solutions containing simple and quaternary chlorides. The dissolution of iron under anodic polarisation at 250°C followed parabolic kinetics in contrast to logarithmic

kinetics at 25°C. The steady state corrosion rate increased with temperature according to an activation energy of 41 $kJ.mol^{-1}$ and remained less than 10 $\mu A.cm^{-2}$ up to 300°C.

Parabolic kinetics are thus found in a number of metal oxidation reaction systems in gaseous and aqueous media. The hydrothermal dissolution of manganese metal is accompanied by the formation of precipitated manganous hydroxide. As noted above, if the precipitate forms at the surface and results in the formation of surface layers then the physical electronic and structural properties of these layers can influence the rate of dissolution of the metal.

1.2.4.1 Surface Characteristics of Manganese Oxyhydroxides in Aqueous Systems

A review follows of how the surface properties of a manganese metal particle could influence hydrothermal dissolution and oxidation mechanisms. Interfacial phenomena during leaching of oxides have been reviewed by Warren & Devuyst (1973) and Osseo-Asare (1984). Warren & Devuyst show that anionic species and defect structures can make leaching an anisotropic process and proposed a general mechanism for leaching. The surface of a metal or oxide can react with water to form surface hydroxyls:

$$M_2O_{(ss)} + H_2O_{(aq)} \rightarrow 2MOH_{(ss)}$$

where: (ss): surface species

The amphoteric dissociation of the surface hydroxyl groups gives rise to negative or positive surface charge:

$$MOH_{(ss)} + H^+_{(aq)} = MOH_2^+{}_{(ss)} \quad \text{(Adsorption of } H^+\text{)}$$

$$MOH_{(ss)} = M^+_{(ss)} + OH^-_{(aq)} \quad \text{(Basic dissociation)}$$

$$MOH_{(ss)} = MO^-_{(ss)} + H^+_{(aq)} \quad \text{(Acid dissociation)}$$

The surface charge is a characteristic of the type of oxide and is dependent on the concentration of potential determining ions in solution, H^+ and OH^- ions. No excess surface charge will be present at the point of zero charge, i.e. pH_{pzc}. The magnitude of pH_{pzc} is dependent on the oxidation state of the cations in the solid with typical values shown in Table 1.1. Osseo-Assare (1984) showed that generally in acidic solutions, the oxides with the highest pH_{pzc} have the highest dissolution rates.

Table 1.1 Points of zero charge for generic oxides

Oxide	pH_{pzc}
M_2O	>11,5
MO	8,5-12,5
M_2O_3	6,5-10,4
MO_2	0-7,5
MO_3	<0,5

Note: M represents a metallic cation

The magnitude of the surface charge as estimated by pH_{pzc} for different forms of manganese is shown in Table 1.2. A value of 17,08 is calculated for Mn metal from data by Gmelins (1973). $Mn(OH)_2$ has a pH_{pzc} of 12,4. Measurements for Mn_3O_4 were made for this thesis, details of which are given in Appendix A.

Table 1.2 pH_{pzc} of selected manganese surfaces

Species	pH_{pzc}	Reference
α-Mn	17,08	Gmelins (1973)
β-$Mn(OH)_2$	12,4	Bauer *et al.* (1985)
α-Mn_3O_4	3,3	#This thesis
γ-MnOOH	1,8	Healy *et al.* (1966)
δ-MnO_2	1,5	Healy *et al.* (1966)
α-MnO_2	4,6	Gray (1978)
γ-MnO_2	5,5	Healy *et al.* (1966)
β-MnO_2	7,3	Healy *et al.* (1966)

#Note: See Appendix A for experimental details

On this basis, Mn metal as expected, would have relatively high dissolution rates in acidic solutions. The surfaces of α-Mn and β-$Mn(OH)_2$ in pH 7,0 solutions are thus strongly positively charged in comparison to the oxides. Regions of significant charge gradient can therefore form in the vicinity of oxide islands present on the metal surface that would exhibit lower dissolution rates. Dissolution of metal into saturated manganous hydroxide solutions at pH 9-10 will result in a lowering of the positive surface charge of the metal and hydroxide surface portions while the oxide portions become more negative. This implies that an increase in pH should inhibit the dissolution process. The electrostatic fields associated with the double layer capacitance of a metal particle in demineralised water in this system extend over greater distances than compared to typical metallurgical

solutions that have high ionic strength and significant charge shielding characteristics. The magnitude of the zeta potentials in the pH range 9-10 (-30 to -40mV) reported in Appendix A indicates that a suspension of Mn_3O_4 particles will be relatively well dispersed and stable while hydroxide particles at the same conditions would tend to coalesce. This would have some influence on oxidation mechanisms and particle morphology.

1.2.5 Aqueous Oxidation of Transition Metals and Equilibrium Diagrams

The oxidation of a metal in aqueous media can occur as a dissolution reaction that may be accompanied by the formation of soluble and precipitated forms of hydroxides or oxides. It is useful to rank the tendency for dissolution according to the reduction potential of the metal. This has been termed the thermodynamic nobility or immunity by Pourbaix *et al.* (1974). The formation of metallic complexes, passivating films and kinetic effects will create effects such as immunity and passivation. This is termed practical nobility. The practical nobility ranking of a series of metals can be obtained by the extent that the immunity and passivation domains do not overlap with the stability domain of water in the pH range 4 to 10. The theoretical and practical nobilities of a number of metals taken from Pourbaix are given in Table 1.3.

Table 1.3 Nobility ranking of metals according to Pourbaix *et al.* (1974)

Metal	Thermodynamic nobility ranking	Reaction Couple	Electrode Potential [V]	Practical nobility ranking
Cu	13	Cu^{2+}/Cu	+0,337	16
Ni	21	Ni^{2+}/Ni	-0,250	29
Co	22	Co^{2+}/Co	-0,277	30
Cd	24	Cd^{2+}/Cd	-0,403	36
Fe	25	Fe^{2+}/Fe	-0,440	28
Zn	32	Zn^{2+}/Zn	-0,763	37
Mn	37	Mn^{2+}/Mn	-1,179	43
Be	42	Be^{2+}/Be	-1,847	18
Mg	43	Mg^{2+}/Mg	-2,360	41

Ref. Pourbaix (1974) extracted from a list of 43 metals and metalloids

This partial list was extracted from a schedule containing 43 metals and metalloids. Although manganese metal does not have the highest thermodynamic nobility ranking of Pourbaix's metal series it does have the lowest practical nobility. It is therefore the most active metal in an aqueous medium with products of corrosion that have the smallest passivation domain.

The potential (Eh)-pH diagrams of Pourbaix *et al.* (1974) map the domains of thermodynamic stability of the metals and their reaction products at 25°C, 1 atmosphere pressure and unit activity of dissolved species. Robins (1968) reviewed the application of Eh-pH diagrams to hydrothermal precipitation processes particularly in the Fe, Ni and Cr metal systems. A number of similarities exist in the structures and sequences of the oxidation products between these systems.

Hydroxides with the general formula $M(OH)_2$, where M = Ca, Mn, Cd, Mg, Fe, Ni and Co, have similar crystal structures to the layered structure of brucite, $Mg(OH)_2$. In addition, Fe, Ni, Co and Mn also have similar oxidation sequences that yield spinel (M_3O_4) structured oxides as the first solid products of oxidation (*vide infra* table 1.5). The overlapping of regions of stable and metastable hydrated oxides such as FeOOH or MnOOH can complicate these systems. Additional mapping of these conditions is therefore required. These observations are discussed further below. The oxidation of manganese, both in soluble and solid form, is used extensively in many industries and is known to occur in many natural, biological and geological environments. The corrosion of metallic manganese in acid or alkaline media yields manganous (Mn^{2+}) ions. The chemical oxidation of these ions by oxidising agents such as oxygen, ozone, peroxide, bromine, chlorine, persulfate or nitrate generally results in the formation of the oxidation states of Mn^{3+}, Mn^{4+} or mixed state combinations. The electrochemical oxidation of Mn^{2+} to Mn^{3+}, Mn^{4+}, Mn^{6+} and Mn^{7+} is known with some of these species being soluble over a wide pH range (e.g. manganate $MnO_4^{=}$ and permanganate MnO_4^{-} ions). Precipitated oxidation products are generally only partially soluble in strong acid solutions. Solid manganese oxides can further be oxidised in aqueous media or in two-phase gas-solid reactions. Elevated temperatures can be used to increase the reaction rate and alter the conditions of stability of individual oxide species.

Other chemical reactions of Mn^{2+} ions in water include hydrolysis that is promoted at higher temperatures. Cation hydrolysis increases the solubility of the dissolved cations with precipitation of solid hydroxides occurring simultaneously at elevated pH conditions. Baes & Mesmer (1976) presented a classification of metallic cations based on their resistance to hydrolysis. Hard cations, Ca, Mg, Sr and Ba, generally grouped as pre-transition metals, do not hydrolyse and have hydroxide forms in which the OH groups are directly bonded to the cation, i.e. $Ca(OH)_2$, $Mg(OH)_2$, $Sr(OH)_2$, $Ba(OH)_28H_2O$. M-OH bonding is ionic in nature in these compounds.

Manganese belongs to a group of divalent transition metals which have some covalent nature in their hydrolysis products bonding and are termed "medium" in terms of resistance to hydrolysis. Unfilled d-orbitals influence the hydrolysis reaction mechanisms and product forms of these metals. The sequences of the different forms of soluble hydrolysis products,

as shown in the preponderance diagrams of Baes & Mesmer, are shown in Table 1.4. Mn and Fe have similar hydrolysis product forms with Ni and Co showing an absence (or very low concentrations) of the 1st and 4th hydrolysis products.

The magnitude of the first hydrolysis constant of the medium cations correlates linearly with the ratio of ionic charge to M-O interatomic distance. In addition, these cations have polynuclear species that form by OH bridging of two cations viz. M_2OH^{3+}. Perrin (1962) has excluded the formation of soluble polynuclear manganese complexes below the point of hydrolysis. Some authors, e.g. Hem (1981), however still postulate that the polymerisation of deprotonated aquo-Mn^{2+} ions results in precursors for the sheet-like hexagonal structures of $Mn(OH)_2$ or β-MnOOH. The behaviour of manganese in this respect may therefore not be anomalous. The resolution of this uncertainty requires an experimental technique that can measure hydrolysis parameters close to the precipitation of $Mn(OH)_2$.

Table 1.4 Hydolysis sequences of divalent cations with medium hydrolysis resistance

Cation	1st H.P.	2nd H.P.	3rd H.P.	4th H.P.
Be^{2+}	$BeOH^+$	$Be(OH)_2$	$Be(OH)^-_3$	$Be(OH)^=_4$
Mn^{2+}	$MnOH^+$	$Mn(OH)_2$	$Mn(OH)^-_3$	$Mn(OH)^=_4$
Ni^{2+}		$Ni(OH)_2$	$Ni(OH)^-_3$	
Co^{2+}		$Co(OH)_2$	$Co(OH)^-_3$	
Fe^{2+}	$FeOH^+$	$Fe(OH)_2$	$Fe(OH)^-_3$	$Fe(OH)^=_4$
Zn^{2+}	$ZnOH^+$	$Zn(OH)_2$	$Zn(OH)^-_3$	$Zn(OH)^=_4$
Cu^{2+}	$CuOH^+$	$Cu(OH)_2$	$Cu(OH)^-_3$	$Cu(OH)^=_4$
Cd^{2+}	$CdOH^+$	$Cd(OH)_2$	$Cd(OH)^-_3$	$Cd(OH)^=_4$

Ref. Baes & Mesmer (1976)

Shaded blocks indicate the absence of a co-ordinated product.

$1^{st}...4^{th}$ H.P. = First to fourth Hydrolysis Products respectively.

Soft metals in the post-transition groups of the periodic table have filled d-orbitals and their hydrolysis products have significant covalent nature. Divalent metals in this group include Sn, Hg, Pd and Pt. All the medium and soft divalent metals discussed have stable, solid forms of hydroxide $M(OH)_2$ in the stability domain of water. It is thus possible to precipitate all these hydroxides at low oxidation potentials by raising the pH of a solution containing a divalent form of the metal cation. Baes & Mesmer showed that the hydrolysis behaviour of the metallic elements can be predicted from their positions in the periodic table.

Pourbaix's Eh-pH diagrams for medium divalent metals also show similarity in terms of the sequence of the solid oxidation products obtained by subjecting metals to increasing oxidising potentials. These sequences are shown in Table 1.1Table 1.5 for the unhydrated forms of the higher oxides. The shaded entries are product forms that are not stable in the normal stability domain of water at 25°C. Fe, Co, Ni and Mn all show similar oxidation sequences under these conditions. The stability domains of Ni and Co metal overlap with the stability domain of water at 25°C at neutral pH in comparison to Fe and Mn metal, which appear below the stability domain of water. This implies that Ni and Co metal will not be corroded by water in these regions in comparison to Mn and Fe.

Table 1.5 Solid oxidation product sequences for medium divalent metals in aqueous systems according to Pourbaix's diagrams

Valence / Cation	1+	2+	2,66+	3+	4+
Mn		$Mn(OH)_2$	Mn_3O_4	Mn_2O_3	MnO_2
Ni		$Ni(OH)_2$	Ni_3O_4	Ni_2O_3	NiO_2
Co		$Co(OH)_2$	Co_3O_4	Co_2O_3	CoO_2
Fe		$Fe(OH)_2$	Fe_3O_4	Fe_2O_3	
Zn		$Zn(OH)_2$			ZnO_2
Cu	Cu_2O	$Cu(OH)_2$			
Cd		$Cd(OH)_2$			

Ref.: Pourbaix *et al.* (1974) Column headings refer to oxidation state of cation
Shaded entries are not stable in the normal stability domain of water
Hydrated forms of higher oxides have been excluded.

The oxidation chemistry of Mn and Fe in pure water at 25°C should thus be similar. However, Mn metal is further removed from the stability domain of water and the stability domains of $Fe(OH)_2$ and Fe_3O_4 overlap. The higher oxide forms of the transition metals Mn, Ni, Co and Fe (except for FeO_2) also all show similar forms of the higher oxides. The oxidation mechanisms for the different metals under these conditions should therefore be similar.

Pourbaix predicted that Mn metal would spontaneously dissolve or corrode in water albeit at low reaction rates. Brenet & Picquet (1984) discussed the corrosion of manganese and stated ".. between pH 7 and 13, Mn has tendency to be covered with $Mn(OH)_2$ which can be slightly oxidised to MnOOH by oxygen always present in aqueous solution." The chemical and physical properties of this passive layer will therefore influence the overall reaction kinetics and mechanisms. Osseo-Asare (1981) pointed out that the stability of

$Mn(OH)_2$ increases with decreasing Mn concentration; $[Mn^{2+}]_{(aq)}$ affects reaction mechanisms and pressure has a small effect on equilibrium. Klingsberg & Roy (1959) and Bricker (1965) investigated the stability of phases in the Mn-O-OH system. Bricker's seminal work on the $Mn\text{-}O_2\text{-}H_2O$ system investigated the stability relations of seven synthetic manganese oxides/hydroxides. Reaction paths between these components and Eh-pH diagrams are shown in Figure 1.2 for the system at 25°C, Mn^{2+} activities of 10^{-6} molar and 1 atmosphere pressure. Bricker showed that the oxidation of $Mn(OH)_2$ can result in Mn_3O_4, or β-MnOOH at ambient temperature. Hydrothermal oxidation pathways have not been reported in the literature.

Figure 1.2 Reaction pathways in the system $Mn\text{-}O_2\text{-}H_2O$ at 25°C and 1atm total pressure according to Bricker (1965).

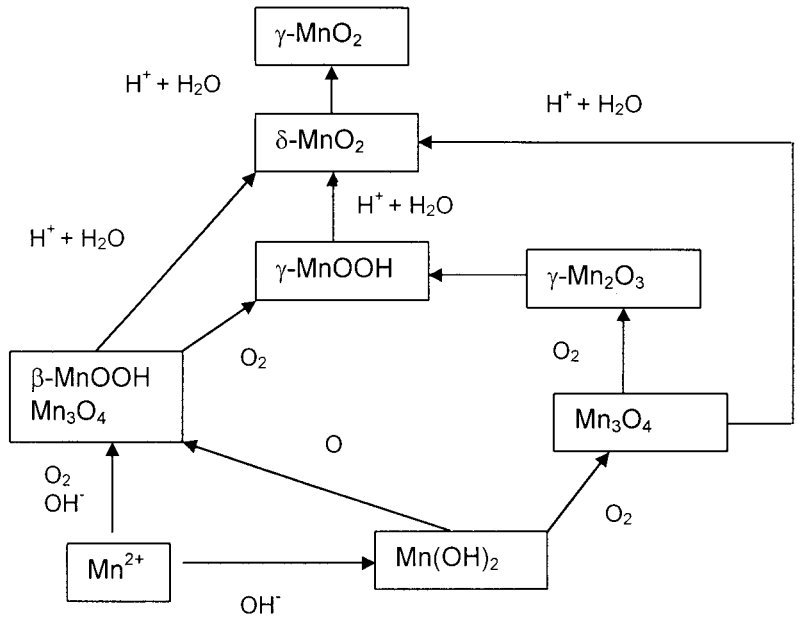

The electrochemistry of manganous hydroxide $Mn(OH)_2$, manganese dioxide MnO_2 and manganese oxyhydroxide MnOOH (manganite or groutite) is well researched due to the commercially important Leclanche cells. Brenet *et al.* (1963) recalculated the Eh-pH diagram for manganese and showed that the region of thermodynamic stability of MnOOH overlapped with that of Mn_3O_4 and Mn_2O_3. Brenet & Picquet (1984) established stability regions for different hydration states of these oxyhydroxides in equilibrium with MnO_2. Chouaib & Picard (1989) plotted high-alkalinity equilibrium diagrams and showed that it was possible to produce a range of oxyhydroxides with the general formula $MnO_{1+x}.zH_2O$ at ambient temperature under carefully controlled redox and pH conditions. They also showed that the electrochemical activity of the precipitates, as measured by integrating the reduction voltammetric curves, increased linearly with increasing hydration

(z). In addition, an activity increase was noted with increasing oxidation states of Mn (e.g. Mn^{4+} in MnO_2). Anhydrous Mn_3O_4 showed no electrochemical activity.

MacDonald (1976) reported on the effect of temperature on the stability field extents of manganese oxide/hydroxides. The stability fields for MnO and $HMnO_2^-$ were predicted to shift to lower pH for potential independent reactions with increasing temperature. The domain of MnO in particular increased significantly with an increase in temperature to 300°C. MacDonald claimed that potential dependent reactions such as the corrosion of Mn are not sensitive to temperature. MacDonald used equilibrium data for MnO for calculation purposes, as thermodynamic data for the hydroxide was not available. The calculation of the domain of stability of $Mn(OH)_2$ is addressed in Chapter 3 and the increase in domain area is confirmed. In addition to the effect of oxide hydration, the chemistry of crystalline forms of manganese is characterised by the presence of defect structures that are discussed further in later sections of this thesis.

Jenne (1967) reviewed the basis of construction of Eh-pH diagrams as applicable to soil systems and discussed the shortcomings of diagrams published in the literature. House (1987) discussed the limitations in using Eh-pH diagrams further with respect to hydrometallurgical systems. A summary of some of these limitations is shown in Table 1.6.

Table 1.6 Limitations in using Eh-pH diagrams published in literature

• Reversibility is assumed
• Metastable species are ignored as the diagrams do not show kinetics
• Rates of transformation may vary between species
• Local concentration conditions may vary from bulk measurable quantities
• Complex ion effects can be ignored
• Solid solution transformations may be ignored
• Criss & Cobble's (1964) assumptions apply to simple systems only
• Structural mapping of different allotropic solid state species is not extensive
• Defect structures are generally not recognised
• Hydrated oxides are often mapped as simple oxides

The last three entries have been added to Jenne and House's list of limitations as these have particular relevance to the manganese system. Notwithstanding these limitations, the diagrams are still useful if they are constructed for specific reaction systems. Investigations have been made into mapping the conditions under which metastable and hydrated manganese oxides can form. Brenet *et al.* (1968) used affinity-pH plots to simultaneously map the stability domains of the hydrated and unhydrated manganese oxides at room temperature over a pH range of 0 to 14. The products of Mn^{2+} oxidation by oxygen in ammonium chloride at pH 9 and 25°C were analysed by XPS, TEM (Transmission

Electron Microscopy) and XRD by Murray *et al.* (1985). This work was a confirmation of previous work by Feitknecht *et al.* (1962). The primary product was porous Mn_3O_4 (hausmannite) with traces of β-MnOOH (feitknechtite) and γ-MnOOH (manganite). Both Mn_3O_4 and β-MnOOH converted to γ-MnOOH over a period of months. Hem & Lind (1983) investigated the relative stability of β-MnOOH, γ-MnOOH and Mn_3O_4 precipitated from oxidising solutions containing Mn^{2+} up to temperatures of 37°C. Mn_3O_4 formed at temperatures above 25°C while the hydrated oxides formed at lower temperatures. The structure of the hydrate was dependent on the type of anion present in solution. $SO_4^{=}$ gave γ-MnOOH and α-MnOOH while Cl^-, NO_3^- and ClO_4^- gave β-MnOOH. All the species investigated were metastable and converted to more stable forms upon ageing in these solutions. The stability of the precipitates increased according to the sequence:

$$\beta\text{-MnOOH} < \alpha\text{-MnOOH} < Mn_3O_4 < \gamma\text{-MnOOH} < \beta\text{-}MnO_2$$

The stability domains of the manganese oxyhydroxides in aqueous systems up to 37°C have thus been investigated extensively. Very little work has been published on stability domains in aqueous systems above this temperature.

Conventional gas-solid equilibria can also be used to determine the stability domains of the manganese oxides at higher temperatures. Schaefer (1982) studied the gas-solid equilibria of O_2, MnO, Mn_2O_3 and Mn_3O_4 at high temperature. This work reviewed previous experimental work e.g. Mah (1960) and presented results from electrochemical measurements. A comprehensive re-examination of the thermodynamic properties of manganese oxides, recently been undertaken by Fritsch & Navrotsky (1996), has confirmed the accuracy of earlier investigations. Keller *et al.* (1991) addressed the point defect chemistry of non-stoichiometric $Mn_{1-\Delta}O$ in high temperature equilibrium with $Mn_{3-\sigma}O_4$. Oxides of manganese have ranges of composition in which non-stoichiometric ratios of the ions occur in the solid state lattice. In $Mn_{1-\Delta}O$, Δ varies between 0 and 0,1 while σ can vary between –0,0012 and +0,0024 in $\alpha\text{-}Mn_{3-\sigma}0_4$ at temperatures above 1100°C. This confirms the observation made by Smeltzer (1986) that the lower oxides of the transition metals show higher deviation from stoichiometry. The degree of non-stoichiometry increases significantly for Mn_3O_4 prepared in aqueous systems (*vide infra*). Keller *et al.* (1991) showed that electrochemical equilibrium studies must take into account point defects in the determination of the free energy of equilibrium if accurate oxygen activity measurements are required. The manganosite-hausmannite equilibrium was shown to have an oxygen activity equilibrium equation of:

$$\log a_{O2}\ (MnO/Mn_3O_4) = 11{,}5 - 23100/T$$

Reduction oxidation equilibria are also used extensively in the study of mixed oxide (e.g. $MnFe_2O_4$) systems - Tang *et al.* (1991). Mapping the stability domains of the oxides using conventional oxidation-reduction equilibria is included in Chapter 3 to complement the Eh-pH diagrams.

1.2.5.1 Homogeneous Oxidation of Soluble Mn Species

The oxidation of soluble manganese forms must be considered when evaluating heterogeneous oxidation mechanisms. The sparing solubility of manganese in water means that these species will be present in low concentrations.

The oxidation of soluble manganese is used in potable and industrial water treatment processes and is an important consideration in the chemistry of natural water systems. Pourbaix's diagram for manganese shows that the formation of higher oxidation states of solid manganese directly from soluble Mn^{2+} at equilibrium requires progressively decreasing pH and increasing redox potential conditions. Metallic systems such as Fe, Ni, Co, Pb, Ti and V also exhibit this behaviour. A mechanistic framework for this observation has not been reported in the literature but this could be inferred from considerations of the stereochemistry of dissolved metallic ions. Kinetic effects may alter the practical application of Pourbaix's diagrams, e.g. the oxidation rates of Mn^{2+} and Fe^{2+} ions generally increase at higher pH conditions. Higher oxidation states under these conditions can also be achieved through heterogeneous oxidation reactions.

Homogeneous oxidation of Mn^{2+} by oxygen has been reported on extensively in the literature, e.g. Kessick & Morgan (1975), Pankow & Morgan (1981), Hem (1981), Hem & Lind (1983), Groth (1987) and Davies & Morgan (1989). The reaction is autocatalytic as the solid reaction products increase the rate of reaction - Hem (1981). Overall, oxidation may proceed according to the following reactions:

$$3Mn^{2+}_{(aq)} + \tfrac{1}{2}\, O_{2(aq)} + 3H_2O_{(aq)} \rightarrow Mn_3O_{4(s)} + 6H^{+}_{(aq)}$$

$$2Mn^{2+}_{(aq)} + \tfrac{1}{2}\, O_{2(aq)} + 3H_2O_{(aq)} \rightarrow 2MnOOH_{(s)} + 4H^{+}_{(aq)}$$

The first reaction is favoured at increased temperature and is more sensitive to temperature than the second. Hem (1981) attributed this to be due to a higher energy barrier required for removing surplus water molecules during the formation of Mn_3O_4. The homogeneous oxidation of Mn^{2+} at ambient temperature and pressure is known to be a slow process that is more difficult to achieve as the pH of solution decreases. In comparison, substantial oxidation of Fe^{2+} will take seconds to hours compared to hours or days for Mn^{2+} - Groth (1987) and Pankow & Morgan (1981). The rate of oxidation displays pseudo first-order kinetics in dissolved manganous ion activity $[Mn^{2+}]$ if the amount of precipitate surface is large in comparison to $[Mn^{2+}]$. The reaction rate is also

proportional to pO_2 and $[OH^-]^2$. The rate expression suggested by several of the above authors for the autocatalytic oxidation of Mn^{2+} at constant pH and oxygen concentration has the form:

$$\frac{d[Mn^{2+}]}{dt} = -k_1[Mn^{2+}] - k_2[Mn^{2+}]A_{Mnppt}$$

where: $[Mn^{2+}]$: concentration of dissolved manganous ions $[mol.l^{-1}]$

k_1: rate constant for homogeneous oxidation $[s^{-1}]$

k_2: rate constant for heterogeneous oxidation $[liter.m^{-2}s^{-1}]$

A_{Mnppt}: total surface area of precipitated solids $[m^2m^{-3}]$

The rate constants reported in most of the above works generally only apply to the experimental conditions being investigated and are not in consistent units. A comparison of reaction rates with this thesis can therefore not be made. Pankow & Morgan (1981) have discussed mathematical aspects of autocatalytic kinetics.

Groth's (1987) review discussed a more general kinetic equation of similar form:

$$\frac{d[Mn^{2=}]}{dt} = -k_0[Mn^{2+}][OH^-]^2\, p(O_2)T - k_3[Mn^{2+}][Mn_xzH_2O][OH^-]^2 p(O_2)T$$

Oxidation of manganese was expected to proceed via similar kinetics to that of soluble iron. For the case of manganese, x = 1,3-1,5 and the precipitate is thus not a fully oxidised product. The surface of the precipitated solid is semiconducting and can ionise adsorbed oxygen molecules. The ionised oxygen then oxidises soluble manganese and not surface absorbed Mn^{2+} ions. When x = 2 the catalytic effect is lost as MnO_2 strongly absorbs Mn^{2+}. The author did not know of a similar description for iron.

The mechanisms of oxidation have also been discussed by Kessick & Morgan (1975) who suggested that the rate determining step of the Haber-Weiss type of auto-oxidation mechanism applies to the kinetics of oxidation of soluble $Mn(OH)_2$. It was suggested that the rate-determining step of soluble manganese removal involves a one-electron transfer through the loss of a hydrogen atom:

$$Mn(OH)_{2(aq)} + O_{2(aq)} \rightarrow MnOOH_{(s)} + HO_2$$

This reaction has a transition state of the form:

$$HO\text{-}Mn_{(aq)}\text{-}O\text{---}H\text{---}O_2$$

This intermediate arises after hydroxyl ions have displaced water molecules in the inner hydration shell of the hexaquo Mn^{2+} ion. The probability of simultaneous displacement of water and collision with oxygen is considered low. Fallab (1967) pointed out that the Haber-Weiss mechanism has not been proven conclusively. A definitive study and confirmation of the mechanism of homogeneous oxidation of Mn^{2+} is therefore outstanding.

It is possible to oxidise Mn^{2+} by electrochemical action at an anode surface to Mn^{3+} or MnO_2. This is an important reaction for the manufacture of battery active electrolytic MnO_2 and occurs at oxygen evolving anodes in electrowinning circuits which contain dissolved manganese ions (e.g. Mn & Zn electrowinning). The Mn^{3+} undergoes disproportionation to Mn^{2+} and Mn^{4+} which hydrolyses to electrochemically active, hydrated $MnO_{2(s)}$ according to the equilibrium reaction:

$$2Mn^{3+}_{(aq)} + 2H_2O_{(aq)} = MnO_{2(s)} + Mn^{2+}_{(aq)} + 4H^{+}_{(aq)}$$

Pourbaix *et al.* (1974) discussed the general thermodynamics of disproportionation reactions and showed that the amphoteric properties of a species can give rise to unstable, stable and metastable domains on an Eh-pH diagram. Welsh (1967) showed that it is possible to stabilise the Mn^{3+} ion in solutions that have high acidity (200g.l^{-1} H_2SO_4) and moderately low temperature (20°C). The kinetics of the disproportionation reaction was 4th order in $[Mn^{3+}]$ and again the surface of the precipitated solid was the preferred site for the reaction. Under alkaline conditions, the Mn^{3+} is unstable with a negligible solubility. The oxidation reaction of Mn^{2+} to Mn^{3+} at an anode surface which is evolving oxygen appeared to be a simple electron transfer process that is favoured at lower current densities.

The precipitated solids can influence reaction mechanisms and kinetics. Heusler & Grzegorzewski (1990) reported a mechanistic study of the oxidation process on a Pt electrode. Two statistically independent charge transfer processes, consisting of unhydrated manganese ions and oxygen complexes with 4 water molecules, were proposed to account for the kinetics measured from rotating ring-disc and rotating quartz frequency balance experiments. The rate determining steps in the charge transfer process involve:

$$Mn^{2+}_{(aq)} \Longleftrightarrow Mn^{2+}_{(s)}$$
$$\{O^{2-}\cdot 4H_2O\}_{(ads)} \Longleftrightarrow O^{2-}\cdot 4H_2O_{(s)}$$

where: $\{O^{2-}\cdot 4H_2O\}_{(ads)}$ denotes the hydrated oxygen adsorbed at the oxide side of the double layer.

The adsorbed oxygen ions are formed in a fast equilibrium reaction with hydrogen ions and water according to:

$$H_2O_{(aq)} \Longleftrightarrow \{O^{2-}\}_{(ads)} + 2H^+_{(aq)}$$

Transient currents were found to be only due to manganese ion transfer and consequently variations in the stoichiometry of the oxide could be expected. Hydrated oxide layers were formed in these experiments. Large positive overpotentials created high rates of nucleation with small crystals that enclosed excess water. This and later works, e.g. Zhang & Park (1994) and Kao & Weibel (1992), confirm uncertainties which surround the identification of the reaction intermediates. However, it is generally accepted that Mn^{3+} is an intermediate of the electrochemical formation of MnO_2.

The above works confirm that both chemical and electrochemical oxidation mechanisms are strongly influenced by the solid state chemistry of the products of reaction. These aspects are discussed further in the following sections on the heterogeneous oxidation of iron and manganese hydroxides.

1.2.5.2 Heterogeneous Oxidation of Iron Hydroxides and Mixed Iron-Manganese Oxides

Transition metal hydroxides have been studied for more than one hundred years. The following is a synopsis of an article which addresses some of the structural and mechanistic considerations relevant to the oxidation of $Fe(OH)_2$.

Olowe & Génin (1991) reported on the products obtained from oxidation of precipitated $Fe(OH)_2$ in precisely controlled experiments conducted at room temperature. The influence of the initial ratio of soluble reactants (viz. $R=[FeSO_4.7H_2O]/[NaOH]$) was classified into three types of sulphate based solutions reacting with air.

- "Acid" solutions contained excess metal ions and yielded lepidocrocite (γ-FeOOH) and goethite (α-FeOOH) upon oxidation of the hydroxide. Intermediates containing sulphated ferrous hydroxides (green rust 2) were identified.
- Stoichiometric addition of reacting ions or "neutral" solutions yielded Fe_3O_4 (magnetite) from a hydrated intermediate $Fe(OH)_2.xFeOOH$.
- "Alkaline" solutions containing an excess of OH^- yielded goethite (α-FeOOH) from amorphous and hydrated $yFe(OH)_2.zFe(OH)_3$ intermediates.

Goethite was the most dominant product of oxidation in both extremities of the "acid" and "alkaline" regions. The analytical techniques used to characterise products and intermediates included XRD, Mössbauer Spectroscopy for quantitative phase composition

and Transmission Electron Microscopy (TEM). A ratio of R=0,625 was a characteristic point at which a crystalline basic sulphate phase appeared within the hydroxide phase. Oxidation times for complete conversion did not increase with increasing R beyond this characteristic point. Oxidation times with excess hydroxide were roughly half of those with excess metal ion. Six different characteristic points with different mechanisms of oxidation and intermediates were proposed which allowed for quantitative prediction of solid phase compositions. At the stoichiometric value of R=0,5 the proposed mechanism was:

$$3Fe(OH)_{2(s)} + \tfrac{1}{2}\, O_{2(aq)} \rightarrow Fe(OH)_2.2FeOOH + H_2O_{(aq)}$$

$$Fe(OH)_2.2FeOOH \rightarrow Fe_3O_{4(s)} + 2H_2O_{(aq)}$$

The corrosive dissolution of iron in oxygenated pure water can thus yield Fe_3O_4 directly without the stabilisation of hydrated oxides. The other mechanisms at different values of R will not be discussed further. A detailed analysis of the mechanisms of structural transformations in the solid state was not included in Olowe & Génin's work.

The iron system also shows some difference to the manganese system in the structural form of the predominant oxyhydroxide product, as stabilisation of iron in a 4+-oxidation state is not possible. Goethite has an orthorhombic crystal habit while feitknechtite and manganite are hexagonal and monoclinic, respectively. Mechanisms of structural transformation that are proposed for iron and manganese oxidation processes thus cannot be interchanged freely. It is anticipated that similar care must be taken when transposing mechanisms of oxidation of transition metals such as $Co(OH)_2$ and $Ni(OH)_2$ to $Mn(OH)_2$. Olowe & Génin's work, however, does demonstrate the importance of the history of solution conditions on product composition and oxidation mechanisms.

1.2.6 Heterogeneous Oxidation of Manganous Hydroxide

The oxidation sequences of transition metals are determined by fundamental electronic structures and form complicated networks of reaction pathways between different structural forms of the intermediates and reaction products as shown in Figure 1.2. Manganous hydroxide is the starting species for many of the solid state oxidation pathways in the manganese system. The following paragraphs discuss oxidation sequences with oxygen and electrochemical action.

Gmelins (1973) reviewed the oxidation of solid manganese hydroxide by oxygen based on work by Bricker (1965) and Klingsberg & Roy (1959). High purity $Mn(OH)_2$ oxidises slowly in air at ambient temperature. Oxidation starts at amorphous centres and then proceeds to crystalline sites within individual particles. Higher temperatures favour the

formation of sheet-structured crystalline β-$Mn(OH)_2$. Preparations of $Mn(OH)_2$ from manganese metal (360°C, pH_2O = 136atm, 48hrs in a Ag-lined pressure bomb) and other starting solutions have been described by Bricker (1965). Oxidation at ambient conditions leads topotactically to β-MnOOH or a mixture of β-MnOOH and Mn_3O_4. Direct conversion of metal to Mn_3O_4 is possible as well. Oxidation of metal in the temperature region 150 - 400°C in air proceeds with linear kinetics for the weight change with respect to time and the formation of a porous layer of Mn_3O_4. This suggests that the oxide layer does not have strong passivating characteristics. Further oxidation to higher oxides shows parabolic kinetics for the weight change with respect to time which is indicative of solid state diffusion control as discussed above for gas phase oxidation processes.

Davies & Morgan (1989) investigated the heterogeneous oxidation of Mn^{2+} on the surfaces of a number of different metal oxides (α-FeOOH, γ-FeOOH, δ-Al_2O_3 and SiO_2). It was proposed that the mechanism of Mn^{2+} oxidation that accounted for the increased rate of oxidation proceeded via the following steps:

- Mn^{2+} complexation with bidentate surface hydroxyl groups to form co-ordinated surface structures
- Adsorption of oxygen to form a Mn^{2+}- O_2 complex
- Formation of a Mn^{3+}- O_2^- superoxide complex following electron transfer
- Precipitation of products

The initial rate of oxidation was dependent on the initial equilibrium concentration of bidentate surface species. The metal oxides with higher surface concentrations of OH-groups displayed proportionately higher oxidation rates. Values for the OH site density parameters are shown in Table 1.7. Anionic ligands generally lower the oxidation rates due to complexation with Mn^{2+}, similarly, cations compete for surface adsorption sites and also reduce oxidation rates. Davies & Morgan (1989) reported activation energies, oxidation rates and mass transfer coefficients for oxygen for their experiments.

Table 1.7 OH-groups surface site density for different metal oxides

Oxide	Site density [OH-groups.nm^{-2}]
α-FeOOH	13
γ-FeOOH	9,6
δ-Al_2O_3	5,0

Ref. Davies & Morgan (1989)

From these results it can be anticipated that the oxidation of Mn^{2+} on a $Mn(OH)_2$ surface should proceed at higher rates than for these solids. Davies & Morgan point out that different kinetics can be expected in systems that are supersaturated with solid $Mn(OH)_2$. As the reaction proceeds, adsorption and oxidation will reduce the bulk concentration of Mn^{2+}. If the particles of $Mn(OH)_2$ are porous then replenishment of Mn^{2+} for adsorption could conceivably occur from within the particles via a dissolution reaction that maintains the solubility equilibrium.

The above studies suggest that the solid products of manganese oxidation may be anhydrous or hydrated and may contain cations with mixed valence states. More recent work by Kaczmarek & Wolska (1993a,b) shows that cation deficient Mn_3O_4 can be formed from oxidation of manganous hydroxide at temperatures below 50°C. This work is discussed in more detail below and in section 5.4.3.

The electrochemical oxidation of precipitated manganous hydroxide has been investigated by a number of researchers, e.g. Ambrose & Briggs (1971), Briggs & Davies (1979), Bauer *et al.* (1985), Gosztola & Weaver (1989), Desoukki *et al.* (1990) and Hernandez *et al.* (1991). Experiments conducted in alkaline conditions on cathodically deposited hydroxide films on the surface of manganese metal electrodes have to incorporate specific controls to limit the effect of dissolved oxygen which alters the electrochemical properties of the films. Cathodically deposited hydroxides are crystalline. The product obtained after complete electrochemical oxidation is generally "δ-MnO_2" that also has a sheet-like structure, with the rate of charge transfer being limited by a solid phase reaction - Ambrose & Briggs (1971). It is also possible to evolve oxygen from these electrodes at sufficiently high current densities. The electrochemical oxidation of $Mn(OH)_2$ showed two steps in the polarisation curves and was irreversible as no hydroxide formation could be detected during reduction of MnO_2. Ambrose & Briggs (1971) argued that a two step oxidation process such as:

$$Mn(OH)_{2(s)} + OH^-_{(aq)} \rightarrow MnOOH_{(s)} + H_2O_{(s)} + e^-$$
$$MnOOH_{(s)} + OH^-_{(aq)} \rightarrow MnO_{2(s)} + 2H_2O_{(aq)} + e^-$$

was an oversimplification particularly since MnOOH could not be identified on the XRD patterns. The development of a more complex model that recognised the influence of individual crystallites and the collapse of the sheet structure was suggested. Briggs & Davies (1979) also identified a two stage oxidation process and the "δ-MnO_2" end-product and pointed out similarities with the oxidation of $Ni(OH)_2$. The sheet-like structure of the $Mn(OH)_2$ was stable over a wide range of composition (viz. $MnO_{1,2}$ or 40% Mn^{3+}) suggesting considerable structural hysteresis. A diffusion coefficient of 10^{-11} $cm^2.s^{-1}$ for the rate controlling solid state process was estimated from the current-time curves.

Bauer *et al.* (1985) found that inserting $Al(OH)_3$ into the $Mn(OH)_2$ resulted in five fold increase in charge capacity and improved faradic efficiency. They also showed that the electrochemical characteristics of the oxidation products depended on the method of film preparation. Films formed at lower pH (e.g. pH 10 *c.f.* pH 13) gave oxidation products which contained the electrochemically inactive spinel structured Mn_3O_4.

These studies suggest that chemical and electrochemical oxidation may proceed via similar solid state reaction mechanisms.

Mn_3O_4 formed by oxidation of $Mn(OH)_2$ is unstable in water under certain Eh and pH conditions and may be oxidised further. Murray *et al.* (1985) showed that the solution pH and dissolved manganese concentrations under these conditions were consistent with Giovanoli's coupled pair of manganese oxide protonation and manganous re-oxidation half-reactions:

$$3Mn_3O_{4(s)} + 6H^+_{(aq)} \rightarrow 6MnOOH_{(s)} + 3Mn^{2+}_{(aq)}$$
$$3Mn^{2+}_{(aq)} + ½\ O_{2(aq)} + 3H_2O_{(aq)} \rightarrow Mn_3O_{4(s)} + 6H^+_{(aq)}$$

A progressive decrease in pH can therefore be expected for under these reaction conditions.

1.2.7 Structural Aspects of Oxidation

Manganous ions form hydrates with octahedrally co-ordinated water molecules, $Mn(H_2O)_6^{2+}$ - Chiswell & Mokhtar (1986). These species have relatively large Stokes (3,68Å) and hydration (4,38Å) radii in comparison to metal-metal (1,24Å) interatomic distances - Gmelins (1973). The theoretical and experimental hydration energies of the divalent transition metals increase with increasing atomic number (viz. Mn<Fe<Co<Ni) which is explained by d-orbital ligand field splitting - Cotton & Wilkinson (1976). The rate constants for water molecule exchange from the inner sphere of the metal ions at 25°C are given in Table 1.8. Manganese is thus the most reactive of this series of metals and forms one of the least stable hydrates. Stereochemical and mechanistic considerations of the redox reactions of dissolved ions are given in Basolo & Pearson (1967). Structural characteristics of dissolved ions can be directly linked to various physical, chemical and kinetic effects. For example, Vijh & Randin (1975) studied the deaquation of ionic species during metal deposition reactions. The deaquation process contributes significantly to the overpotential for deposition. The rate constants of inner-sphere, water substitution processes were shown to correlate linearly with the exchange current density for metal deposition processes.

Table 1.8 Rate constants for exchange of co-ordinated water from metal ions at 25°C

Cation	k_1 [sec^{-1}]	E_a [$kcal.mol^{-1}$]
Mn^{2+}	3×10^7	8,7
Fe^{2+}	3×10^6	8,3
Co^{2+}	1×10^6	8,6
Ni^{2+}	3×10^4	12,2

Ref.: Basolo & Pearson (1967)

The octahedral co-ordination of manganese with 6 oxygen atoms is also the basic building block used to explain most of the solid state structures of manganese oxides and oxyhydroxides. Sherman (1984) analysed the nature of the chemical bonding in different manganese octahedra using molecular orbital theory and was able to confirm some of the spectroscopic transition energies of manganese oxides. A summary of Sherman's results for the nature of the M-O bond in different co-ordinations is given in Table 1.9. The argument is presented that while crystal field theory has been successful in explaining the chemistry of the transition metals its physical basis is unfounded. Molecular orbital theory provides the correct physical approach. The nature of the Mn-O bonding in Mn^{2+} clusters is ionic and becomes more covalent as the formal oxidation increases. Crystal field splitting increases and exchange splitting in the d-orbitals decreases with increasing covalence. This explains the exchangeable cationic nature of Mn^{2+} in complex oxides and the low solubility of Mn^{4+} in solution. Mn^{3+} and Mn^{4+} can substitute in manganese oxide lattices. Tailhades *et al.* (1997) used this bonding approach to explain the higher oxidation reactivity at high temperature of Mn cations in octahedral interstices compared to tetrahedral Mn cations.

Table 1.9 Nature of bonding in octahedral clusters of manganese oxides

Oxidation state	Cluster	%Covalent
Mn^{2+}	MnO_6^{10-}	29,5
Mn^{3+}	MnO_6^{9-}	69,3
Mn^{4+}	MnO_6^{8-}	73,6

A summary of the crystal structure parameters of manganese and its oxides is given in Appendix B. The crystal structure of α-Mn has been described by Sully (1955) as a

"simple", body-centred, cubic lattice with 58 atoms in the unit cell. There are 4 kinds of atoms (X, A, D_1, D_2) in the unit cell with 2 clusters of 29 atoms which have a local tetrahedral symmetry. Proult & Donnadieu (1995) showed that the structure consists of a topologically close packed (TCP) lattice with clusters of atoms having 16 fold co-ordination and that classic interpretations have ignored defect (vacant lattice positions) structures. TCP lattices are so-called major skeletons with clusters in 12, 14, 15 and 16 fold co-ordination forming a continuous network. α-Mn and isostructures, such as the chi phase $Fe_{36}Cr_{16}Mo_{12}$, are known examples of the anomalous 13-fold co-ordination of clusters that have a discontinuous major skeleton. Proult & Donnadieu (1995) proposed a unit cell consisting of two 17-atom clusters and four 16-atom clusters sharing atoms to give 58 atoms total per unit cell. The 16 atom clusters are distorted polyhedra built from vacant (¼¼¼) lattice positions in the 17-atom clusters. These defects create large numbers of translation boundaries that can be described by fault vectors, R. Surprisingly, only two of these vectors could be identified for α-Mn, R = 1/4<111> and R = 1/3<110>. The authors conclude that earlier descriptions of the structure of α-Mn are valid but these should be adapted to recognise defect structures.

Solid divalent hydroxides exist in different crystalline and amorphous forms. The hydroxides of a number of divalent metals (e.g. Mn, Co, Ni, Fe, Mg, Cd and Zn) form an isostructural series of crystalline structures termed brucite ($Mg_3(OH)_6$) sheets. The structure can be visualised as consisting of layers of hydroxyl ions in hexagonal closest packing with the metal cations occupying the interstices - Hurlbut (1971).

The hydroxyl ions occupy the apices of a regular octahedron with the metal cation at the centre. These octahedra then join by sharing the (111) faces to form sheets. Figure 1.3 is a schematic representation of an individual octahedron and a partial sheet of four combined octahedrons. The resultant trioctahedral sheets form patterns of interlocking hexagonal rings of hydroxyl ions with the metal cation in the centre of each ring. Hydroxyl ions are shared between adjacent octahedra and three cations are coordinated with each hydroxyl octahedron (*vide infra* Figure 1.4). The hydrogen atoms of the hydroxyl ions are located normal to the oxygen sheets and thus with the cations form cationic layers sandwiched between the oxygen layers. These layers (also termed Van der Waals space) possess intercalation properties that can substitute small ions (e.g. Li in birnessite type MnO_2). Gibbsite ($Al(OH)_3$) sheets accommodate trivalent cations which only fill two thirds of the octahedral interstices. The dioctahedral sheet forms patterns of hexagonal rings of cations with the site at the centre of each ring being unoccupied. Both the gibbsite and the brucite sheets are electrically balanced. Lattice parameters for a number of examples of the brucite structured hydroxides are given in Table 1.10.

Figure 1.3 Brucite sheet structure

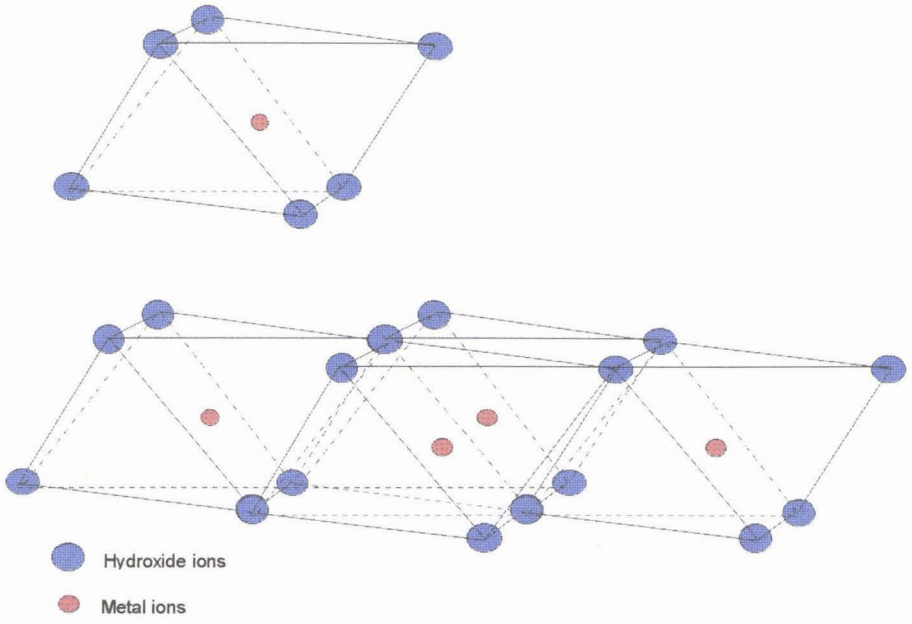

Figure 1.4 Brucite sheet. Large spheres hydroxyl, small spheres metal cations

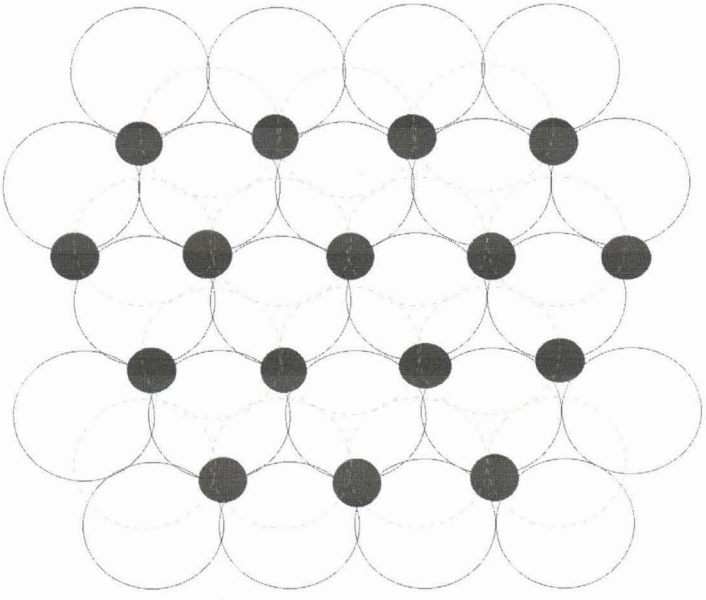

Table 1.10 Structural parameters for divalent hydroxides

Formula	*a* [Å]	*c* [Å]	Density [g.cm^{-3}]
β-$Mn(OH)_2$	3,34	4,68	3,258
β-$Co(OH)_2$	3,17	4,66	3,697
α-$Ni(OH)_2$	3,07	4,61	3,940
$Fe(OH)_2$	3,24	4,47	3,400
$Mg(OH)_2$	3,13	4,75	2,363
α-$Zn(OH)_2$	3,11		2,667
α-$Cd(OH)_2$	3,49	4,69	4,810

Ref. Gmelins (1973)

a: Metal-metal ion interatomic distance

c: Interlayer distance between sheets

$Cd(OH)_2$ is stable allotrope.

Several of these hydroxides have two allotropes, e.g. Co and Ni, while Zn has six. The amorphous form of manganous hydroxide is usually termed α-$Mn(OH)_2$. The distortion of the lattice in the *c* direction for the Fe, Mn, Co and Ni systems, given by the c/a ratio, increases with increasing cation size as expected. Successive sheets sometimes become disordered to give a "turbostratic" structure as reported for β-$Ni(OH)_2$ - Delahaye-Vidal *et al.* (1995). Nørlund-Christensen (1965) and Nørlund-Christensen & Olliver (1972) determined the chemical and magnetic structures of $Mn(OH)_2$ using structural refinement techniques.

The thermal dehydration of the hydroxides is possible according to the general reaction:

$$M(OH)_{2(s)} \rightarrow MO_{(s)} + H_2O_{(g)}$$

Robins (1968) showed that this reaction typically occurs in the temperature range 200°C to 500°C for a number of divalent metals. This hydration reaction is used in this thesis to quantify the extent of the $Mn(OH)_2$ oxidation reaction.

α-Mn_3O_4 (hausmannite) has a tetragonally distorted spinel structure caused by the Jahn-Teller effect associated with a d^4 electronic configuration on Mn^{3+}. The tetragonal distortion can be visualised as an elongation in the *c* axis of the MnO_6 octahedra. A reversible phase transition to a cubic phase, β-Mn_3O_4, occurs in neutral atmospheres at 1160°C. Spinel structures consist of face-centred cubic packed oxygen atoms and include Ni_3O_4, Fe_3O_4, Co_3O_4 - Hauffe (1965). Each unit cell (8 units of AB_2X_4) has 64

tetrahedral (A sites) and 32 smaller octahedral (B sites) interstices. Figure 1.5 shows these arrangements for half of the unit cell of the tetragonal spinel.

Figure 1.5 Spinel structure of Mn_3O_4

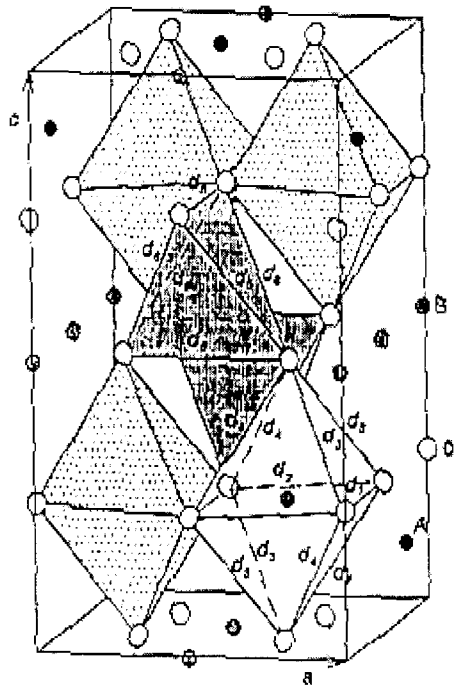

Ref.: Vila *et al.* (1996)

o : oxygen atoms, • : manganese atoms

Each family of ions in the structure forms interlaced face centred cubic sublattices and the distribution of ions within each sublattice has a significant effect on the physical, magnetic and chemical properties of these materials. The divalent metal ions usually occupy eight of the A sites while 16 trivalent metal ions occupy the B sites in a normal spinel, i.e. $8*(M^{2+})[N^{3+}{}_2]O^{2-}{}_4$. Inverse spinels have the formula $8*(N^{3+})[M^{2+}N^{3+}]O^{2-}{}_4$ where only half the trivalent ions occupy octahedral positions and no divalent cations occupy tetrahedral sites. Mn_3O_4 is classed as a normal spinel in this respect. A range of intermediate spinels exists between these limits of cation distribution with defects and microtwinning being common structural features.

Keller & Dieckmann (1985), Kaczmarek (1993a) and Couderc *et al.* (1994) have reported on these features for hausmannite. The high temperature defect structure of Mn_3O_4 has been studied by Keller & Dieckmann (1985) who found that cationic vacancies at high oxygen activities and manganese interstitials at low oxygen activities are the dominant defect species for both α-Mn_3O_4 and β-Mn_3O_4. The transition temperature for the equilibrium of these phases was found to increase with increasing non-stoichiometry from

1134,6°C to 1176,2°C at the triple point for $Mn_{1-\Delta}O$:α-$Mn_{3-\sigma}O_4$:β-$Mn_{3-\sigma}O_4$. Frondel (1953) analysed a naturally occurring mineral called hydrohausmannite and determined that the structure was similar to synthetic manganese oxyhydroxides obtained from the oxidation of $Mn(OH)_2$ with one additional XRD reflection (002) noted in comparison to the anhydrous Mn_3O_4. The stoichiometry of this mineral also suggested a defect structure. Frondel (1953) proposed that a similar range of solid solutions apply for the hydrated oxides as for Verwey & de Boer's anhydrous defect structures. This series can be represented by the following sequence:

$$(Mn_4^{2+})[Mn_8^{3+}]O_{16} \Leftrightarrow (Mn_{4-3x}^{2+}Mn_{2x}^{3+}V_x)\,[Mn_8^{3+}]O_{16} \Leftrightarrow V_{1\ 1/3}\,Mn_{10\ 2/3}^{3+}O_{16}$$

α-Mn_3O_4 (x=0) γ-Mn_2O_3 (x=$1^1/_3$)

where: V: cationic vacancies

(Mn_x): species in a tetrahedral interstice

[Mn_x]: species in a octahedral interstice

(Note: Other authors, Oku *et al.*(1975) claim a different filling of interstices in γ-Mn_2O_3 , $V_{1\ 1/3}\ Mn_{2\ 2/3}^{3+}\ [Mn_8^{3+}]O_{16}$ i.e.,. two thirds of the tetrahedral interstices are filled.)

The unit cell for the hydrated series of compounds was represented by:

$$(Mn_{4-2x}^{2+}Mn_x^{3+}V_x)\,[Mn_8^{3+}]O_{16-x}(OH)_x$$

Frondel (1952) found a value of x = 1,155 for the naturally occurring mineral. The equivalent unit cell according to Starke for the series of hydrated iron oxides was:

$$(Fe_{8-x}^{2+}V_x)_8\,[Fe_{16}^{3+}]O_{32-2x}(OH)_{2x}$$

Feitknecht *et al.* (1962) later found that synthetic hydrohausmannite was actually a mixture of two phases, α-Mn_3O_4 and β-MnOOH (feitknechtite), which was confirmed by Bricker (1965) who recommended rejection of the name hydrohausmannite. The hydrated series that Frondel (1953) proposed is therefore not a correct interpretation. The distribution of vacancies and hydroxyl groups in the structures of hydrated Mn and Fe oxides can also not be compared on this basis. This type of comparison between different metals could account for variations in oxidation mechanisms and the stoichiometry of the oxidation products.

The defect structures of anhydrous and hydrated hausmannite have been analysed by Kaczmarek & Wolska (1993a, 1993b, 1994). Anhydrous manganese oxides were prepared by decomposing a number of manganese salts in air at 1000°C. Products with Mn^{3+}/Mn^{2+} ratios up to 3 were obtained which retained the hausmannite structure. The defect

concentrations of these oxides were dependent on the Mn^{3+}/Mn^{2+} ratio and were shown to be due to cationic vacancies in the tetrahedral (A) sublattices for $Mn^{3+}/Mn^{2+} < 2,4$. These vacancies are due to oxidation of Mn^{2+} to Mn^{3+} in the A sublattice. When the Mn^{3+}/Mn^{2+} increased above 2,4, "saturation" of the A sublattice occurred with further vacancies distributing randomly between the A and B sublattices. General structural formulas were proposed for the unit cells of these structures that are similar to Verwey & de Boer's unit cell (*vide supra)*:

$(Mn_{8-3x}{}^{2+}Mn_{2x}{}^{3+}V_x)\ [Mn_{16}{}^{3+}]O_{32}$ $\quad Mn^{3+}/Mn^{2+} < 2,4$

$(Mn_{8-3x}{}^{2+}Mn_{5x/2-1/6}{}^{3+}V_{x/2+1/6})\ [Mn_{97/6-x/2}{}^{3+}V_{x/2-1/6}]O_{32}$ $\quad Mn^{3+}/Mn^{2+} > 2,4$

The oxidation of $Mn(OH)_2$ prepared by precipitation of $Mn(NO_3)_2$ with NaOH at room temperature showed significantly different distributions of defects. These products also retained significant quantities of structural water (3% m/m H_2O) and hydroxyl ions and only showed β-MnOOH after prolonged oxidation times. The oxidation state of the Mn cations was controlled by varying the exposure time to the oxidant (air). However, the amount of hydroxylation appeared to be rather accidental. Vacancies in the hydrated oxides were found to be randomly distributed between the A and B sublattices. A general formula for the unit cell was proposed:

$(Mn_{8-3x+y}{}^{2+}Mn_{5x/2-y}{}^{3+}V_{x/2})\ [Mn_{16-x/2}{}^{3+}V_{x/2}]\ O_{32-y}(OH)_y$

where: x : number of vacancies per unit cell

y : number of OH groups per unit cell

The hydroxyl groups have a significant influence on the anionic sublattice and the creation of vacancies in adjoining sublattices. Stoichiometric deviations of Mn^{3+}/Mn^{2+} up to 2,97 were recorded. The hausmannite structure was able to accommodate the hydrates and oxidation variations without a major shift in the XRD peak positions while the relative intensities of the peaks did change. This was also found by Simon (1943). Kaczmarek & Wolka's (1993b) structural formula for the hydrated hausmannite unit cell is significantly different to that of Frondel (1953) (*vide supra*). Frondel's formula allows one vacancy to appear for every hydroxyl group inserted into the structure. In comparison, Kaczmarek & Wolska allow different ratios of cation vacancy to hydroxyl group. This work is however significant in identifying vacancies in both A and B sublattices for hydrated manganese oxides. The nature of the solid state oxidation mechanism that accounts for these features has not been elucidated in the studies that have been reviewed here.

In summary, considerable structural rearrangement occurs in the oxidation of Mn to its oxides. The final products of hydrothermal oxidation are tetragonally distorted spinel structures that have XRD patterns that are similar to the naturally occurring mineral

hausmannite or Mn_3O_4. The hausmannite structure is able to accommodate substantial crystalline water and cationic defects that are distributed in the A and B sublattices and some debate is ongoing with respect to the valence of the manganese ions. This aspect was addressed in the investigations on the structural characteristics of the oxidation products of hydrothermal oxidation of $Mn(OH)_2$ in Chapter 4.

1.2.8 Summary of Literature Review and Conclusions

A summary of observations made and the conclusions that can be drawn from the above review is given in the following paragraphs.

- The literature on the study of the dissolution and oxidation of the different forms of manganese is extensive and covers many areas of technological importance. Hydrothermal dissolution of manganese metal particles in this work occurs in alkaline conditions while corrosion technology generally focuses on dissolution processes that occur under acidic conditions. Research into the alkaline dissolution of manganese metal thus requires different perspectives for understanding the possible corrosion or dissolution mechanisms.

- The oxidation of metals and alloys in gas and liquid phases results in the formation of surface layers of oxides and/or hydroxides. These surface layers have a significant influence on the physical and chemical properties of the metals. The rate of oxidation before the establishment of the layer is usually higher than in the growth stage when slower solid state diffusion processes determine kinetics. The layers may contain single or multiple phases of oxides and/or hydroxides. Parabolic kinetics in gas and aqueous systems are a result of reactions that are controlled by the rate of diffusion of lattice defects such as vacancies and interstitials. Short-circuit diffusion effects are known that can increase oxidation rates by several orders of magnitude. These effects are due to point, line and boundary defects in the crystal lattice. Manganese has been reported to exhibit higher rates of oxidation in comparison to the other transition metals and is classified as an active metal. Linear kinetics have been reported for low temperature (150°C to 400°C) oxidation of manganese metal. Oxide formation under these conditions does not coincide with effective passivation during the oxidation reaction. High temperature oxidation exhibits solid state diffusion controlled parabolic kinetics. A kinetic and mechanistic study of the active dissolution and oxidation of manganese metal in aqueous, alkaline media at elevated temperatures has not been reported.

- The dissolved oxygen content of water may influence the initial mechanisms of dissolution at metallic or oxide portions of a manganese surface. The catalytic effects of oxygen in dissolution mechanisms have not been reported for manganese metal.

- The surface of newly formed manganese metal will reduce any available oxygen to form manganese oxides. The formation of metallic dusts in the presence of oxygen will thus result in the formation of surface oxides. Moisture in the air can adsorb on the surface to form limited quantities of manganous hydroxide. These products are formed in the simplified oxidising sequence:

  $$Mn \rightarrow MnO \text{ (or } Mn(OH)_2) \rightarrow Mn_3O_4 \rightarrow Mn_2O_3$$

- Potential-pH diagrams have been reported which define the stability domains of the different forms of manganese and its oxyhydroxides both for low and high temperature regimes. The estimation of domain limits in these works is based on thermodynamic data for the anhydrous divalent oxide (MnO). Thermodynamic data for the hydroxides of manganese is lacking particularly at elevated temperatures. Limitations in the use of the Eh-pH diagrams have been reviewed and extended.

- Studies on the surface phenomena of the lower oxides of manganese are limited in comparison to those for MnO_2. MnO_2 can be formed by the action of strong oxidants, thermal decomposition or electrolysis. The lower oxides of manganese such as MnO have higher degrees of non-stoichiometry and consequently exhibit higher rates of lattice diffusion than oxides such as Mn_3O_4 and Mn_2O_3.

- Similarity exists between the behaviour of the transition metals Mn, Co, Fe and Ni in a number of aspects viz., form of Eh-pH diagram, hydrolysis and oxidation sequences and the structure of the divalent hydroxides and spinel oxides. This behaviour is predictable and can be inferred from the electronic structures of the metals and their compounds. Similarities between the mechanisms of oxidation for these metals have not been reported. Although the divalent hexaquo manganese ion is the least stable and most reactive of this group of metals, the oxidation of soluble manganese occurs at much lower rates than ferrous oxidation under the same solution conditions.

- The rate of oxidation of soluble manganese is increased substantially by catalytic and autocatalytic reaction mechanisms that are mediated by the hydroxyl groups on the surfaces of various solid oxides.

- Oxidation studies of solid $Mn(OH)_2$ in the literature are generally conducted at ambient temperatures. Kinetic studies have not been reported in which the rate of

oxidation is controlled by a surface reaction or a solid state diffusion process. The product of chemical oxidation of $Mn(OH)_2$ by oxygen is generally a mixture of Mn_3O_4 and β-MnOOH. Manganese oxides with decreasing crystallinity are produced in the sequence Mn_3O_4, β-MnOOH and δ-MnO_2 by air oxidation of $Mn(OH)_2$ suspended in water at low temperature. Mn_3O_4 is formed exclusively at temperatures above 30°C. The product of electrochemical oxidation of Mn^{2+} ions is generally MnO_2 that forms due to the disproportionation of Mn^{3+} ions.

- The mechanisms of iron hydroxide oxidation are dependent on the ratio of metal to hydroxide activity used for the formation of the solid hydroxide reactant. A similar observation has not been explicitly reported in the literature for manganous hydroxide oxidation.

- $Mn(OH)_2$ can be precipitated in a crystalline form at elevated temperature or by cathodic deposition at room temperature. The crystalline hydroxide is relatively resistant to oxidation in comparison to the amorphous hydroxide that is highly reactive. Limited information has been published on the morphology of these particles and the Mn_3O_4 particles produced by hydrothermal oxidation, particularly in systems that contain no complexing reagents.

- The structural forms of manganese are characterised by the presence of numerous allotropes and defect structures that exist within the metal and its oxides. Manganese ions exhibit a 6-fold octahedral co-ordination in the soluble form and in many solid state structures. $Mn(OH)_2$ has a layered structure which is characteristic of many of the hydroxides that have divalent cations. Collapse of the separation of these layers is a requirement for oxidation and can eventually form so-called "z-disordered δ-MnO_2" that has a tetragonally distorted spinel structure which can accommodate relatively large amounts of crystalline water and cationic vacancies. The defects in the anhydrous structure are cationic vacancies that are distributed in the tetragonal and octahedral lattice interstices. Hydrated forms of Mn_3O_4 have anionic defects in addition to the cationic defects. These are due to the influence of the hydroxyl ions on the oxygen sublattice. The defect structure of Mn_3O_4 produced from hydrothermal oxidation of $Mn(OH)_2$ has not been reported in the literature.

1.2.9 Specific Objectives and Contributions

The above literature survey has identified a number of opportunities to extend the scientific knowledge of the hydrothermal oxidation of manganese. Further, contributions to scientific knowledge can also be made with respect to characterising the physical, chemical and structural properties of the intermediates and products of this process. Using this as a basis, the following research areas were selected for this thesis.

Equilibrium considerations

Equilibrium studies were undertaken to determine the limits of stability of chemical reactants and identify all possible reaction pathways and final product states. The review of the thermodynamics of the equilibrium of manganese and its oxyhydroxides at elevated temperature showed that extensive research has been done in this field of science. The literature studies on the mapping of the manganese system on Pourbaix diagrams however ignored the hydrated form of manganous oxide (i.e. $Mn(OH)_2$) and used thermodynamic data based on MnO. In this thesis, the thermodynamic properties of $Mn(OH)_2$ were estimated to achieve more realistic Pourbaix-type mapping conditions.

Manganese metal dissolution mechanisms

Experimental studies were conducted to obtain data for kinetic and mechanistic investigations of the hydrothermal dissolution reaction with the accompanying precipitation of manganous hydroxide. The rate of this reaction and particle morphology changes of both solid phases was measured using a non-isothermal experimental design with polydisperse manganese metal. The design of the dissolution experiments included control of the equilibrium hydrogen partial pressure in the reactor using a methodology that has not been found in the literature surveyed. In this way the influence of hydrogen partial pressure on the non-isothermal dissolution reaction could be investigated in a controlled manner. A mathematical analysis is presented for the interpretation of non-isothermal kinetics and reaction mechanisms in a reaction system that contains polydisperse shrinking particles. This analysis is rigorous and can be extended in principle to any non-isothermal, polydisperse reaction system. The analysis and experimental design presented allows estimation of activation energy and rate parameters from a single experiment which is in contrast to traditional experimental designs which require a number of experiments at different but constant temperatures. In addition, the effect of varying particle size in a polydisperse system is also accommodated explicitly in the analytical procedure. Traditional experimental designs ideally require monodisperse particle systems where repeated experiments are conducted at similar reactions conditions with a range of particle sizes at controlled increments. This becomes impractical in the sub millimetre/micron particle size range. The need for repeated experiments is eliminated by making additional analytical measurements and using an appropriate data processing methodology.

The experimental data on dissolution rates is also evaluated from an electrochemical perspective. The precipitation of $Mn(OH)_2$ occurs in series with the dissolution of the metal and hydrolysis of the corrosion products. The morphology of the precipitated manganous hydroxide and the oxidation intermediates was analysed and quantified. This modelling provided the basis for determining the oxidation mechanisms of oxidation.

Manganous hydroxide oxidation

The oxidation of $Mn(OH)_2$ particles to Mn_3O_4 by oxygen in a mechanically agitated, gas-sparged reactor is a three-phase reaction system. Experiments were conducted to measure the rate of oxidation during this oxidation reaction. Thermogravimetric analytical methods were developed and used to measure the extent of oxidation in the solid phase. The measurements were validated by liquid and gas phase measurements. A systematic approach was used to characterise the hydrodynamic conditions in the reactor using mathematical models available in literature. Using this knowledge framework it was possible to identify the rate controlling mass transfer process. It was not possible with the experimental design and current state of scientific knowledge to quantify and validate the spatial distribution of mass transfer in the sparger, impeller and circulation zones of the reactor.

The structural transformations of the reactants and intermediates in the oxidation sequences were examined within the limits of the framework established by the research into equilibrium mapping. The reacting system consisted of manganese metal and manganese oxide/hydroxide particles suspended in water that had solution potentials that varied from oxidising to reducing conditions. The dependence of the ideal structural forms of the solid phases relative to these processing conditions were therefore determined using additional thermodynamic mapping. Morphological and crystal structure aspects of the transformation of the layered structure of $Mn(OH)_2$ to the distorted spinel (hausmannite) Mn_3O_4 were measured, analysed and modelled. These features again are important with respect to the behaviour of this material in the soft ferrite manufacturing process. Here mixing and oxidation processes are used to obtain spinel structured precursors for ceramic components that are tailored to obtain specific magnetic and electrical properties.

Other considerations

Modelling of any complex system can tend to focus attention to a narrow area of scientific interest with a high level of detail. This has to be balanced against the opposing trend of developing generalised and empirical models that do not provide descriptions of the fundamental phenomena inherent in the process. Parameters and model structures were defined in this work at what is considered an appropriate degree of detail, in a standard format, so that the findings presented may be applied to other reacting systems. The

integration of the different components of understanding into a consistent holistic master-model of scientific knowledge remains the challenge of any work of this nature.

The hydrothermal process is conducted in solutions that are free of anionic ligands such as Cl^- or $SO_4^{=}$. The interaction of solid and liquid phases that have a degree of high chemical purity reduces the uncertainty associated with predicting certain physical, chemical and thermodynamic parameters with these phases. The elucidation of the mechanisms of reaction and rate controlling processes is facilitated to some extent by this feature as it reduces the number of ionic species that could be present in the reaction pathways of the system as well as eliminating the need to consider interactions of these ligands with dissolved manganese ions. The oxidation of manganous hydroxide under these conditions could be considered as a standard system for investigating mass transfer phenomena.

There are unique chemical and physical aspects in the manganese oxyhydroxide system, as well as similarity with other metal oxyhydroxide systems such as iron, nickel and cobalt. Technological interchange with these systems was included in this thesis. This study will therefore have appropriate relevance to technological and scientific developments in these systems.

The above considerations are therefore the main substance and contributions of this thesis.

2 HYDROTHERMAL MANGANESE METAL DISSOLUTION EXPERIMENTS

2.1 INTRODUCTION

A number of experimental investigations were conducted to measure reaction rates for the hydrothermal dissolution of manganese metal particles and to determine kinetics and rate-controlling reaction mechanisms.

The following section gives a description of the general conditions for non-isothermal manganese dissolution and hydroxide formation with discussions on the experimental design and how this is influenced by mechanistic considerations. This is followed by descriptions of the dissolution experiments. One experimental study reported in the literature is discussed together with three experimental studies that were undertaken as part the experimental investigations of this work. The experimental conditions in these tests cover hydrothermal Mn metal dissolution reactions in the absence and presence of complexing reagents, under isothermal and non-isothermal conditions and using different reactor pressure control methodologies. The development of kinetic and mechanistic models using the experimental results reported here is presented in Chapter 3.

2.2 EXPERIMENTAL DESIGN AND MECHANISTIC CONSIDERATIONS

The definition of the reacting system for this thesis was obtained from observation and analysis of a mechanically agitated reactor containing a suspension of manganese metal powder particles (~180g/ℓ) in demineralised water. After adding the metal, the reactor was closed and heated from ambient conditions by the direct injection of steam. The total reactor pressure subsequently increased with a rise in temperature and water vapour pressure. Once significant dissolution of manganese metal started, a further increase in total pressure was noted due to the evolution of hydrogen. The manganese dissolution reaction with evolution of hydrogen is exothermic ($\Delta H^{r}_{25°C}$ = -302,8 kcal.mol^{-1}) and the temperature and pressure subsequently increased at a rate higher than achieved by steam addition.

An autothermal condition was reached after which no external energy input was required to increase the rate of reaction. Thereafter the pressure in the reactor was controlled to below the safe working pressure by venting gas from the headspace of the reactor. Temperature and pressure responses in the autothermal temperature range obtained from one of the reactors used for the experimental investigations are shown in Figure 2.1. The figure includes the water vapour and hydrogen partial pressure curves. These were

calculated from the temperature curve (*vide infra* section 2.3.4 for details). The temperature can be seen to increase from 115°C to 180°C and with the water vapour pressure, forms a pair of sigmoidal curves. The total pressure curve is approximately bell-shaped with a maximum at 1900kPa(g).

Figure 2.1 Pressure and temperature responses for hydrothermal manganese dissolution

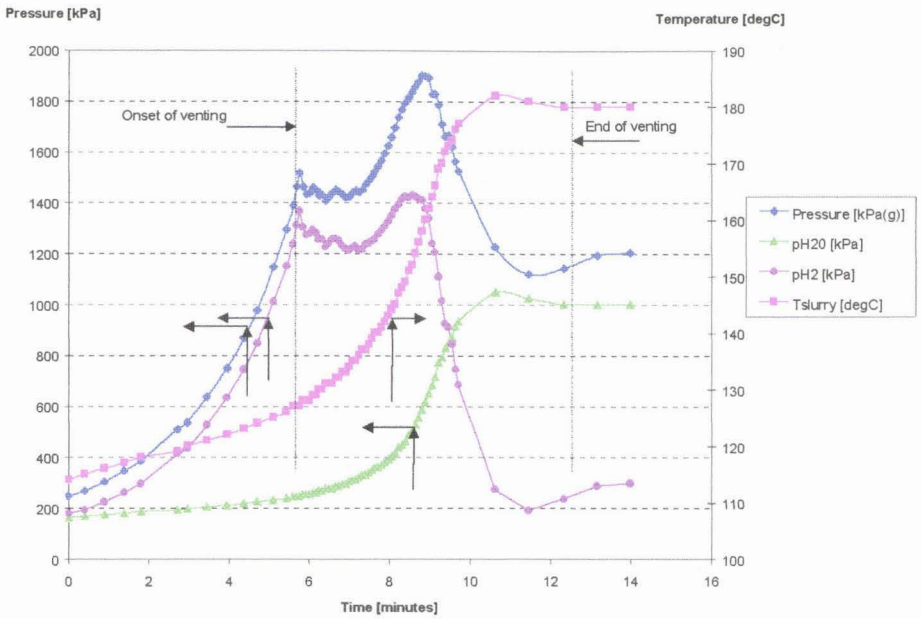

One of the practical objectives of work conducted for this thesis was to develop the experimental and data processing procedures to the point where useful kinetic information could be obtained from the above data. This development is discussed in section 2.3

The dissolution of manganese metal in water can theoretically proceed via a number of mechanisms that can be described by the following reactions:

$$Mn_{(s)} + 2H^{+}_{(aq)} \rightarrow Mn^{2+}_{(aq)} + H_{2(g)} \qquad (1)$$

$$Mn_{(s)} + 2H_2O_{(aq)} \rightarrow Mn^{2+}_{(aq)} + H_{2(g)} + 2OH^{-}_{(aq)} \qquad (2)$$

$$Mn_{(s)} \rightarrow Mn^{2+}_{(aq)} + 2e^{-} \qquad (3)$$

For each of the above mechanisms it is predicted that the most likely position of hydroxide precipitation is at the metal surface. The experimental data obtained thus needs to analysed with this as a possible kinetic and mechanistic feature of the hydrothermal dissolution of manganese.

In addition to the above, the overall dissolution and precipitation reaction requires that the influence of hydrogen needs to be taken into account.

$$Mn_{(s)} + 2H_2O_{(aq)} \rightarrow Mn(OH)_{2(aq/s)} + H_{2(g)} \qquad (4)$$

This reaction is irreversible and should not be affected by higher partial pressures of hydrogen. However the presence of hydrogen could decrease the redox potential of the solution and reduce the oxidising capability of water. The rate of reaction may also be reduced if hydrogen-stabilised intermediates limit the transport of reactants to the surface of the metal (*vide infra* section 3.2 for more details).

The manganous ions from the dissolution reactions (1) to (3) undergo hydrolysis and form hydrates and/or hydroxides. The literature survey of Chapter 1.2 showed that the conditions in the reactor favour the presence of manganous hydroxide. This reaction can be represented simply by:

$$Mn^{2+}_{(aq)} + 2OH^-_{(aq)} = Mn(OH)_{2(aq)} \qquad (5)$$

Manganous hydroxide has sparing solubility and as soon as the extent of dissolution exceeds the solubility product of this hydroxide, solid manganous hydroxide will precipitate to form a faint pink or white suspension according to the equilibrium reaction:

$$Mn(OH)_{2(aq)} = Mn(OH)_{2(s)} \qquad (6)$$

The pH of slurry samples taken from the reactor was found to be typically pH 9,5-10 at the end of the dissolution process which is the pH of a solution containing saturated $Mn(OH)_2$. Calculations showed that this condition was reached when less than 0,02% of the total metal added to the reactor had dissolved. Therefore the pH of the solution during the dissolution reaction would be relatively constant throughout the whole dissolution reaction, notwithstanding the influence of temperature on the $Mn(OH)_2$ equilibrium.

The redox potential of the slurry will vary due to temperature changes and hydrogen partial pressure during the dissolution reaction. Dissolved oxygen initially present in the water would oxidise manganous hydroxide (estimated from total oxygen content at ~1% of metal added) according to the reaction:

$$6Mn(OH)_{2(aq)} + O_{2(g)} \rightarrow 2Mn_3O_{4(s)} + 6H_2O_{(aq)} \qquad (7)$$

The Mn_3O_4 from this reaction can be reduced to MnO (*vide infra* Figure 3.1) according to the reaction:

$$Mn_3O_{4(s)} + H_{2(g)} \rightarrow 3MnO_{(s)} + H_2O_{(l)} \quad (8)$$

Here the manganous oxide will immediately hydrate to form hydroxide as the process occurs below the decomposition temperature of $Mn(OH)_2$:

$$MnO_{(s)} + H_2O_{(aq)} = Mn(OH)_{2(s)} \quad (9)$$

The equilibrium aspects of these reactions are discussed further in Chapter 3.

The design of a Mn dissolution experiment under the conditions described above requires consideration of the following parameters:

- The nature of the manganese metal starting material (electronic and chemical composition, particle size, particle shape and crystal structure).
- The medium in which the dissolution reaction takes place (water at a certain pH and redox potential in the presence/absence of complexing reagents or catalysts).
- The apparatus used for testwork (mechanically stirred reactor).
- The experimental procedure adopted (batch or continuous process with varying pH or redox conditions).
- The temperature and pressure during the experiment (non/isothermal and non/isobaric).
- The sampling of process variables and reaction intermediates during the experiments (particle morphology, size distribution, chemical composition and gas composition).

Each experiment in section 2.3 is reported with increasing detail on each of the above parameters as it was found that in the literature reviewed, one or more of these parameters were not incorporated into the experimental design.

The experimental design was limited by the availability of suitable analytical measuring equipment. Analytical measurements on electronic structures of the metal were not available. Elevated temperature and pressure conditions in the reactor in the presence of suspended solids precluded the use of a certain online analytical instruments, e.g. pH probes. In addition, as both the metal and hydroxide are dispersed solids, a mixture of solid phases exists during each experiment. The analysis of these phases could only be achieved offline on samples taken and analysed by appropriate material characterisation techniques.

The dissolution experiments are discussed relative to these general observations and the mechanistic reaction framework in more detail below.

2.3 Mn DISSOLUTION EXPERIMENTS

The literature review of Chapter 1.2 has shown that limited experimental data is available on the hydrothermal dissolution of electrolytic manganese metal. No studies could be found in the literature on reaction kinetics for manganese dissolution in pure water above 100°C. Kinetic models and reaction mechanisms have generally been derived from studies at ambient temperatures in solutions containing complexing reagents. The literature data and experimental testwork conducted for this thesis can be summarised as follows:

(a) Ohta *et al* (1990) have reported on a study of the aqueous oxidation of manganese metal in the presence of amino acid and ammonium complexing reagents. These experiments were conducted in non-pressurised apparatus below 100°C. Additional information on product morphology using these conditions is available in a patent by Wakao & Hashimoto (1990).

(b) Exploratory laboratory scale testwork was conducted up to the boiling point of water in apparatus consisting of a boiling flask connected to a gasometer. The kinetic data obtained from this testwork was analysed using shrinking particle kinetic equations.

(c) Data was obtained from one non-isothermal run on a large ($4,5m^3$) reactor. Experimental data was collected as the temperature, total pressure, vent-valve opening and valve pressure drop at different venting times. The conversion rate was estimated from the vented gas flowrate using flow equations for the valve and assuming equilibrium vapor pressure conditions in the reactor headspace. A simple model of the solid phase was used to calculate reaction rates and determine dissolution kinetics.

(d) Due to the limitations of the measurements that could be made on the large reactor, a set of non-isothermal experiments was conducted on a smaller reactor ($0,4m^3$). The experimental procedure was modified so that hydrogen evolution gas flowrates could be measured. In addition, the pressure control procedure was changed so that these experiments were conducted with the equilibrium hydrogen partial pressure (pH_2^*) being kept constant in each run. A number of different hydrogen partial pressure conditions were tested. The experimental campaign included repeat measurements so that reproducibility could be quantified.

Samples were taken of the reactor contents during dissolution. These were subjected to chemical and physical analysis and used to validate the gas evolution measurements. The experimental data was analysed relative to a number of non-isothermal, mathematical models for polydisperse shrinking particles in section 3.3

Each of the above studies represents a progressive stage in the refinement of the experimental procedure that ultimately led to the design for the non-isothermal hydrothermal dissolution experiments as conducted in the small reactor. The final experimental procedure made it practically possible to obtain reaction rate data that could be used to investigate the dissolution reaction mechanisms using a unique and original perspective. Each of experimental investigations (a) to (d) are described and evaluated in the following sections.

2.3.1 Literature Data

Experimental design and results

Ohta *et al.* (1990) stated that temperatures in excess of 120°C are required to achieve hydrothermal dissolution of manganese metal in the absence of complexing reagents. These authors found that increased rates of reaction can be obtained by reacting electrolytic manganese with water containing amino acids and ammonium salts. Their experimental design is summarised in Table 2.1. The authors did not explain how the temperature in the experiments was controlled. It is therefore assumed that there was some form of cooling mechanism was used and that isothermal conditions were maintained during the experiments.

Continuous pH measurements showed that the pH rose rapidly to slightly above (typically 8,5) the saturation pH for $Mn(OH)_2$ before reducing to a constant value thereafter. The slight overshoot of pH was attributed to metastable supersaturation conditions and steady pH readings were obtained after less than 2,0% of the total reaction time had elapsed. The addition of the amino acids lowered the solution pH (to typically 7,9-8,5) in comparison to reagent free $Mn(OH)_2$ systems by complexing increased amounts of soluble manganese. These pHs were independent of the amount of amino acid added. The rate of gas evolution reduced from an initial high rate to the point where $Mn(OH)_2$ could be observed to precipitate. This rate decrease was presumably due to the formation of a precipitate at the surface of the metal. Once saturated conditions had been established, the rate of gas evolved followed a convex parabolic trajectory until 100% of the metal had reacted. Metal with smaller particle sizes produced higher rates of reaction which increased in proportion to the amount of amino acid added.

Table 2.1 Experimental design for testwork by Ohta *et al.* (1990)

Variable parameters	Constant parameters	Measured parameters
Type of amino acid (0,065 and 0,52M)	Electrolytic Mn metal -140#(104μm)	Slurry pH
Type of ammonium salt	Batch laboratory scale experiment 1,2gMn/40ml demin. water	H_2 gas volume evolved
Sparging with N_2 or O_2 throughout experiment	Stirring conditions	BET/XRD/TEM on product
Temperature at intervals	Isothermal experiment (claimed though no reference made to cooling)	Temperature
	Atmospheric pressure	

The kinetics of dissolution after saturation conditions had been established were found to fit the equation:

$$1-(1-V/V_f)^{0,33}= k\ t$$

where: k : reaction rate constant

V/V_f: fraction of reacted metal from amount of hydrogen gas evolved

This is equivalent to a spherical shrinking core model with first-order, chemical reaction control. The reaction rate constant was found to depend on the hydrogen ion $[H^+]$ concentration and the anion concentration of the dissociated amino acid base group $[A^-]$. A range of amino acids was chosen to cover a number of different base group activities. All the rate constants for the mono-amino carboxylic acids were approximately correlated by the equation:

$$k = 10^{5,7}\ \beta^{0,5}\ [H^+]\ [A^-]$$

where: β: stability constant of amino acid

Typical rate constants are listed in Table 2.2. The highest reaction rates were obtained for the amino acids with highest stability constants. The effect of temperature on the nitrogen-sparged runs varied. Generally an increase in temperature resulted in an increase in rate constant. However with ammonium acetate, a decrease in k with decreasing reagent concentration was noted. The k-T profile for 0,13M ammonium acetate had a maximum at 70°C. This was attributed to the thickness of hydroxide films retarding the H^+ diffusion rate to the metal surface.

Table 2.2 Rate constants and conversion times for Mn metal dissolution with amino acid catalysts

Additive	Side group	pI	k (N_2 runs)	T_{O_2}	T_{N_2}	T_{N_2}/T_{O_2}
Glycine	Uncharged Polar	6,0	3,37	100	297	2,97
L-Asparagine	Uncharged Polar	10,8	3,99	120	251	2,09
α-Alanine	Aliphatic	6,0	2,84	105	352	3,35
dl-Valine	Aliphatic	6,0	1,22	200	820	4,10
β-Alanine	Aliphatic	6,0	0,52	72	1923	26,70
Glutamic Acid	Acidic	3,2	1,69	125	592	4,72
L-Asparatic Acid	Acidic	3,0	0,68		1470	
L-Lysine	Basic	9,8	0,45	322	2222	6,90
L-Arginine	Basic	11,2	0,07	350	14285	40,80
CH_3COONH_4			4,44	150	225	1,50
NH_4Cl			0,89		1123	
Glycylglycine			7,01	85	143	1,68

Note: pI: Isoelectric pH of amino acid
-140 mesh metal (d_{pmax}=104 μm)
N_2 run 50°C, 0,13M amino acid
O_2 run 60°C, 0,26M amino acid
k: rate constant (min^{-1} *1000)
T_{O_2/N_2}: Total conversion time (minutes) for oxygen and nitrogen runs respectively.

The rate of dissolution increased in experiments conducted with oxygen sparging during dissolution. The time taken to convert the metal totally under these conditions was thus longer in comparison to runs done with nitrogen sparging. These runs also showed the characteristic initial step and flat profiles in pH during the experiment. The pH decreased to the starting pH at the end of the experiments. The rate controlling process under these conditions was no longer a chemical surface reaction but the rate of oxygen transfer as changing stirring rates altered the rate of reaction. The amount of hydrogen evolution decreased as the metal was oxidised directly to Mn_3O_4 according to the overall reaction:

$$3Mn_{(s)} + 2O_{2(aq)} = Mn_3O_{4(s)} \qquad (10)$$

The above reaction can also be written as the sum of two reactions to include the oxidising capability of water:

$$6Mn_{(s)} + 6H_2O_{(aq)} + 3O_{2(aq)} = 6Mn(OH)_{2(s)} \qquad (11)$$

$$6Mn(OH)_{2(s)} + O_{2(aq)} = 2Mn_3O_{4(s)} + 6H_2O_{(aq)} \qquad (12)$$

Final product yields of $Mn(OH)_2$ and Mn_3O_4 were almost 100% in the nitrogen and oxygen sparging runs respectively. The rate of reaction for oxygen-sparged experiments increased with increasing temperature. Here though, reaction rate maximums were obtained which were dependent on reagent type. This was attributed to a decrease of oxygen solubility at higher temperatures and to varying hydroxide film thickness for the nitrogen-sparged experiments. The solid products from the oxygen runs had specific surface areas that increased with lower reaction temperature, higher amino acid concentration and lower amino acid dissociation constants. A range of BET surface areas of 5 to 40m^2/gm was obtained. High reaction rates thus favoured the production of lower surface areas. XRD confirmed the presence of Mn_3O_4 and TEM showed spherically shaped grains.

The rate of dissolution increased in experiments conducted with oxygen sparging during dissolution. The time taken to convert the metal totally under these conditions was thus longer in comparison to runs done with nitrogen sparging. These runs also showed the characteristic initial step and flat profiles in pH during the experiment. The pH decreased to the starting pH at the end of the experiments. The rate controlling process under these conditions was no longer a chemical surface reaction but the rate of oxygen transfer as changing stirring rates altered the rate of reaction. The amount of hydrogen evolution decreased as the metal was oxidised directly to Mn_3O_4 according to the overall reaction:

$$3Mn_{(s)} + 2O_{2(aq)} = Mn_3O_{4(s)} \qquad (13)$$

The above reaction can also be written as the sum of two reactions to include the oxidising capability of water:

$$6Mn_{(s)} + 6H_2O_{(aq)} + 3O_{2(aq)} = 6Mn(OH)_{2(s)} \qquad (14)$$

$$6Mn(OH)_{2(s)} + O_{2(aq)} = 2Mn_3O_{4(s)} + 6H_2O_{(aq)} \qquad (15)$$

Final product yields of $Mn(OH)_2$ and Mn_3O_4 were almost 100% in the nitrogen and oxygen sparging runs respectively. The rate of reaction for oxygen-sparged experiments increased with increasing temperature. Here though, reaction rate maximums were obtained which were dependent on reagent type. This was attributed to a decrease of oxygen solubility at higher temperatures and to varying hydroxide film thickness for the

nitrogen-sparged experiments. The solid products from the oxygen runs had specific surface areas that increased with lower reaction temperature, higher amino acid concentration and lower amino acid dissociation constants. A range of BET surface areas of 5 to 40m^2/gm was obtained. High reaction rates thus favoured the production of lower surface areas. XRD confirmed the presence of Mn_3O_4 and TEM showed spherically shaped grains.

Further details on this process and product characteristics are given in the patent by Wakao & Hashimoto (1990). (Note: Wakao is a common author to both these works.) An experimental design similar to the above was used to obtain products ranging from 0,02 to 6,2μm grain sizes. This corresponds to BET measurements ranging approximately from 0,2 to 63m^2/g. Repeated use of the recycled reaction filtrate resulted in lower grain sizes. The results presented by these authors are summarised in Table 2.3 below.

Table 2.3 Mn_3O_4 grain sizes from simultaneous dissolution and oxidation of Mn metal.

Additive	Concentration of additive (mol.ℓ^{-1})	Temperature (°C)	Time (hr)	Average grain size (μm)
Ammonium acetate	0,5	50	10	0,03
Ammonium sulphate	0,5	50	3	0,07
Ammonium chloride	0,5	50	5	0,23
Ammonium nitrate	0,5	50	>6	6,20
Ammonium oxalate	0,2	60	>8	6,20
Ammonium formate	0,2	60	1,5	0,02
Glycine	0,26	50	4	0,21
β-Alanine	0,26	50	2,5	0,07
α-DL Alanine	0,26	50	3	0,14
Glycylglycine	0,26	50	3,5	0,02
L-Monosodium glutamate	0,26	50	3	0,02
α Amino-isobutyric acid	0,26	50	3	0,09
L-Glutamate	0,26	50	4	0,07

Note: Reactor charge ratio: 1,8mol Mn metal/liter of water

Conclusions

The conclusions that can be drawn from the investigations of Ohta *et al.* (1990) may be summarised as follows:

- The time required for complete dissolution in these experiments is longer than for the complexing reagent free hydrothermal experiment discussed in section 2.3.4. Reaction times in the order of hours were required to complete dissolution/oxidation.

- The rate of reaction for non-oxidative dissolution of Mn metal in the presence of complexing reagents up to temperatures of 80°C can be modelled by spherical shrinking core kinetics with first-order, chemical reaction control.

- The rate of reaction during simultaneous dissolution and oxidation of manganese metal in the presence of complexing reagents is limited by the rate of oxygen mass transfer. The enhancing effect of oxygen on the dissolution rate of Mn metal in the presence of complexing reagents is demonstrated as anticipated in the literature survey of Chapter 1. It has however not been shown that oxygen in the absence of the complexing reagent will have a similar effect.

- The mechanism of dissolution in the absence of oxygen and the presence of complexing reagent agrees qualitatively with the general model of dissolution discussed by Osseo-Asare (1984).

- Mangano-manganic oxide with a wide range of grain sizes (0,02-6,2μm) and BET surface areas (5 to 40m^2/g) can be obtained through Mn dissolution and oxidation processes in the presence of complexing reagents. The grain size of the product is inversely proportional to temperature and directly proportional to the complexing reagent concentration and the dissociation strength of the amino acid. These features have been reported in the literature, e.g. Mendelovici & Sagarzuzu (1988) prepared non-stoichiometric hausmannite with BET surface areas ranging from 30,7 to 47,8m^2/g using hydrothermal hydrolysis of manganese alkoxide precursors.

- The fact that Ohta *et al.* did not refer to how the temperature in the experiments was controlled is of some concern. If there were significant temperature fluctuations in the reactor then the kinetic models would contain experimental error. In addition, if cooling coils were used to control the reactor temperature then temperature gradients could exist in the vicinity of these coils that could introduce further errors.

2.3.2 Isothermal Laboratory Experiments at 95°C

Ramanane (1987) conducted exploratory dissolution experiments on Mn metal by measuring the mass of water displaced from a reservoir by the gas evolved from reaction mixtures up to the boiling point at 1,4cm Hg pressure. The experimental design is given in Table 2.4 with the apparatus depicted in Figure 2.2.

Table 2.4 Design of isothermal Mn dissolution experiments

Variable parameters	Constant parameters	Measured parameters
	Electrolytic Mn metal 80%~-300 +20μm 50g Mn/750ml water	
	Batch laboratory scale experiment (1ℓ vessel)	H_2O mass displaced by H_2 gas evolved
	Demineralised water N_2 flush in head space only	
	Stirring conditions Magnetic type	
Temperature (Range 84-95°C)	Isothermal experiment	Temperature
	1,4cm Hg above atmospheric pressure	Pressure

After introduction of metal into preheated water, a delay of 3 to 10 hours was observed before water displacement was obtained. Lower reaction temperatures resulted in increased delay times for water displacement. Isothermal conditions could not be maintained, particularly when cold metal was dropped into preheated water at the start of an experiment. Long reaction times were measured and half-hourly logging of water displacement increments was terminated after 12 hours where typically 75-80% conversion had been obtained. A further 12 hours was then allowed for completion of the reaction. Corrections were not made to the masses of water displaced for gas composition changes during the experiment due to the unavailability of suitable gas analysis equipment.

Figure 2.2 Experimental apparatus for isothermal Mn dissolution

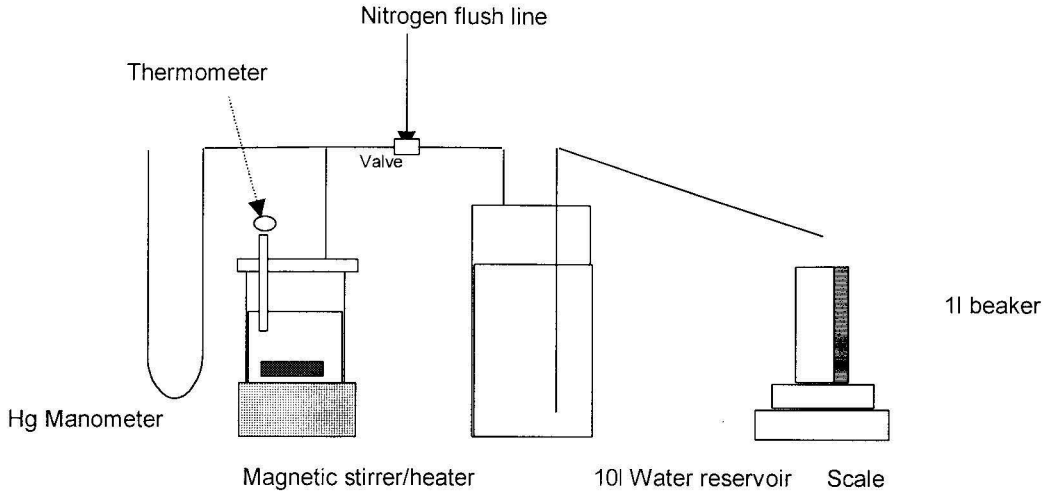

A summary of the experimental results obtained is included in Table 2.5. Due to the very low reaction rates at temperatures below 80°C only a narrow temperature range could be investigated.

Table 2.5 Results for isothermal dissolution experiments

Run	Temperature (°C)	Reaction Time (hrs)
1	92,2	22,7
2	94,6	20,2
3	93,9	19,6
4	92,0	18,4
5	84,6	25,2
6	88,1	29,9
7	94,4	15,5
8	93,7	19,6
13	84,0	41,0
14	84,1	38,5

Total reaction time differences in excess of 20% were thus obtained at similar reaction temperatures. Ramanane (1987) tested a number of spherical, non-porous, shrinking core models assuming a monodisperse particle size distribution. The monodisperse assumption introduces significant errors as discussed in the next sections of this thesis. It was concluded that a model incorporating first order, chemical reaction control at the surface gave the best fit for the kinetics of the process. An activation energy of 70 kJ/mol was estimated from an Arrhenius plot. This is in the same order of magnitude as that

reported by Hurlen & Valand (1964c) for the dissolution of metallic manganese in 0,5M H_2SO_4 in the temperature range 0-50°C i.e. 63kJ/mol.

Although the results of the above experiments do not conform to acceptable standards of repeatability, they do give qualitative data on the rate of Mn dissolution in a system that does not contain complexing reagents. The data confirms the effectiveness of the reagents discussed in section 2.3.1 as reaction times in the order of 3 to 4 hours could be obtained at temperatures that are 10 to 20°C lower. If an activation energy of 70kJ/mol is correct for this process, then the reagents induce an effective 35 fold increase of rate, as a 5 fold reduction in rate is expected between 95 and 70°C due to the effect of temperature alone.

A spherical shrinking core model, first order in solid manganese with chemical reaction at the surface can be used to describe the kinetics for Mn dissolution in the presence and absence of complexing reagents. Catalytic effects are not occurring due to the high concentrations of complexing reagent that were required to achieve the increased rates of dissolution.

2.3.3 Non-Isothermal Large Scale Reactor Experiment

A simplified analysis of one non-isothermal hydrothermal Mn dissolution run on a large reactor is made below. This experiment and its analysis are described here as this was the basis of the small reactor experiments. In addition, the data obtained is assessed qualitatively as an introduction to the more rigorous methodology used for the small reactor runs. The apparatus used for collecting data consisted of a mechanically agitated reactor with a vent valve to atmosphere that was used to control the headspace pressure. A PID controller was used for this purpose. The set-up is shown diagrammatically in Figure 2.3 with the experimental design being tabulated in Table 2.6.

In this experiment, a slurry of manganese metal in water was heated by the injection of live steam through sparge lines with the vent valve in a closed position. The total pressure in the reactor rose as a result of the increase in water vapour pressure and the generation of hydrogen. The pressure increased rapidly above 60°C. Above 100°C, the reactor achieved autothermal conditions. Venting of the steam and hydrogen limited the pressure to below the maximum safe working pressure of the vessel. Figure 2.4 shows the parameters monitored at 30 second time intervals during the autothermal portion of the reaction.

Figure 2.3 Large reactor experimental arrangement

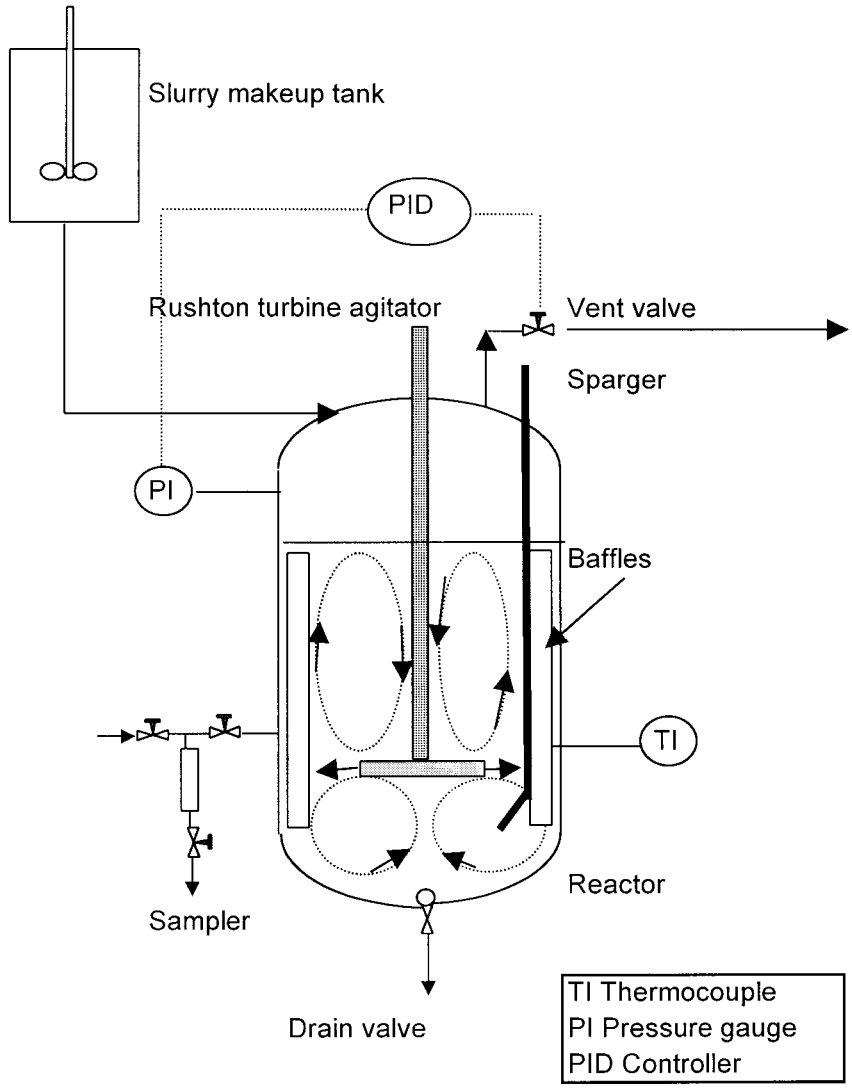

Table 2.6 Design of non-isothermal Mn dissolution experiment in a large reactor

Variable parameters	Constant parameters	Measured parameters
	Electrolytic Mn metal 80% ~-300 +20μm 280g Mn/lt. water	Slurry pH offline Mn in $Mn(OH)_2$ slurry
	Batch reactor ($4m^3$ vessel)	Vent valve opening Pressure drop across valve
	Demineralised water not flushed with N_2	
	Rushton turbine stirrer 180rpm	
	Non-isothermal 110-180°C	Temperature
	Non-isobaric 0-1800kPa(g)	Pressure

Figure 2.4 Pressure, temperature and valve opening profiles for non-isothermal dissolution of Mn

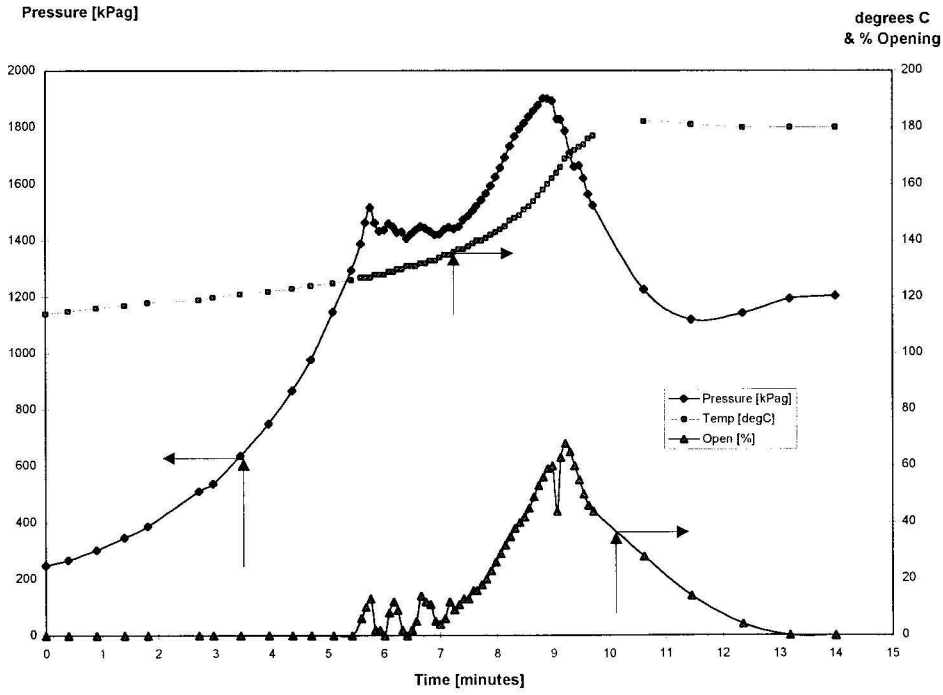

A number of observations are made with respect to the profiles in the figure above:

- The total duration of the venting portion of the dissolution reaction was approximately 13 minutes. The temperature of the reactor rose from 114°C to a final value of 180°C. The temperature-time curve is approximately sigmoidal with the maximum rate of temperature change (36°C.min^{-1}) occurring at 169°C. The rate of temperature increase was approximately uniform up to this temperature. The maximum valve opening corresponds to the maximum in the rate of temperature change signifying that the highest dissolution rate occurs here.

- The pressure profile has two regions of rapidly increasing pressure that are exponential in shape viz., 0 to 5 minutes and 7 to 9 minutes. A region of approximately constant pressure separates these regions during which the vent valve began opening to control the pressure in the reactor. The point of maximum rate of pressure rise (492kPa.min^{-1} at 147°C) during venting does not correspond to the maximum rate of temperature change. This is attributed to energy transport imbalances between the vapor and liquid phases in the reactor. The profile of the vent valve opening follows a sharp bell shaped curve with a number of deviations recorded at the beginning of venting (5 to 7 min) and at the maximum opening position (9 min). These deviations were due to the action of the automatic PID feedback controller.

- One pH measurement of 9,5 was obtained on a cooled sample (40°C) taken at the end of the dissolution reaction. This corresponds to the pH of a saturated $Mn(OH)_2$ solution. At 100°C a pH of 9 is predicted for saturated $Mn(OH)_2$ that decreases to 8,2 at 180°C due to the effect of temperature on solubility equilibrium. (See Appendix C, Fig. C1 for details). The amount of manganese dissolution required to saturate the water with hydroxide is small (~0,02% of total mass of metal added) and the pH conditions during venting are therefore expected to be essentially constant. The measurement of pH consequently has limited benefit as an indicator for the extent of the reaction.

Calculation of Reaction Rates and Extent of Conversion

Parameters for determining the kinetics of manganese dissolution were extracted from the above profiles according to the following procedure:

a) The water vapour partial pressure (v_p in kPa(a)) in the reactor headspace was estimated from the reactor temperature (T in °C) by the equation:

$$v_p = 10^{\left(7{,}106 - \frac{3027}{1{,}8T + 413{,}3}\right)}$$

A comparison of calculated and actual data is given in the following table. The error of the calculated vapor pressures does not exceed 0,5% for the temperature range of the experiments.

Table 2.7 Comparison of calculated and actual vapor pressure data

Temperature (°C)	v_p (kPa) Steam tables*	v_p (kPa) Calculated
25	3,2	3,2
50	12,3	12,4
75	38,6	38,5
100	101	101
125	230	231
152	500	498
175	900	899
201	1600	1601

*The data used for the correlations was taken from the steam tables of Mayhew & Rogers (1977).

The headspace temperature was assumed to be the same as the liquid content in the reactor i.e. the liquid and vapour phases are in equilibrium.

b) The hydrogen partial pressure in the headspace (pH_2*) was calculated from the difference between the total reactor pressure and the water vapour partial pressure. The assumption was made that the headspace only contained steam and hydrogen. This is reasonable as the mass of air present initially in the reactor headspace is a small fraction of the total amount of gas vented and would be displaced from the headspace during the initial stages of venting. The pH_2* varied from 179kPa to 1430kPa at the maximum pressure reached in the reactor. This partial pressure curve is plotted in Figure 2.1.

c) The mass composition and the density of the gas in the headspace were then calculated from the partial pressures assuming ideal gas behaviour. The calculated density of the headspace gas varied from about 0,9 to 4,5kg.m^{-3} during the process. Constant gas viscosity was assumed.

d) The massrate of gas vented was estimated by the following equation that was supplied by the valve manufacturer (Valtec) who base their calibration on ANSI/ISA-S75.01-1985:

$$M^{O} = 2{,}555\ C_V\ Y \sqrt{\frac{dP\rho}{1000}}$$

where: M^{O} : $kg.hr^{-1}$

$C_v = 1{,}74174 - 0{,}1693*(\%Open) + 0{,}01387*(\%Open)^2$

(Obtained by curve fitting supplier data, valid for %Open≠0)

$$Y = 1 - 0{,}392\frac{dP}{P_1}$$

dP : Pressure drop across valve in kPa

ρ : Density in $kg.m^{-3}$

P_1 : Upstream pressure in kPa

e) The total amount of metal converted was obtained by the stoichiometry of the overall dissolution equation:

$$Mn_{(s)} + 2H_2O_{(aq)} = Mn(OH)_{2(s)} + H_{2(g)}$$

and by integrating the hydrogen content of the gas flowrate over the total reaction time. This accounted for only 10% of the metal added initially. The main source of error here was found to be due to the assumption of equilibrium in the headspace during venting. The transfer of hydrogen gas through the headspace nullifies the assumption of equilibrium that requires a closed system at steady state. To enable further analysis of the data the fraction of metal converted was calculated from the total volume of gas measured and not on the basis of the mass of metal added initially. The results are therefore not suitable for use in detailed kinetic or mechanistic evaluations.

f) Dissolution rates when the control valve was closed (i.e. up to 5,5 minutes venting time) were estimated from changes in the total pressure and hydrogen partial pressure in the headspace. Here the assumption was made that the headspace is a closed system containing ideal gases with a fixed volume. The change in pressure is therefore directly proportional to change in mass of gas in the headspace volume. The volume changes in the system were assumed negligible as the volume expansion due to hydroxide formation is balanced by water consumption and manganese dissolution. The solid metal particles also represented a small fraction (6%) of the total slurry volume. Approximately 2% of

the metal initially present needed to dissolve to raise the reactor headspace pressure to 1100kPa.

g) The metal particles were assumed to be uniform, non-porous spheres with a solid density of 7200kg.m^{-3}. The particle size at any stage of conversion was obtained from the following equation:

$$d_p = d_{po}\ (1-X_t)^{0,33}$$

where: d_p : Particle diameter in microns at time t

d_{po} : Initial particle diameter (25 micron)

X_t : Fraction of metal converted at time t

The extent of manganese dissolution is shown as a function of time in Figure 2.5 together with the change in temperature and particle diameter. The profiles show features that are implicit with the assumption of spherical shrinking particle kinetics of uniform size. At 177°C, 96% of the metal dissolving will correspond with the particle diameter having shrunk to 8,5 micron. This implies that submicron particle size effects are not present during the greatest portion of the reaction.

Figure 2.5 Metal conversion, particle diameter and temperature profiles during hydrothermal Mn dissolution

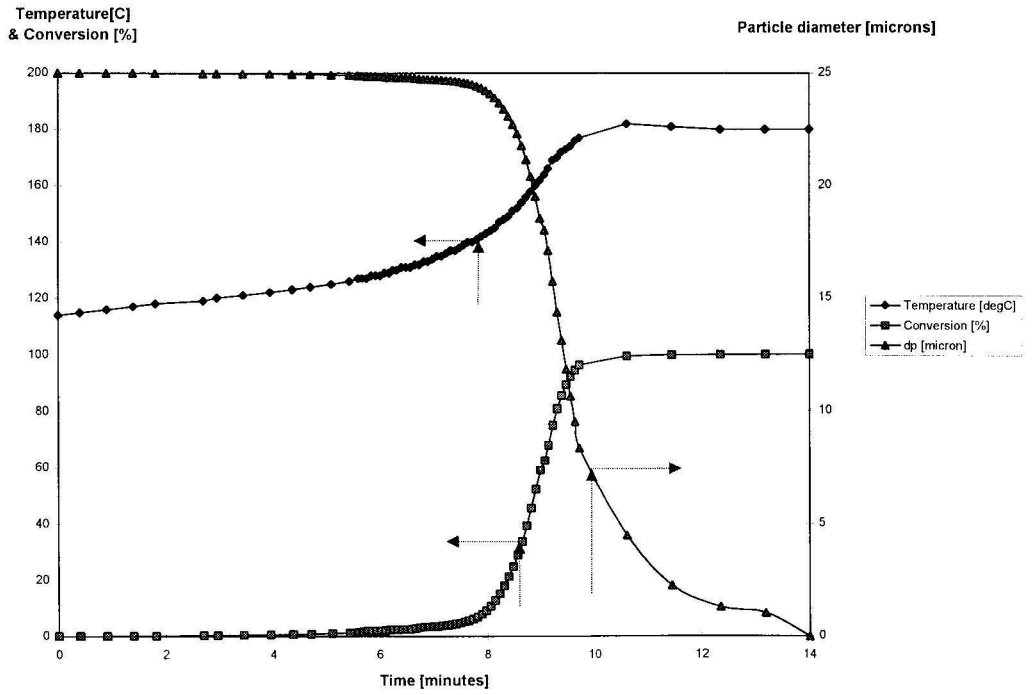

h) The total surface area of manganese metal present at any time during the reaction was calculated from the equation:

$$Area_{Mn} = 6\times10^{6}\,(1-X_t)\,m_{t=o}/(\,d_p\,\rho_m)$$

where: d_p: Particle diameter (micron) at time t

ρ_m: Density of metal (7200kg/m^3)

X_t: Extent of conversion (%/100) at time t

$m_{t=o}$: Mass of metal initially added to reactor (kg)

Again it is assumed that the particles are spheres of uniform diameter.

i) The specific dissolution rate (M^O) was calculated by dividing the instantaneous reaction rate by the total surface area of particles remaining after each sampling time interval. The variation in total particle surface area and specific dissolution rate as a function of Mn metal conversion is plotted in Figure 2.6.

Figure 2.6 Variation of total particle surface area and specific dissolution rate as a function of conversion

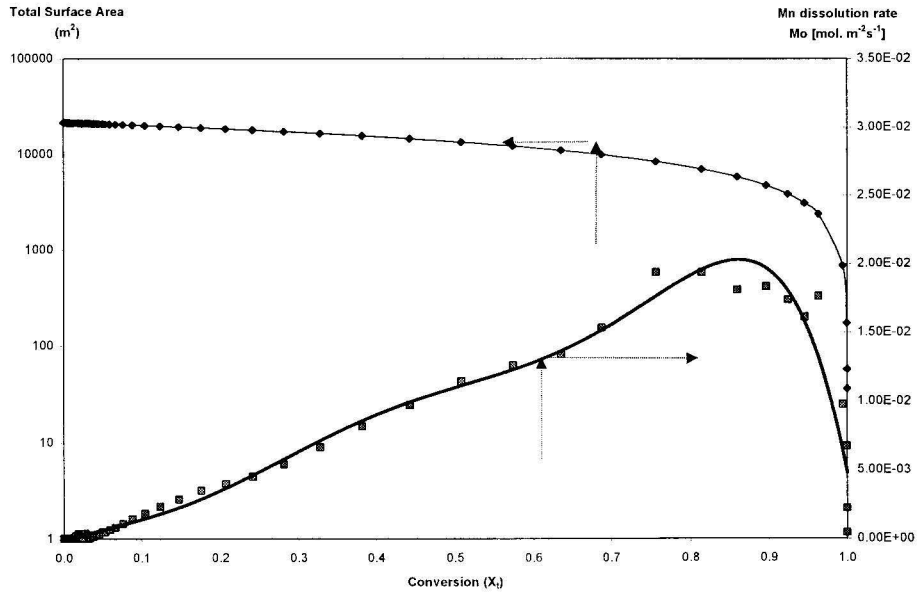

The calculated total surface area of the particles shows that the total reaction area decreases continuously from an initial value of $2,1x10^5$ to 0 m^2 at completion of conversion. The surface area of metal is therefore in the order of 10000 m^2 ($4m^2/m^3$ of liquid) for most of the reaction. The specific dissolution rate increases

approximately linearly with respect to the extent of conversion up to approximately 90% conversion (174°C and 9,6 minutes reaction time). This would correspond to a kinetic regime of relatively slowly shrinking particles. Above this temperature and extent of reaction, the model suggests that rapid decreases in particle size and surface area occur as the particles shrink to extinction.

j) The extent of reaction is plotted as a function of temperature in Figure 2.7. It can be seen that an approximately linear relationship exists for these parameters above 145°C. This can be expected from energy balance considerations and the fact that the enthalpies of all the manganese oxides, hydrogen, water and oxygen are linear functions of temperature between 110 and 180°C.

k) An Arrhenius plot of the logarithm of the specific reaction rate versus the inverse temperature is shown in Figure 2.8. It is evident that there is considerable scatter and systematic deviation about the linear least-squares regression line. A coefficient of fit (R^2) of 0,82 was obtained. The activation energy obtained from the slope of the regression line is 98,9kJ/mol that indicates the rate of the process is controlled by a reaction rather than a diffusion process. Further the magnitude obtained for this activation energy suggests that this parameter increases with an increase in temperature if this is compared with the data of Hurlen & Valand and Ramanane as discussed above.

Figure 2.7 Conversion temperature profile for non-isothermal Mn dissolution experiment.

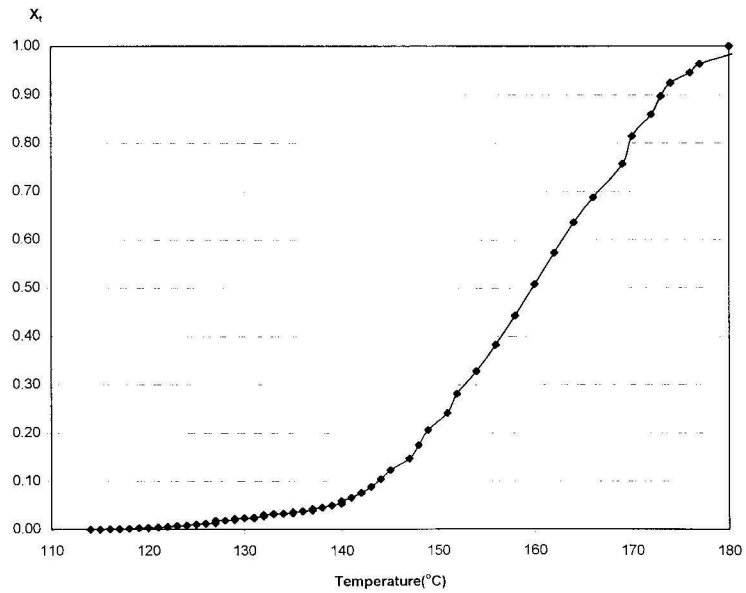

Figure 2.8 Arrhenius plot for large reactor run

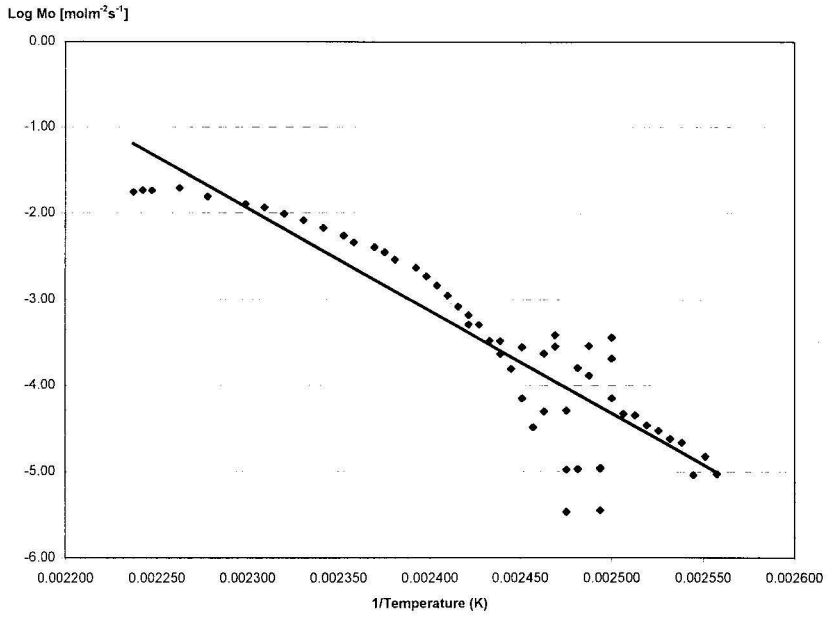

Conclusions

Further analysis and interpretation of the above data was not conducted due to the qualitative methods used in obtaining the reaction rate data. The conclusions that can be drawn are:

- The rate of hydrothermal dissolution of manganese increases significantly above 110°C with an approximately linear relationship being obtained between the extent of conversion and temperature under these experimental conditions.

- Additional analytical measurements are required with respect to the characterisation of the starting metal and reaction intermediates for conclusive identification of reaction kinetics.

- Vapor-liquid equilibrium cannot be assumed between the headspace and the slurry during venting.

- An improved experimental procedure is required to isolate the effect of varying hydrogen partial pressures during a non-isothermal experiment.

- Improved gas flowrate measurement techniques are required.

- The activation energy for Mn dissolution could in principle be obtained from a single non-isothermal experiment. The experimental procedure must however include additional measurements to validate modelling assumptions and reduce experimental errors.

2.3.4 Non-isothermal Reactor Experiments

Experimental design

A set of runs with improved experimental design and control was conducted on a pilot scale autoclave. This design was obtained after reviewing the analysis conducted above and after a series of modifications had been made to the pilot scale equipment. A summary of the experimental design finally used is given in Table 2.8 with the equipment configuration shown diagrammatically in Figure 2.9.

Table 2.8 Experimental design for pilot scale reactor experiments

Variable parameters	Constant parameters	Measured parameters
	Electrolytic Mn metal -325# Nominal 190g Mn/liter water	Slurry pH Mn in $Mn(OH)_2$ slurry Particle size distributions & morphology (All offline measurements)
	Batch reactor ($0,4m^3$ vessel)	Hydrogen gas flowrate Water vapour vented
N_2/no flush	Demineralised water 14μS/cm	
	Rushton turbine stirrer 180rpm	
	Non-isothermal	Temperature 25-180°C
pH_2* constant @ 400,600,800&1000kPa	Venting strategy	Pressure 0-1500kPa(g)

Three different hydrogen partial pressure (pH_2*) settings of 600, 800 and 1000kPa were selected for investigation. pH_2* was estimated by the difference between the total and water vapor pressures. This difference was kept constant during each run, i.e. the pressure was controlled to a fixed increment above the water vapour pressure. Runs were also conducted at 400kPa pH_2* and with N_2 flushing of the demineralised water at

the start of a run. The hypotheses that were raised and the shortcomings that were identified in the previous experimental work could be addressed from this experimental design and equipment configuration.

Description of equipment

The reactor was an insulated, baffled, stainless-steel, pressure vessel. Electrical heating elements were fitted to the shell but the greatest heating effect was achieved by direct steam injection through sparge lines. A Rushton turbine with a double mechanical seal and a variable speed motor (AC frequency inverter) was used for agitation. Standard aspect ratios were used for the reactor and agitator. Due to difficulties associated with measuring gas flowrates directly after the vent valve on the reactor, it was decided to pass the gas through a closed quench vessel that condensed the water vapour content of the gas stream. A calibrated orifice located downstream of the condensing vessel was used to measure the flowrate of hydrogen. This eliminated the need for gas composition measurement in the headspace.

Figure 2.9 Pilot scale equipment configuration

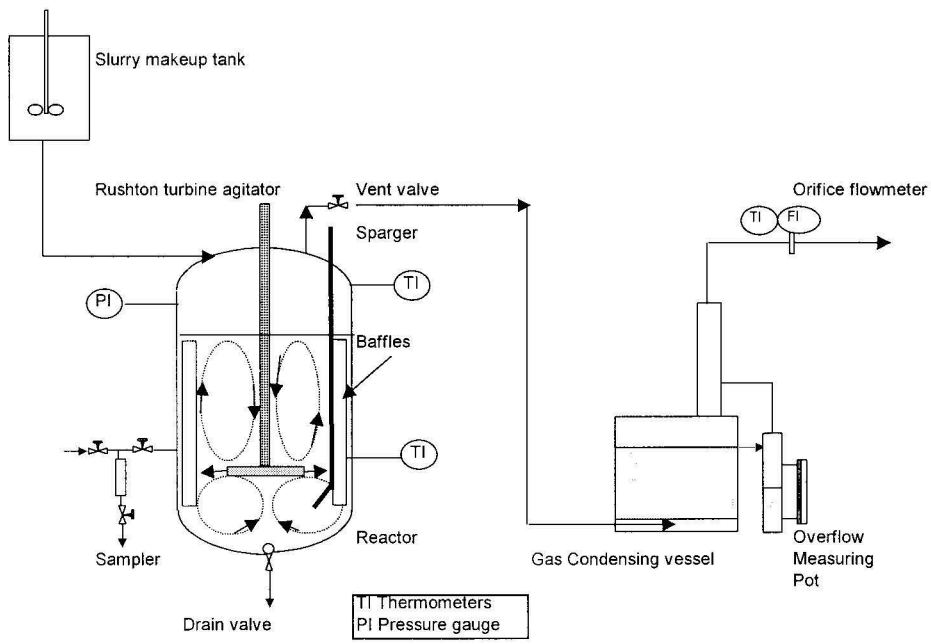

The gas composition for gas flowrate calculations was corrected for the water vapour content that would arise from the vapour pressure in the condenser. As the gas was essentially at ambient conditions leaving the condenser, this correction had a minor affect on the hydrogen gas composition. The liquid level in the condenser was kept constant by an overflow nozzle with the overflow being collected in the measuring pot. The differential and total amount of water vapour vented from the reactor during a run could

be obtained by measuring the volume collected in the measuring pot. A hydraulic balancing line between the measuring pot and the condensing vessel ensured a steady overflow by allowing the gas carryover to disengage from the liquid overflow.

The headspace and slurry temperatures (resistance thermocouples), headspace pressure and the differential pressure (dP) of the orifice flowmeter (Yokogawa type) were logged at 10 or 15 seconds time intervals during an experimental run by a Grant Squirrel® datalogger. These were subsequently downloaded onto a PC for data processing. The pressure transmitter was calibrated using a dead-weight tester to an average error of +0,35%. The temperature transmitter outputs checked against standard tables up to 200°C to less than +0,2% error. The gas flowrate was calculated using the following methodology:

- Ideal gas behaviour was assumed (Z=1).

- The gas was assumed to be a binary mixture of water vapour and hydrogen. The mole fraction of water vapour was obtained from the equilibrium vapor pressure curve given in section 2.3.3 paragraph (a). Typically the water vapour content was estimated to be <1% of the gas volume. The volume of headspace above the condenser and the line to the flowmeter would be filled with air until the vent valve was opened. No correction was made to the gas composition for this effect, as this headspace volume was small relative to the gas volume vented.

- The viscosity of the binary gas mixture was calculated using the method described in Bird *et al.* (1960) p25.

- The gas flowrate was calculated from dP readings and equations given in ASME MFC-3M-1989 for an orifice meter with corner pressure taps. A trial and error approach was used to calculate the Reynolds number and discharge coefficient with 4 iterations being sufficient to get consistent flowrate readings.

This calculation methodology was checked by weighing a nitrogen gas cylinder that was connected upstream to the orifice meter. The calibration curve is given below. An average error of all readings of 4,0% was obtained. This reduces to 2,1% in the range of gas flowrates actually measured.

Figure 2.10 Calibration data for orifice meter

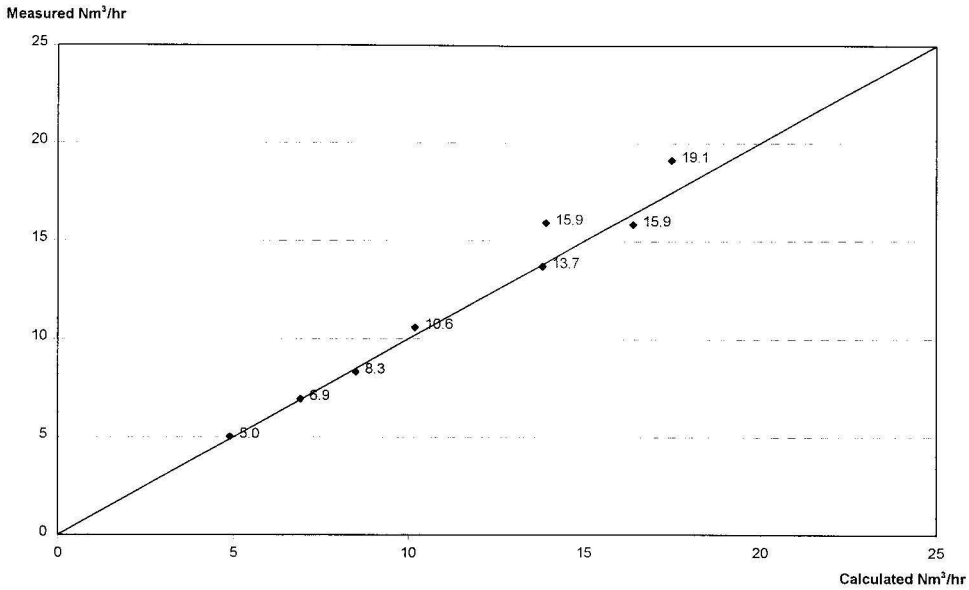

Experimental procedure

The manganese metal used for the experimental testwork was blended from six 250kg lots in a rotary blender. Two 750kg drums were filled with the discharge of the blender. Feed material for the testwork was taken from these drums. The reactor was charged by adding a metal slurry that was made up in a separate mixing vessel. In all runs except for the nitrogen purge run the steam was opened after charging the slurry to heat the reactor to autothermal conditions. In the case of the run with nitrogen purging, the slurry was sparged with bottled nitrogen for 10 minutes before sparging with steam.

Once autothermal conditions had been reached (above 110°C) the steam flow was stopped. The temperature and pressure was monitored and the pressure in the reactor was controlled manually. This eliminated pressure fluctuations due to poor pressure control that were recorded in the large reactor. The pressure control strategy resulted in overall non-isobaric conditions during the experiment but a constant pH_2*. This was achieved by controlling the reactor pressure to setpoints that were obtained by adding the required pH_2* pressure increment to the water-vapour pressure of the reactor. A table of pressures and temperatures calculated for each pH_2* increment was used to adjust the reactor pressure using the slurry temperature. This method of pressure control allowed the reactor pressure to be controlled to within an average 5,6kPa of the required pressure. This represented a 0,7% deviation from setpoint.

Samples of slurries were taken using a sampling probe and were immediately quenched directly into demineralised water. These were subsequently dried in a drying oven before

being analysed. Samples were also taken during the oxidation stage that followed the dissolution stage of the runs. These were used for evaluating kinetics and particle morphology during manganous hydroxide oxidation.

Experimental results

The experimental results obtained from the pilot reactor runs are discussed below in the sequence of input material characterisation, raw data collected during a run and data analysis. The processed data was used as a basis for the kinetic and mechanistic modelling study in Chapter 3.

Appendix D gives a detailed description of the chemical, SEM/EDS image analysis and particle size distribution analyses that were used to characterise the metal used for the hydrothermal testwork. The SEM images show the presence of two phases. The metal appears as bright images of compact, angular and elongated particles. The large particles show cracks indicative of the fracture of a brittle material that could have arisen during the preparation of the polished sections. The oxide phase appears as dull images that are present as separate particles and as rims on the metal particles. Individual particles of foreign material (e.g. $CaSO_4$) could not be found. The analytical procedure and software used for the image analysis was not able to quantitatively resolve the oxide into separate particle or rim-on-metal particle categories. The term particle in the discussion below therefore refers to both categories. Image analysis was used to estimate the relative proportions of the two phases and the particle size and shape factor distributions of each phase. On this basis it was estimated that 18% of the metal mass is in oxide form. A metal oxide content of 6,2% is calculated by assuming that the chemically analysed oxygen content of the metal is present as Mn_3O_4. As image analysis cannot fully account for the oxide content in the depth of the polished section it is assumed that the chemical oxygen assay result is more reliable. The maximum oxide particle (or image) size measured 38μm while metal particles up to 425μm were found with a resolution of 2μm. The oxide particles are thus significantly smaller than the metal particles. Shape measurements ($Perimeter^2/Area$) show a relatively narrow range of sphericity with the oxide particles being in general more elongated than the metal. The particle size analyses show that repeatable results could be obtained using a Malvern analyser. The $D_v(0,5)$'s of the distributions measured varied between 28 and 31μm. The Malvern results gave size distributions that were coarser than those obtained by screening in the +45μm size range. This would be explained by the elongated shape of the particles. Detailed results are given in Appendix D. Particle size distributions based on the number, area and volume of particles were calculated from the Malvern results and are plotted in Figure 2.11.

Figure 2.11 Particle size distributions of metal

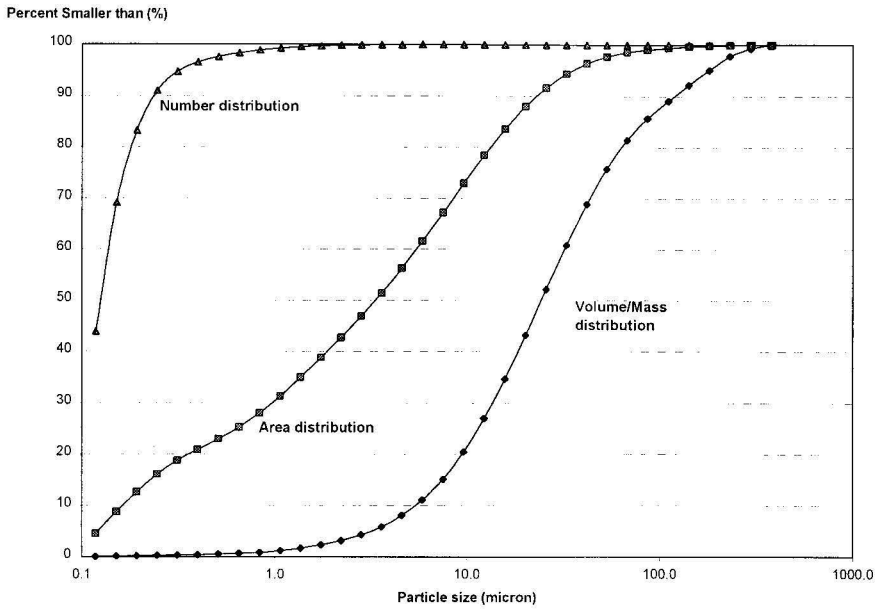

This figure shows that although the volume fraction of particles below 1 micron is small (~1,2%), the area and number contributions of particles in this size range are significant i.e. 31 and 99% respectively.

Datalogger readings obtained for the autothermal portion of one run are shown in Figure 2.12. These readings were typical for all runs. A number of features are apparent in Figure 2.12:

- The dP curve is bell-shaped with some noise evident in the readings. This noise was due to manual adjustments being made to control the vent valve opening and the unsteady nature of the gas disengaging from the water in the condenser.

- The headspace pressure curve increases monotonically indicating improved pressure control in comparison with the large reactor run to a maximum of 1272kPa that occurs soon after the vent valve was closed. A pressure decrease was noted thereafter which was attributed to a gas leak from the reactor headspace. 20 minutes after the vent valve was closed, the reactor pressure was lowered to facilitate the addition of air for the oxidation of the manganous hydroxide.

- The slurry temperature increases monotonically from 118 to 169°C, which is similar to the profile obtained on the large reactor. The time taken for this reaction was however longer than for the large reactor run. A 4°C temperature rise is noted after

the vent valve was closed. This indicates that a portion of the metal continued to react during this time.

Figure 2.12 Datalogger readings for pilot scale reactor experiment with pH_2*=600kPa

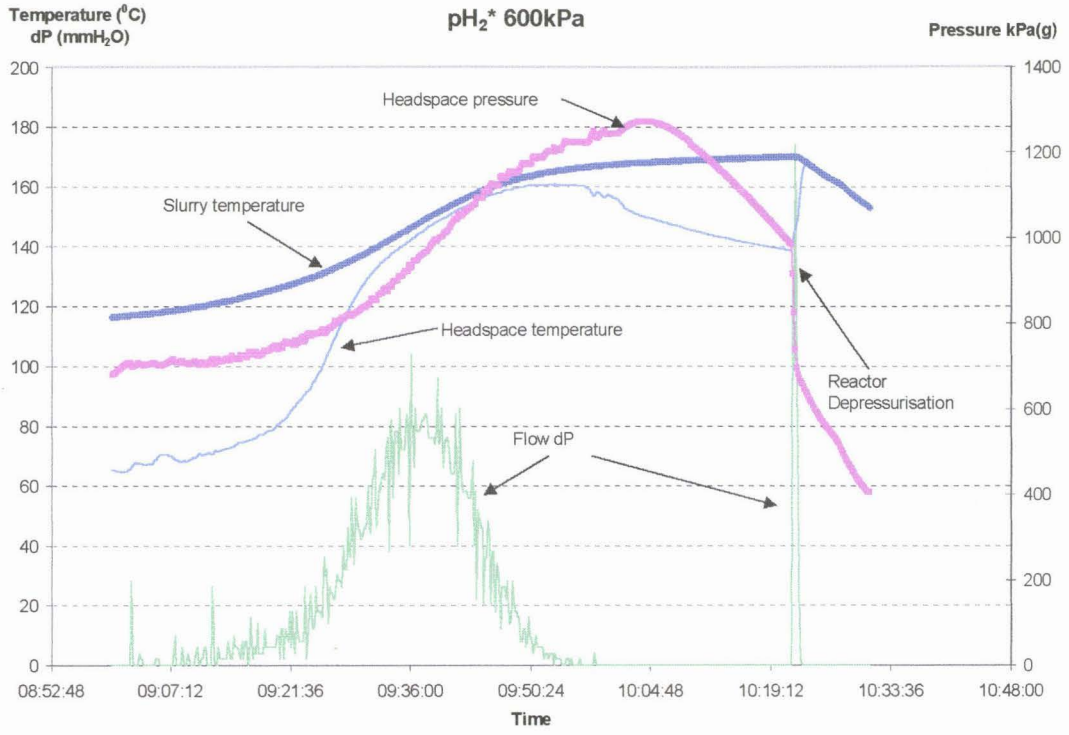

- The headspace temperature reading is lower than the slurry temperature for most of the run. The difference between these readings confirms that thermal equilibrium conditions did not exist between the slurry and reactor headspace. The difference reduces significantly during high venting rate conditions.

Table 2.9 gives a summary of the experimental conditions and results obtained for all the runs. Slurry temperature and pressure readings for all runs are shown in Figures E1 to E3 in Appendix E. These figures show that the total pressure in the reactor was controlled consistently relative to the slurry temperature for all runs in the temperature range 123 to 169°C.

Table 2.9 Summary of pilot reactor experimental results

pH_2* (kPa)	Water Condt. (μS/cm)	T (°C) @ start	T (°C) @ end	T (°C) Max	P (kPa) Max	Vent Time (min)	Condenser H_2O (ml)	Total H_2 vented (Nm^3)
1000	15,4	120,8	170,5	173,4	1713	37,0	4000	11,02
1000	16,8	119,6	170,0	174,7	1793	37,8	4627	13,89
1000	14,0	121,7	172.8	177,3	1778	27,8	4706	12,23
800	22,7	122,8	170,8	173,6	1529	29,5	5887	12,67
800	14,4	115,4	163,3	167,9	1423	50,0	-	11,24
800	0,1	121,7	170,7	174,2	1538	37,8	5098	12,01
600	16,4	116,9	167,0	170,0	1267	53,0	5882	11,59
600	4,7	122,3	173,8	174,1	1345	46,3	7059	13,75
600	7,3	126,4	172,4	174,1	1358	35,3	7059	12,17
600 (N_2 flush)	19,7	133,6	176,3	180,5	1462	40,0	7843	12,57
400	-	114,4	154,3	158,8	900	60,0	-	11,16

A comparison is made in Figure 2.13 of the average dissolution or venting periods as measured by the duration that gas was vented from the reactor. Qualitatively the average dissolution times decrease with increasing pH_2*. This is expected as increased water vapour pressure content and higher energy losses will result when venting the reactor at lower pressure. The large variation in the venting times is due to the differences in the temperature at the start of the venting period ($T\ (°C)_{@start}$ in Table 2.9) and in determining the onset and end of the venting period. The 400kPa pH_2* run was not repeated as a result of the low reaction rates requiring extended reaction times for complete conversion. The single value obtained for the dissolution time however confirms the observed trend. Nitrogen purging the reactor prior to introduction of steam required extended steam sparging times for the reactor to reach autothermal conditions. In this run, the highest start temperature was recorded. The absence of oxygen in the reactor at the start of the dissolution reaction clearly reduced the rate of dissolution prior to venting. This confirms the observations made by Ohta *et al.* (1990) that higher rates of dissolution are obtained in the presence of oxygen.

Figure 2.13 Effect of headspace hydrogen pressure (pH_2*) on venting time

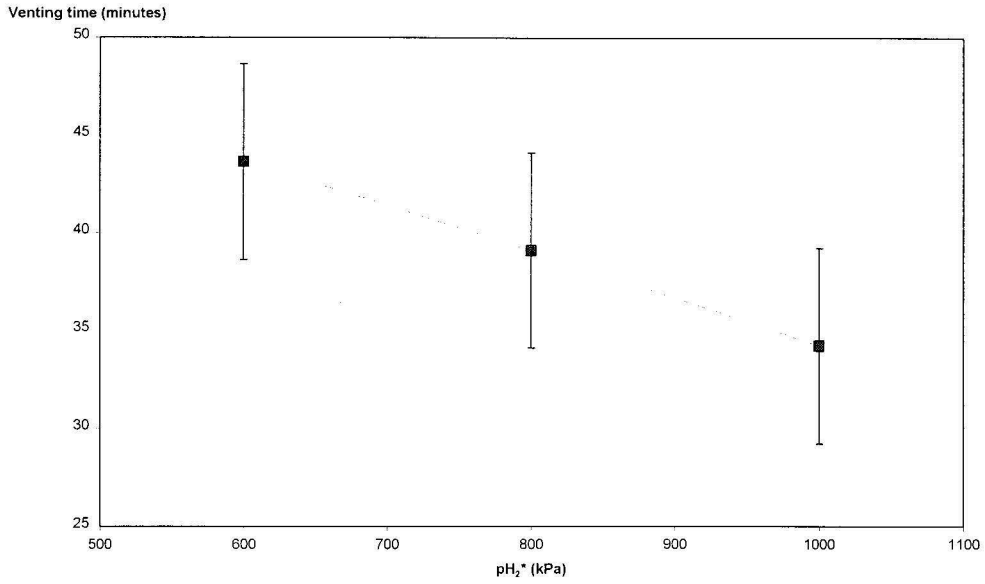

The total amount of hydrogen collected during venting for all the runs was on average 80% (sdev 6%) of the value calculated stoichiometrically from the amount of metal added corrected for 6,2% oxide content as analysed above. The closure of the mass balance requires estimation of gas leakage rates and the quantity of metal reacting before and after the venting period. This is discussed further below.

200ml samples of the reactor contents were taken at 5 minute time intervals for three runs, each at different pH_2*, filtered, dried and analysed for total manganese content using a permanganate potentiometric titration method. The total manganese content of these samples ranged from 69 to 87%. The confidence limit for these results, established by 272 analyses on an internal standard sample, corresponds to one standard deviation of 0,56% of the manganese content. These results were converted to fractional conversion values by assuming that each sample consisted of metal and manganese oxide in the form of Mn_3O_4 (*vide infra* section 4.2 for more detail). Corrections were applied to establish kinetic effects for the venting portion of the dissolution reaction only. Here the conversion values were adjusted for available Mn in the head-feed metal and for the fraction that converted in the reactor prior to venting. All the gas flowrate results were converted to fractional conversion profiles by dividing the cumulative gas volumes by the integrated gas volume over the whole venting period. The kinetics based on solid phase measurements (with estimated error bars) and H_2 gas volume measurements are shown in Figure 2.14 to Figure 2.16. The release of accumulated hydrogen evolved prior to venting can be seen as the spikes in the gas flowrate readings at zero venting times in all the figures.

Figure 2.14 Non-isothermal Mn dissolution kinetics at 600kPa hydrogen partial pressure

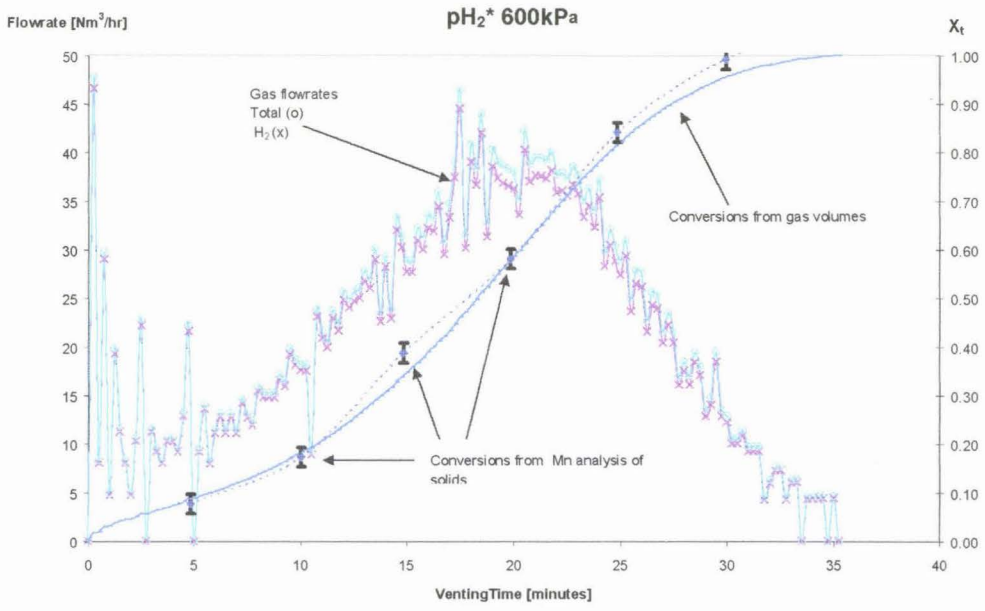

Figure 2.15 Non-isothermal Mn dissolution kinetics at 800kPa hydrogen partial pressure

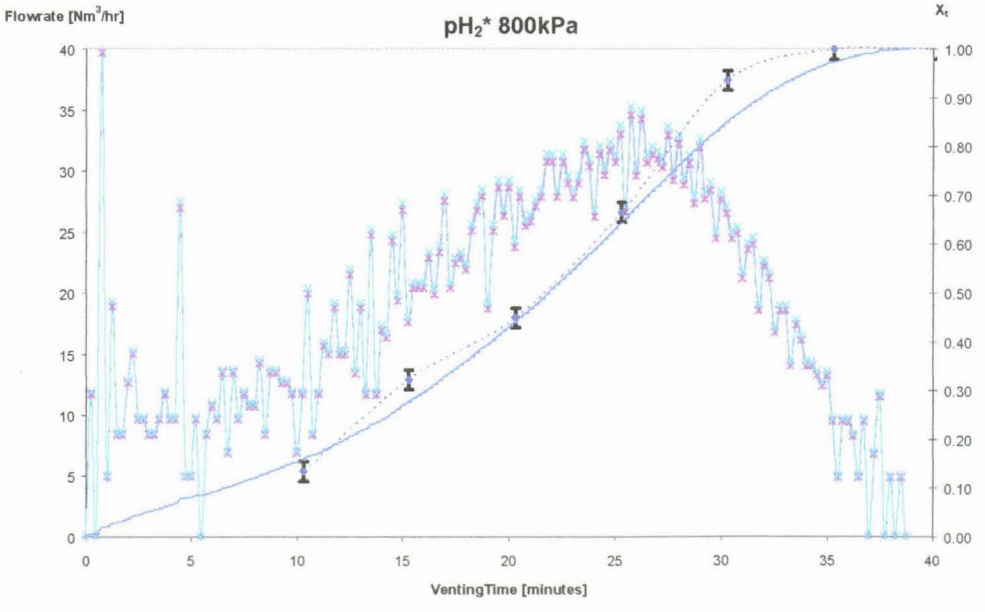

Figure 2.16 Non-isothermal Mn dissolution kinetics at 1000kPa hydrogen partial pressure

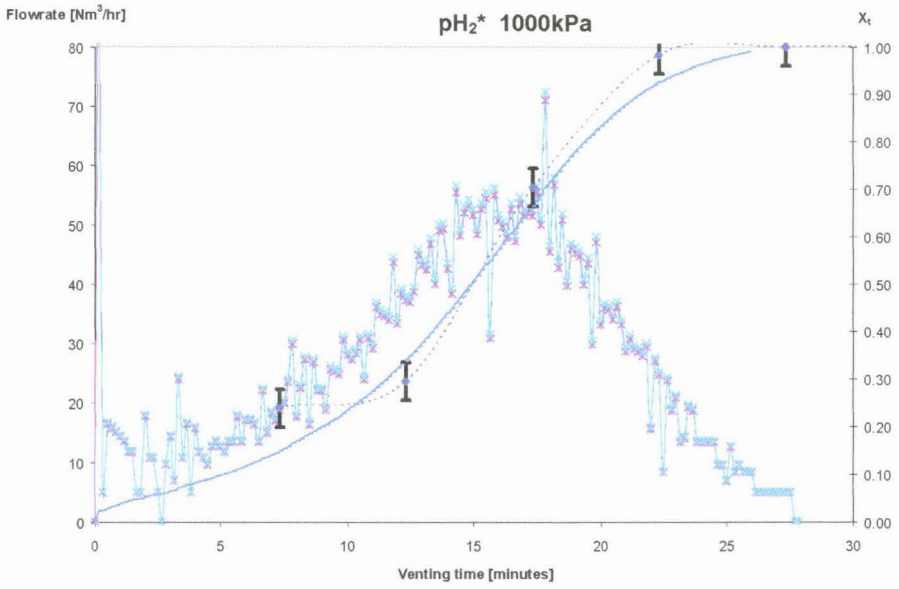

The correlation obtained in the kinetics based the gas volume data and solids analyses suggests that this data may be useful for further kinetic evaluation. The relative positions of these curves in each of these figures confirm the observation that the gas flowrate measurements are conservative. The rapid decrease in the pressure profiles above 169°C in the figures E1 to E3 in Appendix E confirms that perfect sealing conditions could not obtained. An estimate was made of the amount of metal that reacted in the post-venting period using the fractional rise of temperature. This calculation showed that for all runs an average 6,2% of the metal reacted in this period. The mass balance closure therefore improves to 86%. Further closure can be achieved by including the fraction of metal that dissolves in the presence of oxygen prior to venting. This would occur without the evolution of hydrogen. Calculations using estimates of the oxygen content in the liquid feed and reactor headspace indicate that up to 4% of the metal could dissolve without hydrogen evolution. 90% closure of the hydrogen mass balance is obtained if this effect is included.

The cumulative conversion curves for each of the experiments were plotted relative to the slurry temperature readings measured at each time interval in Figure 2.17 for the experiments conducted at pH_2* 1000kPa. Similar plots for the pH_2* 800kPa and pH_2* 600kPa experiments are given in Appendix E, Figures E4 and E5, respectively.

Figure 2.17 Temperature dependent cumulative conversion plots for experiments at pH_2*1000kPa

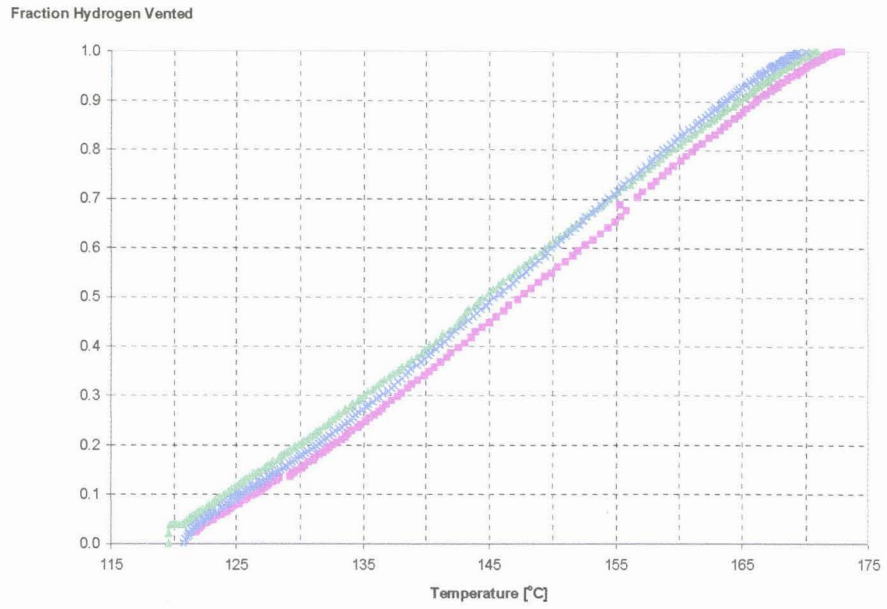

The extent of the dissolution of manganese during the venting of hydrogen was therefore directly proportional to the temperature of the slurry in the reactor. A similar observation was obtained for Ramananes' experiments for a narrow range of conversion as seen in section 2.3.2. Linear regression of the plots gave coefficients of fit (R^2) that ranged from 0,995 to 0,998. The goodness-of-fit increased with increasing pH_2*. The plots also show that it was possible to replicate the experiments in a narrow temperature-conversion domain.

The determination of specific reaction rates and elucidation of reaction mechanisms required measurements of the variations in metal particle morphology during the dissolution process. Particle size analyses and SEM images were obtained on the dried samples taken during the experiments for this purpose. The experimental procedures used to obtain this data were similar to those described in Appendix K. The $D_v(0,1)$, $D_v(0,5)$ and $D_v(0,9)$ of the particle size distributions measured are given in Table 2.10. Two-dimensional and three-dimensional plots of the data for one set of samples taken during a dissolution experiment are shown in Figure 2.18 and Figure 2.19 respectively. A decrease in the proportion of metal fraction (Mean dp ~ 19μm) with a concomitant increase in proportion of the oxide size fraction (Mean dp ~ 6μm) is evident. These distributions were used in the kinetic and mechanistic modelling exercise described in Chapter 3.

Table 2.10 Results of particle size analyses conducted on dried hydrolysis intermediates

pH_2*(kPa)	600			800			1000		
Sample	D_v10	D_v50	D_v90	D_v10	D_v50	D_v90	D_v10	D_v50	D_v90
1	1,85	13,5	42,6	1,97	14,3	57,9	1,50	11,1	43,8
2	1,57	11,4	46,0	1,68	11,3	47,7	1,32	8,15	45,2
3	1,36	6,51	39,8	1,43	8,10	43.8	1,16	5,43	34,5
4	1,14	4,79	25,8	1,22	5,85	42,7	1,13	4,87	31,2
5	1,06	4,23	14,8	1,20	5,08	33,4	1,00	4,24	13,6
6	1,03	4,16	12,2	1,09	4,40	13,5	1,00	4,37	17,4
7	1,02	4,28	12,0	0,97	4,21	12,5	0,92	4,14	12,2
8	1,03	4,39	12,7	1,01	4,36	11,7	1,00	4,43	12,8

Note: All dimensions in μm

Figure 2.18 Particle size distributions of samples taken during hydrothermal dissolution of Mn metal (2-dimensional)

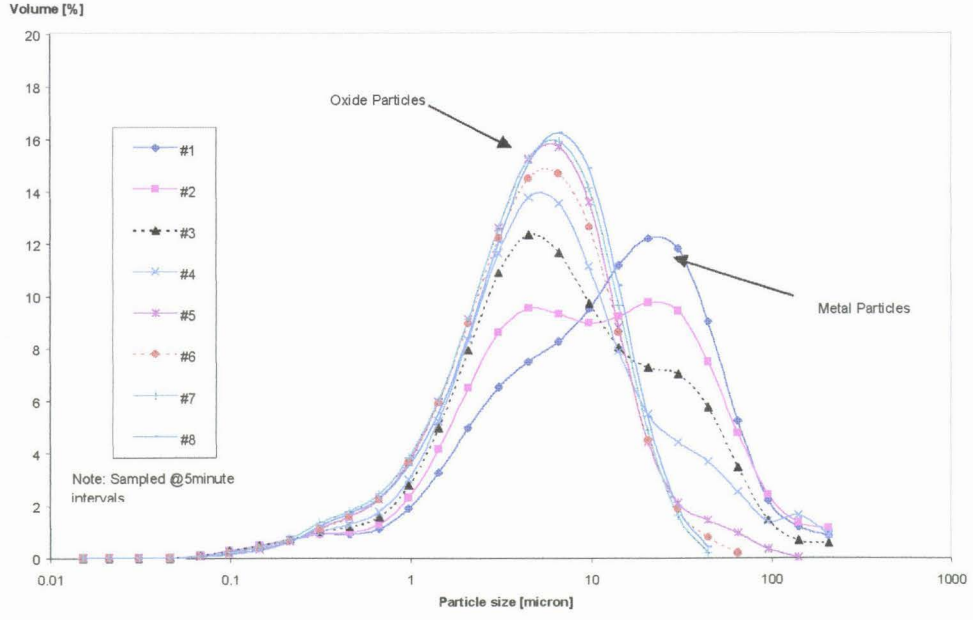

Figure 2.19 Particle size distributions of samples taken during hydrothermal dissolution of Mn metal (3-dimensional)

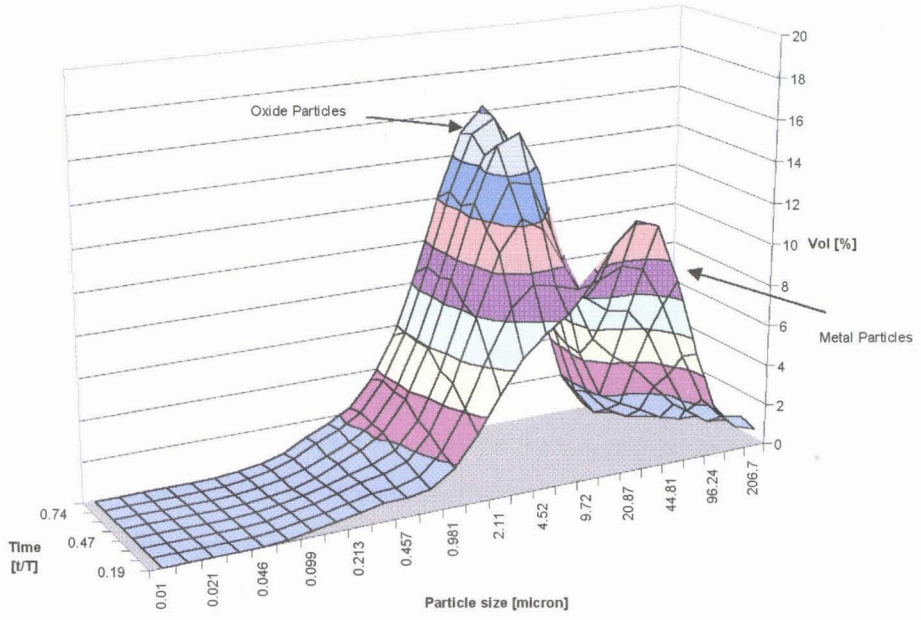

Z axis:% volume , Y axis: fraction of total venting time, X axis: particle size.

SEM images taken on these samples are included in Appendix D. The images show that rounding of the sharp edges of the particles occurs as the dissolution reaction progresses. The metal occurs as segregated particles and as occlusions in a background of large (~100μm) globular oxide particles. Extensive oxide rimming occurred on a number of the metal particles. In addition, a number of metal and oxide macroparticles or clusters are observed. The occlusion and cluster features are expected to be due to the sample preparation procedure, as this required the samples to be dried before mounting for the SEM. The large macroclusters are not observed in the Malvern PSD results which were also obtained on dried samples. The analytical PSD procedure includes the use of ultrasound and a dispersant that would break down weakly bound aggregated particle-structures. Clusters were not observed under optical microscope on smears of the unfiltered reactor contents. SEM on slurry samples smeared onto an aluminium stub also confirmed this observation. These effects are discussed in more detail in section 4.2.10.

2.4 Summary of Results from Dissolution Experiments

The above testwork has demonstrated how the experimental procedure was developed to measure reaction rates in a non-isothermal, polydisperse, hydrothermal dissolution and precipitation reaction system. Variations of this experimental procedure are used in the synthesis of high purity manganese oxides.

The rate of reaction for non-oxidative dissolution of manganese metal in the presence of complexing reagents up to temperatures of 80°C can be modelled by spherical shrinking core kinetics with first-order, chemical reaction control. The mechanism of dissolution in the absence of oxygen and the presence of complexing reagent agrees qualitatively with the general model of dissolution discussed by Osseo-Asare (1984). The rate of reaction during simultaneous dissolution and oxidation of manganese metal in the presence of complexing reagents is limited by the rate of oxygen mass transfer.

The enhancing effect of oxygen on the dissolution rate of Mn metal in the presence of complexing reagents was confirmed as anticipated in Chapter 1. Exploratory testwork conducted in pure water showed that the absence of oxygen in the initial stages of hydrothermal dissolution inhibits the dissolution of the metal. However, once autothermal conditions are achieved, with high hydrogen partial pressures, the influence of oxygen becomes insignificant. This suggests that the oxygen has a similar effect to the complexing reagents, i.e. it prevents the build-up of passivating layers of manganous hydroxide on the surface of the metal. In this case however it is achieved by oxidising the hydroxide which then spalls away from the surface.

Laboratory scale dissolution experiments conducted in pure water in the temperature range 84 to 95°C showed poor reproducibility and required long reaction times. Complete conversion was not achieved in the majority of runs. In analysing these results, Ramanane (1987) assumed monodisperse solid particles and found that a spherical, non-porous, shrinking core model with first order, chemical reaction control at the surface gave the best fit for the kinetics of the process. An activation energy of 70 kJ/mol was which is similar to that reported by Hurlen & Valand (1964c) for the dissolution of metallic manganese in 0,5M H_2SO_4 in the temperature range 0-50°C i.e. 63kJ/mol. Although the results of this testwork do not conform to acceptable standards of repeatability, they do confirm the effectiveness with which the use of complexing reagents results in increased rates of reaction in this system. It is postulated that the increased reaction rates with complexing reagents are due to increased dissolved manganese contents which limit the precipitation of manganous hydroxide in the reaction layer adjacent to the metal surface. Catalytic effects are probably not occurring due to the high concentrations of complexing reagent that were required to achieve the increased rates of dissolution.

The time required for complete dissolution of metal particles in Ramanane's testwork is considerably longer than for the pure water hydrothermal experiments i.e. hours compared with minutes. The rate of hydrothermal dissolution of manganese increases significantly above 110°C with an approximately linear relationship being obtained between the extent of conversion and temperature under these experimental conditions.

Reliable reaction rate data could not be obtained from the large scale reactor run due to the absence of equilibrium between the gas and liquid phases in the headspace of the reactor. This condition was necessary for the calculation of gas composition and mass flowrate of the venting gas stream. The testwork however showed that by making certain simplifying assumptions it is possible, in principle, to obtain the activation energy for manganese metal dissolution from a single non-isothermal experiment. By analogy, this experimental procedure is similar to the method of dynamic thermogravimetric analysis where kinetic parameters are obtained by conducting non-isothermal experiments within specifically controlled temperatures. The testwork also showed that the pressure of the reactor needed to be controlled in a predictable manner so that useful data may be gathered for meaningful interpretations of the rate-controlling reaction mechanisms.

More reliable reaction rate measurements were obtained by modifying the pilot scale experimental apparatus and by conducting additional reaction extent measurements on the solid phase in the reactor. Particle size distributions measurements were also made that clearly show two dispersed solid phases. The particle size distributions of the manganese metal and manganous hydroxide phases however overlap and deconvolution is necessary to be able to determine specific reaction rates for the dissolution reaction. This analysis is performed in Chapter 3. The problem of how to control the pressure was solved by choosing to conduct the experiments at fixed pressure increments above the vapour pressure curve of water. Thus, although the experiments were conducted under non-isothermal and non-isobaric conditions, the temperature and pressure was coupled in a well characterised and predictable manner. This control methodology therefore allowed the dissolution experiments to be conducted at fixed hydrogen partial pressures. This feature has not been reported before for this reaction system.

The plots of temperature versus reaction extent obtained for the pilot reactor experiments were more linear than for the single large scale run indicating better experimental control. In addition, the repeatability of the runs was confirmed by the close proximity of the temperature versus reaction extent plots at fixed hydrogen partial pressure increments. Reproducibility under these conditions cannot be assessed by a single parameter and a locus of points must be mapped in an appropriate domain of comparison. This is discussed further in Chapter 3 where it is shown that the repeatability can be assessed from Arrhenius plots.

3 EQUILIBRIUM AND KINETIC ASPECTS OF MANGANESE METAL DISSOLUTION

3.1 INTRODUCTION

The phase equilibria relevant to this reaction system have been introduced in section 1.2 where it was found that there is a need to confirm the limits of stability of manganous hydroxide. An analysis is first presented of the limits of stability of the species in this reaction system through the use of Eh-pH diagrams which were calculated specifically for the conditions expected in the pilot scale reactor. The equilibrium considerations are used to determine limiting conditions for the kinetic studies on the dissolution of manganese metal

The preliminary analyses of dissolution rate measurements reported in section 2.3.3 for the large reactor suggested that it is possible to obtain an Arrhenius parameter for the hydrothermal dissolution of Mn metal using a single non-isothermal experiment that is monitored appropriately. The experiments that were conducted in the pilot scale reactor demonstrated that it is possible to control a hydrothermal Mn metal dissolution experiment to consistent and predictable temperature and pressure conditions. In addition, by controlling the reactor at a fixed pressure increment above the vapour pressure curve of water, the equilibrium hydrogen partial pressure in the reactor during the reaction remained constant. In this manner, experiments could be conducted at different but constant hydrogen partial pressure. The effect of hydrogen on reaction kinetics and mechanisms could therefore be investigated further using appropriate kinetic models and data processing procedures. The results obtained from the experiments specifically needed to be analysed from the perspective of coupling the kinetics from solid particle analyses and particle morphology measurements with the kinetic measurements obtained by gas evolution. This analysis is conducted using shrinking particle models that include polydisperse metal particles with non-isothermal conditions. The development of these models and procedures are first described below. Thereafter the reaction mechanisms that could be elucidated from this analysis are discussed. Finally the electrochemical kinetics identified in Chapter 1 are addressed.

3.2 EQUILIBRIUM MODELLING ANALYSIS

In Chapter 1 a review was made of the different methods available for mapping the equilibria of two and three phase reaction systems. Equilibrium considerations determine the limits of stability of the species that could participate in a reacting system. The following sections

analyse the equilibria relevant to the Mn-O_2-H_2O system using a number of different mapping techniques. First the stability of the solid phases with respect to oxygen and hydrogen is determined using gas-solid equilibrium data. It is assumed that the solid phases are defect free and may be represented as stoichiometric oxides. The solution equilibria of the soluble manganese ions are then investigated at ambient and at elevated temperatures. Finally the stability domains of both the soluble and solid components are plotted together in Eh-pH diagrams.

3.2.1 Oxidation Reduction Equilibria

Gas-solid oxidation and reduction equilibria can be used to determine the influence of O_2 and H_2 on the stability of the manganese oxides, MnO_2, Mn_2O_3, Mn_3O_4 and MnO. Figure 3.1 and 3.2 quantitatively define the domains of stability of manganese oxides under oxidising and reducing conditions respectively. Data for plotting the equilibrium curves was obtained from Mah (1960) and MacDonald (1976). Appendix F contains a copy of the spreadsheet used to generate these equilibrium diagrams.

Figure 3.1 Dissociation equilibria of manganese oxides

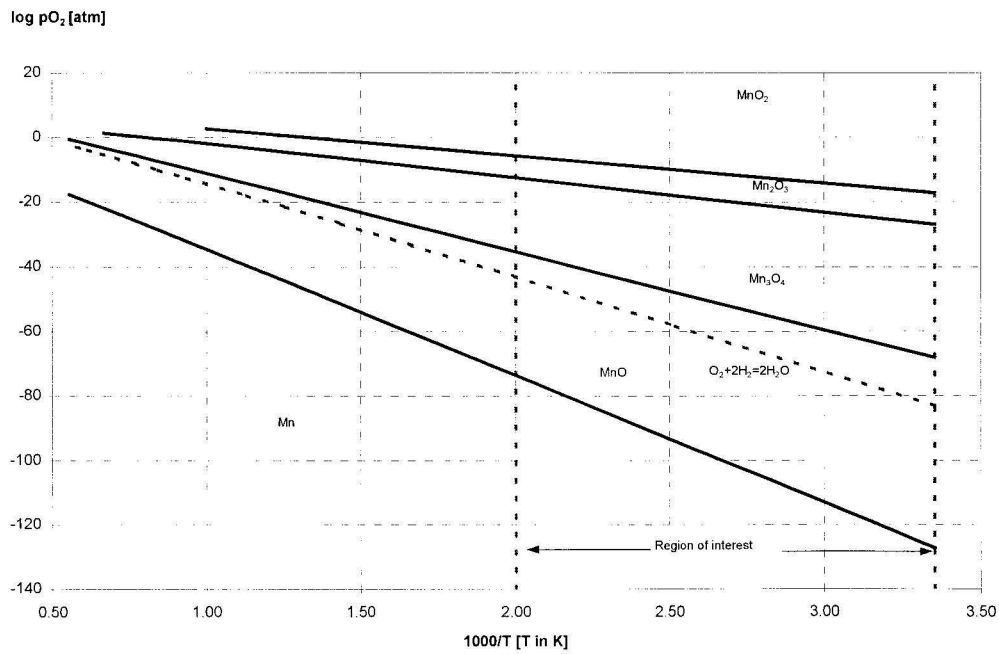

Figure 3.1 shows that the thermodynamically stable form of manganese during the initial stages of manganese metal dissolution (log $pO_2 \approx -0,67$) and final stages of oxidation of manganous hydroxide (log $pO_2 \approx -0,08$) is MnO_2. The stability field of the MnO_2 decreases as the temperature increases and the oxygen partial pressure is reduced. The lower oxidation

states require progressively lower oxygen partial pressures for thermodynamic stability. The conditions for the transitions in the oxide series as reviewed in Chapter 1 viz.:

$$Mn \rightarrow MnO \rightarrow Mn_3O_4 \rightarrow Mn_2O_3 \rightarrow MnO_2$$

can be quantitatively obtained from Figure 3.1. These reactions can also result in the formation of metastable intermediates whose chemical composition will be determined by kinetic considerations.

Figure 3.2 Reduction equilibria of manganese oxides

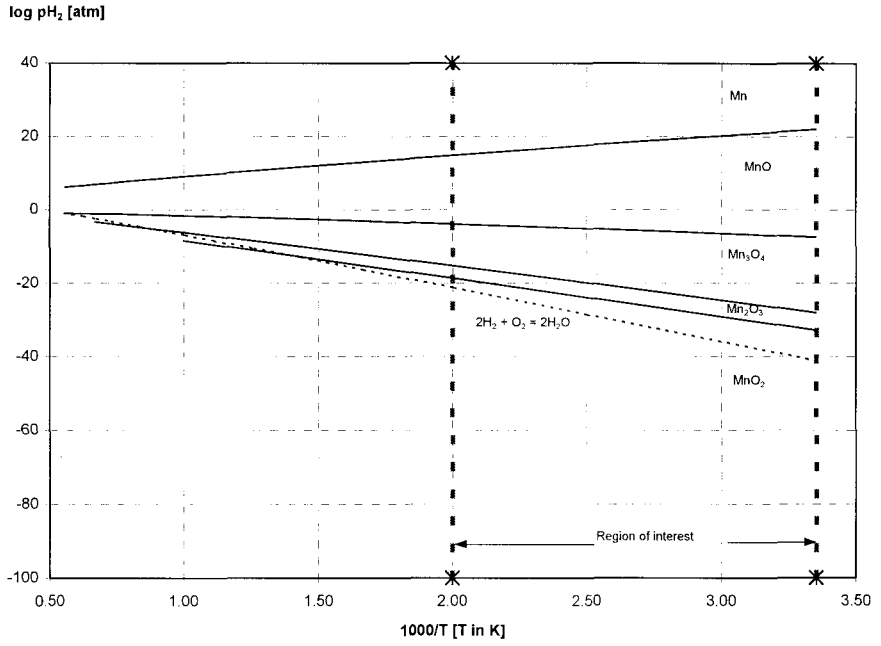

Figure 3.2 applies to the final stages of manganese metal dissolution (log $pH_2 \approx 0,8$) and the early stages of manganous hydroxide oxidation (log $pH_2 < -1,0$). The stabilising action of hydrogen on manganous oxide/hydroxide is evident, as these are the stable phases MnO and Mn_3O_4 at these processing conditions.

3.2.2 Manganese Hydrolysis

The idealised solid forms of manganese that are relevant to this study have been considered in the above section for two-phase systems. An understanding of the stability of soluble manganese species is essential for elucidation of the mechanisms of dissolution and precipitation. The soluble species that can be considered are listed in Table 3.1 according to Pourbaix *et al.* (1974).

Manganese ions will be considered in the 2+ oxidation state only as Mn^{3+} ions are stable at high potential (+1V) and low pH (<0). Permanganate and manganate ions are stable over a broad pH range that varies with potential. Alkali conditions increase ionic stability and MnO_4^{2-} may form at potentials as low as 0,2V at pH 14. This potential is still considerably higher than that expected for the strongly negative corrosion potentials.

Table 3.1 Soluble manganese species

Species	Oxidation State	Name
Mn^{2+}	2+	Manganous ion
$HMnO_2^-$	2+	Dimanganite ion
Mn^{3+}	3+	Manganic ion
MnO_4^{2-}	6+	Manganate ion
MnO_4^-	7+	Permanganate ion

Ref. Pourbaix *et al.* (1974)

It can be seen from Pourbaix's diagram that the regions of stability of these ions are separated from the stability domain of manganese metal by the stability domains of the solid phases of Mn_3O_4, Mn_2O_3 and $Mn(OH)_2$. The ionic species of interest in this study thus reduce to Mn^{2+} and its hydrolysis products.

Table 3.2 Manganous ion hydrolysis products at 25°C

Species	Equilibrium Constant	-log K
$MnOH^-$	K_1	10,59
$Mn(OH)_2^0$	K_2	22,20
$Mn(OH)_{2(S)}$	K_{sp}	15,35
$Mn(OH)_3^-$	K_3	34,80
$Mn(OH)_4^{2-}$	K_4	48,30
$HMnO_2^-$	K_5	19,08

Ref. Pourbaix *et al.* (1974), Baes & Mesmer(1976)

The hydrolysis products and their equilibrium constants obtained from Baes & Mesmer (1976) and Pourbaix *et al.* (1974) are listed in Table 3.2. The manganous ion Mn^{2+} occurs as the hexaquo ion and is stable up to the precipitation of the solid hydroxide. Hydrolysis of the ion occurs according to the general reaction:

$$Mn^{2+}_{(aq)} + x\,H_2O = Mn(OH)^{(2-x)+}_{x(aq)} + x\,H^+ \qquad (x = 1,2,3,4)$$

This reaction is only detectable at pH's approaching $Mn(OH)_2$ precipitation. The $Mn(OH)_2^\circ$ species represents the soluble form of $Mn(OH)_2$. The above equation for the hydrolysis equilibrium reaction shows that the solubility of Mn will decrease with increasing pH due to mass action. The dimanganite ion $HMnO_2^-$ has considerable influence on the distribution of hydrolysis products and on the total soluble manganous ion content. The relatively high value of the hydrolysis constant for $HMnO_2^-$ results in an increase in total Mn solubility at elevated pH. The effect can be seen more clearly in the speciation plots for the ions in Figure 3.4 and Figure 3.5. This increase in solubility is also accompanied by the formation of a regime where active dissolution of manganese metal is possible - Brenet *et al.* (1963). The solubility curve for manganese (and other divalent systems e.g. Ni, Cd, Zn) as a function of pH thus shows a minimum at a characteristic pH. Figure 3.3 shows this curve at a temperature of 25°C for manganese calculated from the equilibrium constants in Table 3.2 for a system saturated with solid manganous hydroxide.

Figure 3.3 Variation of concentration of total soluble manganese with pH at 25°C

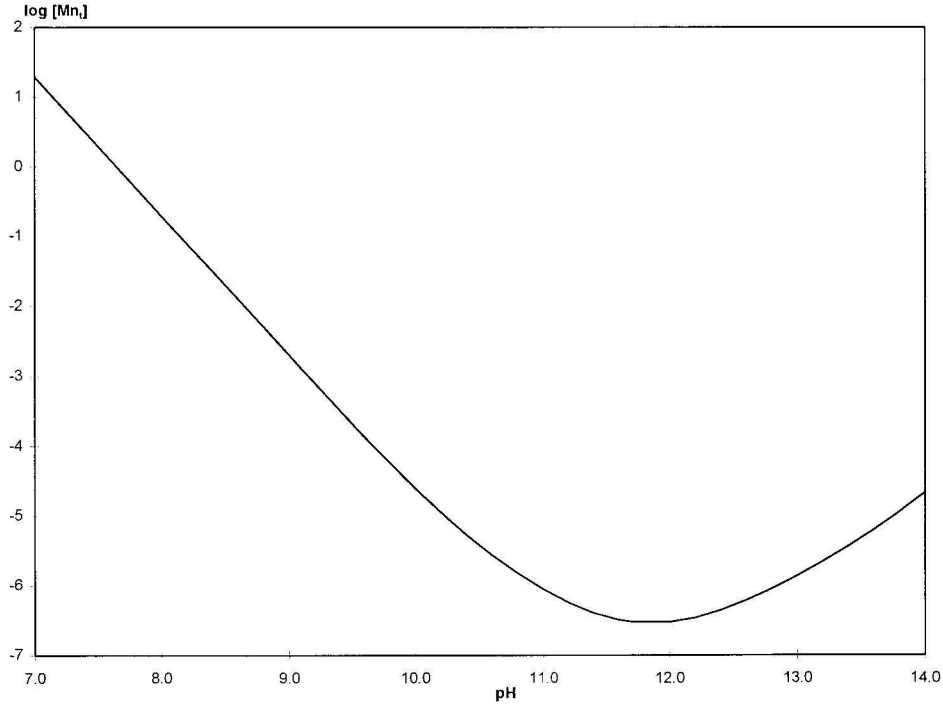

3.2.2.1 Distribution of Hydrolysis Products at Ambient Temperature

Solving the hydrolysis equations at any pH gives the distribution of soluble species shown in Table 3.3. The change in the speciation of soluble manganese ions as a function of pH at ambient temperature is shown in Figure 3.4. The total soluble manganous ion concentration under these conditions is approximately 5,8 x 10^{-5}mol.ℓ^{-1} of contained Mn^{2+}. The relative contribution of the third and higher hydrolysis products to the total soluble ion concentration

is small. Further calculations show that only if the pH rises in excess of 11 do these ions start contributing significantly to the total solubility.

Table 3.3 Distribution of soluble Mn^{2+} species

Ion	Percentage(%) Soluble Species
Mn^{2+}	84.8
$MnOH^{+}$	15.0
$Mn(OH)_2^{o}$	0.2
$Mn(OH)_3^{-}$	3.38×10^{-4}
$Mn(OH)_4^{=}$	6.73×10^{-8}
MnO_2H^{-}	9.03×10^{-4}

Water at 25°C, pH 9,8, saturated with $Mn(OH)_2$

Figure 3.4 Speciation plot of soluble Mn^{2+} species at 25°C

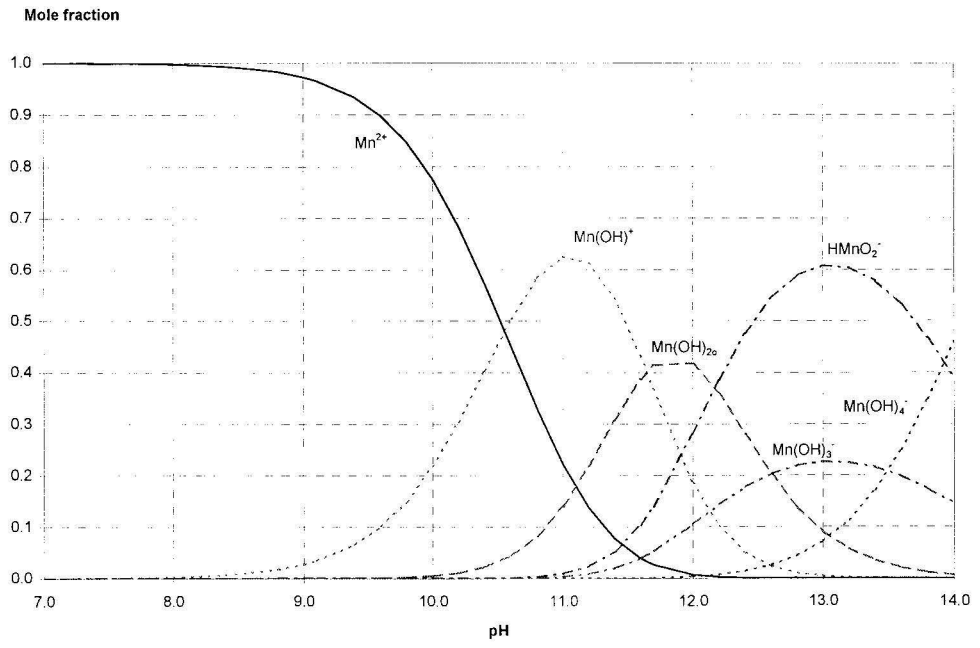

The overlapping stability of these ionic species cannot be shown explicitly on Eh-pH of diagrams and these equilibria are read more easily from a distribution diagram similar to Figure 3.4.

3.2.2.2 Distribution of Hydrolysis Products at Elevated Temperature

The effect of temperature on the hydrolysis constants for each of the species in Table 3.3 must be known before their speciation at higher temperatures can be determined. Bhandage *et al.* (1987) found that a dearth existed with respect to thermodynamic information on hydroxide systems. This was still the situation during this research. Data for the variation of the first and second hydrolysis products of the manganous ion with temperature is available in Gmelins (1973) and Baes & Mesmer (1976). Limited data was reported by Rodrigues (1983) on the effect of temperature on the solubility product of $Mn(OH)_2$. MacDonald (1976) studied the theoretical corrosion behaviour of manganese at elevated temperatures and excluded the hydrolysis products listed above due to lack of equilibrium data. MacDonald used thermodynamic data for MnO in his study and found that the hydrolysis of manganese was favoured with increasing temperature. MacDonald also excluded the Mn^{2+} hydrolysis products, apparently due to their poor stability with respect to temperature. $Mn(OH)_2$ is known to dehydrate in the temperature range 166°C to 200°C i.e.:

$$Mn(OH)_{2(s)} \Leftrightarrow MnO_{(s)} + H_2O_{(g)}$$

This reaction occurs in gas-solid systems but has not been reported for aqueous systems. Simon (1943) reported that complete dissolution of precipitated manganous hydroxide occurs above 190°C in aqueous systems, though Tareen *et al.*(1982) found it to be stable above 500°C. Solubility information under these conditions is also not available from the literature. The stability of $Mn(OH)_2$ up to temperatures of 180°C in aqueous suspension is confirmed in this thesis. The $Mn(OH)_2$ dehydration reaction is used as one method for estimating the extent of oxidation of $Mn(OH)_2$ in Chapter 4.

Appendix C details the calculations that were used to estimate the speciation of soluble manganese ions at higher temperature. The speciation plots are repeated at for a temperature of 125°C in Figure 3.5.

A change in the distribution is clearly apparent with $Mn(OH)_2^0$ and $Mn(OH)_3^-$ not making a significant contribution to the total solubility of Mn^{2+} at higher temperature. $MnOH^+$ becomes a more dominant component at pH 11 in comparison to the ambient temperature distribution. The total solubility increases and the minimum solubility in Figure 3.3 shifts to a higher pH value. The solubility of $Mn(OH)_2^0$ is two orders of magnitude lower than Mn^{2+} under these conditions. Additional measurements of manganese solubility and speciation at elevated temperatures are required to confirm and improve the understanding of the chemistry of this system.

Figure 3.5 Speciation plot of soluble Mn^{2+} species at 125 °C

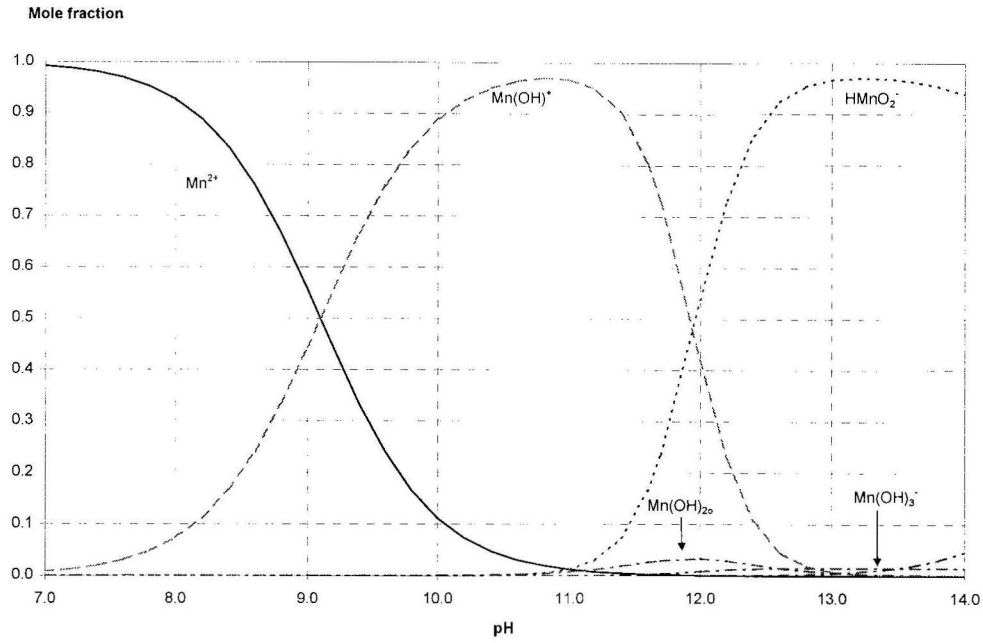

3.2.3 Electrochemical Equilibria

The influence of solution parameters such as pH and redox potential on the stability of solid and soluble manganese species can conveniently be represented on Pourbaix-type diagrams. These diagrams are usually presented in a standard format i.e. unit activity of all species, temperature at 25°C, 1 atmosphere total pressure, solid oxide species are stoichiometric, only predominant species are shown and only one form of allotropic structures is considered. MacDonald (1976) calculated Eh-pH diagrams for the manganese-water system in the temperature range 25 to 300°C. For this thesis, elevated temperature Eh-pH diagrams are recalculated below at a temperature of 125°C and at the 0,0001M total soluble manganous concentration. These conditions are expected to be typical for the manganese dissolution reaction already discussed and to experiments conducted on hydrothermal oxidation of $Mn(OH)_2$ that are discussed in more detail in section 5. The procedure of MacDonald (1976) was used to generate the diagrams. A synopsis of the method follows.

The reactions that occur in aqueous systems can be represented by the general half-cell reaction:

$$aA + xH^+ + ze^- = bB + cH_2O$$

The half-cell potential referred to the standard hydrogen electrode is obtained from the general equation:

$$E_T = -\Delta G_T^{O}/zF - 2{,}303RT/ZF(b\ \log a_B - a\ \log a_A) - 2{,}303xRT/zF\ pH_T$$

Here $-\Delta G_T^{O}$ is the standard Gibbs energy change of the whole cell reaction which is represented by:

$$aA + (x-z)\ H^+ + z/2\ H_2 = bB + cH_2O$$

The Gibbs energies for the substances that have specific heat capacity data (i.e. solid and gases) are corrected to the temperature of interest with the formula:

$$G^{o}_{T_2} = G^{o}_{T_1} - S^{o}_{T_1}[T_2 - T_1] - T_2 \int_{T1}^{T2} \frac{Cp^{o}}{T} dT + \int_{T1}^{T2} Cp^{o} dT$$

Heat capacity data is generally not available for dissolved species. The Gibbs energies for these are estimated using the formula:

$$G^{o}_{T_2} = G^{o}_{T_1} - [S^{o}_{T_2} T_2 - S^{o}_{T_1} T_1] + \frac{(T_2 - T_1)}{\ln\left(\frac{T_2}{T_1}\right)}[S^{o}_{T_2} - S^{o}_{T_1}]$$

S^{o}_{T} is the absolute entropy of an ion at temperature T, which is estimated using the correspondence principle of Criss & Cobble (1964). The simplifying assumptions that have been made in the preparation of the diagrams presented here include:

a) the exclusion of all soluble manganese species with oxidation states higher than 2+,

b) the exclusion of 2+ oxidation states which are present in very low proportions relative to the concentrations of the predominantly soluble species,

c) the exclusion of reactions involving MnO_2.

The free enthalpy of formation data from MacDonald (1976) was used to generate the equilibria with the exception of the hydrolysis equilibria and solubility product of $Mn(OH)_2$ as defined in Appendix C. The inclusion of the solubility product equation:

$$-\log K_{sp} = (474/T + 1{,}974)^2$$

indicates that the precipitation of $Mn(OH)_2$ at 25°C in a solution containing unit activity Mn^{2+} ions occurs at a lower pH (7,65) than predicted by MacDonald (9,11). Appendix G includes a printout of the electronic spreadsheet that was used to generate the diagrams shown in the following figures. A simplified diagram at standard conditions is shown in Figure 3.6.

The hydrolysis equilibria for $MnOH^+$ and $HMnO_2^-$ correspond closely to MacDonald's values and are represented in the diagram by the two dashed vertical lines at pH 10,54 and 11,83. The domain of stability of $Mn(OH)_2$ is therefore larger if available data in literature is used to estimate solubility product in comparison to using data for MnO.

Figure 3.6 Standard simplified Eh-pH diagram for Mn-O-H_2O at 25°C

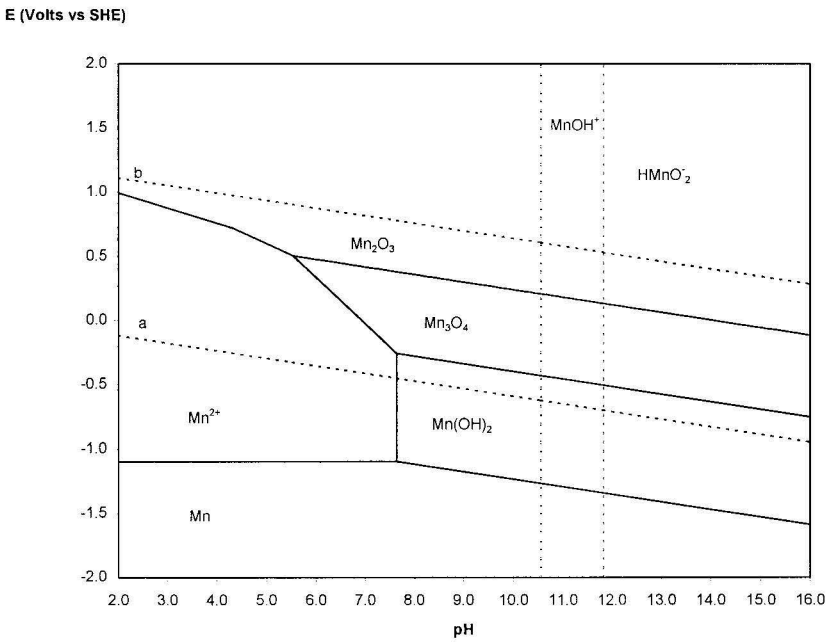

The diagram shows that the domain of $Mn(OH)_2$ stability extends into the region of water stability (i.e. above line *a*) at low redox potentials. The stable solid species at higher redox potentials in aqueous solutions is Mn_3O_4. The influence of temperature on the domains of stability of the species can be seen in Figure 3.7, which is the above diagram recalculated at 125°C. The difference between the pH of precipitation of $Mn(OH)_2$ calculated by the above empirical relationship and by MacDonald's method reduces at higher temperature, viz. 6,96 compared to 6,63.

The hydrolysis and solubility product equilibria shift to lower pH values and the stability domain of $MnOH^+$ reduces at elevated temperature. This is consistent with the trends

expected. The domain of Mn_3O_4 reduces marginally which increases the domain of Mn_2O_3. Mn_3O_4 is therefore less stable at higher temperatures.

Figure 3.7 Simplified Eh-pH diagram for Mn-O-H_2O at 125°C

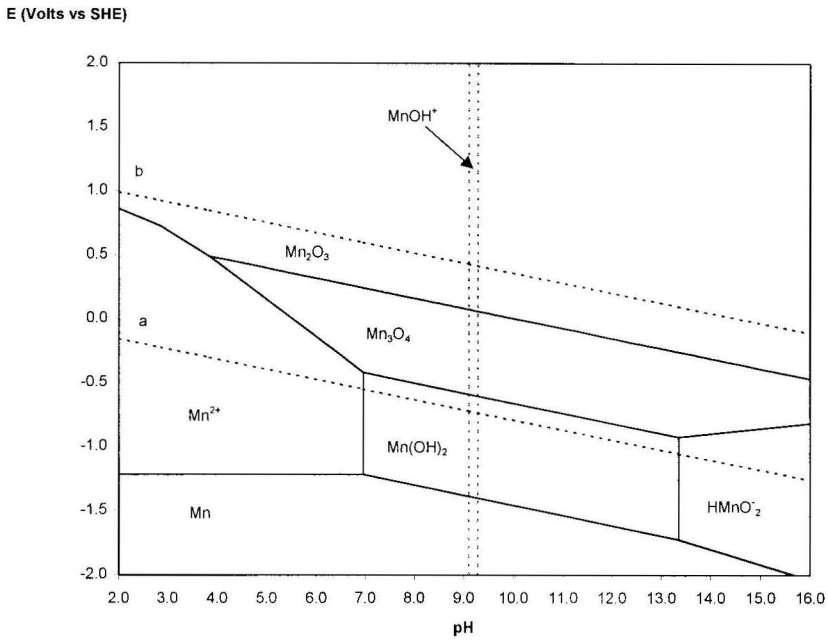

The standard diagram was modified further to take into account low concentrations of dissolved species that would be applicable to the expected experimental conditions. This is shown in Figure 3.8.

The domain of stability of $Mn(OH)_2$ at low concentrations reduces as the limits of stability of Mn^{2+} and $HMnO_2^-$ extend. The tendency to precipitate Mn_3O_4 at lower redox potentials and more alkaline pH's increases. The field of active corrosion of the metal is also extended to higher pH values.

The equilibrium potential of solid manganese will also vary with radius of curvature according to the Gibbs Thomson equation. This variation can be significant in systems with small particles. Calculations detailed in Appendix H show that the equilibrium potential of manganese becomes more negative as the particle size decreases. A 54mV reduction in potential can be expected at a radius of 0,01μm in comparison to a flat surface. At 10μm the variation is negligible. The significance of this effect becomes apparent when the dissolution of small metal particles to extinction is considered. The decrease in potential as the particles become smaller will increase the driving force for the corrosion of the overall process as the equilibrium curve will shift further away from the hydrogen evolution equilibrium on the

Pourbaix diagram. This effect will complement the active corrosion process independent of temperature.

Figure 3.8 Simplified Eh-pH diagram for Mn-O-H_2O at 125°C with 0,0001M of each soluble species

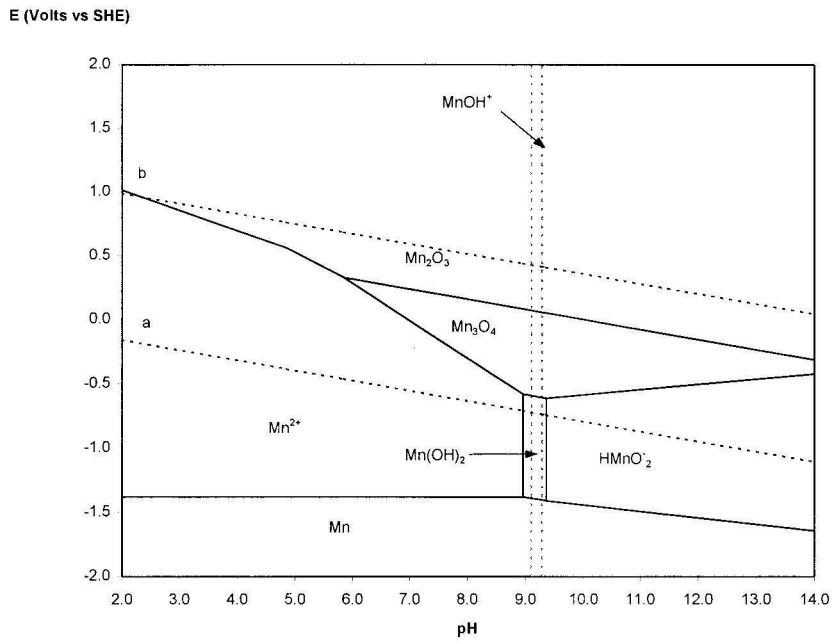

3.2.4 Conclusions

The conclusions that can be drawn from the equilibrium considerations presented in the above sections may be summarised as follows:

- The equilibrium considerations of hydrothermal dissolution and aqueous oxidation of manganese metal can be explained and quantified in terms of relatively simple ideal reactions and reacting species.

- The dominant soluble species at ambient temperatures are expected to be the Mn^{2+} hexaquo ion, $Mn(OH)_2^0$ and $MnOH^+$. At elevated temperatures the domain of stability for $Mn(OH)_2^0$ is reduced and Mn^{2+} and $MnOH^+$ become more dominant. The solubility of manganous ions increases with an increase in temperature. The total concentration of Mn^{2+} ions in solution is low at ambient temperature due to the sparing solubility of $Mn(OH)_2$, viz. $5{,}8 \times 10^{-5} mol.l^{-1}$.

- Measurements of manganese solubility at temperatures above the dehydration of $Mn(OH)_{2(s)}$ are required to resolve the different observations made by Simon (1943) and Tareen *et al.* (1982) concerning the extent of solubility at these conditions. Mn speciation and solubility measurements should also be made in the elevated temperature regime below this condition.

- Active dissolution of manganese metal is known to be theoretically possible at very high pH. This process is facilitated by solubility and speciation considerations at elevated temperature. The domain of stability of the dimanganite ion increases at higher temperature and in low ionic strength solutions. This ion and the reduced solubility of $Mn(OH)_2^0$ reduces the occurrence of precipitates on the corroding metal surface which could block the dissolution reaction.

- Two phase gas equilibrium considerations indicate that MnO_2 is the stable oxide phase under oxidising conditions. Other oxide phases formed under these conditions will thus be metastable and their rate of conversion will be dependent on kinetic considerations. Reducing conditions will favour the formation of manganous hydroxide and oxide due to the action of gaseous hydrogen. These domains of stability are confirmed for three phase systems.

- Eh-pH-type diagrams have been constructed at elevated temperatures using data available in the literature. Previous work in this field has ignored the influence of hydrolysed ions that extend the domains of stability of manganous hydroxide into lower pH regimes.

- The domain of stability of Mn_3O_4 reduces at elevated temperature and in low ionic strength solutions. A domain of processing conditions for the production of predominantly Mn_3O_4 is however predicted from the available literature data.

- The tendency for metal particles to actively dissolve to extinction is promoted by the lowering of the surface potential as a result of increased particle curvature.

3.3 MODELLING OF HYDROTHERMAL MANGANESE METAL DISSOLUTION KINETICS

3.3.1 Isothermal shrinking particle kinetic models

Single particle systems

Levenspiel (1972) derived objective functions that model the kinetics of a number of gas-solid reaction systems (*vide Levenspiel* Table 1 p 273). These include systems of shrinking and non-shrinking particles with sharp reaction interfaces under different rate controlling mechanisms. Additional models that account for the kinetics of more complex heterogeneous systems have been compiled by Doraiswamy & Sharma (1984). The models of Levenspiel therefore represent the simplest forms of kinetic models for heterogeneous reactions. The generic objective function that models the reaction kinetics of a single spherical particle that shrinks as a result of a first order surface reaction or diffusion controlled process takes the form:

$$X_t = 1 - \left[1 - \frac{t}{\tau}\right]^{3/n} \qquad (1)$$

where: t : Reaction time (minutes)

τ : Time for complete reaction (minutes)

X_t : Extent of reaction (0 to 1)

n= 1 (1st order chemical reaction rate control)

1,5 (Large particle film diffusion rate control)

2,0 (Small particle film diffusion rate control (Stokes regime))

The term 'extinction time' (τ) is used in the following discussion to denote the time required for shrinking particles to react to completion. This parameter is dependent on fluid and solid properties, reaction stoichiometry and the rate controlling mechanism. Equations given by Levenspiel to calculate this kinetic parameter for different rate controlling mechanisms in gas-solid systems are given in Table 3.4.

Table 3.4 Equations for extinction time parameters

Chemical reaction	Large particle film diffusion	Small particle film diffusion
n=1	n=1,5	n=2,0
$\tau_r = \frac{\rho_b R_o}{bk_s c_{a(g)}}$	$\tau_{lp} = \frac{constR_0^n}{c_{a(g)}}$	$\tau_{sp} = \frac{\rho_b \gamma R_0^n}{2bDc_{a(g)}}$

where: ρ_b : Density of reacting particle (mol.cm^{-3})

γ : Gas mole fraction

R_0 : Initial radius of particle (cm)

$c_{a(g)}$: Gas concentration (mol.cm^{-3})

b : Stoichiometry factor for solid

k_s : First order reaction rate constant (cm.s^{-1})

D : Molecular diffusion coefficient (m^2.s^{-1})

The assumptions that are made in the derivation of the above functions are:

- The particle is spherical and shrinks uniformly during the reaction.
- The gas concentration $c_{a(g)}$ does not change during reaction.
- The particle is in free-fall or rise and the Ranz-Marshall or Frössling correlation (Bird *et al.* (1960)), viz. Sh=2+0,6(Re)$^{1/2}$(Sc)$^{1/3}$, is used to predict the dependence of the film diffusion coefficient on particle size for small particles. (Note: Sh=Sherwood number, Re=Reynolds number and Sc= Schmidt number.) The dependence of the gas film diffusion coefficient (k_g) for large particles on slip velocity (u) is $k_g \sim (u/dp)^{1/2}$. The effect of changing particle size on mass transfer is therefore taken into account.
- The density of the unreacted particle remains constant during the reaction.

Kinetic plots of these equations are shown in Figure 3.9. The small particle film diffusion and chemical reaction models can thus be regarded as theoretical limits for the actual kinetics if the shrinking particle system conforms to the above assumptions.

Figure 3.9 Kinetic plots for single spherical particles in gas solid reactions systems

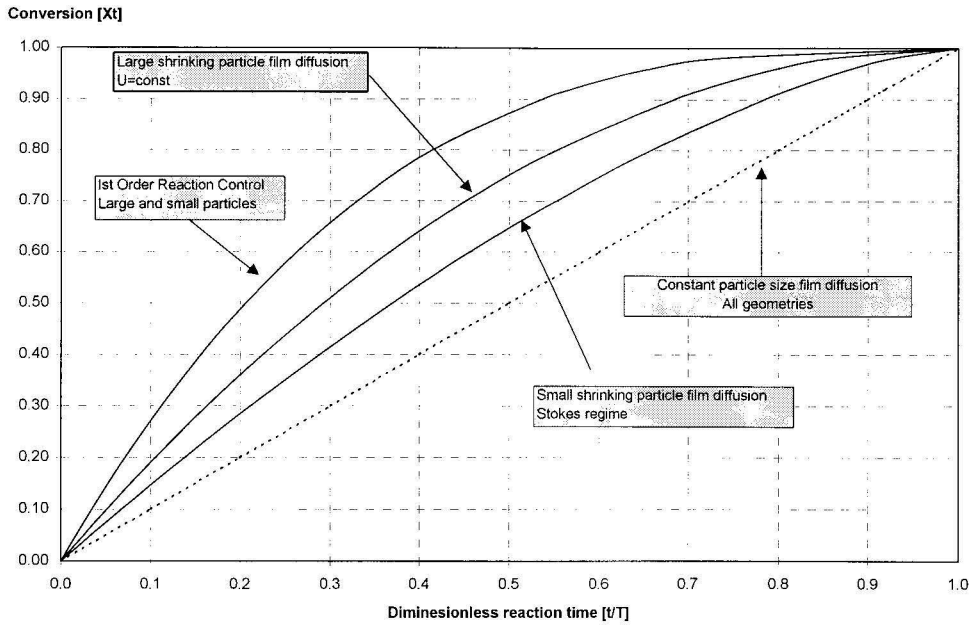

The equations listed in Table 3.4 can be applied to liquid-solid systems directly in the case of a chemical reaction rate control mechanism in the solid phase. The accurate prediction of film diffusion coefficients for liquid systems with suspended particles in mechanically agitated vessels is more complex. Here the assumptions made in the derivation of the Ranz-Marshall correlation and the relevance of this correlation to liquid-solid systems needs to be examined more closely.

The original form of the correlation was derived to estimate forced convection heat transfer coefficients for a single sphere submerged in a flowing stream under Stokes conditions. The assumptions that apply to the use of the correlation in the manganese dissolution system are listed in Table 3.5 with an applicability check column.

Bird *et al.* (1960) showed that the Ranz-Marshall correlation applies to systems with low mass transfer rates. Clearly the above criteria do not strictly apply to the reaction system. In addition, the applicability of some of the criteria may also change during the course of the reaction. Notwithstanding these shortcomings, numerous mass transfer studies in particulate systems have used this correlation with modifications to successfully predict film mass transfer coefficients. Harriott (1962) presented seminal work on this issue by conducting experiments over a wide range of conditions for the Schmidt (Sc) and Reynolds (Re) numbers. Harriott pointed out that the film diffusion coefficients predicted by the Ranz-Marshall correlation would be the minimum expected under all flow conditions.

Table 3.5 Ranz-Marshall assumptions

Criteria	Applicability
Single particle system	No
Spherical particle	No
Rigid particle	Yes
Smooth particle	No
Non-rotating particle	No
Laminar flow	No
Incompressible flow	Yes
Straight flow lines	No
Flow at steady state	No
Mean free path of fluid molecules << particle size dp	Yes/No (Complete dissolution)

The Sherwood number (Sh) will approach a minimum of 2 which represents diffusion in an infinite stagnant medium. For small particles (<10μm) this condition is obtained independent of the magnitude of the Schmidt and Reynolds numbers. Larger particles (>100μm) have mass transfer coefficients that are essentially independent of particle size. The mass transfer regime around a large dissolving manganese particle would thus vary between these theoretical diffusion regimes. The correlation is therefore used in the following analysis keeping these limitations in mind.

Polydisperse Isothermal Shrinking Particle Systems

The general form of equation (1) in a system containing a range of particle sizes which can be characterised in terms of distinct particle classes, *i*, is:

$$X_{ti} = 1 - \left[1 - \frac{t}{\tau_i}\right]^{3/n} \qquad (2)$$

The kinetics for a polydisperse particle system are obtained by integrating the contribution of individual particles or classes of particles as suggested by Levenspiel. The polydisperse conversion function then takes on the form:

$$X_t = \sum_{i=1}^{p} w_i X_{ti} \qquad (3)$$

From Table 3.4 the extinction times of individual particle classes (i) are scaled relative to the largest particle class (p):

$$\frac{\tau_p}{\tau_i} = \left(\frac{R_{op}}{R_{oi}}\right)^n \qquad (4)$$

Substituting equations (4) and (2) into equation (3) gives:

$$X_t = \sum_{i=1}^{p} w_i \left(1 - \left[1 - \frac{t}{\tau_p}\left(\frac{R_{op}}{R_{oi}}\right)^n\right]^{3/n}\right) \qquad (5)$$

where: p : Number of particle classes

w_i : Weight fraction of particle class i

τ_p : Extinction time for largest particle class

R_{op} : Initial radius of largest particle class

R_{oi} : Initial radius of particle class i

The scaling of extinction times relative to the extinction time for the largest particle class simplifies the programming of the calculations in matrix form in an electronic spreadsheet. Equation (5) shows that the overall extent of conversion of a polydisperse particle size distribution may be modelled if the initial particle size distribution and the overall time taken for the reaction are known.

Figure 3.10 Shrinking particle kinetics for an isothermal polydisperse particle system

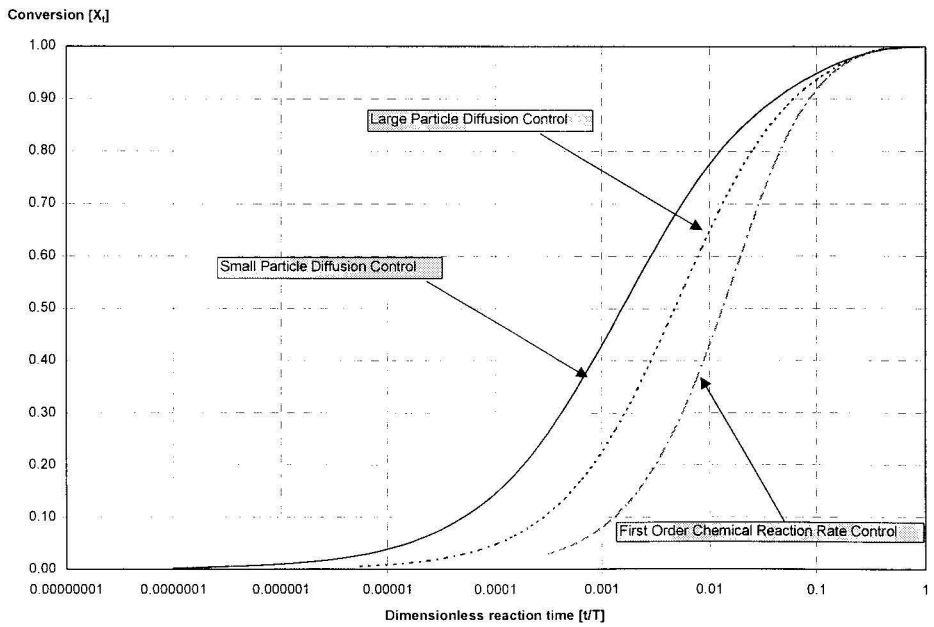

The size intervals of the particle classes used in the calculations were selected on the basis of a geometric progression (ar^n) as measured by the Malvern Mastersizer®. The kinetics of an isothermal polydisperse reaction system with an initial particle size distribution obtained for the metal as analysed by the Malvern is plotted in Figure 3.10. Note that although the shape of kinetic curves for the different rate controlling mechanisms are similar in shape, the abscissa is in logarithmic units. This shape of the curve is therefore an inherent feature of the particle size distribution. The spatial separation of the curves in this domain identifies the accuracy to which an isothermal experimental procedure must conform so that the correct rate controlling mechanism may be identified. It can be seen that the dissolution experiments described in section 2.3 conform to this criterium.

3.3.2 Non-isothermal polydisperse model

An inspection of Table 3.4 shows that the extinction time parameters for chemical reaction and small particle film diffusion control can be represented by the generic equation:

$$\tau = \frac{\rho_s dp^n}{K\Phi} \qquad (6)$$

where: K : Generic rate constant of diffusion coefficient

Φ : Generic fluid concentration parameter

dp : Diameter of particle

Here the generic rate constant (K) represents rate parameters that are functions of temperature. For activated chemical reactions and solid state diffusion processes the rate parameter is exponentially dependent on temperature through an Arrhenius relationship. The temperature dependency of molecular diffusivity coefficients in liquids is more complex as these are directly proportional to temperature and are also dependent on the viscosity (μ) of the liquid, i.e. D~constT/μ for dilute systems- Treybal (1968). Viscosity is however also exponentially dependent on reciprocal temperature. For the purposes of the following analysis it will be assumed that the temperature dependency of diffusivity is determined by an exponential viscosity-temperature relationship only. The generic concentration parameter (Φ) is a term that takes into account the reaction stoichiometry and gaseous reactant concentration. In the case of gas-solid reactions, both K and Φ can vary significantly with temperature and therefore there is a need to control this variable in the design of experiments for this system. The generic extinction time equation also applies in principle to liquid-solid systems with the proviso that the

diffusivity coefficient is modified to take into account complex mass transfer phenomena as discussed above in section 3.3.1. However, the temperature dependency of K remains unchanged. In the manganese dissolution system, the temperature dependency of the reactant (water) concentration is limited to a small volume expansion dependency and therefore Φ can be assumed to be constant. A further assumption is then made that the temperature effect of the reaction at different time intervals can be scaled according to an Arrhenius exponential temperature dependency in the case of chemical reaction and film diffusion control. Equation (5) then takes the form:

$$X_t = \sum_{i=1}^{p} w_i \left\{ 1 - \left[1 - \frac{t}{\tau_p} e^{-\left(\frac{E_a}{R}\left[\frac{1}{T_o} - \frac{1}{T}\right]\right)} \left(\frac{R_p}{R_i}\right)^n \right]^{3/n} \right\} \qquad (7)$$

where: E_a: Activation energy parameter (kJ mol^{-1})

R : Gas constant (kJ mol^{-1} K^{-1})

T : Temperature at time t (K)

T_o : Initial temperature (K)

In summary, the kinetics of a non-isothermal polydisperse reaction can be simulated by Equation (7) with knowledge of the metal particle size distribution, temperature profile during the reaction and an activation energy value. Note that an Arrhenius (k_o) rate parameter is not required. The assumption of introducing the temperature scaling term into the objective function in this manner is discussed further below. The kinetic plots for the analysed metal particle size distribution assuming a linear temperature conversion profile between 116 and 165°C and an activation energy of 170 kJ.mol^{-1} for all models (i.e. different values of n) are shown in Figure 3.11 together with X_t-t/τ data for one experiment.

The magnitude of the activation energy was found by testing all three kinetic models for the sensitivity of this parameter in the range 18 to 250 kJ.mol^{-1}. From this analysis it was clear that only the chemical reaction model could predict the shape of the conversion curve. Note that the abscissa in Figure 3.11 now has a non-logarithmic scale in comparison to Figure 3.10. In addition, the magnitude of Arrhenius parameters obtained from the Arrhenius plotting procedure described below agreed closely with that obtained from the sensitivity analysis. Further validation of the chemical reaction control mechanism was made by analysing the kinetics using the measured particle size distributions of samples taken during the dissolution reaction.

Figure 3.11 Non-isothermal kinetic plots for dissolving manganese metal

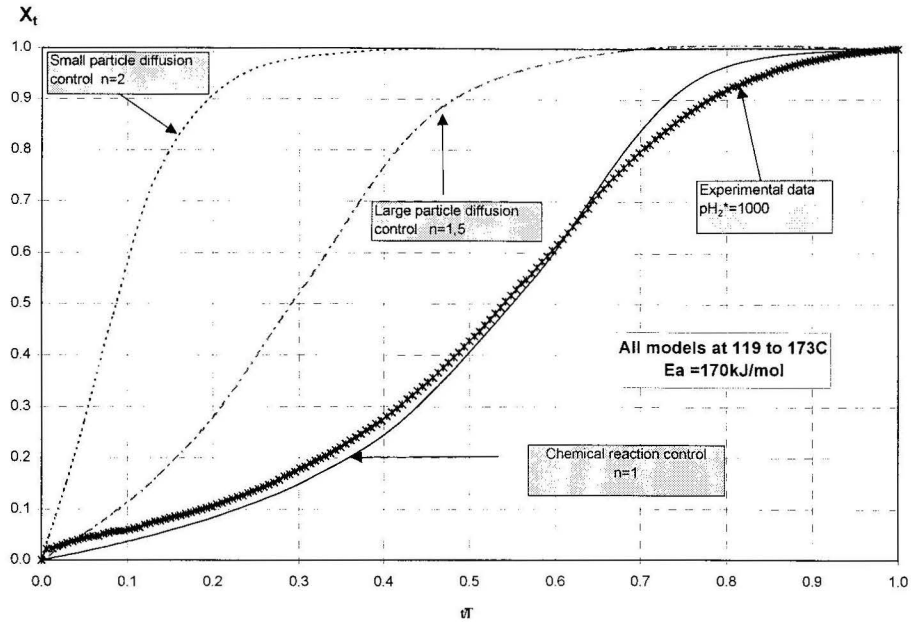

Before proceeding with this analysis the validity of introducing the exponential temperature scaling parameter into equation (5) is checked. The differential equation for a single, spherical shrinking particle with surface chemical reaction control under non-isothermal conditions where the temperature is directly proportional to the extent of conversion has the following form:

$$\int_{R}^{r_c} \exp\left[\frac{-E_a}{R_g\left(a\{1-(\frac{r_c}{R})\}^3+b\right)}\right] dr_c = k_0^{*} t \qquad (8)$$

where : r_c : Radius of unconverted particle at time t

R : Initial Radius

Rg : Gas constant

a,b : Constants in the equation $X_t=aT+b$

k_o^{*} : Reaction rate parameter independent of temperature

$X_t=1-(r_c/R)^3$

As equation (8) does not have an analytical solution it was solved by numerical integration using Mathematica® software (ver. 3.0) at different extents of conversion. The results obtained are compared with the values predicted by the objective function method for a single particle in Table 3.6. The objective function method predicts the kinetic conversion time (X_t –t) profile to within 0,19% error. The error in predicting the

conversion from the dimensionless time is less than 0,15%. This is less than the expected errors in the analytical data or raw data measurements.

Table 3.6 Comparison of numerical integration of rate equation with objective function method values

X_t	t/τ Numerical	t/τ Objective
0,10	0,03614	0,03609
0,20	0,07504	0,07492
0,30	0,11731	0,11710
0,40	0,16380	0,16347
0,50	0,21576	0,21529
0,60	0,27517	0,27452
0,70	0,34548	0,34463
0,80	0,43376	0,43267
0,90	0,55954	0,55817

Note: R/Rp=1 *Ea/R*=18 *a*=51 *b*=388 k_o=1

Kinetics based on particle size analysis data and model simulation

The analysis of the experimental data up to this stage does not conclusively confirm the validity of a chemical reaction rate controlling mechanism as the polydisperse size distribution of partially dissolved metal particles has not been taken into account. A kinetic model which incorporates the correct rate controlling mechanism should also be checked with respect to the change of particle size distributions of the solid phases during the dissolution process. As described, a number of samples of the reactor contents were analysed for particle size distribution. It is evident from Figure 2.18 that the metal and hydroxide particle size distributions overlap and that the results are in the form of volume based measurements. A reaction simulation was calculated using the matrix based methodology described in Appendix I.

These calculations consisted of combining the required mass ratios of metal and hydroxide using the starting particle size analysis of the metal and the final particle size distribution of the hydroxide at a given reaction extent. The particle size distribution of the hydroxide phase was assumed to be constant during the reaction. The relative proportion of this phase to the metal phase did however vary. The mass based distributions were then converted to volume based distributions using the densities for the compact Mn metal and porous hydroxide $Mn(OH)_2$. Simulations for models incorporating film diffusion and chemical reaction controlled kinetics are shown in Figure 3.12 and Figure 3.13

respectively These figures are plan views of the surface contour plots in Figure 2.19. The calculation methodology used to generate these figures is given in Appendix I.

Figure 3.12 Simulation of kinetics with film diffusion control based on measured initial metal particle size analysis

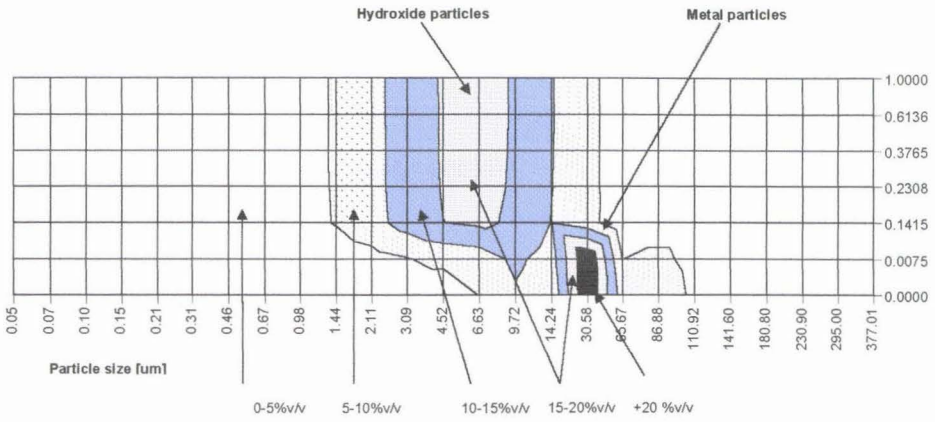

Figure 3.13 Simulation of kinetics with chemical reaction rate control based on measured initial metal particle size analysis

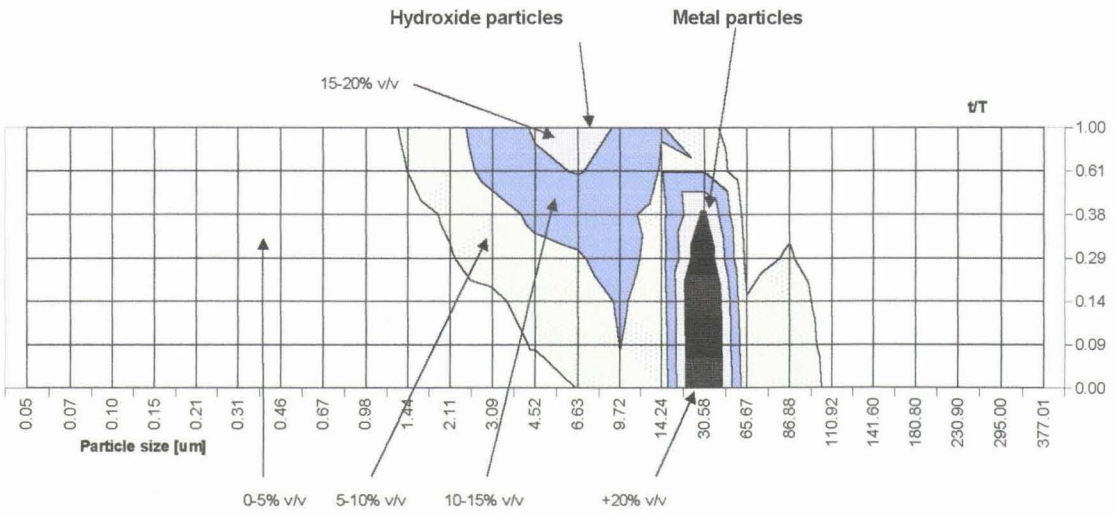

Comparison of these figures shows that the kinetics of the metal particles in the 20-60μm range can be used to determine the reaction rate controlling mechanism. This size fraction drops to 0-5% volume after less than 10% of the reaction time for the film diffusion model while in the chemical reaction model this fraction is still present above 10% vol. after 40 to 50% of the reaction has been completed. The above figures can be compared to the equivalent contour plots for the experimental particle size analyses reported on Appendix E, Figures E6, E7 and Figure 3.14 below. It is confirmed in all plots that 20-60μm sized metal particles were measured from 30 up to 60% conversion. The rate controlling mechanism of the reaction is therefore a surface chemical reaction, first order in the unreacted solid manganese content.

Figure 3.14 Experimental PSD pH_2* 600kPa

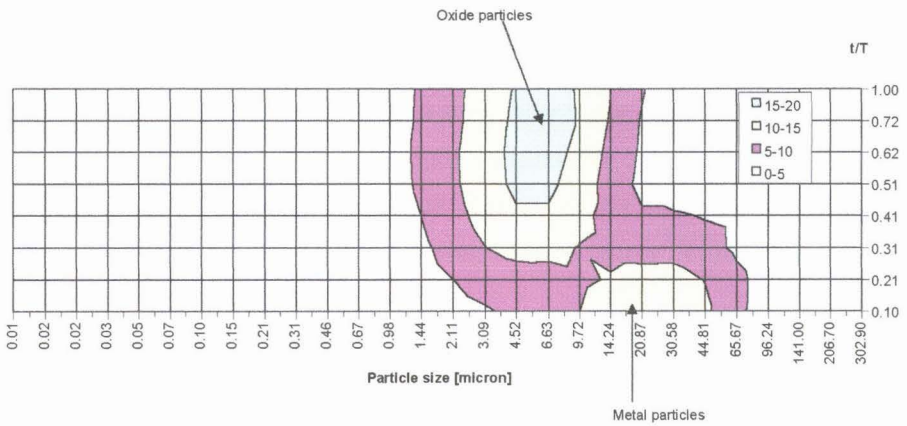

Arrhenius kinetic plots

Further confirmation of the rate controlling mechanism in a chemical reaction system can be obtained from the magnitude of the activation energy parameter in an Arrhenius plot. The plot can, in addition, show whether more than one rate controlling mechanism or mixed control is present. In the following analysis, these plots also quantify the extent of reproducibility of the reaction rate measurements. Table 2.9 shows that the start and end temperatures for the hydrogen venting period varied between experiments at the same pH_2*. A comparison is thus required which normalises this effect. The Arrhenius plot achieves this requirement by comparing the specific reaction rates ($mol.m^{-2}s^{-1}$) for different runs at the same inverse temperature. This plot should thus allow for the

assessment of reproducibility and identification of systematic trends in the reaction rates or kinetic regimes.

The reaction rate data as estimated by stoichiometry from the gas flowrate measurements in Figure 2.14 to Figure 2.16 represents the integral sum of reaction rates of all the particles in the reactor. To be able to obtain specific reaction rates it is necessary to apportion the integral rate into reaction rates per class of particle sizes. In section 2.3.3 it was assumed that only one class of particle size exists which is clearly an oversimplification as a relatively wide range of small particle sizes was measured. The normal procedure to measure specific reaction rates for heterogeneous systems is to conduct separate experiments on particle sized fractions obtained through classification or screening. This procedure could not be followed as screening is not possible below 25μm and there were safety risks associated with using dynamic classification equipment with the explosive metal dust. These procedures also generally do not result in homogeneous particle sizes within a classified particle size fraction.

The methodology that was used to determine surface-area specific reaction rates was to divide the instantaneous reaction rate at each time interval by the total surface area calculated from the predicted particle size distributions under different rate controlling mechanisms. The calculation procedure consisted of following the reaction progress for each class of particles subject to a flux of material (N) that was adjusted proportional to the ratio, $N(dp_{max}/dp_i)^n$. This calculation required a number of assumptions:

- All particles within a size class were kinetically homogeneous.

- The kinetic model could be applied over the whole temperature range of the experiment.

- The particle size distribution of partially reacted metal at the beginning of the venting period could be estimated by the assuming the dissolution kinetics of one of the three limiting models applied to the head-feed metal size distribution.

The first assumption will produce reaction rate results that represent the average dissolution rates of all equally sized particles that may however not be kinetically homogeneous due to chemical or structural factors, e.g. the oxide layering in the head-feed material could cause varying rates of reaction during the initial period of dissolution. This variable could not be analysed fully in the experiments due to the lack of suitable material characterisation techniques. The second assumption can be verified by an Arrhenius plot of the data that is linear over the whole range of measured temperatures. This is discussed further below. In the case of the third assumption, the hydrogen gas

mass balance shows that the metal was partially converted at the onset of the venting period. This effect was incorporated into the kinetic models by adjusting the particle size distribution for the amount of metal that had dissolved prior to the venting period. The correction resulted in small adjustments (<0,7% of dp) to the average particle size and did not alter the shape of the conversion profiles.

The surface-area specific reaction rates were calculated using similar matrix calculations to those used for predicting the particle size distributions shown in Figure 3.12 and Figure 3.13. The physical significance of the chemical reaction model in this procedure is that all particle classes will have the same specific reaction rate or flux of dissolving manganese ions at the surface. Mathematically the model is therefore valid for a first order chemical reaction occurring strictly at or very close to the surface of the metal, e.g. adjacent to the double layer. The physical significance of the diffusion-controlled models cannot be visualised simply as the diffusion fluxes will vary with particle size as discussed in section 3.3.1. The Ranz-Marshall correlation predicts that the film diffusion coefficient will increase with decreasing particle size as a particle shrinks below 2μm in diameter. Therefore, for particles that have constant concentration gradients across a liquid film at the surface, the diffusion flux will increase as the particles shrink. A similar effect would be observed under certain conditions for the chemical reaction model in the final stages of particle shrinkage or extinction as the specific reaction rate is inversely proportional to the surface area of the particles.

Figure 3.15 Arrhenius Plot for pH_2* 800kPa

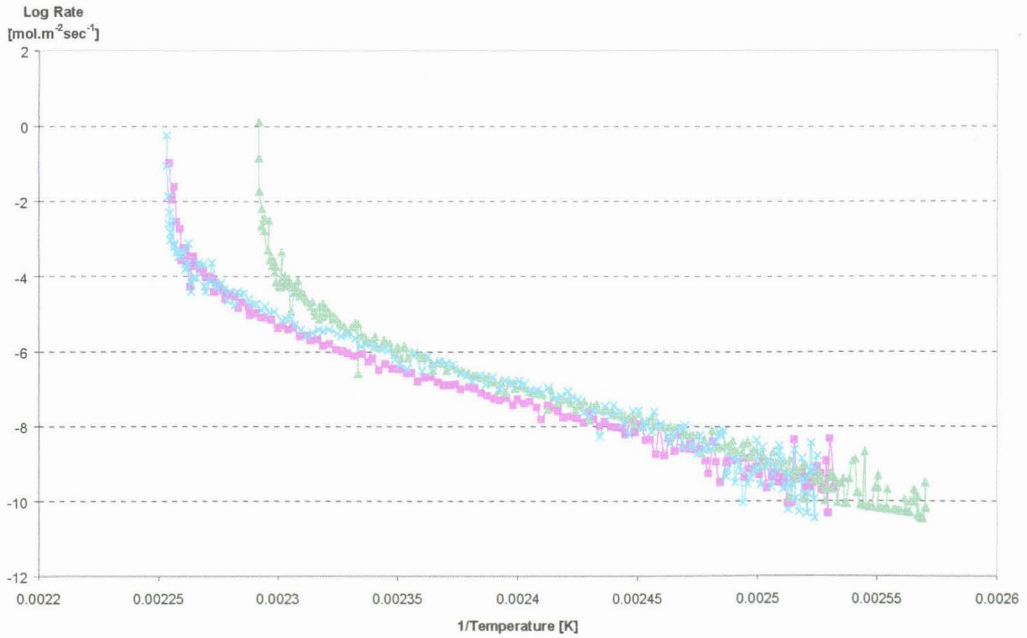

The Arrhenius plots for the pH_2* 800kPa experiments calculated on the basis of the above methodology are presented in Figure 3.15. Figures E8 and E9 in Appendix E show the plots for the pH_2* 600 and 1000kPa experiments, respectively. The combined data for all experiments is plotted in Figure K10. By comparing experiments at the same pH_2*, the reproducibility of the runs is confirmed. The plots show noise in the results at the beginning of the venting period and a deviation from linearity at the end. The noise was obtained in the flowrate readings at low venting rates. A summary of the Arrhenius parameters obtained by regression of the linear portion of the curves is tabulated below. The average activation energy of all the experiments is 168 $kJ.mol^{-1}$ (sdev 8) which confirms a chemical reaction rate controlled process. The data shows no consistent trends in the magnitude of the parameters obtained at different pH_2*. The rate of the dissolution reaction is therefore not influenced by dissolved or gaseous hydrogen in the temperature and pressure range of the experiments.

Table 3.7 Summary of Arrhenius parameters

pH_2 (kPa)	Ea ($kJ.mol^{-1}$)	$\log k_o$ ($mol.m^{-2}.sec^{-1}$)	R^2
1000	164	44,4	0,9869
1000	154	37,5	0,9687
1000	157	38,2	0,9950
800	166	40,7	0,9632
800	175	43,7	0,9776
800	172	42,6	0,9809
600	172	42,1	0,9681
600	170	41,6	0,9763
600	179	44,4	0,9869

A significant increase in the specific rate of reaction is evident in the Arrhenius plots towards the end of the reaction. This deviation in linearity suggests that a different rate controlling mechanism could apply to this kinetic regime. This mechanism is however not a diffusion controlled process as the activation energy that would be obtained here is higher than that for the chemical reaction controlled portion of the process. This conclusion cannot be substantiated unequivocally as the estimation of the specific reaction rate requires the assumption of a kinetic model with a specific controlling mechanism to calculate the reacting surface areas. If the rate controlling mechanism changes then there would be uncertainty with respect to the accuracy of the calculated surface areas. In Figure 3.11 it was shown that a simple shrinking particle model with a single activation energy parameter could reproduce the experimental kinetics. The Arrhenius activation energy for this plot was estimated by linear regression of all the data points in the complete temperature range of the experiment. The activation energy

obtained over the whole temperature range from this plot, $Ea^{\#}$, was numerically 5% higher than that obtained by regression in the linear portion of the plot. This would explain the systematic deviation observed in Figure 3.11 between the experimental and modelled conversion curves. The lower activation energies obtained for the large reactor run (98,9kJ.mol^{-1}) and Ramanane's experiments (70kJ.mol^{-1}) would be due to the assumption of monodisperse particles which introduces significant errors into the estimation of the surface area available for reaction.

Figure 3.16 Total area and conversion profiles for pH_2* 1000kPa

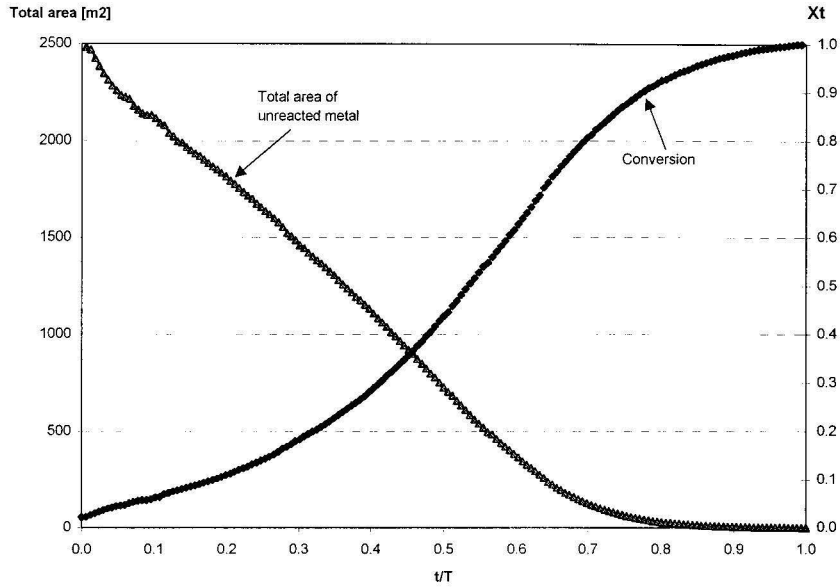

In the large reactor experiments it was suggested that the latter stages of reaction could correspond to a rapidly shrinking particle kinetic regime. A plot is made in Figure 3.16 of the variation in total area as estimated by the polydisperse kinetic model together with the extent of conversion profile. The total surface area decreases linearly as expected for this process up to 70% conversion. The average particle size of the unreacted metal is plotted as a function of temperature (Note this is equivalent to reaction extent as conversion is directly proportional to temperature) in Figure 3.17. The rate of decrease of particle size can be seen to increase in the final stages of the reaction.

This effect is further confirmed by the increase in the specific dissolution rate that is predicted by this model as shown in Figure 3.18. Here an alternate method of representing reaction rate data is used to express the rate in terms of an anodic dissolution current (i_a) that is equivalent to the specific dissolution rate ($i_a=nzM^{O}$).

Figure 3.17 Variation of average particle size of unreacted metal at different reaction temperatures

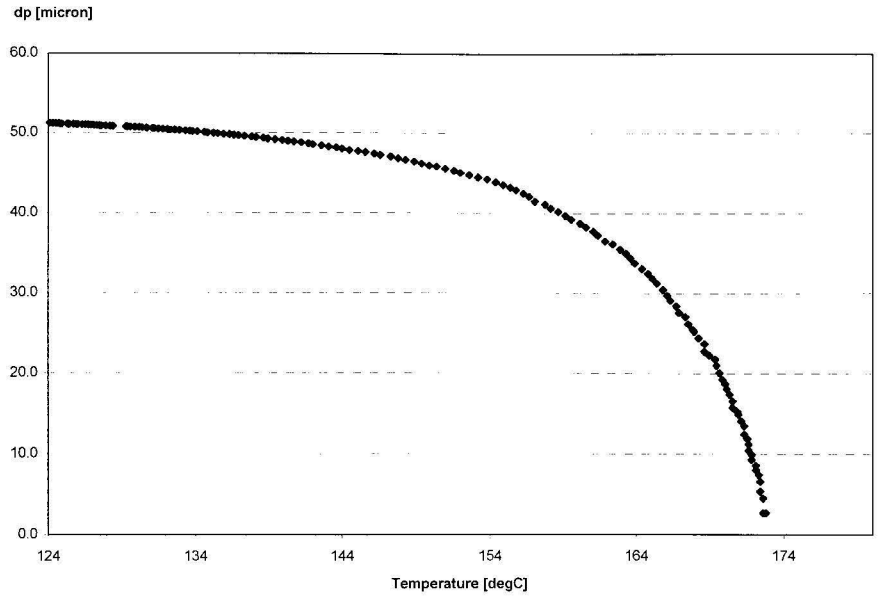

At 70% conversion the model predicts that the corrosion current density (CCD) has risen to 1000A.m^{-2}. The maximum CCD achieved was calculated to be in the order of 10000A.m^{-2}, though the linear portion of the Arrhenius plot corresponds to a CCD of 3000A.m^{-2}. These corrosion currents are an order of magnitude higher than the corrosion current for iron at a temperature of 300°C - Heusler (1990). Hurlen & Valand (1964a) measured corrosion currents between 10 and 1000A.m^{-2} for Mn metal dissolving in acid solutions at ambient temperature. The hydrothermal dissolution rate is therefore up to 3 and possibly 10 times higher than the maximum corrosion rate recorded by these authors. More carefully controlled experiments are required to confirm these findings.

The dissolution rate and extent of supersaturation will also influence the morphology of the precipitated $Mn(OH)_2$. High rates of dissolution will favour nucleation processes relative to the growth of precipitates with small particle sizes being formed consequently. Details of the physical characterisation analyses conducted on the hydroxide phase are given in the next chapter. A discussion is however made here of the some of the morphological features of the hydroxide phase in terms of kinetic effects. SEM analyses of the hydroxide precipitate show a highly aggregated material made up of smaller spherical grains or crystallites, 0,1μm in diameter. The particle size distribution measurements in Figures K5 , K6 and K7 give an average particle size of the aggregates of about 5μm. Söhnel & Garside (1992) reviewed some of the aspects of the influence of the level of supersaturation ratio S_o on the nucleation mechanism, the growth mechanism

and the particle morphology of a precipitate and referred to Walton's table shown in Table 3.8.

Figure 3.18 Corrosion current for hydrothermal dissolution of manganese metal

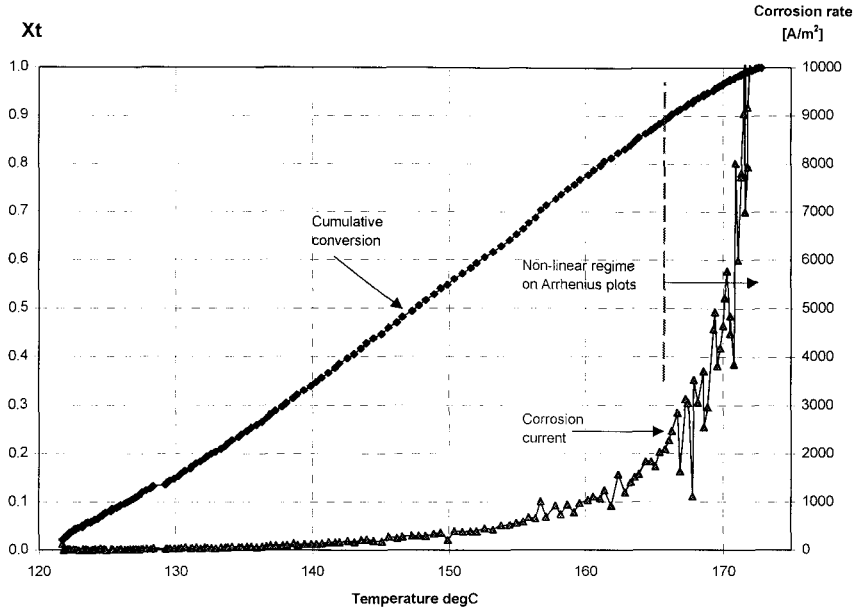

The relatively small primary particle size and the aggregated nature of the $Mn(OH)_2$ precipitation products accompanying the dissolution of manganese metal particles indicate that the precipitation reaction most likely follows homogeneous nucleation with diffusion controlled growth mechanisms at high ratios of supersaturation (S_o>100-1000).

3.3.3 Conclusions

- Non-isothermal reaction rates for hydrothermal dissolution of manganese metal were estimated by analysing experimental data obtained from two differently sized reactors (0,35m^3 & 4.0 m^3). An experimental procedure was derived whereby the non-isothermal hydrothermal manganese dissolution experiments could be conducted under controlled temperature and pressure conditions. By conducting the experiments at a constant hydrogen overpressure above the vapour pressure curve of water, it was possible to obtain reaction rate data for Arrhenius type plotting from one experiment.

Table 3.8 Walton's Table: Effect of initial supersaturation on particle morphology

Initial Supersaturation S_o	Nucleation mechanism	Growth mechanism	Particle Morphology
<2	Heterogeneous	Surface reaction	Compact crystal shape, well developed
2-10	Heterogeneous	Surface reaction	Compact crystal shape, well developed
10-50	Heterogeneous	Compound	Ill-developed crystals, dendrites
>100	Homogeneous	Diffusion or compound	Small, isometric crystals often agglomerated
>1000	Homogeneous	Diffusion	Very small particles or colloids, amorphous, agglomerated

Note: $S_o=c/c_{eq}$

where: c: concentration at supersaturation

c_{eq}:concentration at equilibrium

- The reaction was found to be first order in manganese and zero order in water. The rate controlling mechanism was confirmed by a number of independent measurements to be due to a chemical reaction at the surface of the metal. A polydisperse non-isothermal shrinking core model with chemical reaction control was used to predict the experimental kinetics. Hydrogen pressure does not affect the kinetics in the temperature range 115 to 172°C and 600 to 1000kPa pH_2*. The Arrhenius activation energy Ea was estimated to be 168 $kJ.mol^{-1}$ in the temperature range 115 to 172°C. This is higher than activation energies for manganese oxidation reactions reported to in the literature, e.g. Gmelins (1973), 115$kJ.mol.^{-1}$ for gaseous oxidation of Mn metal in the temperature range 600 to 800°C.

- The Arrhenius plots did deviate from linearity in the early and final stages of the dissolution process suggesting a possible shift in rate controlling mechanism. In the final stages of reaction this shift would correspond to a process with a higher activation energy precluding diffusion controlled processes. However, gas flowrate readings were lower and subject to higher noise levels at these points in the process. The confirmation of a regime of "rapidly shrinking" cannot therefore be made unequivocally on the basis of the above analyses.

- Although the starting metal particles were angular in shape, the assumption of spherical shrinking particles adequately predicted the kinetic behaviour of the metal.

The morphology of the precipitated hydroxide phase consisted of aggregated particles that would have been formed at high supersaturation conditions. Homogeneous nucleation and diffusion controlled growth are the expected mechanisms for particle morphology modification.

3.4 Summary of Results from Kinetic and Equilibrium Modelling

Non-isothermal reaction rates for the hydrothermal dissolution of polydisperse manganese metal particles were measured in experiments conducted on the reactors. An experimental procedure was derived whereby the non-isothermal hydrothermal manganese dissolution experiments could be conducted under controlled temperature and pressure conditions. It is shown that it was possible to obtain reaction rate data over a range of temperatures from a single experiment and that the effect of hydrogen partial pressure on reaction kinetic could be investigated systematically.

Gas-solid and gas-liquid-solid equilibrium considerations show that the measurements made during the experiments that were conducted to study the hydrothermal dissolution and aqueous oxidation of manganese metal may be explained in terms of relatively simple reactions and reacting species.

The gas-solid equilibrium considerations indicate that MnO_2 is the stable oxide phase under oxidising conditions. Other oxide phases formed under these conditions will thus be metastable and their rate of conversion will be dependent on kinetic considerations. Reducing conditions favour the formation of manganous hydroxide and manganous oxide. These domains of stability are confirmed for three phase systems. The domain of stability of Mn_3O_4 reduces at elevated temperature and in low ionic strength solutions. A narrow domain for the stabilisation of Mn_3O_4 that overlaps the experimental processing conditions is however predicted from the available literature data.

Eh-pH diagrams for the Mn-O-H_2O system have been constructed at elevated temperatures using data available in the literature. Previous work in this field has ignored the influence of hydrated species that extend the domains of stability of manganous hydroxide into lower pH regimes. At elevated temperatures the domain of stability for soluble manganous hydroxide, $Mn(OH)_2^0$ is reduced, the Mn^{2+} and $MnOH^+$ become more dominant and the overall solubility of manganese ions is increased. The increase in solubility of manganese ions may be partly responsible for the active dissolution of manganese metal that occurs above 110°C. In solutions with elevated pH (>9,5) the domain of stability of the dimanganite ion becomes significant. The change in speciation to less $Mn(OH)_2^0$ also contributes to the active dissolution conditions. $Mn(OH)_2^0$ is the

precursor to the layered structures of precipitated $Mn(OH)_2$. A lower concentration of these precursors will inhibit the precipitation of manganous hydroxide at the surface and prevent the blocking effect of this species that is observed when comparing the rates of reaction obtained in dissolution experiments conducted with or without oxygen.

The hydrothermal manganese metal dissolution reaction in pure water was found to be first order in manganese and zero order in water. The rate controlling mechanism was confirmed by a number of independent measurements to be due to a chemical reaction at the surface of the metal. This is consistent with the available literature. The partial pressure of hydrogen does not significantly affect the kinetics of dissolution in the temperature range 115 to 172°C and 600 to 1000kPa pH_2*. The Arrhenius activation energy Ea was estimated to be 168kJ.mol^{-1} in the temperature range 115 to 172°C. This value is considerably higher than that reported in the literature for corrosion experiments conducted under acidic conditions at lower temperature. A different reaction mechanism therefore controls the reaction under these conditions and it is postulated that the reaction does not proceed via hydrogen ions.

Although the starting metal particles were angular in shape, the assumption of spherical shrinking particles adequately predicted the kinetic behaviour of the metal. The morphology of the precipitated hydroxide phase consisted of aggregated particles that form under highly supersaturated conditions. Homogeneous nucleation and diffusion controlled growth are the expected mechanisms for particle morphology modification of the precipitated manganous hydroxide. Dissolution of the metal particles to extinction is facilitated by the lowering of the surface potential of the metal due to the effect of increased particle curvature.

A calculation methodology has been presented which makes it possible to analyse the rate controlling mechanisms of polydisperse, non-isothermal, reaction systems. In this work the methodology was successfully applied to a system where a chemical surface reaction controls the rate of dissolution in a non-isothermal reaction system where the temperature is directly proportional to the extent of reaction. The usefulness of this method should be tested in other reaction systems.

4 HYDROTHERMAL $Mn(OH)_2$ OXIDATION EXPERIMENTS

4.1 INTRODUCTION

A number of experiments and measurements were made to determine the kinetics and mechanisms of hydrothermal oxidation of a suspension of manganous hydroxide particles by oxygen in a mechanically agitated reactor. The oxidation of manganous hydroxide can be described by the overall reaction:

$$6Mn(OH)_2 + O_{2(aq)} \rightarrow 2Mn_3O_{4(s)} + 6H_2O_{(aq)} \qquad (1)$$

Here $Mn(OH)_2$ refers to both the dissolved and solid forms of manganous hydroxide. The literature survey and equilibrium modelling of the previous chapters have shown that the oxidation of manganous hydroxide may proceed by homogeneous or heterogeneous reaction mechanisms. A simplified framework for these reaction pathways may be written as:

$$6Mn(OH)_{2(s)} + O_{2(g)} \rightarrow 2Mn_3O_{4(s)} + 6H_2O_{(aq)} \qquad (2)$$

$$6Mn(OH)_{2(aq)} + O_{2(g)} \rightarrow 2Mn_3O_{4(s)} + 6H_2O_{(aq)} \qquad (3)$$

$$6MnOH^+_{(aq)} + O_{2(g)} \rightarrow 2Mn_3O_{4(s)} + 6H^+_{(aq)}. \qquad (4)$$

Reactions (3) and (4) are homogeneous oxidation reactions while reaction (2) is a heterogeneous fluid-solid reaction. If the oxidation process is rate controlled by reaction (3) then dissolution of the solid hydroxide is required to maintain the solubility equilibrium of manganous hydroxide. This would result in the formation of a new class of particles. The topochemistry of the oxidation intermediates will also differ according to these mechanisms. In ideal limiting conditions, the heterogeneous mechanism will result in particles containing solid solutions of hydroxide and oxide, while the homogeneous mechanism will result in a mixture of particles that are single phases of hydroxide or oxide. The morphology of the oxidised product will be dependent on the morphology of the manganous hydroxide particles in the case of the heterogeneous mechanism. This does not apply strictly to the homogeneous mechanism. Knowledge of the morphology of the reaction intermediates is therefore essential for the determination of reaction kinetics and reaction mechanisms. The morphology of the dispersed particles was also used to determine interfacial areas for the mass transfer analyses presented later.

The morphology and structural characteristics of intermediates and products of the reaction were determined by a number of analytical techniques so that the extent of

conversion of the solid phase could be quantified. The analytical techniques used include chemical analysis, particle size analysis, porosimetry, thermogravimetric analysis, optical and scanning electron microscopy (SEM). Structural characteristics of the solid phases were also investigated by means of X-ray diffraction (XRD). A number of studies have been reported in the literature that investigate the morphological and structural characteristics of the intermediates and products of manganous hydroxide oxidation at ambient temperatures. These features have not been reported as extensively for the hydrothermal oxidation of manganous hydroxide prepared from electrolytic manganese metal.

The composition, morphology and structure of hydrothermally produced manganese oxides are important characteristics when considering the application of these materials as raw materials for soft ferrite production processes. Kolenbrander *et al.* (2000) discussed the influence that the morphology of iron oxide raw materials has on the reactivity of Mn,Zn-ferrites. A similar study has not been reported for the manganese component though it is known that this is a critical consideration for most Mn,Zn-soft ferrite materials. The results presented below thus provide an essential building block in the characterisation of these materials. This information, together with the understanding of the influence of processing conditions on physico-chemical properties, can be used for optimising the characteristics of these materials and for developing tailored products that match the needs of more specialised soft ferrites or other applications.

The testwork described below was conducted with the above considerations in mind. The remaining sections in this Chapter discuss the experimental conditions, solid phase characterisation analyses and kinetic and structural measurements that were made on samples taken during experiments of hydrothermal oxidation of manganous hydroxide which had been precipitated in the absence of complexing reagents or anions. The interpretation of these results is given in Chapter 5

Experimental Conditions and Observations

In practical terms, the product of the hydrothermal dissolution of manganese metal is a white slurry that turns a light brown colour upon contact with air. Oxidation experiments were conducted by sparging air or oxygen into the reactor at a controlled rate after the dissolution experiments described in Chapter 2 had been completed. Details on the reactor geometry, physical properties of reactants and the hydrodynamic conditions in the reactor during an oxidation experiment are given in Appendix J.

The limited solubility of $Mn(OH)_2$ results in powerful buffering effects as saturated solutions with high solids contents only require a small amount of hydroxide dissolution to maintain the

solubility equilibrium. The buffering effect was evident in the relatively constant pH conditions that were measured on samples taken from the reactor during the experiments. Experimental results obtained are plotted in Figure 4.1.

Figure 4.1 Variation in filtrate pH and soluble Mn for oxidation experiments

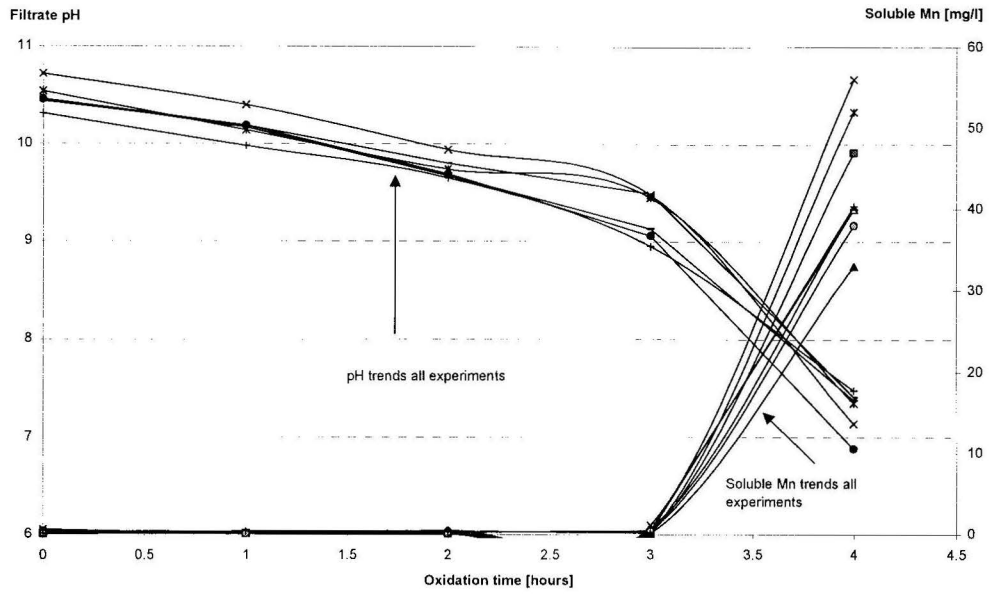

The pH of the filtrates obtained from samples taken during the runs was measured at 25°C using a Metrohm pH meter while the soluble Mn contents were obtained by atomic absorption spectroscopy. The completion of oxidation could be seen by a sharp decrease in solution pH and a corresponding increase in soluble Mn content when the system become unsaturated after 3 hours oxidation time according to reaction (3). This is anticipated from the equilibrium modelling exercise presented in section 3.2. A separate experiment was conducted to obtain solution potential readings that are shown in Figure 4.2. This shows the change in the solution pH_t (pH corrected for temperature) and redox potential, mV(SCE)- (millivolts relative to the saturated calomel electrode) as obtained on samples taken from the reactor during the experiment. The saturation pH (pH_{sat}) as calculated from the manganous hydroxide solubility product is included to highlight when conversion of hydroxide was completed.

The variation in this line at 210 minutes is due to the temperature at which the offline pH measurement was made, as not all these measurements were made consistently at the same temperature. Up to about 180 minutes reaction time, the pH in the solution (pH_t) is relatively stable while the increase in redox potential is almost linear. The inflection point in the pH_t line at 180 minutes can again be noted as the buffering action of the manganous

hydroxide is lost with complete oxidation. This rise in redox potential has also been observed by Bricker (1965).

Figure 4.2 Variation in pH and redox potential during oxidation of a suspension of manganous hydroxide with air at 120 °C

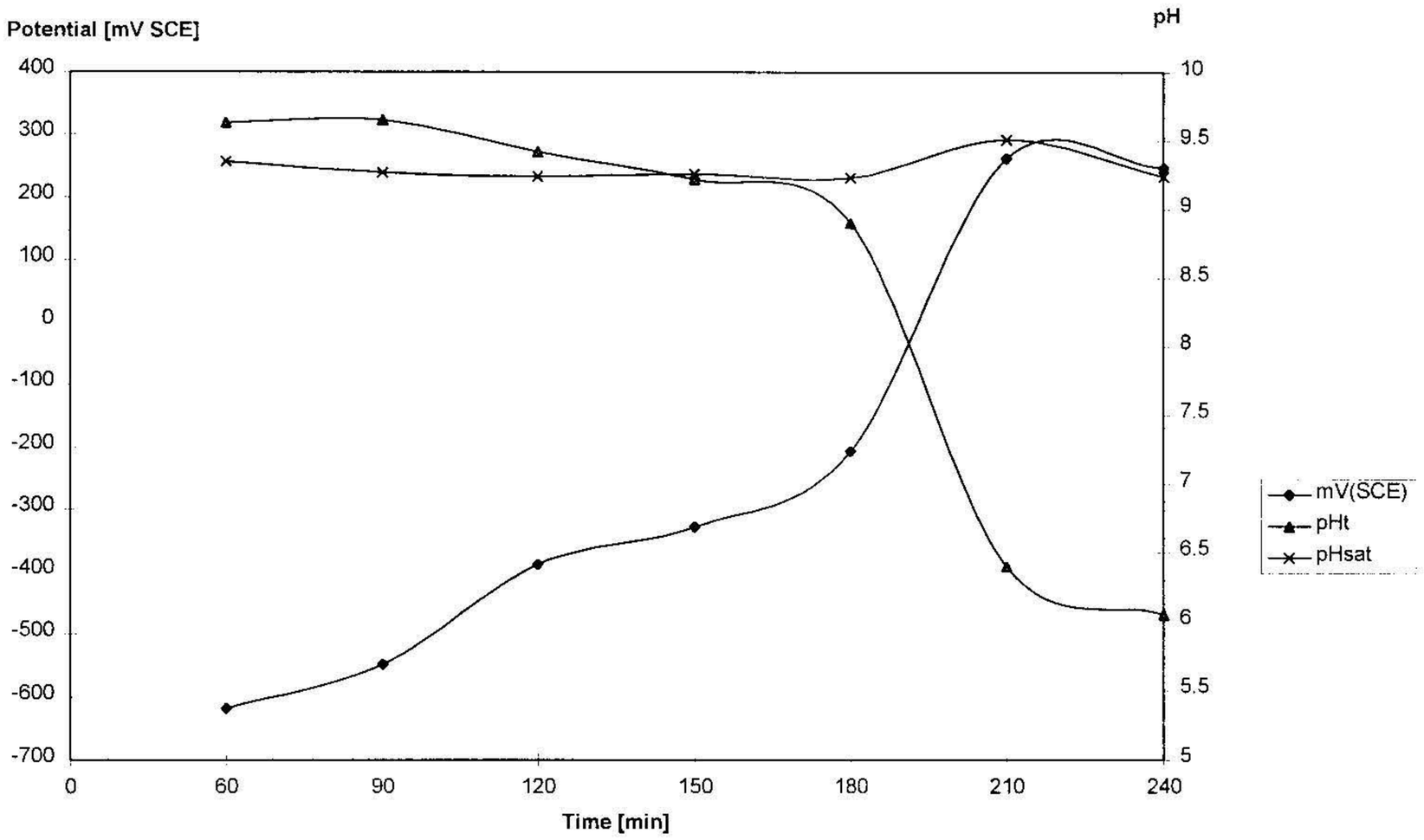

The presence of increasing quantities of Mn_3O_4 raises the redox potential due to the reaction:

$$3Mn^{2+}_{(aq)} + 4H_2O_{(aq)} = Mn_3O_{4(s)} + 8H^{+}_{(aq)} + 2e^{-} \qquad (5)$$

with: $Eh = E^{o} - 0{,}236pH_t - 0{,}0891 \log (aMn^{2+})$ – Bricker (1965)

In addition, the dissolved oxygen content of the liquid phase would increase once the $Mn(OH)_2$ was completely oxidised. This stage of oxidation can be characterised as a two-phase system with the activity of the Mn_3O_4 increasing as the manganous hydroxide is converted.

4.2 SOLID CHARACTERISATION AND KINETIC INVESTIGATIONS

A number of measurements were made on solid samples that were taken during the oxidation reaction and on completely oxidised samples. These analyses included:

- Particle size distribution measurements made at different time intervals during the oxidation process on samples of suspensions. Pore size distribution by Hg porosimetry, surface area by nitrogen absorption (BET), scanning electron microscopy (SEM) and optical microscopy observations were made on dry manganese oxide products.

- Thermogravimetric and chemical analyses of partially and completely oxidised manganous hydroxide.

- Measurements for determining the kinetics of oxidation of manganous hydroxide and the identification of rate controlling mechanisms.

- Powder XRD traces of hydrothermal $Mn(OH)_2$ oxidation intermediates and Mn_3O_4 products.

These analytical measurements are described in more detail in the paragraphs that follow. Interpretation of the results using mathematical models is presented in Chapter 5.

4.2.1 Analyses of Particle Morphology

Particle size analysis

The variations in particle size distribution of the metal and hydroxide phases during a hydrothermal dissolution experiment has been discussed and modelled in section 3.3. Full details of the analytical method used for particle size measurement are given in Appendix K. The particle size analyses method described in Appendix K confirmed the aggregated nature of the hydroxide as the particle size distributions measured were sensitive to chemical and ultrasound dispersion. Prolonged application of ultrasound at energy levels that were approximately an order of magnitude higher than expected in the experimental reactor resulted in a measurable breakdown of aggregates with the formation of smaller particles. The measurements were however repeatable and are thus a relative indication of the extent of dispersion of the hydroxide particles.

The introduction of air into the reactor resulted in further measurable changes in the particle size distribution of the hydroxide phase as this was progressively oxidised to

mangano-manganic oxide during an oxidation experiment. The overall change in the particle size distribution of the reactor contents for one experiment is summarised in Figure 4.3. The figure shows that the average particle size ($D_v(4,3)$) of the metal started at 51,5μm. These particles then decrease in size due to the dissolution and reprecipitation of a hydroxide phase with an average particle size of 5,6μm. Precipitated manganous hydroxide is usually obtained as a finely divided material with elevated temperature and recrystallisation is necessary to generate particles of 200μm in diameter - Bricker (1965) and Tareen *et al.* (1982).

Figure 4.3 Particle size distribution during dissolution and oxidation

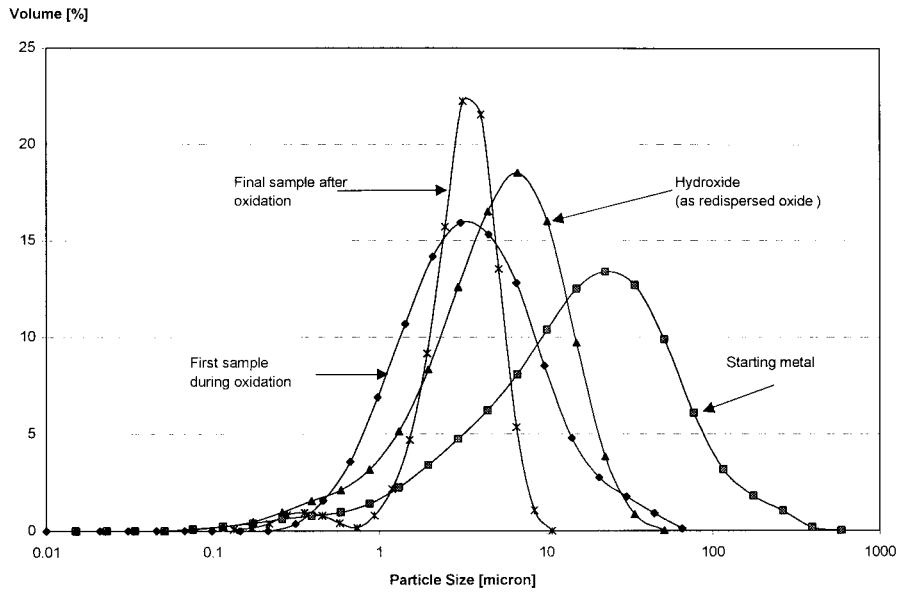

The oxidation of the hydroxide particles is accompanied by a narrowing of the size distribution with a small decrease in the average particle size, $D_v(4,3)$, from 4,7 to 3,9μm for the beginning and end samples respectively. The difference in average particle size between the hydroxide sample taken at the end of dissolution and the first oxidation sample is due to the former being analysed in an oxide state, while the oxidation sample was analysed directly as a wet suspended sample. This is investigated and reported further in Appendix K. A non-porous particle of $Mn(OH)_2$ will decrease in size as it is oxidised to Mn_3O_4 via a solid state reaction. Therefore, additional structural modifications that include some form of growth or aggregation mechanisms took place during filtering and drying of the hydroxide samples.

The measured change in particle size distribution of samples taken during a typical oxidation experiment and analysed directly is shown in Figure 4.4. All measurements taken during the oxidation experiments are plotted in Appendix K Figures K1-K9.

It can be seen that the average particle size of the second sample is significantly smaller than the first sample. Thereafter the spread of the distributions become more narrow and the average particle size increases as oxidation progresses. Table K1 in the Appendix summarises the $D_v(0,9)$, $D_v(0,5)$ and $D_v(0,1)$ moments, i.e. the particle size below which 90, 50 and 10% respectively of the volume of particles present can be expected, for each sample taken at 1 hour intervals during oxidation in nine experiments. These oxidation experiments were conducted on the hydroxide slurries produced from the hydrothermal dissolution experiments at controlled hydrogen partial pressure (Note: 3 repeats @ pH_2* 600,800,1000).

Figure 4.4 Particle size distributions for oxidation intermediates

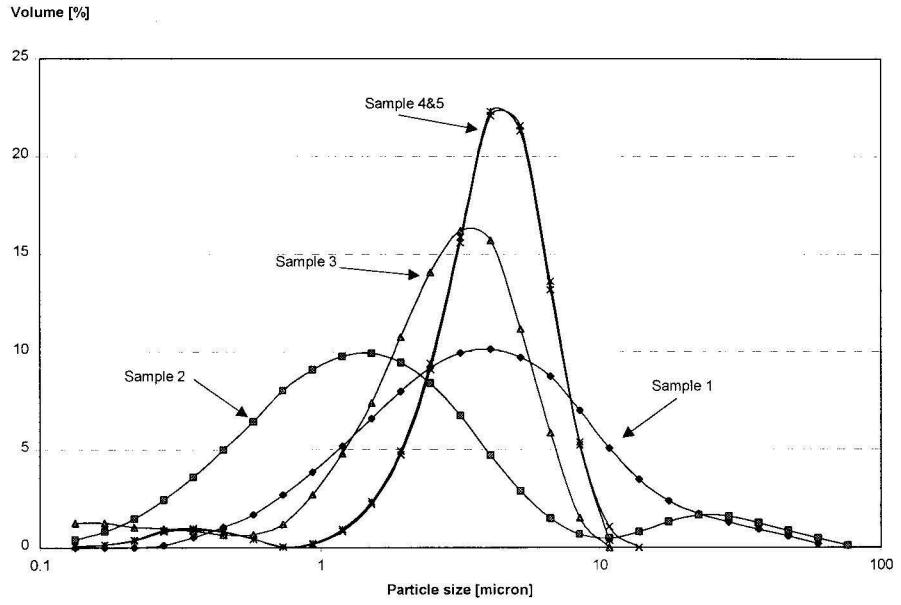

It can be seen in Table H1 that there is no systematic effect of pH_2*pressure on the particle size distribution. The total and hydrogen partial pressure therefore do not influence the morphology of the manganous hydroxide precipitate or its oxidation products. The average and standard deviations of the $D_v(x)$ values for each time interval taken over all the values, are shown in Table 4.1. Samples 1, 2 and 3 all show increased variability of particle size in comparison to the other samples. Inspection of the Figures H1–H9 shows that all the distributions for samples 2 and 3 are bimodal. Clearly a second phase of aggregated particles is formed during the oxidation reaction. The relatively high variation (~10-20%) of the $D_v(0,1)$ and $D_v(0,9)$ values for the first three samples in comparison to the last two indicates that a consolidation of particle size is taking place during the oxidation reaction. The variability of the first samples may be partly due to a partial dissolution of hydroxide particles that was noted when these samples were added to the dispersing chamber of the particle size analyser.

The consolidation and sharpening of the frequency distribution with increasing extents of oxidation indicates that smaller aggregates are growing larger and the largest aggregates are dissolving or breaking down. The above observations and processes are analysed further in section 5.3. The growth processes observed would be due to aggregation or agglomeration mechanisms. Here the term agglomeration is used in the context of a material in which the constituent particles are firmly bonded together while aggregation refers to electrostatic or capillary type binding mechanisms.

Table 4.1 Particle size distribution parameters at increasing oxidation time

Sample	Average all runs			Sdev all runs			Sdev/Average		
	$D_v(0,1)$	$D_v(0,5)$	$D_v(0,9)$	$D_v(0,1)$	$D_v(0,5)$	$D_v(0,9)$	$D_v(0,1)$	$D_v(0,5)$	$D_v(0,9)$
1	0,89	3,01	10,6	0,02	0,41	2,03	0,02	0,13	0,19
2	0,49	1,76	10,6	0,09	0,36	5,37	0,18	0,20	0,51
3	0,88	2,54	4,79	0,23	0,33	0,36	0,26	0,13	0,07
4	1,74	3,65	5,99	0,11	0,07	0,11	0,06	0,02	0,02
5	1,83	3,72	6,04	0,09	0,07	0,08	0,05	0,02	0,01

#Note: All data is given in micrometer

The formation of a second phase of particles suggests that the oxidation reaction may include a homogenous oxidation mechanism. Homogeneous and heterogeneous oxidation mechanisms of manganous hydroxide have been reviewed in Chapter 1. Feitknecht *et al.* (1962) have shown that the formation of β-MnOOH, the product of ambient temperature oxidation of $Mn(OH)_2$, requires a thin liquid film which limits the diffusion of Mn^{2+} ions to the bulk phase for precipitation and oxidation to Mn_3O_4. The conversion of cuboidal β-MnOOH to acicular γ-MnOOH also took place via soluble intermediates in the thin film of absorbed water on the surface of β-MnOOH particles. Kiyama (1978) identified the presence of a dissolution-precipitation reaction during the formation of ferrite particles in a system containing $Fe(OH)_2$, $Mn(OH)_2$ and $Co(OH)_2$. Dissolution and reprecipitation mechanisms in similar reaction systems have thus been reported in the literature.

Optical and Scanning Electron Microscopy

Optical microscopy was conducted using an Olympus reverse stage microscope at 400x (2,5μm resolution) and 1000x (0,625μm resolution) magnification on samples that did not have any form of dispersion applied to them. This revealed that the aggregated clusters were generally not larger than 10μm in diameter. SEM at low and high magnification (*vide infra* Appendix K) confirmed this observation. The SEM images show that the aggregates are made up of euhedral and subhedral crystals with diameters in the order of 0,1 to 0,2μm.

One effect noted with the particle size analysis of submicron sized aggregated materials is that the analytical method can affect the state of aggregation and hence the measured particle size distribution may not be representative of conditions in the reactor. The particle size analysis method described in Appendix K included the use of ultrasound at average energy levels that were higher than in the reactor and a chemical dispersing reagent. The particles measured by the Malvern therefore represent aggregates that are comprised of crystals which are held together with relatively high binding forces. A further assessment was made of this by analysing a reactor slurry sample directly without filtering or additional dispersion using the SEM and the optical microscope. This analysis showed that the particle size range in the SEM image and optical microscope observations is in the same order of magnitude as that obtained in the Malvern, i.e. manganese oxide particles larger than 20μm are not present in the reactor during the oxidation reaction in significant numbers. The presence of weakly bound aggregates smaller than 20μm diameter in the reactor can therefore not be excluded in the discussions on reaction mechanisms and particle morphology. Also, the changes in particle size distribution must have been due to forces which are greater than the dispersing effects of ultrasound and the chemical dispersant.

Surface area and porosity analysis

Specific surface area analysis of oxidation intermediates could not be conducted on the samples in the in-situ reactor condition, as conventional BET analysis requires dry material. The sample preparation and drying procedure adopted resulted in continued oxidation of unconverted hydroxide and also introduced a change in particle morphology as noted above. This was further confirmed in the TGA analyses described below. A number of liquid-phase, adsorbent-based surface area measurement techniques are available for materials such as electrolytic manganese dioxide ($ZnCl_2$ adsorption) and activated carbon (iodine adsorption). These could also not be applied using conventional analytical procedures as these could not exclude the ingress of oxygen in sample preparation. Notwithstanding these shortcomings, BET measurement of dried oxidation intermediates did yield useful data on the development of particle morphology during the process.

Specific surface area (BET) was measured using single point nitrogen absorption at 77K using a Micromeritics® Surface Area Analyser. The method required a dry powder sample that was obtained after drying for 12 hours in a drying oven at 105°C in air. Degassing at 120°C for 20 minutes was conducted as part of the method and the average of the adsorption and desorption volumes of nitrogen was used for calculation of the BET. Average values obtained from all runs are shown in the Table 4.2. The BET values for individual runs did not show any systematic trends with respect to pH_2*, i.e. the

dissolution of manganese metal at different hydrogen partial pressures did not affect the surface area of the hydroxide and its oxidation products.

Table 4.2 BET analyses for all controlled pH_2* experiments

Sample	Mean $m^2.g^{-1}$	Sdev $m^2.g^{-1}$	Sdev/Mean	Number of Readings
1	18,3	1,5	0,08	9
2	16,7	0,9	0,05	9
3	14,2	0,5	0,04	9
4	13,6	0,5	0,04	9
5	13,8	0,4	0,03	9
IQAS#	11,2	0,4	0,04	958

#IQAS refers to an internal quality assurance standard sample

The BET therefore decreases from a maximum of $18,3m^2g^{-1}$ to $13,8m^2g^{-1}$ at the end of the oxidation process. The variability of the surface area reduces with increasing oxidation time and approaches the reliability of the analytical procedure. The equivalent particle diameter for a solid material can be estimated from the BET measurement if the solid density is known. The formula used to estimate the equivalent particle diameter from the specific surface area assumes that the solid is made up of spherical and compact particles of uniform particle size:

$$d_{cry}=6/(\rho_s \text{ BET})$$

where: d_{cry}: Equivalent particle diameter (μm)

ρ_s: Solid density ($kg.dm^{-3}$)

BET: Specific surface area (m^2g^{-1})

The solid density was measured by helium pycnometry. Typical values of 3,95 and 4,72 $kg.dm^{-3}$ were obtained for the first and final samples respectively. It should be noted that the solid density obtained from crystallographic measurements is $4,834kg.dm^{-3}$. The dried intermediate crystallites are therefore not a consistent single phase of crystalline Mn_3O_4 and may contain closed voids that are inaccessible to the permeating gas in the BET measurement. Substituting the above values gives equivalent diameters of 0,08μm for the first and 0,09μm for the last samples drawn from the reactor. These equivalent diameters are an order of magnitude lower than the $D_v(0,5)$ and confirm the aggregated nature of this material. The BET measurements also correspond to the diameters obtained for the spherical crystals within an aggregated particle observed from the SEM images. The hydroxide particles thus contain a substantial degree of porosity that exists

within the individual aggregates that make up the solid phase. The decrease of the specific surface area with increasing oxidation time is discussed in the context of the mathematical model proposed to account for the porous structure of the solid phase in Chapter 5.

Porosimetry measurements were made on a dry milled sample taken after completion of the oxidation reaction to further analyse the nature of the porosity of the material. Measurements of macroporosity and mesoporosity were made using the Hg intrusion method on a Micromeritics Auto-Pore® 9200 analyser. A summary of the results from the porosimetry analysis is given in Table 4.3.

Table 4.3 Porosimetry measurements on dried Mn_3O_4 reactor discharge sample

Pore types	Pore diameter (nm)	Pore Volume (cm^3g^{-1})
Total pores	>10 000	0,60
Macropores	10 000 - 60	0,35
Mesopores	60 - 3	0,06
Micropores	< 3	0,19

The micropore volume was calculated from the difference of the total porosity (estimated from the formula $(1-\rho_p/\rho_{sol})$, where ρ_p is the particle density from Hg displacement, typically 1-1,2kg.dm^{-3}) and the sum of the macro and mesopore volumes. A significant portion (~60%) of the pore volume of the product is thus derived from macropore structures whose size can be characterised by dimensions that are of the same order of magnitude as the aggregated particle sizes. This is confirmed by the SEM images in Appendix K. The change in macro and mesoporosity was measured for one set of samples taken during an oxidation run with results presented in Table 4.4.

Table 4.4 Hg Porosimetry results for samples of dried oxidation intermediates

Oxidation Time (minutes)	Macroporosity ($cm^3.g^{-1}$)	Mesoporosity ($cm^3.g^{-1}$)
0	0,7506	0,0086
60	0,7466	0,0014
120	0,6661	0,0044
180	0,5997	0,0022

The Hg-intrusion pore size distributions show the formation of significantly increasing proportions of pores in the size range 200-400nm with increasing oxidation time viz., the distributions grow narrow and sharper in this size range, however the total macroporosity

and mesoporosity decrease with increasing oxidation time. The milled sample however differs from the oxidation intermediates by having a lower macroporosity and higher mesoporosity. The sample preparation procedure, as in the particle size analyses, therefore affects these readings.

4.2.2 Thermogravimetric and kinetic investigations

The limited solubility of manganous hydroxide results in only a small fraction (<0,02%) of the total manganese content of the reactor being present in soluble form. The product of oxidation will thus consist of a solid phase, which depending on the mechanism of oxidation, may exhibit different phase distributions within the particle distributions. Two limits of these phase distributions have been anticipated. The first limit assumes that oxidation proceeds via a homogeneous oxidation mechanism and will ideally result in a mixture of single-phase particles. The other limit assumes that heterogeneous oxidation is the rate controlling mechanism and will result in multi-phase particles with topochemical effects being present. Phase characterisation can therefore be used to confirm the predominant reaction mechanism.

Quantitative analysis of mixed oxidation states of solid manganese using conventional wet analytical chemistry relies on indirect measurement. The sample digestion procedures generally quantitatively reduce the higher oxides and dissolve the Mn^{2+}. This change in the oxidation state of manganese lattice ions may not always occur in an easily predictable manner, particularly if defect structures are present. The reducing agents used for analysis also generally do not differentiate between the higher oxidation states of manganese (Mn^{3+}, Mn^{4+}). The preferred analytical techniques need to analyse the samples in the solid state, without altering the oxidation states and structure of the material. Thermogravimetric analytical procedures that conform to some of these requirements were used to characterise the products of manganous hydroxide oxidation. The technique was also used to determine oxidation kinetics by analysing samples taken at increasing reaction times from the reactor.

4.2.2.1 Kinetic measurements for the oxidation of hydrothermal manganous hydroxide by air.

Two methods were used to measure the rate of oxidation of the manganous hydroxide slurry obtained from the hydrothermal dissolution of manganese metal. The first method used thermogravimetric analysis of slurry samples taken during a number of oxidation experiments. In the second method, the rate of oxygen uptake by the hydroxide slurry

was measured with different rates of air addition and agitator speed using oxygen analysis of the gas phase leaving the reactor.

Oxidation kinetics by thermogravimetric analysis of oxidation intermediates

The decomposition of solid manganous hydroxide at slightly elevated temperature (<250°C) in an inert atmosphere proceeds according to the ideal overall reaction:

$$Mn(OH)_{2(s)} \rightarrow MnO_{(s)} + H_2O_{(g)}$$

The change in mass of a sample due to bound water loss in a thermogravimetric experiment will thus yield quantitative information on the amount of $Mn(OH)_{2(s)}$ present in the sample and on the extent of reaction. Analysis of the kinetics of the decomposition reaction may also reveal the presence of intermediates or complex phases. The above reaction has been discussed in the literature although kinetic aspects of this reaction have not been reported. In addition to quantifying the extent of oxidation, the following analysis thus also addresses mechanisms of decomposition.

Experimental

Manganous hydroxide suspension samples were taken in a 2 litre, nitrogen purged sampler at 30 minute intervals during the oxidation stage of an experimental run and stored under a protective film of kerosene after cooling to room temperature.

Within 5 days of sampling, a 1000mg sample of suspension was transferred into a cylindrical alumina sample holder and subjected to thermogravimetric analysis. Thermogravimetric curves were obtained on a Netzsch® STA409E simultaneous TG, DTG, DTA analyser using a dynamic method in a high purity nitrogen gas atmosphere (99,999% N_2, <2ppmO_2, 400cm^3min^{-1}). The furnace was heated in two steps, the first dried the suspension at 100°C under constant temperature conditions. A linear heating program (20°C.min^{-1}) was then initiated to heat the dry sample to the decomposition temperature that occurs at temperatures in excess of 150°C. A typical set of TG, DTG and DTA curves obtained is shown in Figure 4.5. The unusually pointed peaks on the DTG and DTA curves for the evaporation process $H_2O_{(l)} \rightarrow H_2O_{(g)}$, are due to the experimental heating program which maintains constant temperature conditions while drying the sample. This can be clearly seen on the mass curve that decreases from 200mm to 100mm at 100°C without a temperature change.

Figure 4.5 Thermogravimetric curves for dehydration and decomposition of a manganous hydroxide suspension sample

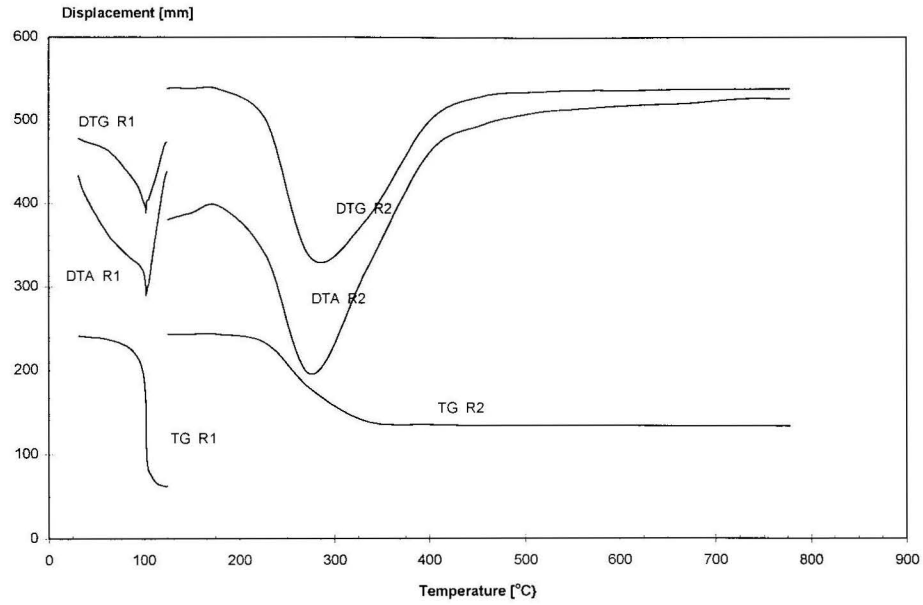

Reaction 1: $H_2O_{(l)} \rightarrow H_2O_{(g)}$

Experimental conditions:

Sample mass: 1030,8mg

Heating time: 15 minutes

Atmosphere: UHP N_2 400cm^3min^{-1}

TG: 1mm = 4mg

DTG: 1mm = 0,2mg.min^{-1}

DTA: 1mm ≈ 0,1°C

Heating program: Up at 50°C min^{-1} to constant temperature of 120°C

Reaction 2: $Mn(OH)_{2(s)} \rightarrow MnO_{(s)} + H_2O_{(g)}$

Experimental conditions:

Sample mass: 312,8mg

Atmosphere: UHP N_2 400cm^3min^{-1}

TG: 1mm = 0,5mg

DTG: 1mm = 0,05mg min^{-1}

DTA: 1mm ≈ 0,4°C

Heating program: Up to 800°C at 20°C min^{-1}

Cooling curves are not shown.

The DTG and DTA curves for the decomposition of solid manganous hydroxide show single event peaks. The decomposition reaction therefore does not proceed via an intermediate that is distinctly different to manganous hydroxide. In addition, no other

intermediate products of oxidation are present in the temperature range from 300°C to 800°C. This range spans the stability range of hydrated manganese oxides. It is on the basis of this observation that the second reaction on the TG curve is assigned only to the decomposition of manganous hydroxide. The temperature for the onset of decomposition was found to vary from 180°C to 225°C for all the samples of manganous hydroxide analysed for this work.

The above observations are in agreement with the studies reported in the literature review of Gmelins (1973). The first reports of this reaction by Simon (1943) and Rode (1955) suggested a two step decomposition occurring in the temperature range 145°C to 210°C. Klingsberg & Roy (1959) mapped the pH_2O *vs.* temperature equilibrium above 300°C and also briefly discussed the crystal chemistry of the dehydration of brucite lattices for $Ca(OH)_2$, $Mg(OH)_2$, $Ni(OH)_2$ and $Mn(OH)_2$, as has Robins (1968). The hydroxides with larger cations and more ionic nature in the M-O bond have higher stability and consequently higher decomposition temperatures than hydroxides with smaller cations and a more covalent M-O bond. This is analogous to the hydrolysis resistance of hard and soft divalent hydroxides discussed in section 1.2. Berg & Kovyrzina (1963) however confirmed a single event reaction at 166°C to 200°C with the temperature of decomposition being dependent on pressure.

Pure $Mn(OH)_2$ will lose 20,25% mass due to the evolution of water vapour according to the reaction:

$$Mn(OH)_{2(s)} \rightarrow MnO_{(s)} + H_2O_{(g)}$$

The extent of oxidation was then estimated from the stoichiometry of this reaction. The change in mass for this reaction is 53,5mg (107mm on TG scale). This is 17,1% of the mass at the start of the linear heating program and therefore corresponds to 84,5% $Mn(OH)_2$. A further assumption is made that the solid phase only consists of $Mn(OH)_2$ and Mn_3O_4. The Mn_3O_4 content of this sample is therefore 100-84,5=15,5%. Further validation of this two component assumption was obtained from the XRD analyses on freeze-dried oxidation intermediates.

The above thermogravimetric analysis experiment was repeated on all samples taken at increasing oxidation times for a number of experiments conducted at different hydrodynamic conditions (viz. air flowrate, impeller type and frequency of agitator rotation). Plots of the extent of conversion at different oxidation times for these experiments are shown in Figure 4.6.

This figure shows that for the experimental conditions, the oxidation of solid $Mn(OH)_2$ to Mn_3O_4 proceeds via approximately linear kinetics. While care was taken to minimise the exposure of samples to air after sampling, complete elimination of the oxidising reaction was not always completely successful. This will tend to increase the extent of oxidation and create a convex shaped curve as the samples taken at the beginning of oxidation will be more prone to this error. Further confirmation was therefore required for assessment of kinetics and rate controlling mechanisms.

Figure 4.6 Conversion time plots for manganous hydroxide oxidation at different hydrodynamic conditions

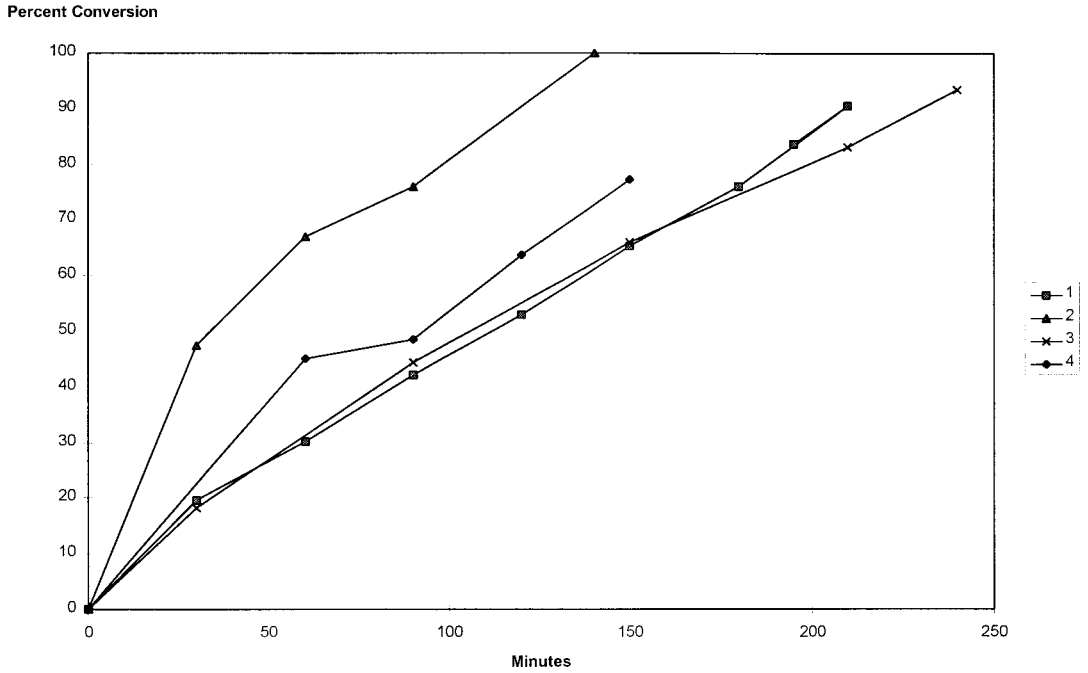

1) 3 Blade axial flow impeller 380rpm: 60kg.hr^{-1}m^{-3}
2) 4 Blade Rushton turbine impeller 248rpm: 100kg.hr^{-1}m^{-3}
3) 4 Flat Blade radial flow impeller 405rpm: 46kg.hr^{-1}m^{-3}
4) 4 Flat Blade radial flow impeller 405rpm: 100kg.hr^{-1}m^{-3}

All runs were conducted at ~25% solids suspension, 400kPa(g), 120°C average temperature with air sparging.

Oxidation kinetics measured by oxygen analyses of reactor offgas.

The experiments conducted above showed that the rate of oxidation of manganous hydroxide slurry by air was affected by experimental variables such as agitator type, agitator speed and air flowrate. Further experiments were conducted where the oxygen

content of the offgas from the reactor was measured using a paramagnetic oxygen analyser (Magnos 16, Hartman and Braun calibrated to ambient air composition).

Figure 4.7 shows the results obtained by plotting the datalogger readings of oxygen in the offgas, reactor pressure and air flowrate to the reactor taken at 10 second intervals during an experiment where the air flowrate was adjusted to different rates during the experiment. It can be seen that although the pressure was controlled to close tolerances, the air flowrate varied considerably at any instant of time. Notwithstanding these conditions it can clearly be seen that the oxygen analysis of the offgas assumes a flat profile once the flowrate adjustment had stabilised. A further experiment was conducted where the air flowrate to the reactor was kept constant and the agitator speed was varied. The results are plotted in Figure 4.8 with the calculated oxygen utilisation.

Figure 4.7 Oxygen profile during experiment conducted at different air flowrates

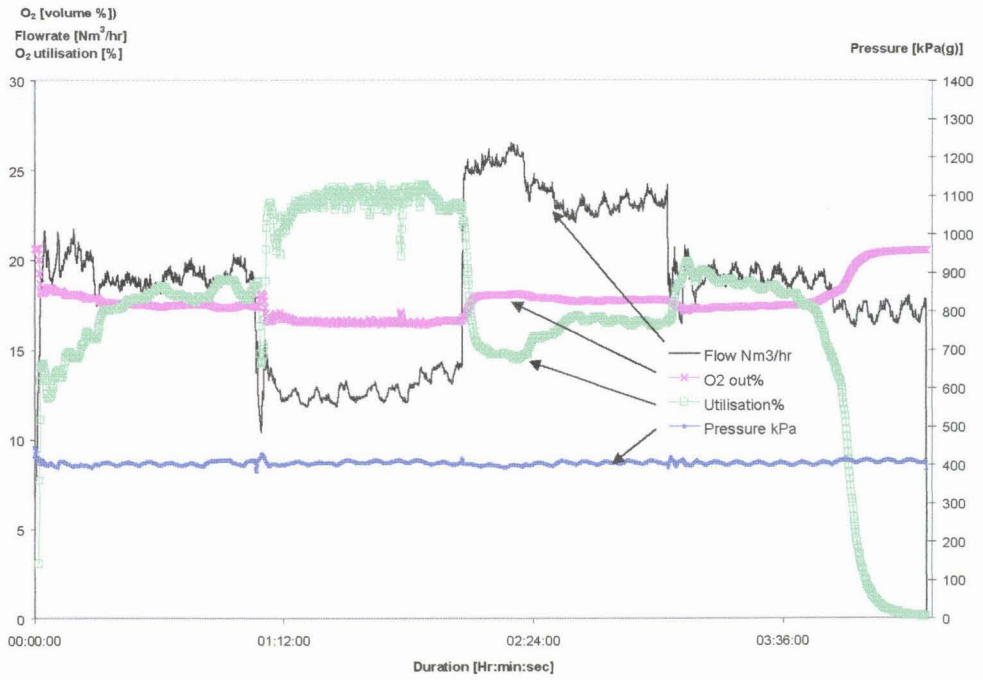

Figure 4.8 Oxygen profiles during experiment conducted at varying agitator speed

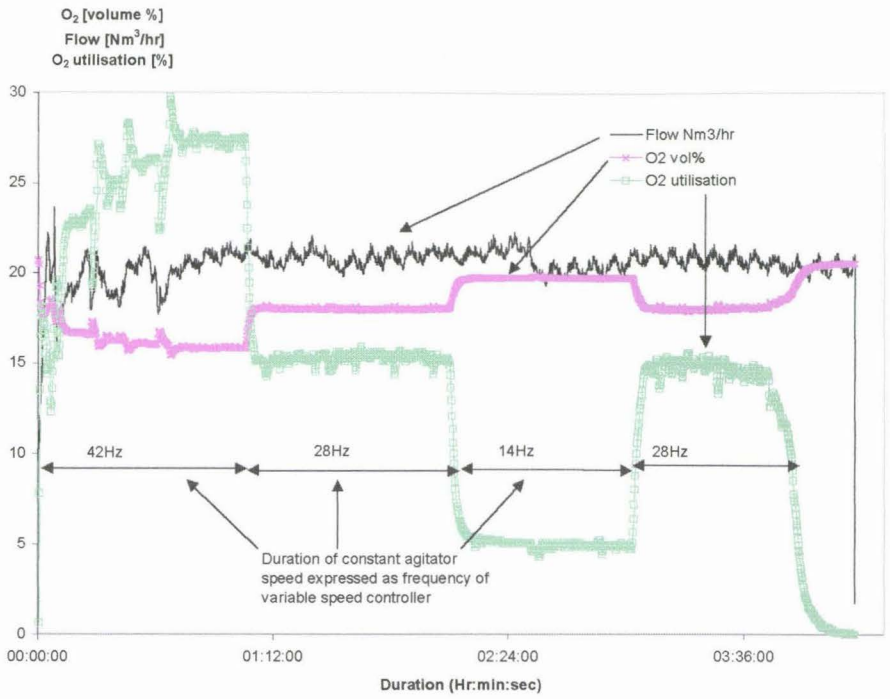

The oxygen analysis and utilisation profiles show sharp steps and flat plateau's where constant oxygen absorption rates were measured with good reproducibility being evident at the 28Hz frequency/speed setting. Decreasing the rotational speed of the agitator resulted in lower rates of oxygen absorption and in lower utilisation efficiencies of the oxygen. These profiles confirm that the process is limited by the rate of oxygen addition to the reactor i.e. mass transfer control. The hydrodynamic and mechanistic aspects of the kinetics measured above are discussed further in section 5.1.

4.2.2.2 Thermal analysis for characterisation of dried oxidation products.

A number of different analytical techniques were used to characterise the products obtained during the hydrothermal oxidation of manganous hydroxide. Thermogravimetric analysis of dried oxidation products revealed that Mn_3O_4 formed by hydrothermal techniques has unusual reactivity. These experiments are described in more detail below.

Experimental

A reactor discharge sample was filtered and dried to less than 0,5% moisture at 105°C in a drying oven. The thermogravimetric analysis experiment consisted of heating the dry

sample at a constant heating rate in a cylindrical alumina sample holder in an air atmosphere to 1200°C (viz. dynamic thermogravimetric analysis). Thermogravimetric curves were recorded on a Netzsch® STA409E simultaneous TG, DTG, DTA analyser. TG, DTG and DTA denote the mass loss/gain, derivative or rate of mass change and differential temperature (measured relative to an identical empty sample holder) curves respectively.

Figure 4.9 TG, DTG and DTA curves of Mn_3O_4 in an air atmosphere.

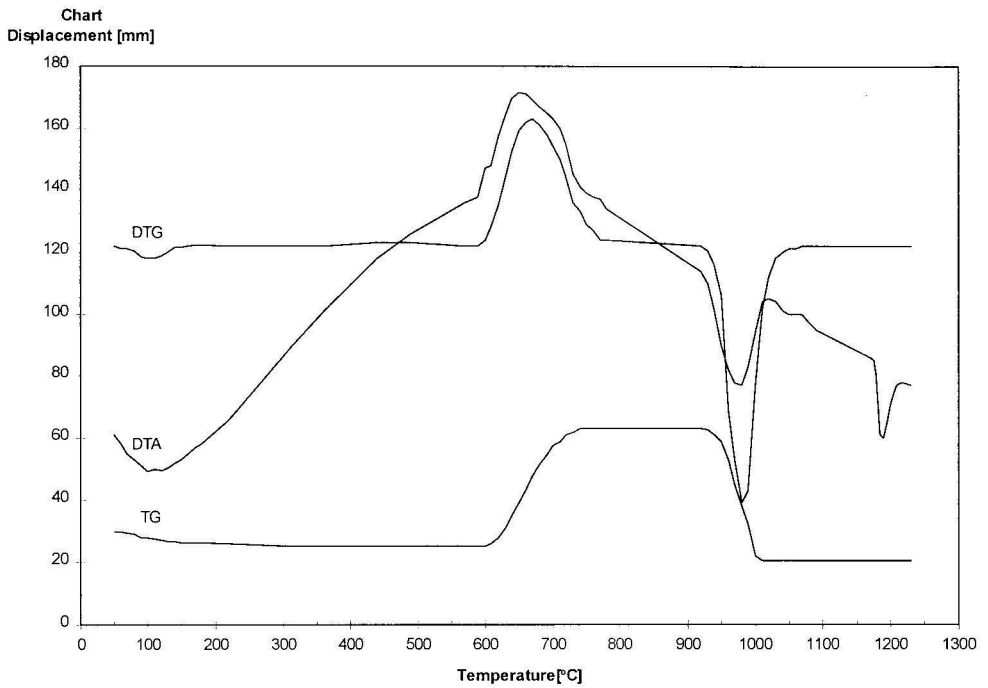

Experimental conditions: Sample mass 240,1mg
Atmosphere: Medical grade air at 250cm^{3}min^{-1}.
TG: 1mm = 0,2mg
DTG: 1mm = 20μg.min^{-1}
DTA: 1mm ≈ 0,01°C
Heating rate:10°C.min^{-1}

Three reactions can be observed in the TG, DTG and DTA curves shown in Figure 4.9. The DTA curve is a dome-shaped background curve with one exothermic and two endothermic superimposed events. The dome-shaped background is due to the choice of empty sample holder and the decision not to apply background linearisation to the thermal response of the furnace chamber.

Two reactions are noted on the TG curve that start at 590°C and 920°C. The 590°C event can be represented as the equivalent oxidation of Mn_3O_4 to Mn_2O_3:

$$4Mn_3O_{4(s)} + O_{2(g)} \rightarrow 6Mn_2O_{3(s)} \qquad (1)$$

The equilibrium temperature for this reaction in an air atmosphere is estimated from Figure 3.1 at 879°C. From Figure 4.9 it can be seen that the oxidation of the sample has been completed at this temperature, as no further weight gain is recorded on the TG curve. The X-ray diffraction pattern of a sample quenched from this temperature in a quartz tube heating furnace corresponded to JCPDS pattern No. 41-1442 which is cubic Mn_2O_3 or synthetic bixbyite.

The decomposition of Mn_2O_3 to Mn_3O_4 at 920°C is the second event on the TG curve:

$$6Mn_2O_{3(s)} \rightarrow 4Mn_3O_{4(s)} + O_{2(g)} \qquad (2)$$

A comparison between the mass loss recorded by the TG curve and the theoretical mass change for reaction (2), shows that slightly more mass is lost than expected if the sample was 100% stoichiometric Mn_2O_3 at this temperature, viz. 3,5% compared to 3,378% of the mass of Mn_2O_3. This deviation can be reconciled by buoyancy correction on the baseline which was not applied in the analytical procedure. Close examination of the TG curves shows that the mass change for reaction (1) is less than the mass change for reaction (2) indicating that a small portion of the Mn^{2+} ions are not oxidisable and presumably reside in stable lattice positions. The percent mass change on the TG trace for reaction (1) corresponds to a phase that is 97,2% of the mass of the sample with the Mn^{2+} content being oxidisable according to the stoichiometry $Mn^{2+}Mn_2^{3+}O_4$.

The third event is recorded on the DTA curve and is a phase transition without mass change at 1172°C. This phase transition is reversible and consists of tetragonally distorted spinel α-Mn_3O_4 transforming to a cubic spinel phase β-Mn_3O_4, Golikov *et al.* (1989).

Thermogravimetric analysis of a dried reactor discharge sample heated in air at 1100°C for 3 hours did not show TG events corresponding to reactions (1) and (2). The phase transition was however noted. The reactivity of the hydrothermally prepared Mn_3O_4 by heating in air is therefore an unusual structural feature in comparison to naturally occurring Mn_3O_4 or materials which have been prepared by high temperature processing routes.

An attempt was made to validate the TGA results by chemical analysis. Total manganese was determined by potentiometric titration with permanganate solution (0,15N) in a pyrophosphate buffered, neutral pH solution following digestion in concentrated hydrochloric acid. Manganese in the higher oxidation state (3+) was

determined by digesting the sample in dilute (25%m/m) sulphuric acid in the presence of potassium iodide which reduces the higher oxidation state manganic ions to soluble manganous ions. The iodine released by reduction was back-titrated with (0,02M) sodium thiosulphate. The manganic content is obtained by assuming only the 3+ oxidation state is present in the sample and the manganous content is obtained by the difference of the total manganese and manganic content. Table 4.5 is a comparison of the wet chemical analysis results of total manganese (TMn), manganic ion (Mn^{3+}) and calculated manganous ion (Mn^{2+}) compared to TGA analysis and stoichiometric Mn_3O_4.

Table 4.5 Chemical analysis of dried final product

	Analysis [%]	Calculated [%]	Theoretical [%]
TMn	71,5	71,9	72,03
Mn^{3+}	47,3	48,5	48,02
Mn^{2+}	24,2	23,3	24,01
Mn^{3+}/Mn^{2+}	1,96	2,08	2,00

The comparison shows that the thermogravimetric analysis underestimates the Mn^{2+} content and overestimates the Mn^{3+} content in comparison to wet chemistry and the theoretical ratios of these ions. The uncertainty in these values is however in the same order as the inaccuracy of these analytical techniques (1 sdev on chemical analysis = 0,4% Mn). The oxidation states of the manganese ions are discussed further in section 5.4

4.2.3 Structural Investigations

The crystal structures of oxidation intermediates were analysed to validate the chemical and thermogravimetric analyses described above. Crystallographic analysis using powder X-ray diffraction (XRD) techniques was conducted on freeze-dried and air-dried samples taken from the reactor during the oxidation process. The experimental investigations and observations for both types of samples are described separately below. These experimental results are analysed further using structural modelling in section 5.4.

4.2.3.1 XRD Analysis of Freeze-Dried Reactor Samples

Experimental

Samples of suspensions were taken from the 250 litre pilot scale reactor at 30 minute intervals in nitrogen purged samplers. After cooling the samples were transferred to glass containers, sealed with a protective kerosene film before freeze drying and XRD analysis. The containers were stored under an argon atmosphere in a high-purity glovebox. The samples were frozen in liquid nitrogen in the glovebox and subsequently transferred to a freeze-drier. After freeze drying, the samples were returned to the glovebox where they were prepared for X-ray analysis. A thin, transparent, "WRAP" film was used to prevent oxidation during data collection on the X-ray diffractometer. Powder X-ray diffraction patterns were collected on an automated Rigaku diffractometer with CuK_α radiation, monochromated by a graphite single crystal for the 2θ range: $5°<2\theta<120°$. A scan rate of $1°2\theta$ min^{-1} was employed. The X-ray analysis was completed within 10 days of sampling the reactor suspensions. A typical X-ray pattern is shown in Figure 4.10 while Appendix L contains all the traces that were obtained.

Figure 4.10 Typical XRD trace for a freeze dried sample taken during hydrothermal oxidation of a suspension of $Mn(OH)_2$

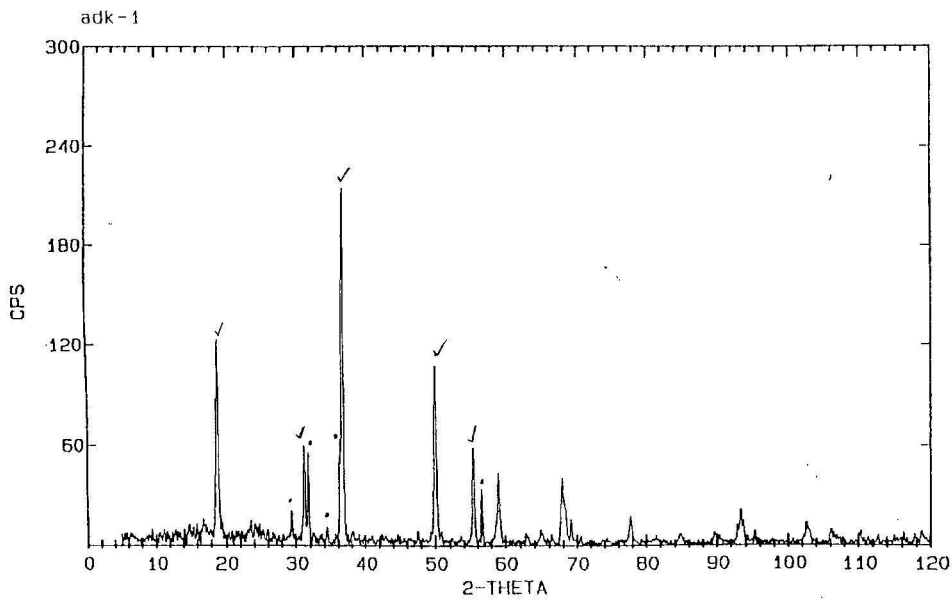

Identification of the crystal phases present in these samples is given in Figure 4.5. The table includes an unknown phase that was detected in a number of samples. The

diffraction pattern for this phase was identified by subtracting the patterns for $Mn(OH)_2$ and Mn_3O_4 from the 170 minute pattern. Comparing this pattern with those available for the manganese oxyhydroxides in the databank of the Joint Committee of Powder Diffraction Standards (JCPDS) gave some similarity to the pattern JCPDS 2-829 ($MnO_{1,48}$ $0,15H_2O$). Figure 4.6 lists the d-spacing and intensities compared to JCPDS 2-829.

Table 4.6 Phase identification at different extents of oxidation

Time [minutes]	$Mn(OH)_2$	Mn_3O_4	Unknown
0	Predominant		Minor
30	Predominant	Trace	
60	Minor	Major	Trace
90	Major	Major	Major
120	Major	Major	Trace
150	Minor	Predominant	Trace
170	Minor	Major	Major

Table 4.7 Comparison of "unknown phase" diffraction pattern with JCPDS 2-829.

Unknown		JCPDS 2-829		
d (Å)	I/I_o	d (Å)	I/I_o	[hkl]
		5,00	90	101
5,64	10			
4,72	14	4,71	90	002
3,4	8			
3,05	41	3,13	70	003
2,83	100	2,81	100	
2,62	20			
2,49	82	2,52	100	
		2,38	60	004
2,01	8	2,06	70	220
1,93	13			
		1,81	60	
		1,72	50	223
1,63	54	1,65	50	303
		1,59	70	
		1,56	100	
1,48	12			
1,42	8	1,45	100	400
1,39	17			
1,37	13			
1,05	10			

Observations

- $Mn(OH)_2$ was detected in all the samples indicating that this phase is crystalline.

- The X-ray diffraction measurements confirm the presence of crystalline $Mn(OH)_2$ and Mn_3O_4 as separate major phases at the beginning and towards the end of the oxidation process respectively.

- Peaks for the most intense reflections of the well-known hydrated allotropes of manganic oxide viz. α-, β-, and γ-MnOOH are not observed in any of the patterns.

- The trends in the qualitative phase analysis for all components indicate some anomalies, e.g. the third sample contains only minor quantities of $Mn(OH)_2$ and major quantities of Mn_3O_4. No trend is apparent for the Unknown phase. This suggests that this phase is not a well-defined oxidation intermediate.

- Table 4.7 shows that although some correlation exists between the unidentified phase and JCPDS 2-829, some significant reflections are missing, e.g. the peaks at 1,56, 1,59, 1,72 and 1,81 Å d-spacing. The JCPDS 2-829 pattern corresponds to a hydrated manganic hydroxide which was obtained from the ambient air oxidation of hydrothermally prepared $Mn(OH)_2$ by Simon (1943). The structure of this material was similar to hausmannite which illustrates that substantial moisture can be accommodated in the spinel lattice. Simon's diffraction pattern was obtained using Debye-Scherrer focusing on photographic film which could raise some questions of concerning experimental precision. Confirmatory testwork is thus required to substantiate the presence of this phase during hydrothermal oxidation of $Mn(OH)_2$.

4.2.3.2 XRD Analysis of Samples Dried in Air

Experimental

In addition to the oxidation intermediate samples taken at 30 minute intervals during the hydrothermal oxidation of $Mn(OH)_2$ for wet thermogravimetric analysis as described in section 4.2.2.1, samples were also taken during experimental runs that were allowed to cool to room temperature before filtering and drying at 105°C for 24 hours. This sampling procedure resulted in continued oxidation of the hydroxide. 500g of the dried final reactor discharge sample was heated to 1000°C in an air atmosphere for 24 hours and then cooled before being subjected to XRD analysis. This is termed the calcined sample in the following discussion.

Dry samples were hand pressed into the sample holders of the diffractometer. A Siemens® D5000 X-ray diffractometer in Bragg-Brentano configuration using a CuKα X-ray tube with a graphite, single crystal, diffracted beam monochromator was used to generate and record the diffraction patterns. Fixed aperture Soller slits in the incoming and emergent beam paths were used to limit vertical divergence of the X-ray beam. Radiation intensities were measured by a scintillation counter. A step size 0,02Å with counting times of 4,1s.step^{-1} was used to scan the 2-theta range 10 to 100° 2θ. The major peak positions did not shift in reproducibility experiments conducted at dwell times that varied from 1,0 to 4,0s.step^{-1}. A typical pattern for the reactor discharge sample is shown in Figure 4.11. All the patterns that were obtained are given in Appendix M.

Figure 4.11 XRD pattern of reactor discharge sample

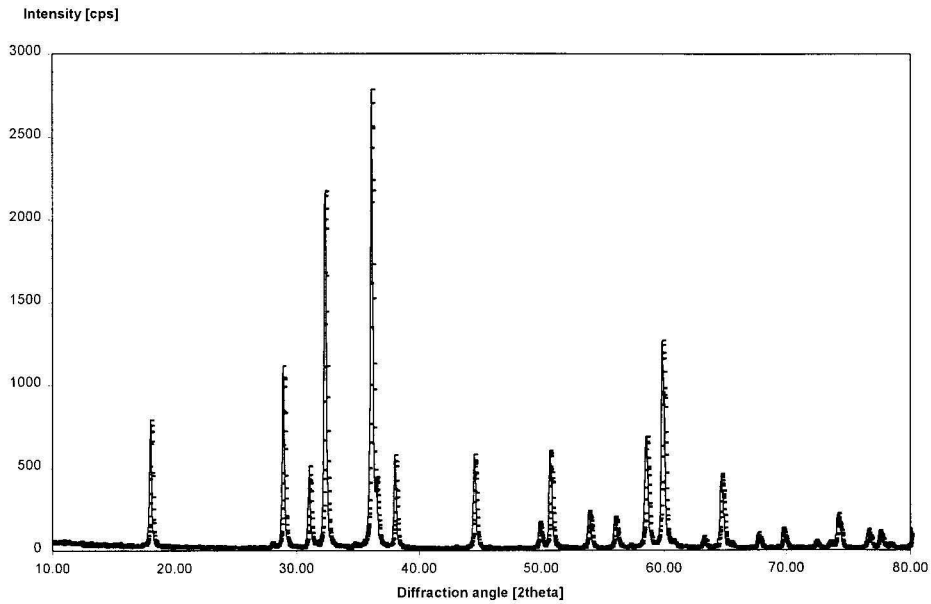

Calibration and alignment of the instrument was done using a quartz standard. The average of the absolute differences in d-spacing of 25 peaks of this standard and the JCPDS 46-1-45 pattern was 0,00035Å.

Reproducibility of the method was checked by repeating the whole sample pressing and recording procedure for one sample. The absolute and relative intensities of the more intense peaks are shown in Table 4.8. Calculating d-spacings from this data showed that differences within <0,0005Å can be obtained with the exception of the shoulder on the most intense peak which was recorded with a 0,0012 difference. The diffraction patterns were smoothed using a Savitsky-Golay smoothing filter and stripped of CuKα_2 peaks using the Rachinger method by the software package Siemens -Eva®. This increased the

number of peaks detected by the peak-searching algorithm in Eva® and gave absolute d-spacings that were closer to the standard pattern for hausmannite JCPDS 24-734. The JCPDS pattern only contains CuKα_1 peaks. Differences in d-spacing of less than 0,004 Å in the low angle region and less than 0,001Å in the high angle region could be obtained between these patterns.

Table 4.8 Comparison of absolute and relative intensities for repeat XRD runs

Sample 60 min			Sample 60 min rerun		
Angle 2θ	I [cps]	I/I_{max} [%]	Angle 2θ	I [cps]	I/I_{max} [%]
18,132	536	28,2	18,133	582	27,8
29,027	750	39,4	29,028	858	41,0
31,154	343	18,0	31,155	379	18,1
32,465	1393	73,2	32,464	1483	70,9
36,227	1902	100,0	36,235	2093	100,0
36,640	360	18,9	36,620	388	18,5
38,143	352	18,5	38,136	386	18,4
44,573	398	20,9	44,567	427	20,4
60,002	837	44,0	59,995	885	42,3

Note:The rerun experiment was performed at marginally shorter dwell time 4,0 sec. c.f. 4,1 sec.

Figure 4.12 Variation in absolute intensity of [211] and [105] peaks at different oxidation times and conditions

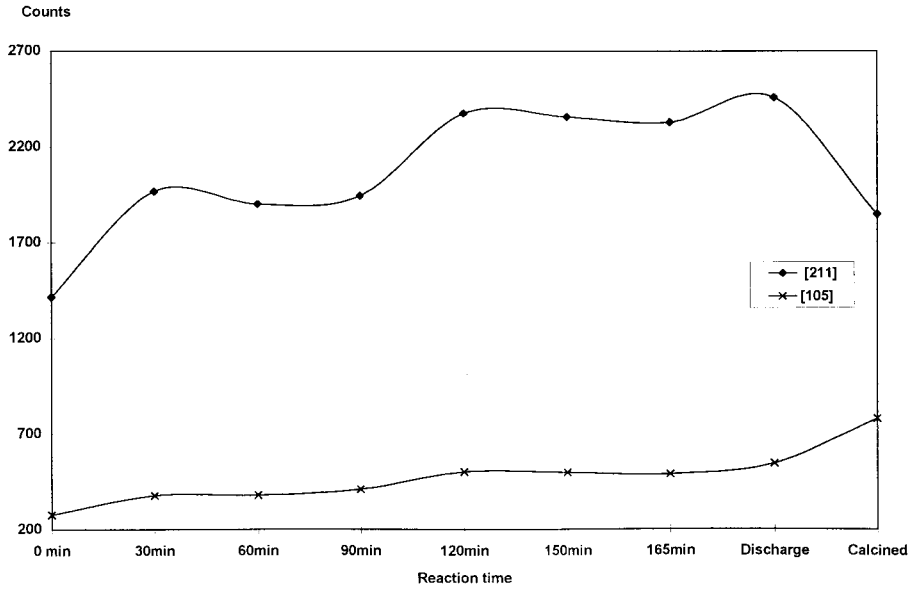

Observations

- The patterns all show narrow well-defined peaks indicative of a crystalline material. The increase in absolute intensities of the patterns during the oxidation reaction indicates that some form of structural consolidation is taking place. This can clearly be seen in Figure 4.12.

- The calcined sample intensities are an anomaly in this respect showing lower maximum intensity, which is attributed to the presence of larger crystallites that could form during the high temperature oxidation of the discharge sample.

- The XRD patterns of all air-dried samples show the characteristic diffraction pattern of the mineral hausmannite given by JCPDS No. 24-734. The absence of the $Mn(OH)_2$ pattern confirms that this phase has been converted.

- Closer inspection of the pattern for the first sample taken during oxidation shows the possible presence of a trace amount (<2%) of a second phase due to reflections at approximately 23, 35, 40 and 47° 2θ. A cubic Mn_2O_3 phase catalogued as JCPDS 78-0390 matches this pattern. The patterns for β-MnOOH, JCPDS 2-829 or MnO (JCPDS 7-230) do not contain the 23° reflection. The 23° reflection also does not correspond to reflections for the other hydrated manganic oxides – manganite and groutite and is not present in samples analysed subsequently. Crystalline secondary hydrated phases are therefore not found in the products of this oxidation procedure.

- Lattice parameters were calculated from the peaks by indexing to the $I4_1/amd$ space group for the different samples and the JCDPS24-734 pattern using a least squares regression analysis with the results being shown in Table 4.9.

- The predominant phase thus detected in all the samples is hausmannite with tetragonal distortions (*c/a*) of the spinel and lattice parameters that are similar to the standard JCPDS pattern. The magnitude of the lattice parameters asymptote towards the values for the standard pattern as the oxidation reaction proceeds confirming the consolidation of the hausmannite structure. The absolute values of the lattice parameters obtained in the above table cover a wider range than those reported by Kazcmarek & Wolska (1993a). These authors found that the *a* and *c* lattice parameters would increase with an increasing Mn^{3+}/Mn^{2+} ratio.

- The dried sample series was analysed for Mn content and Mn_3O_4 content according to the methods described in section 4.2.2.1 so that the Mn^{3+}/Mn^{2+}ratios could be determined. The results are shown in Table 4.10, Figure 4.13 and Figure 4.14. These figures include analytical error bars (1sdev = 25%) for the chemical analyses.

The compositional formula for the sample taken at the beginning of the oxidation reaction (0 minute) is calculated as $Mn_{2,72}O_4$ (or $Mn_{2,04}O_3$) from the chemical analysis. It can also be seen that the ratio of Mn to O increases with increasing oxidation times. The highest Mn to O ratio was obtained for the calcined sample. Included in the table is the calculated Mn^{3+}/Mn^{2+} ratio that ensures electroneutrality in the spinel lattice. It can be inferred from these observations that defects in the form of cationic vacancies must be present in this sample series.

Table 4.9 Lattice parameters for oxidation intermediates

Sample	R^2	Peaks	*a* (Å)	*c* (Å)	Vo (Å^3)	*c/a*
0	0,999986	33	5,757	9,454	313,3	1,161
30	0,999947	36	5,757	9,459	313,5	1,162
60	0,999806	37	5,755	9,456	313,2	1,162
90	0,999904	36	5,750	9,447	312,3	1,162
120	0,999994	39	5,759	9,459	313,7	1,161
150	0,999981	37	5,757	9,454	313,3	1,161
165	0,999968	37	5,758	9,463	313,7	1,162
Discharge	0,999999	38	5,761	9,463	314,1	1,161
Calcined	0,999996	39	5,762	9,466	314,3	1,162
JCPDS 24-734	0,999999	41	5,762	9,470	314,4	1,162

Peaks: Number of peaks used in regression analysis: Vo: volume of unit cell

Table 4.10 Wet thermogravimetric analysis and chemical analysis of dried samples.

Sample	Wet TGA $\%Mn_3O_4$	Dried sample TMn%	x in Mn_XO4	Mn^{3+}/Mn^{2+} ##
0	11,5#	70,0	2,718	16,70
30	20,5	71,0	2,852	4,14
60	49,4	70,7	2,811	5,51
90	73,2	70,8	2,824	4,97
120	94,0	71,2	2,880	3,51
150	100,0	71,6	2,937	2,63
165	100,0	71,4	2,908	3,02
Discharge		71,2	2,880	3,51
Calcined		72,0	2,995	2,04

Anomalous sample according to linear conversion trend

##Calculated from chemical analysis with assumption of electroneutrality

Figure 4.13 Variation of *a* lattice parameter with manganese oxidation ratio

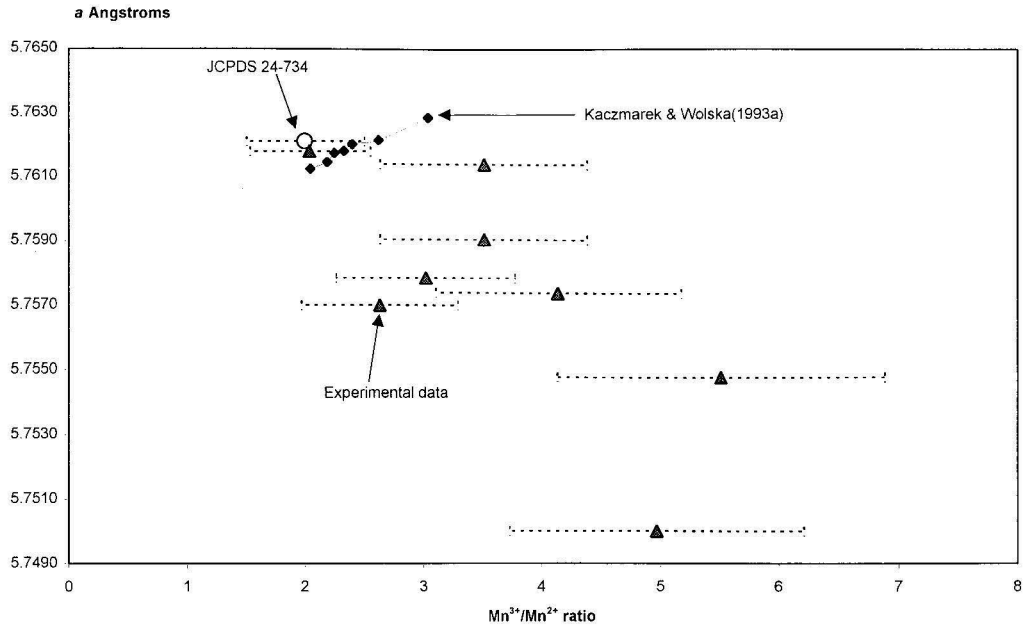

Figure 4.14 Variation of *c* lattice parameter with manganese oxidation ratio

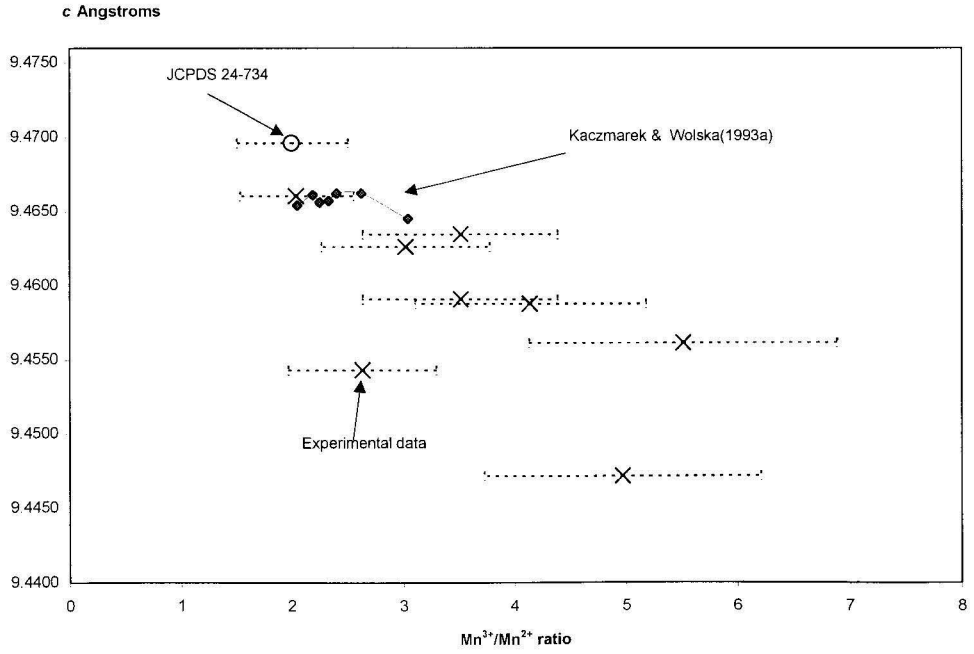

- The lattice parameters reported above thus have the opposite trend reported by Kazcmarek & Wolska (1993a), i.e. the lattice parameters decrease with increasing Mn^{3+}/Mn^{2+} ratio. An increase in the Mn^{3+}/Mn^{2+} ratio is expected to correspond to an increase in the concentration of cation vacancies in the hausmannite structure. Here

the increasing concentrations of vacancies could explain the reduction in the interatomic distances. The presence of major concentrations of vacancies or defects can result in significantly different values for the lattice parameters, e.g. Sanchez-Perreira & Ramos (1997) reported values of *a*=5,823 Å and *c*=9,55 for $Mn_{2,5}O_4$ (or Mn_5O_8) with the hausmannite spinel structure.

- The method of Tsumara *et al.* (1996) was used to check if microstrain and crystallite size effects are present in the patterns. This method assumes that peak broadening of these effects can be added independently according to:

$$Bo\ Cos\theta/\lambda = k/L + 2\varepsilon Sin\theta/\lambda$$

where: Bo:Peak width

$Cos\theta/\lambda$: Diffraction angle/ X-ray wavelength

k: Proportionality constant

L: Crystallite dimension

ε: Microstrain parameter

A plot of Bo $Cos\theta/\lambda$ vs $2Sin\theta/\lambda$ will give slope ε and intercept 1/L respectively where Bo is FWHM (Full Width at Half Maximum) of the most intense peaks in the pattern. Least squares fits did not give good correlation coefficients, typically R^2=0,65 to 0,87 for all samples analysed. The presence of these effects as independent phenomena can therefore not be confirmed.

- The peak intensities of oxidation intermediates and completely oxidised samples are shown in Table M1 of Appendix M together with the JCPDS pattern for hausmannite. The peak intensities were obtained using the peak identification algorithm in the software package EVA®. A number of additional and missing peaks with low intensities were obtained in the high 2θ angle range patterns. These artefacts are ascribed to the mathematical algorithm used for peak identification and the experimental procedure. Studies reported from 1926 to 1965, which include the seminal work of Bricker (1965), have also omitted some reflections, e.g. [202]. It is suspected that these investigations omitted this reflection as it appears close to the most intense line at [211]. The more recent works of Kazcmarek & Wolska (1993a,b) confirm the presence of this line though they miss others. The missing or additional peaks are low in intensity and cannot be used as a quantitative characteristic of the structure.

- The peak intensity patterns of the Discharge and Calcined samples are shown in Table M1. The Calcined sample did not re-oxidise in the thermogravimetric analysis

experiment described in section 4.2.2.1. The Discharge sample shows lower relative intensities than the reflections for the Calcined sample. The relative intensities of the peaks for Calcined sample are generally within 5% of the JCPDS standard with the exception of the [103], [004], [105] and [224] reflections. These patterns are discussed further according to the classification of Xu & Miyazaki (1994) in section 5.4.

4.2.4 Summary of experimental results

The product of the hydrothermal dissolution of manganese metal is a slurry containing a saturated solution of manganous hydroxide at a solids concentration of about 20% m/m.

- The particles of solid $Mn(OH)_2$ consist of aggregates with an average particle diameter of approximately 5,0μm made up of smaller spherical grains that have a diameter of less than 0,2μm. The average particle diameter is not affected by the hydrogen partial pressure in the reactor during the dissolution reaction.

- The hydrothermal oxidation of the manganous hydroxide slurry by air occurs at essentially constant pH conditions due to the limited solubility of $Mn(OH)_2$. The redox potential of the slurry increases with increasing oxidation extent. Upon completion of oxidation, the rate of pH decrease increases which is accompanied by a rapid rise in the soluble manganese content of the slurry.

- Measurements of the particle size distribution of the samples drawn from the reactor during air oxidation show that a second phase of smaller particles formed during oxidation. The distributions are bimodal in the initial stage of oxidation but consolidate to unimodal distributions at the end of oxidation. This is indicative of a dissolution and reprecipitation mechanism. The spreads of the final oxidised particle size distributions are narrower than those for the unoxidised size distributions indicating that progressively, the smallest particles grow and the largest particles are broken down.

- The particle size distributions measured by a laser light scattering technique using a Malvern® particle size analyser were found to be dependent on the method of dispersion and intensive dispersion conditions resulted in the deaggregation of particles. The method of sample preparation also had an effect on the extent of dispersion and aggregation. An analytical procedure was however developed whereby consistent and reproducible measurements of the particle size distributions could be obtained.

- The particle size distributions of slurry samples that were dried and redispersed were found to contain significantly larger quantities of submicron particles than slurry samples analysed without drying. Here again, the sample preparation procedure affected the extent of dispersion. The increase in deaggregation with drying is partly attributed to the loss of the binding action due to the surface tension of water from the interstices of the aggregates.

- Hg porosimetry and surface area measurements (BET) show that the pore structure of the aggregates is determined mainly by macro and mesopores i.e. large pores. The surface area and total porosity of samples taken during oxidation and dried in the presence of air were found to decrease with increasing extent of oxidation.

- The hydrothermal oxidation of manganous hydroxide followed linear conversion kinetics as determined by thermogravimetric analysis of slurry samples taken during oxidation and continuous oxygen analysis of the reactor offgas stream. The rate of reaction was affected by rate of air addition, the stirring speed of the agitator as well as the impeller geometry. These findings are consistent with a mass transfer rate limited chemical reaction. Increasing the agitator speed resulted in an increase in reaction rate as well as oxygen utilisation.

- Thermogravimetric analysis of oxidation intermediates found no evidence of the hydrated manganic oxides α-MnOOH, β-MnOOH or γ-MnOOH. In addition the dehydration reaction of $Mn(OH)_2$ in the temperature range 250 to 300°C was found to follow a single step decomposition mechanism. This supports the observation that these manganic hydroxides are not a feature of the hydrothermal oxidation of $Mn(OH)_2$.

- Both the hydroxide phase and the dried products of oxidation were found to be crystalline by X-ray diffraction. The predominant reflections for α-MnOOH, β-MnOOH or γ-MnOOH were not found in any of the patterns. XRD analysis of freeze dried oxidation intermediates suggests that a third structural phase may form during oxidation. The X-ray pattern of this phase did not match any of the patterns on the JCPDS database but is similar to a manganic hydroxide phase with a hausmannite structure found by Simon (1943). The presence of this phase during oxidation was not consistent and further experimental investigations into Simon's work are required to validate this finding.

- The intermediate samples taken during oxidation that were dried in the presence of air have a distorted spinel structure that can be oxidised in air at relatively low temperature (~600°C). This is in contrast to the stable forms of naturally occurring

hausmannite and synthetic Mn_3O_4 prepared by high temperature processes. Thermodynamic considerations (vide supra Figure 3.1) also confirm that Mn_3O_4 should not oxidise under these conditions. These hydrothermally prepared structures are therefore metastable.

- The d-spacings of the XRD patterns of the dried oxidation intermediates are similar to the standard materials hausmannite patterns catalogued on reference crystallographic databases but differ in the relative intensities of the predominant reflections. The lattice parameters *a* and *c* increased with increasing extent of oxidation (and reduction of Mn^{3+}/Mn^{2+} ratio) though the extent of tetragonal distortion *c/a* and unit cell volume remained essentially constant. This is in contrast to investigations reported in the literature for synthetic hausmannite prepared at high temperatures where the *a* lattice parameters increased with increasing Mn^{3+}/Mn^{2+} ratio.

- The hydrothermal oxidation of $Mn(OH)_2$ results in defect structured hausmannite with higher degrees of non-stoichiometry than synthetic materials produced by high temperature processing routes. The concentration of defects generally reduces with increasing oxidation time and is accompanied by an increase in interatomic spacings of the spinel lattice. The end product however remains a reactive mangano-manganic oxide that can take up oxygen into the lattice at elevated temperature.

The findings summarised above provide a basis for further theoretical modelling investigations. These investigations are required to confirm the mechanism of $Mn(OH)_2$ oxidation and to identify the mass transfer limiting step (i.e. gas-liquid, liquid-solid etc). Modelling of the particle morphology needs to be undertaken to reconcile the particle size distribution, BET and porosimetry measurements. A structural analysis is required to reconcile the results from the TGA, XRD and chemical analyses by modelling the valence of the manganese cations, the distribution of these ions and the distribution of cationic defects in the spinel lattice. This work is described in more detail in Chapter 5.

5 KINETIC AND STRUCTURAL ASPECTS OF THE HYDROTHERMAL OXIDATION OF MANGANOUS HYDROXIDE

The experimental investigations into the hydrothermal oxidation of manganous hydroxide derived from manganese metal show that the products of oxidation are porous, reactive, anhydrous, hausmannite-structured materials. These materials exhibit larger deviations from stoichiometry and hence have higher concentrations of structural defects than materials prepared from high temperature (>1000°C) processing routes.

Further theoretical investigations were undertaken to explain the experimental results and observations obtained. The linear kinetics were analysed to determine the rate controlling reaction mechanism within homogenous or heterogeneous reaction frameworks with changing particle sizes due to chemical reaction as well as hydrodynamic action. A more rigorous characterisation of the hydrodynamic conditions present during oxidation was then made together with analysis of the oxygen mass transfer processes.

It was found that the available literature could not explain all the physical and structural properties of the solid phases obtained from the oxidation experiments. Models were therefore constructed to quantify the morphology, valence, cation distribution and defect distribution of the solid phases obtained from the oxidation experiments.

The results of these fundamental investigations are presented below.

5.1 Kinetic and Mechanistic Modelling

Linear conversion kinetics were obtained during the experiments described in section 4.2.2.1 that were conducted to investigate the hydrothermal oxidation of manganous hydroxide. The rate of conversion was also found to be dependent on the rate of air addition, the type of agitator used and the speed of the agitator. These results all confirm that mass transfer is the rate controlling mechanism for the oxidation reaction. These mass transfer processes are analysed in more detail in section 5.2. The mass transfer processes can be considered to proceed within a mechanistic framework that includes homogeneous and heterogeneous chemical reactions.

A linear conversion-time relationship for a homogeneous chemical reaction occurring in a batch stirred reactor can be obtained if the reaction rate is independent of the quantity or concentration of the reactant being monitored or if the concentration of a soluble reactant does not change significantly during the conversion process. A pH buffering action has been noted during manganous hydroxide oxidation experiments -Figure 4.1, Figure 4.2 and by Bricker (1965)-Figure 5.1 respectively. A homogeneous dissolution and oxidation reaction in the bulk liquid phase would account for thus observation i.e. rapid dissolution of hydroxide maintains the pH at saturated conditions.

Figure 5.1 Variation in pH and potential during oxidation of $Mn(OH)_2$ - Bricker (1965)

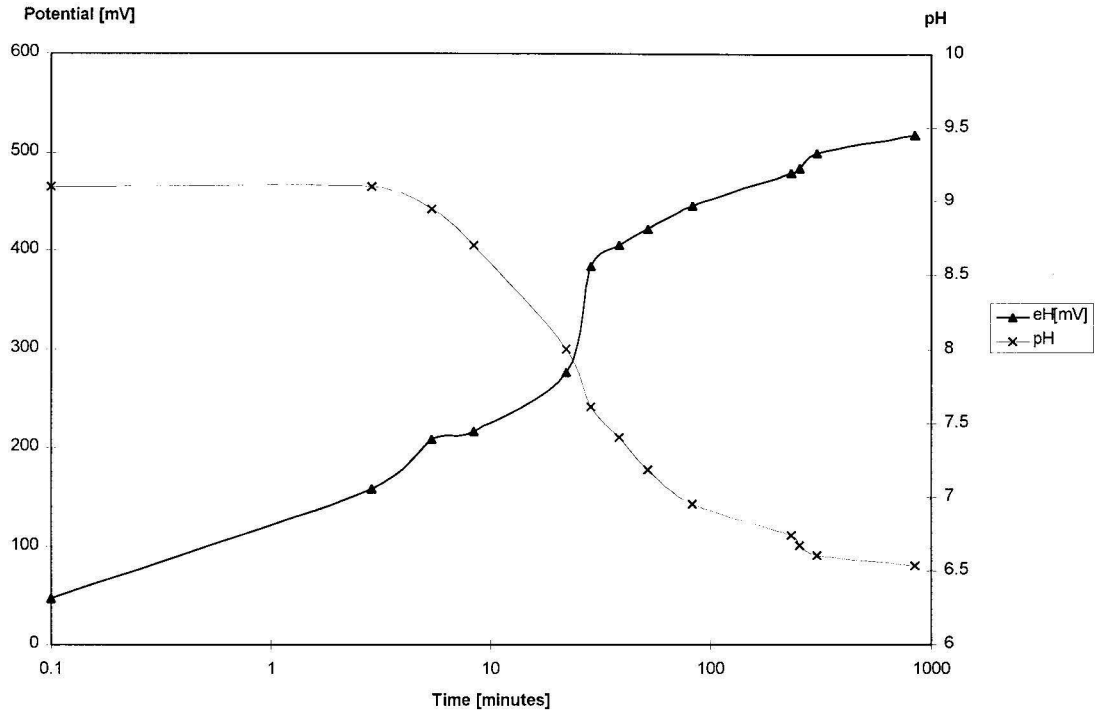

The sparing solubility of $Mn(OH)_2$ means that constant concentrations of soluble hydroxide could be maintained in the bulk liquid phase up to almost complete oxidation of the solid hydroxide.

An alternative mechanism can be postulated for maintaining saturated pH conditions that includes a hybrid heterogeneous-homogeneous mechanism by assuming that preferential oxygen consumption occurs in zones with high energy dissipation. These exist at the sparger inlet or on the trailing edges of the agitator impeller blades. As the contents of the reactor are mixed through these zones, rapid oxidation of $Mn(OH)_{2(aq)}$ occurs at a reaction rate sufficient to oxidise solid $Mn(OH)_2$ directly and lower the local soluble manganous content (heterogeneous mechanism). Equilibrium concentrations of $Mn(OH)_{2(aq)}$ are then re-established in the more quiescent zones of the reactor

(homogeneous mechanism). Most of the studies of mass transfer in mechanically agitated reactor surveyed for this thesis do not account for a spatial variation of mass transfer within the reactor. The hydrodynamic conditions in the hydrothermal oxidation reactor are discussed in more detail in section 5.2. It was however not possible to practically measure in-situ local mass transfer rates with the experimental designs used for this thesis so the hybrid model could not be verified.

In addition, the experimental results show that significant changes occur in the particle morphology of manganous hydroxide during the oxidation reaction. The appearance of a second phase of particles during the oxidation reaction confirms the presence of a dissolution and precipitation process. Levenspiel (1972) and Doraiswamy & Sharma (1984) present models that are available for different rate-controlling mechanisms in heterogeneous catalytic and non-catalytic fluid-solid reaction systems. These models incorporate the geometry of the solid phase to varying degrees of complexity.

Sharp interface (SIM) or shrinking core models have been used extensively to analyse heterogeneous reactions. The existence of a sharp interface that separates solid reactant and product is dependent on the applicability of the pseudosteady state assumption. This is generally valid when the concentration ratio, $C_{Ab}M_B/\rho_B$ is less than 0,001-Doraiswamy & Sharma (1984). The sharp interface moves slowly relative to the diffusion of fluid phase reactants or products. Due to the sparing solubility of oxygen in water this ratio is calculated as $1{,}25\times10^{-5}$ for the experimental conditions. This makes the hydrothermal oxidation of manganous hydroxide reaction similar to gas solid reactions which generally always conform to this requirement.

The particle morphology characterisation analysis presented in section 5.3 shows that the solid phase could be considered as porous aggregates made up of smaller non-porous crystallites which are subject to shrinkage due to chemical reaction. The question is therefore raised whether mass transfer within the precipitated particles could be rate limiting. The Thiele modulus, which is a dimensionless rate of reaction to diffusivity ratio, is used to classify different rate controlling regimes. This parameter is defined as:

$$\phi = \left(\frac{k_v C_{Ab}^{m-1} C_{Bo}^{n} R^2}{D_{eB}} \right)^{0,5}$$

The Thiele modulus for the oxidation reaction can be calculated by substituting typical values for the experimental conditions given in Appendix J:

$k_v = 131\ s^{-1}$ (Based on typical actual rates of conversion)
m=1,n=0 (Reaction rate is independent of solid concentration. Gaseous reactants are generally first order unless adsorption effects are significant)
$D_{eB} = 1{,}07 \times 10^{-8} m^2 sec^{-1}$ (O_2 in water at 110°C)
$R = 1{,}75 \times 10^{-6} m$ (Half the diameter of the aggregates)

Substituting the above values yields a Thiele Modulus (ϕ) equal to 0,19 which corresponds to the situation where the concentration of reactant within the porous particle is uniform with no intraparticle concentration gradients. This confirms the observation that the formation of the daughter phase of oxidised particles must occur in the bulk solution and not within the unoxidised hydroxide particles.

The shrinkage of compact hydroxide particles is expected during hydrothermal oxidation of manganous hydroxide. In the case of porous particles, growth processes can lead to interparticle such effects of pore closure, bridging and sintering. Doraiswamy & Sharma (1984) reviewed models based on single pore, distributed pore and networked pore structures within the solid phase including diffusion processes. The pore size may shrink, grow or remain constant depending on the change in the density of the solid due to chemical reaction. The solid phase characterisation analyses have identified the possibility of closed or isolated pores. In addition, the experimental porosimetry results (Table 4.3) show that the macro and mesoporosity decrease with increasing extent of oxidation. These effects therefore occur as secondary processes to the dissolution and precipitation reaction and are discussed further in section 5.3.

5.1.1 Conclusions

- The concentration ratio $C_{Ab}M_B/\rho_B$ for the hydrothermal oxidation of manganous hydroxide calculates to $1{,}25 \times 10^{-5}$. The pseudosteady state assumption is valid for sharp interface models under these conditions.

- The rate controlling mechanism for the hydrothermal oxidation reaction is oxygen diffusion in films surrounding the air bubbles or the dispersed solid particles. A more formal mass transfer analysis is conducted in the next section to determine which of these film diffusion processes is rate limiting.

- The mass transfer processes need to be considered within the context of the structural rearrangements that take place during the oxidation process. The

shrinkage of compact crystallites due to chemical reaction is accompanied by a consolidation of the $D_v(0,5)$ of the aggregated particles to about 4,0μm with an increase in $D_v(0,1)$ and a decrease in $D_v(0,9)$ with increasing extent of oxidation. This is due to the formation of a second phase of smaller particles by a dissolution and precipitation mechanism. The smallest particles grow and may agglomerate with oxidised aggregates. The largest aggregates are broken down by a combination of chemical dissolution and the hydrodynamic action of the turbulent flow conditions. Structural change processes such as bridging, sintering and pore closure occur in parallel to the interparticle processes that reduce to macro and mesoporosity of the solid phase. A morphological model of the solid particles is described in section 5.3 that quantifies some of these structural changes.

5.2 Mass Transfer Modelling

Analysis of the kinetics of oxidation of $Mn(OH)_2$ in the preceding sections has shown that oxygen mass transfer controls the rate of the oxidation reaction. In a three-phase reactor, the gas mass transfer rate can be controlled by diffusion through gas-liquid films, liquid-solid films or within the solid particles. Mass transfer at phase interfaces is influenced by a number of interdependent phenomena. A systematic approach is therefore required for the analysis of such a system, the analysis of which should take into account at least the following considerations:

- Quantification of parameters (e.g. reactor and stirrer geometry) that characterise the physical (e.g. flow, mixing, suspension of particles, dispersion of gas) and chemical phenomena (e.g. mass transfer) occurring in the reaction system.

- Hydrodynamic conditions together with structural aspects of the reaction suspension will determine the surface areas available for gas-liquid, bulk-liquid and liquid-solid mass transfer. The hydrodynamic conditions will also influence the magnitude of intra- and interphase mass transfer coefficients. Mass transfer rates could vary in the different hydrodynamic zones (i.e. impeller, sparger and recirculation zones) of the reactor. Each of these parameters needs to be quantified.

General conditions in the reactor during experimental runs have been described in Chapter 4. Further details on reactor geometry and operating conditions are described in Appendix J.

Framework for hydrodynamic and mass transfer model

L'Homme (1981) and Mann (1983) present structured frameworks for analysing stirred reactors. L'Homme (1981) classifies reactors according to type of reaction and reactor while Mann (1983) uses two diametrical classifications with respect to vessel type and purpose. Classification by type considers geometry, impeller configuration, gas-input arrangement and baffle disposition. Classification by purpose consists of a number of differentiations. The simplest level addresses physical contact variables such as energy dissipation, hold-up and flow patterns which are then used to determine interphase mass transfer characteristics (i.e. bubble mechanics, surface areas and mass transfer coefficients). The most complex differentiation takes into account the influence of mass transfer and chemical reaction on micro and macro mixing phenomena.

While these classifications are useful to categorise reactors, they do not recognise hydrodynamic operating regimes or specific rate controlling conditions. A more useful approach would be to extend the above classifications to incorporate these features. This requires that the hydrodynamic and operating regimes must be described in terms of criteria that can be quantified relatively simply. The modelling procedure summarised below and presented in detail in Appendix J satisfies these requirements. The model is divided into a number of categories that each contain related parameters. Table 5.1 summarises the grouping of categories while Figure 5.2 shows the interconnectivity of the categories.

The linking of the concept of solution structure concept with the virtual mass transfer analysis was developed specifically for this thesis. This grouping and linking of elements provides quantified criteria that facilitate the analysis of the reaction system. A framework is also provided that can be extended with improvements in the understanding of mechanically agitated, three phase, reactor systems.

Table 5.1 Subsections of a mathematical model for a three-phase stirred reactor

Physical Properties of Reacting Phases
Reaction Characteristics
Reactor Geometry
Geometrical Ratios
Suspension Characteristics
Mixing and Flow Analysis
Dispersion Characteristics
Solution Structure
Mass Transfer Coefficients
Mass Transfer Virtual Analysis

Figure 5.2 Framework of a mathematical model of a three phase reactor

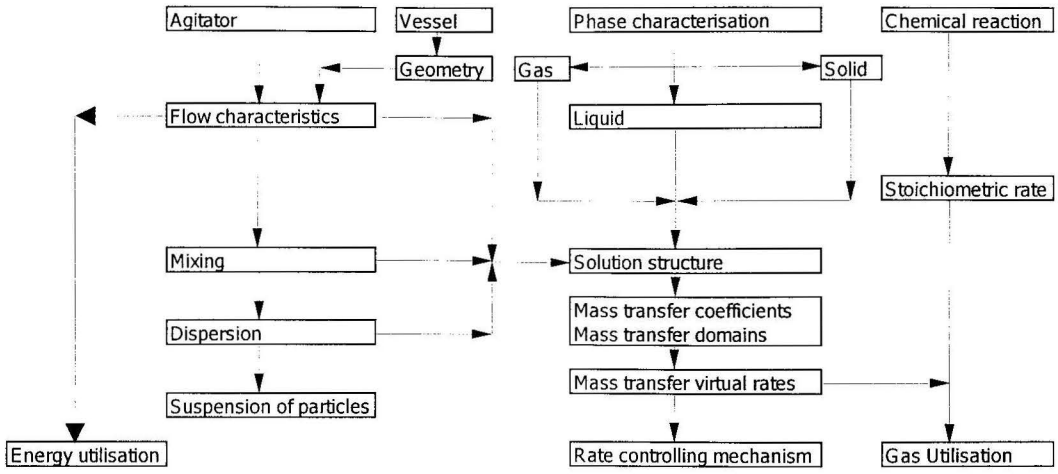

5.2.1 Conclusions

The conclusions that can be made with respect to the hydrodynamic and mass transfer analysis presented in Appendix J can be summarised specifically for this reaction system as follows:

- A creeping flow regime exists local to individual solid particles in the hydrothermal manganous hydroxide oxidation system. The small diameter (<10μm) of these particles makes them effectively neutrally buoyant.

- The diameter of the $Mn(OH)_2$ particles is similar to the length scale of the microscale eddies in the turbulent flow regime.

- The flow regime in the liquid phase is turbulent with a mixing intensity that is capable of fully dispersing gas bubbles throughout the reactor.

- A relatively high energy consumption rate is required to maintain the reactor contents in a well mixed and dispersed condition.

- The impeller used in the experiments can accommodate a higher gas flow as the operating speed is far from the critical speed for flooding.

- The interfacial area for mass transfer from gas bubbles to the liquid is estimated to be three orders-of-magnitude less than the particle interfacial area. The mass transfer coefficient for gas-liquid mass transfer is also three orders of magnitude less than the

liquid-solid mass transfer coefficient. The mass transfer of oxygen from the gas to liquid phase therefore controls the rate of oxidation.

- Validated methods need to be developed for predicting variations in mass transfer rates in the different hydrodynamic zones of two and three phase reactors.

5.3 Modelling of Particle Morphology

The experimental results of Chapter 4 have shown that the solid phase formed during hydrothermal dissolution and oxidation of manganese metal consists of an aggregated material with a log-normal particle size distribution. The progression of oxidation is accompanied by the formation a second class of particles that results in a bimodal particle size distribution within 2 hours of oxidation. The final products of oxidation have narrower log-normal particle size distributions in comparison to the starting hydroxides with the largest particles being generally less than 20μm in diameter. The surface area of dried oxidation intermediates decreases with increasing extent of oxidation. The proportion of pores in the 200 to 300nm range increases while the macroporous and mesoporous volumes generally decrease. These quantitative and qualitative observations need to be reconciled by means of theoretical morphological models.

Mathematical model of non-porous solid

The effect of a chemical reaction on the particle size of a compact, dense, spherical particle may be analysed by comparing the equivalent molar volumes of the products and reactants. Doraiswamy & Sharma (1984) suggest the use of a parameter, Z_v, which can be used to quantify volume changes. Z_v is defined as:

$$Z_V = \frac{\nu_S M_S \rho_B}{\nu_B M_B \rho_S}$$

where: ρ_B: Density of solid reactant (3,258kg.dm^{-3})
ν_B: Stoichiometric equivalent of reactant (6)
M_B: Molecular weight of reactant (88,9526g.mol^{-1})
ρ_S: Density of solid product (4,834kg.dm^{-3})
ν_S: Stoichiometric equivalent of product (2)
M_S: Molecular weight of product (228,8116g.mol^{-1})
Z_v <1 Particles shrink during reaction
Z_v >1 Particles grow during reaction
Z_v =1 Particle size is constant during reaction

Z_v is 0,58 for the oxidation of $Mn(OH)_2$ to Mn_3O_4. Similar relationships can be determined for the ratio of particle diameters and specific surface areas. These show that the diameter of a $Mn(OH)_2$ particle will shrink by a factor of 0,83 as it is converted to Mn_3O_4 by a solid state reaction only. The specific surface area will also reduce by a factor of 0,81. A number of conclusions can be drawn from these calculations and the observations made in the preceding Chapter:

- The narrowing of the particle size distribution during the oxidation reaction is accompanied by the formation and then loss of particles which are less than 1,2μm in diameter and the loss of large particles less than 100μm in diameter. This is attributed to a dissolution and precipitation mechanism.

- The formation and disappearance of the <1,2μm fraction may be influenced by surface charge effects. The large difference in the surface charge of Mn_3O_4 (pH_{pzc} = 3,3) and $Mn(OH)_2$ (pH_{pzc} =12,4) in a liquid suspension at pH 9,5, indicates that small Mn_3O_4 particles could coagulate with $Mn(OH)_2$ particles to form larger particle clusters. The aggressive dispersion conditions used in the Malvern particle size analyser may segregate some of the more weakly bound particle clusters in the <20μm particle size range that would however be stable in the reactor.

- No change would be expected in the BET surface area as measured for the oxidation intermediates if the solid 0,1 to 0,2μm crystals as observed by SEM underwent a solid state reaction on perfectly spherical particles. This is due to the fact that the hydroxide products were completely oxidised in the sample preparation procedure for the BET analyses as no residual hydrates could be detected by XRD or TGA. The increased BET obtained for the early stages of oxidation is therefore due to a different crystal or grain structure that arises as a result of the dissolution and precipitation reaction. Small differences in crystal diameter or a distribution of crystal sizes could account for these effects. The morphological measurements made for this thesis do not have the sensitivity to distinguish these features and a parallel solid state reaction can not been discounted on the basis of these measurements only.

- The particle size distributions are similar for the mass and volume based measurements obtained by different particle size analysis methods described in the preceding chapter. This would be accounted by a solid density that does not change with respect to particle size for a non-porous material. Porous submicron sized particles do not necessarily comply to this condition.

A mathematical model based on a hypothetical structure that accounts for porosity in the solid phase was developed to further reconcile the above morphological measurements and observations.

Mathematical model of porous solid

The solid phase is assumed to consist of uniformly spherical, compact crystallites whose diameter may be represented by the equivalent diameter obtained from surface area measurement (d_{cry}). The crystallites then close pack into a sphere with the equivalent diameter of a particle whose size represents the mean of the particle size interval obtained from particle size measurements (d_{agg}).

Figure 5.3 Schematic of spheres-in-spheres model

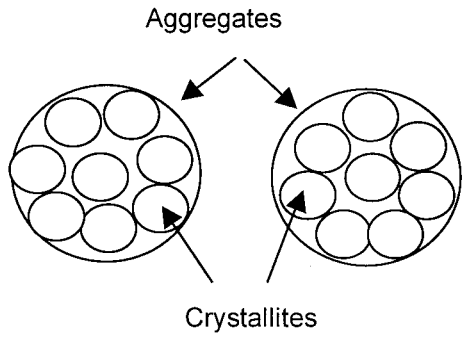

The correlations of Heintz *et al.* (1989) are used to estimate the number of spheres (crystallites) within a sphere (aggregate). These correlations have the form:

$$N_{s/s} = A(R)^3 + B(R)^2 + C(R) + D$$

where: $N_{s/s}$: Number of spheres within a sphere of radius ratio R

R: Radius ratio of aggregate to crystallite d_{agg}/d_{cry}

A,B,C,D are sets of regression constants which are specific to a cubic, body centred cubic (BCC) or face centred cubic (FCC) close packing structures.

The number, mass, surface area and pore volume distributions can then be calculated from the volume based particle size distribution. Detailed calculations for a sample of completely oxidised product are presented in Appendix N. A comparison is also made in of the mass and surface area distributions that would be obtained if the particles were assumed to be compact with no internal porosity.

A number of observations can be made from the calculations tabulated in Appendix N and the assumptions implicit within the spheres-in-spheres model:

- The volume and mass distributions for the compact non-porous model are equivalent, as there is no variation in density with particle size. This feature is also retained in the porous spheres-in-spheres model that however predicts a decrease in effective particle density with decreasing particle size.

- The measured changes in the aggregate particle size distribution are larger than the decrease in size predicted by Heintz's formula for heterogeneous oxidation of aggregated crystallites. The dissolution-precipitation mechanism and other particle aggregation/deaggregation mechanisms therefore significantly affect the particle morphology.

- The number distribution of the compact model predicts that 87,5% of particles are less than 1,0μm in diameter. This size fraction also contributes 23,5% of the total surface area of the sample and creates a bimodal area distribution. The porous model does not exhibit the same skewing of the number distribution relative to the mass or volume distributions. The <1,0μm fraction of particles does not contribute as significantly to the total surface area of the sample and this distribution is unimodal. The porosity distribution of the porous model also follows the broad trend of the number, mass, volume and area distributions.

- Calculation of the total porosity from the distribution of particles for a completely oxidised sample gives a value of $0,15cm^3.g^{-1}$, assuming that the porosity is only associated with interstitial voids in the close packed aggregate structure. This should be compared to the value of $0,35cm^3.g^{-1}$ in Table 4.3. The porous model thus accounts for 42% of the macroporosity of the sample. Nolan & Kavanagh (1992) have shown that random packing of spheres can result with packing efficiencies ranging from 0,509 to 0,639 compared to 0,524 for a primitive cubic close packing which was used in the model. Thus packing efficiency effects alone cannot account for deficiencies in the model. Examination of the SEM images also shows the presence of extended macrostructures of particles. The assumptions of packing structure, uniform crystallite size, uniform density, spherical crystallite and spherical aggregates would have to be challenged with more complex modelling and detailed particle morphology measurements to provide closer reconciliation of the observations.

- The porosity calculations could only be affected by assuming that below radius ratios of R=3,1 (d_{agg}=0,32μm) no porosity exists within particles as Heintz's correlations

predict a negative number of spheres-within-spheres. As the distinction between internal and external aggregate surface area is lost at small radius ratios the mathematical definition of porosity becomes problematical. This calculation thus highlights one of the limitations of the spheres-in-spheres model. The model also cannot account for the development of micropore structure within individual crystallites. The spheres-in-spheres model nevertheless provides useful qualitative and quantitative reconciliation of the measurements of manganous hydroxide particle morphology during oxidation.

- Bimodal distributions of particles formed during precipitation reactions have been reported by a number of investigators especially for sparing soluble products, e.g. Popplewell *et al.* (1989) and Wachi & Jones (1992). Secondary processes can act on individual particles to alter the particle size distributions, crystallinity or morphology of a precipitate - Söhnel & Garside (1992). The cohesive strength of aggregates formed may be low in the case of coagulation or strong because of solid bridging in agglomeration. Coagulation may occur by mechanisms of perikinetic and/or orthokinetic flocculation that may be modelled by conjugation kinetics. These processes are not modelled in this thesis.

- The decrease in the >8μm fraction has been attributed to a dissolution mechanism. However mechanical breakage mechanisms may also accompany the dissolution process. Larger particles can be broken down by hydrodynamic action in zones of high turbulence, e.g. trailing vortices of impellers or bubble wakes. The aggregates are also subjected to shear forces due to microscale eddies - Ayazi Shamlou *et al.* (1994). These eddies are estimated to be of the order of 7,1μm in section 5.2 which is consistent with the reduction of >8μm size fraction. The observation that the majority of particles are approximately half the size of the microscale eddies is consistent with other studies reported in the literature - Söhnel & Garside (1992). Wachi & Jones (1992) simulated the precipitation of potassium sulphate using an aggregated spheres-in-spheres type of model and showed that agglomeration and breakage are necessary mechanisms for the formation of a bimodal distribution. This model was also able to simulate secondary particle characteristics (e.g. specific surface area) for the first time. Wachi & Jones found that the larger particles were formed by crystal agglomeration and not by molecular (or ionic) crystal growth. These observations are useful for mechanism identification purposes. However, the analysis of $Mn(OH)_2$ oxidation in this system requires that the influence of a dissolution and reprecipitation reaction, possibly in parallel with a solid state chemical reaction with changing particle volume, needs to be taken into account. This exercise could be undertaken if the structural modifications within the porous particles could be quantified.

- Sintering or solid bridging are possible mechanisms that can decrease the specific surface area of the oxidised products as well as closing pores through the chemical dissolution-precipitation mechanism. Sintering is a term used to describe structural change processes that are associated with high temperature (viz. half the melting point) processing of materials. The description of this process as solid bridging is therefore considered more appropriate. The solid bridging mechanism does not form tightly bound agglomerates yet it can reduce the expected surface area. The analysis of this solid bridging mechanism requires more quantitative analytical data on strength of the binding forces between crystallites as well more sophisticated models of pore structure and particle morphology.

- The daughter fraction of particles present due to the dissolution-precipitation mechanism will result in a mixture of solid phases during the hydrothermal oxidation reaction. More sophisticated analytical methods are required and more complex morphological models need to be developed that can accommodate this feature.

5.3.1 Conclusions

- A theoretical spheres-in spheres model for the porous products of hydrothermal oxidation of manganous hydroxide is able to account for some of the experimental results and observations.

- A heterogeneous oxidation reaction mechanism will result in a decrease in particle size for crystallites and aggregates of crystallites as manganous hydroxide is oxidised to mangano-manganic oxide. As the decrease in aggregate sizes observed experimentally is larger than predicted by this model a heterogeneous oxidation mechanism cannot be the predominant process.

- Additional mechanisms that change the particle morphology have been identified. These include particle breakage of larger particles by the dissolution-precipitation mechanism of the chemical reaction as well as the hydrodynamic action of the turbulent flow field in the reactor. Aggregation and agglomeration mechanisms are present as the smallest particles were found to grow. These agglomeration mechanisms may by affected by the difference in surface charge between the hydroxide and oxide particles.

- Pore closure effects are apparently present which reduce the macro and mesoporosity of the aggregates. The sphere-in-spheres model is only able to account for approximately 50% of the intra-aggregate porosity.

- More sophisticated material characterisation methods and particle morphology models are required to improve the physical characterisation of the products of hydrothermal oxidation of manganous hydroxide and the understanding of structural change mechanisms in this reaction system.

5.4 Characterisation and Modelling of Solid State Structures

The experimental results obtained from chemical, TGA and XRD analyses were analysed qualitatively and quantitatively using crystal structure models. Knowledge of the valence of manganese cations and the distribution of these cations in the crystal lattice as well as the lattice defect composition are important parameters that need to be quantified if the chemical, physical and electrical properties of these material need to be understood. These properties have a strong influence in terms of how these materials are made as well as how they are applied.

5.4.1 Thermogravimetric analysis of dried reactor samples

Thermal reactivity of $Mn_{3-\delta}O_4$

The first major event recorded on the TG curve at 590°C for a dried reactor discharge sample in Figure 4.9 can be represented as the equivalent oxidation of Mn_3O_4 to Mn_2O_3:

$$4Mn_3O_{4(s)} + O_{2(g)} \rightarrow 6Mn_2O_{3(s)} \qquad (1)$$

This reaction does not occur under these experimental conditions in natural Mn_3O_4 minerals (hausmannite)-Kulp & Perfetti (1950), and Dressel & Kenworthy (1961). It also does not occur in synthetic manganese oxide samples that have been heated in oxidising atmospheres to temperatures in excess of 1200°C-Dollimore & Tonge (1971) and Xu & Miyasaki (1994). It has also been observed in manganite structures prepared by precipitation at high pH-Pattanayak & Rao (1989). The reactivity of this sample must therefore be related to electronic or structural properties which are characteristic of the low temperature hydrothermal oxidation process. Xu & Miyasaki (1994) classified Mn_3O_4 into three reactivity classes:

- Type 1 are derivatives prepared from $MnCO_3$ and electrolytic manganese dioxide (EMD) at temperatures between 1000 to 1050°C which can incorporate oxygen into their lattices when reheated to 570°C to 900°C in an oxygen atmosphere.

- Type 2 are prepared at high temperature and can be oxidised in the presence of Mn_2O_3 or EMD at temperatures above 400°C.

- Type 3 are not oxidisable even in the presence of catalysts. Type 3 are formed from 1 and 2 by heating these in air atmosphere to above 1100°C. Reheating type 3 in air will not result in oxidisation to Mn_2O_3.

The ability of manganese oxides to take up oxygen was first reported in 1934, Nohman *et al.*(1992). It is also well known that certain spinels can be oxidised at elevated temperatures, e.g. Von Bogdandy & Engel (1970). The ability of mixed cation ferrite spinels (MFe_2O_4) to take up oxygen is used commercially in the manufacture of soft magnetic materials. The factors responsible for this reactivity are generally accepted as the valence and defect distribution. The determination of the valence and distribution of cations in the tetrahedral and octahedral sites of spinel ferrites and manganate spinels (MMn_2O_4) is the subject numerous investigations, e.g. Bertaut (1951), Kshirsagar & Biswas (1966), Driessens (1967), Meenakshisundram *et al.* (1982), and Rousset (1993). Tailhades *et al.* (1997) showed that thermogravimetric analysis in conjunction with other solid state analytical measurements can be used to obtain quantitative information regarding the defect structure and cation distribution and oxidation state in spinel structures. On this basis, the authors showed that Mn cations in different lattice sites of spinel ferrites react at different temperatures as shown in Table 5.2. This observation can be used as the basis for quantitative analysis of these species.

Table 5.2 Reactivity of Mn cations in different lattice positions of spinel ferrite structures

Reaction	Oxidation temperature °C
$[Mn^{3+}] \rightarrow [Mn^{4+}]$	300
$[Mn^{2+}] \rightarrow [Mn^{3+}]$	350
$[Mn^{4+}] \rightarrow [Mn^{3+}]$	450
$Mn^{2+} \rightarrow [Mn^{3+}]$	>500

$[Mn^{x+}]$ denotes octahedral lattice positions

Mn^{z+} denotes tetrahedral lattice positions

All reactions are oxidation except $[Mn^{4+}] \rightarrow [Mn^{3+}]$ which is disproportionation.

The reactivity of foreign cations in a manganate spinel has also been reported - Rousset (1993). This type of theoretical framework has however not been reported for low temperature hausmannite structures. Although Table 5.2 does not strictly apply to hausmannite structures, it does suggest that the reactivity of defect mangano-manganic prepared by low temperature hydrothermal synthesis, observed by TGA, is due to oxidation of Mn^{2+} in tetrahedral lattice sites.

The experimental results thus show that the dried product of complete oxidation of manganous hydroxide is a Type 1 mangano-manganic oxide that can incorporate oxygen into its structure at temperatures above 600°C. By characterising this solid phase as $Mn^{2+}Mn_3^{3+}O_4$ an equivalent 97% of the Mn^{2+} is oxidisable.

Further, the stoichiometry of oxidation intermediates shows that excess Mn^{3+} is present in the lattice. The valence of the manganese cations in hausmannite is generally assumed to be $Mn^{2+}Mn_3^{3+}O_4$ though Ardizzone *et al.* (1998), on the basis of XPS and XRD investigations, claim that this is better represented by $Mn_2^{2+}Mn^{4+}O_4$. Similarly, a Mn_5O_8 material with a hausmannite structure that was analysed by Sánchez & Pereira-Ramos (1996) had a cation valence of $Mn^{4+}Mn_4^{3+}O_8$ while the monoclinic variant can be described by $Mn_2^{2+}Mn_3^{4+}O_8$ – Nohman *et al.* (1992).

The chemical analyses and TGA analysis described in section 4.2.2.2 were not able to distinguish between the two valence models for hausmannite. The lack of sensitivity for the chemical analytical procedure is self-evident. A material with a valence of $Mn_2^{2+}Mn^{4+}O_4$ could theoretically exhibit twice the theoretical TGA oxidation reactivity of $Mn^{2+}Mn_3^{3+}O_4$. This could however be reduced by the simultaneous disproportionation of Mn^{3+} to Mn^{4+} in a two step oxidation mechanism. The valence of defect structured manganese oxides must therefore be validated by an independent analytical method and must take the method of preparation into account.

In Figure 4.9, the material becomes unstable at higher temperatures and starts decomposing to Mn_3O_4 at 920°C according to the reaction:

$$6Mn_2O_{3(s)} \rightarrow 4Mn_3O_{4(s)} + O_{2(g)} \qquad (2)$$

Reaction (2) is completed at 1010°C and constitutes the second major event on the TGA curve. Agrawal (1981) reviewed the literature available on this reaction and found that a number of investigators have reported the reaction to occur in the temperature range from 871°C to 1005°C with an average of 948°C. Dollimore & Tonge (1971) found a two-stage decomposition reaction in this temperature region in similar TGA analyses conducted on manganese oxides synthesised from manganese carbonate. The two-stage decomposition reaction was attributed to Mn_2O_3 being present as a mixture of γ-Mn_2O_3 that decomposes between 860 to 910°C and α-Mn_2O_3 that decomposes between 920 to 970°C. This decomposition temperature range thus confirms the XRD analysis results reported in section 4.2.2.2. Therefore, no γ-Mn_2O_3 is present in this material above 750°C. Dollimore & Tonge (1971) also found that samples that had been exposed to higher temperatures for longer periods did not show the presence of γ-Mn_2O_3 as these had been converted to the more stable α-Mn_2O_3.

Bound water in manganese oxides is usually lost in decomposition reactions in narrow temperature ranges, e.g. 350 to 450°C in manganite-Kulp & Perfetti (1950) and Morgan *et al.* (1988) and 200 to 300°C for groutite-Lee et al.(1980). The presence of significant quantities of bound water are thus excluded confirming the anhydrous nature of this material.

Spinel- hausmannite structural transformation

No weight changes were recorded in the TG or DTG curves up to 1200°C in Figure 4.9. The DTA curve shows an endothermic event at 1172°C which is the phase transition of the tetragonally distorted spinel α-Mn_3O_4 to a cubic spinel phase β-Mn_3O_4:

$$\alpha\text{-}Mn_3O_{4(s)} \Leftrightarrow \beta\text{-}Mn_3O_{4(s)} \qquad (3)$$

This phase transition is reversible and is observed as an exothermic event on the cooling DTA curves, which have not been included in Figure 4.9. The cubic spinel to tetragonal hausmannite phase transitions for a number of manganese oxide systems has been studied by Golikov *et al.* (1989). These authors claim that in the pure manganese oxide system, the phase transformation was due to a thermal disordering of the oxygen octahedra. The substitution of foreign ions (e.g. Mg^{2+}, Co^{2+}, Ni^{2+}, Al^{3+}) in binary manganese based spinel systems also allows for decrease in the Jahn-Teller effect by the removal of Mn^{3+} ions from octahedral sites by solid state disproportionation. The high temperature allotropy of pure Mn_3O_4 has been studied extensively by Keller & Dieckmann (1985) who reported that the transition temperature was dependent on the defect structure. Empirical correlations are presented by Keller & Dieckmann from which the degree of non-stoichiometry, δ in $Mn_{3-\delta}O_4$, in both phases and the equilibrium line between the allotropes can be calculated. The oxygen partial pressure-temperature equilibrium line for the phase transition α-$Mn_{3-\delta}O_4 \Leftrightarrow \beta$-$Mn_{3-\delta}O_4$ can be obtained at high oxygen activity (viz., $aO_2 \geq a^*O_2$, where a^*O_2 is oxygen partial pressure for stoichiometric Mn_3O_4) from:

$$\log aO_2 = -3{,}8 + (T/1{,}613 - 871{,}5)^{0,5} \qquad (5)$$

and for low oxygen activity (viz. $aO_2 \leq a^*O_2$) from:

$$\log aO_2 = -0{,}881 + (T/4{,}102 - 340{,}5)^{0,5} \qquad (6)$$

where: T: Temperature in Kelvin

aO_2: Oxygen activity in atm at the α-$Mn_{3-\delta}O_4/\alpha$-$Mn_{3-\delta}O_4$ equilibrium

a^*O_2: Oxygen activity at which $Mn_{3-\delta}O_4$ is stoichiometric (δ=0)

Substituting values of aO_2=0,21atm into equation (5) and solving for the equilibrium temperature gives 1148°C which is lower than measured on the DTA curve i.e. 1172°C. Keller & Dieckmann noted that a number of investigators have reported temperatures close to 1170°C for the phase transition in air. Keller & Dieckmann discounted these investigations, as they did not recognise the defect structure of the high temperature phases of Mn_3O_4. The difference between these temperatures could also be due to the dynamic nature of the experiment that did not allow equilibrium conditions to be established at each temperature.

Keller & Dieckmann also present correlations to estimate the degree of non-stoichiometry in the high temperature phases of Mn_3O_4. These correlations have a mechanistic basis derived from ionic defect equilibria and it is shown that cationic vacancies and manganese interstitials respectively are the predominant defect species at high and low oxygen activities.

$$K_v(\alpha\text{-}Mn_{3-\delta}O_4)=-16350/T + 9,43 \quad (7)$$

$$K_I(\alpha\text{-}Mn_{3-\delta}O_4)=-19070/T + 6,72 \quad (8)$$

$$a^*O_2= aO_2(\delta=0)=(16\ K_I\ /K_v)^{0,75} \quad (9)$$

$$\delta=2(K_v\ K_I)^{0,5}\ \sinh((2/3)\ln(aO_2/a^*O_2)) \quad (10)$$

where: K_v: Equilibrium constant for cationic vacancies

K_I: Equilibrium constant for manganese interstitials

T: Temperature in Kelvin

δ: Degree of non-stoichiometry in $Mn_{3-\delta}O_4$

a^*O_2: Oxygen activity at which $Mn_{3-\delta}O_4$ is stoichiometric (δ=0)

Substituting T=1148°C and aO_2=0,21atm into equations (7) to (10) gives δ=0,00074. The oxygen activity and temperature at which Mn_3O_4 becomes stoichiometric is a^*O_2=0,002642atm and T=1135°C respectively. This degree of non-stoichiometry is lower than that expected for Mn_3O_4 prepared via low temperature (<300°C) processing techniques-Kaczmarek & Wolska (1993b). The non-stoichiometry of the TGA sample analysed above is calculated at δ=0,022 and 0,005 for the chemical and thermogravimetric analyses respectively, which confirms this observation. The work of Keller & Dieckmann cannot be applied further as their defect models only hold for small values of δ and they also do not explicitly quantify the effect of defect structure on the distribution of cations in lattice interstices. These authors point out that the distribution of cations in the tetrahedral and octahedral interstices was not known for temperatures above 25°C. The work of Kaczmarek & Wolska clearly attempts to redress this lack of understanding.

5.4.2 Conclusions

- The tetragonal-to-cubic phase transition α-$Mn_{3-\delta}O_4 \Leftrightarrow \beta$-$Mn_{3-\delta}O_4$ was observed by TGA at a temperature higher than reported in a definitive literature study of this phase transition, though it is recognised that the non-stoichiometry influences this phase transition. Low temperature hausmannite can be prepared with much wider range of non-stoichiometry and defect concentrations. *Ab initio* calculation of the defect composition of high temperature Mn_3O_4 is possible with small deviations (<0,05%) from stoichiometry being a characteristic of this system.

- Hydrothermally prepared Mn_3O_4 does not contain significant quantities of bound water as found in MnOOH type materials.

- Approximately 30% of the manganese contained in hydrothermally prepared Mn_3O_4 can be oxidised to Mn_2O_3. The reactivity of this material is attributed to a valence and cation distribution that is different to that in the normal hausmannite structure prepared by high temperature synthesis.

- The phase transformation of tetragonal to cubic $Mn_{3-\delta}O_4$ is accompanied by a redistribution of cations in the tetrahedral and octahedral sites in the lattice that upon cooling yields a non-reactive Mn_3O_4.

- The valence distribution among the manganese cations found experimentally can be explained by the model $Mn^{2+}Mn_3^{3+}O_4$. However it is possible that the chemical and TGA analyses could give ambiguous results. Additional analytical investigations are required to confirm the valence distribution of hydrothermal mangano-manganic oxide. These must recognise that the method of preparation has significant influence on this parameter.

5.4.3 Structural Modelling of Manganese Oxides

A two stage modelling procedure was used to estimate the defect composition and structure of hydrothermally prepared manganese oxide. First the theoretical intensities of a solid solution series between the limits of composition of Mn_3O_4 and γ-Mn_2O_3 were simulated using ideal lattice positions. Thereafter, Rietveld refinement was used to obtain the occupancies for the cations and vacancies that gave the best fit to the patterns for the above series of samples. These simulations will therefore determine the extent that the actual structure of hydrothermally prepared manganese oxide deviates from an ideal solid solution series between Mn_3O_4 and γ-Mn_2O_3.

Ideal solid solution series model

γ-Mn_2O_3 can be represented by a defect compositional formula as $Mn_{2,667}V_{0,333}O_4$, where V represents the cation vacancies. The charge distribution of the cations is dependent on the valence of the cations. For the purposes of this exercise it was assumed that no Mn^{4+} was in the solid solution series. This is generally accepted for Mn_3O_4 in the more modern literature, e.g. Driessens (1967) and Jarosch (1987) though Ardizzone *et al.* (1998) claim that all the higher oxidation state is 4+. The valence distribution for γ-Mn_2O_3 structures has however not been verified in the literature.

The distributions of vacancies in Mn_2O_3 take a number of forms:

$(Mn_1)_{tet}[Mn_{1,667}\ V_{0,333}]_{oct}O_4$	Vacancies all in octahedral sites
$(Mn_{0,833}\ V_{0,167})_{tet}[Mn_{1,833}\ V_{0,167}]_{oct}O_4$	Vacancies equally distributed in tetrahedral and octahedral sites
$(Mn_{0,667}\ V_{0,333})_{tet}[Mn_2]_{oct}O_4$	Vacancies all in tetrahedral sites

The change in manganese to oxygen ratio is the second degree of freedom that was taken into account in the model. This was allowed to vary in stages from $Mn_{2,67}O_4$ to $Mn_{2,83}O_4$ to Mn_3O_4. The Rietveld refinement program DBWS9411 of Young (1995) was used in pattern generation mode to determine the intensities of the reflections in an expected X-ray pattern. The O atoms were assumed to be in the ideal position (x, y, z: 0, 0,5, 0,25) with A at 0, 0,25, 0,875 and B at 0, 0,5, 0,5 in the space group $I4_1/amd$, cell edges a=5,6713 and c=9,4622.

A summary of results of the simulation for 7 ideal structural models is shown in Table M2 in the Appendices. These models are as follows.

Table 5.3 Schedule of ideal solid solution series models

Model	Formula	Type of Vacancy
1	$Mn_{2,67}O_4$	Octahedral vacancies only
2	$Mn_{2,67}O_4$	Tetrahedral vacancies only
3	$Mn_{2,67}O_4$	Tetrahedral + octahedral vacancies
4	$Mn_{2,83}O_4$	Octahedral vacancies only
5	$Mn_{2,83}O_4$	Tetrahedral vacancies only
6	$Mn_{2,83}O_4$	Tetrahedral + octahedral vacancies
7	Mn_3O_4	No vacancies

The peak intensities were normalised relative to the most intense $K\alpha_1$ peak [121]. Only the more intense peaks of the $K\alpha_1$ reflections are shown in comparison to the calcined and discharge samples.

A number of observations can be made with respect to Table M2:

- The reflections [101], [112], [200], [004] and [220] are sensitive to changes in the cation ratio and vacancy distribution. Adjustment of the ideal atomic positions is not expected to significantly alter the intensities of the reflections.

- There are differences in relative intensities for most of the peaks between the models this is greater than the error in reproducibility for an experimental pattern. This suggests that it should be possible to determine the defect distribution on this basis.

- By comparing the ratios of the [103] to [101] peaks for the discharge, calcined and JCPDS patterns it is evident that only Models 3 and 5, which assume vacancies in tetrahedral and octahedral positions, could approximate the experimental patterns. This is an anomaly as the latter two experimental patterns should resemble model 7 as a reference. In addition, the ratios of the other most intense peaks do not confirm this observation.

- There is no consistent peak overlap for any individual model with those in the experimental and JCPDS patterns. No information was available on the defect structure and composition of the material used to generate the JCPDS pattern. A reference basis of comparison can therefore not be established. The resolution of this problem therefore requires the inclusion of a XRD standard that has a well-defined stoichiometry and defect composition. This additional work could also test different valence distributions in these models.

Rietveld Refinement of Experimental Patterns

Structural refinement calculations were performed using DBWS9411 on the XRD patterns for the dried samples. The refinement procedure was adjusted to obtain the unit cell dimensions and site occupancies that gave the closest fit to the experimental curves. The results of these calculations are shown in the following tables. Table 5.4 lists the lattice parameters and occupancies for the experimental samples. Table 5.5 compares the relative intensities for the discharge sample as calculated and observed experimentally. The Mn_3O_4 pattern from the JCPDS database is included for reference.

Table 5.4 Structural parameters obtained from Rietveld refinement of XRD patterns

Sample	Occ-A	Occ-B	*a* (Å)	*c* (Å)	u	Rp	Rwp	S
0min	0,98	1,03	5,7610	9,462	1,0520	13,06	17,87	1,43
30min	0,98	1,02	5,7610	9,461	0,7051	10,59	15,5	1,23
60min	0,99	1,02	5,7620	9,461	0,6300	10,63	15,6	1,19
90min	0,98	1,01	5,7620	9,461	0,5310	9,88	15,4	1,14
120min	0,97	1,01	5,7620	9,463	0,6744	9,46	14,97	1,19
150min	0,98	1,01	5,7620	9,464	0,6988	9,56	14,92	1,17
165min	0,97	1,00	5,7620	9,463	0,7196	9,83	15,3	1,21
Discharge	0,92	0,90	5,7620	9,466	0,2503	15,89	21,93	1,57
Calcined	0,97	1,00	5,7620	9,465	0,7243	10,02	15,71	1,26

Occ-A/B: Fractional occupancy of tetrahedral and octahedral sites respectively

a, c: Unit cell dimensions Angstroms

u: Overall temperature factor

Rp, Rwp, S: Goodness of fit parameters % that give quantitative estimates of the accuracy of the refinement procedure. S should be less than 1,3.

Table 5.5 Comparison of predicted and observed relative intensities for calcined sample and JCPDS 24-734

hkl	JCPDS	Calc.	Obs.
101	30	22	26
112	40	38	42
200	17	16	16
103	85	75	78
211	100	100	100
202	20	13	15
004	20	19	22
220	20	22	22
105	25	26	25
312	10	10	9
303	8	8	8
321	25	33	28
224	50	57	52
400	20	21	19

The results of the refinement procedure can be summarised as follows:

- The difference in calculated and observed intensities is less than the experimental error suggesting that some confidence can be attributed to the accuracy of the refinement procedure.

- The *a* cell constant remained relatively constant while the *c* parameter increases marginally with increasing oxidation time. The unit cell volumes calculated from these parameters are similar to those obtained by least squares regression in Table 4.9 (V_0min 314 c.f. 313Å^3)

- The variation in *a* and *c* parameters shows a similar trend of increasing unit cell dimensions with increasing oxidation time as obtained from the least squares regression procedure. The variation in absolute values of *a* and *c* is however not as large.

- The occupancies calculated confirm that the defect structure includes tetrahedral vacancies though overfilling of the octahedral sites is also predicted. The overfilling of octahedral sites decreases with increasing extent of oxidation with the final discharge sample also showing octahedral vacancies. This theoretical modelling exercise described above is therefore validated to some extent.

- A large difference in relative intensities between the calcined sample and the JCPDS pattern is noted for reflections [101], [112], [103], [202] and [321]. This confirms the need for a standard Mn_3O_4 reference sample with a well-characterised chemical composition in terms of chemical impurities, valence of cations and defect composition.

Discussion of Solid State Modelling Analysis

All samples of reaction suspensions and products that have been dried in air reveal the characteristic pattern of the tetragonally distorted spinel, Mn_3O_4. The XRD patterns for both Type 1 and 3 Mn_3O_4 are identical in d-spacings with the relative intensities of the more intense peaks for Type 1 being generally weaker than for Type 3. The relative intensity of these peaks increases as oxidation progresses indicating some consolidation of the Type 3 structure. The fact that the completion of oxidation in the sample filtering and drying procedure does not result in identical structures for all materials means this oxidation mechanism is not the same as the oxidation mechanism occurring in the reactor. This confirms the findings that the changes in particle morphology also indicate different reaction oxidation mechanisms being present for these processes.

Investigations into the structural characteristics of synthetic hausmannite structures prepared at ambient and high (>900°C) temperature have been reported in the literature by Kazcmarek & Wolska (1993a,b). Kazcmarek & Wolska (1993a) investigated a number of anhydrous Mn_3O_4 materials prepared by thermal decomposition at high temperature (>900°C) where the Mn^{3+}/ Mn^{2+} ratio varied from 2,05 to 3,04. The variation in X-ray line intensity appeared to be proportional to the degree of oxidation of manganese. This work also predicted a different variation of the *c* lattice parameters with Mn^{3+}/ Mn^{2+} than found here (*vide infra* Figure 4.14). A number of defect structure models (see Table 5.6) with different arrangements of cation vacancies were tested to account for the variation in intensity ratio between certain reflections.

The prediction of the variation in ratios of intensities for I[101]/I[321], I[112]/I[321], I[224]/I[220] using the $I4_1/amd$ unit cell convention was best explained by models I and Ib which simply place all the cationic vacancies in the tetrahedral A-sublattice with the charge balanced by excess Mn^{3+} ions for low non-stoichiometry. This is equivalent to oxidation of Mn^{2+} in an A-sublattice position. At higher non-stoichiometry, $Mn^{3+}/Mn^{2+}>2,4$, the cationic vacancies enter octahedral positions, which is qualitative agreement with the findings of discussed above. The ratio of Mn^{3+} to Mn^{2+} for the Type 1 sample (reactor discharge) of this thesis is 1,96 based on chemical analysis and 2,08 based on TGA. The non-stoichiometry of this material is therefore similar to the lowest non-stoichiometry studied by Kazcmarek & Wolska (1993a). The other oxidation intermediates however span a similar range of manganese cation valences.

Table 5.6 Defect structure models tested by Kazcmarek & Wolska (1993a)

Type	A sublattice Occupancy	B sublattice Occupancy	Anionic Sublattice	Mn^{3+}/Mn^{2+}
I	$V_{Mn} + \Delta Mn^{3+}$	No defects	No defects	
Ia	$V_{Mn} + \Delta Mn^{3+}$ ΔMn^{3+}	No defects V_{Mn}	No defects No defects	<2,4 >2,4
Ib	$\frac{1}{2}V_{Mn}$	$\frac{1}{2}V_{Mn}$	No defects	>2,4
II	ΔMn^{3+}	V_{Mn}	No defects	
III	$\frac{1}{2}V_{Mn} + \Delta Mn^{3+}$	$\frac{1}{2}V_{Mn}$	No defects	
IV	$V_{Mn} + \Delta Mn^{3+}$	No defects	ΣO^{2-}/unit cell =31,5	
V	$\frac{1}{2}V_{Mn} + \Delta Mn^{3+}$	$\frac{1}{2}V_{Mn}$	ΣO^{2-}/unit cell =31,5	

V_{Mn}: Cationic vacancies

ΔMn^{3+}: Mn^{3+} ions in excess of stoichiometry

Kazcmarek & Wolska (1993b) also studied Mn_3O_4 synthesised at ambient temperature by precipitating $Mn(OH)_2$ from a $Mn(NO_3)_2$ solution with NaOH and then oxidising with air. These authors obtained hydrated products which included β-MnOOH with a minimum of ~7,5%OH^- (~5%H_2O) in the stoichiometry range 2,0< Mn^{3+}/Mn^{2+} <3,0. A defect structural modelling exercise similar to the above was presented incorporating the influence of OH groups in the structure and the authors discussed the results relative to a single phase formula for a non-stoichiometric hydrohausmannite. The *c* lattice parameter was shown to decrease with increasing vacancy content while the *a* lattice parameter remained relatively constant throughout. The authors claim that the Mn_3O_4 is a hydrated (hydroxylated) single phase in the stoichiometry range 2,0<Mn^{3+}/Mn^{2+}<3,0 and that β-MnOOH forms on prolonged oxidation. If the OH measured was present as β-MnOOH then it should be detected by XRD. This is in contradiction with the literature where Bricker (1965) and other authors, e.g. Murray *et al.* (1985) have refuted the existence of a hydrated hausmannite. β-MnOOH can only form as a metastable intermediate from $Mn(OH)_2$. This thesis confirms that the products of hydrothermal oxidation of manganous hydroxide are crystalline $Mn(OH)_2$ and anhydrous Mn_3O_4. The formation of hydrated phases from the prolonged oxidation of Mn_3O_4 was not tested experimentally.

Kazcmarek & Wolska (1993b) claim that the main difference in the XRD patterns for Mn_3O_4 prepared at ambient and high (>900°C) temperature is the absence of two additional lines at d-spacings of 2,45 and 1,83 Å for the high temperature sample. This is not confirmed in this work as both the Type 1 and 3 samples show these reflections.

The structural modelling analysis conducted for this thesis confirms the presence of tetrahedral and octahedral vacancies. However, discrepancies exist in the prediction of cell parameters. The resolution of these requires a well-characterised reference standard using additional measurements from other analytical techniques.

It is known that hausmannite made by high temperature calcining can have accommodation twins - Couderc *et al.* (1994). Twinning occurs parallel to the [112] plane in this material. The space group $I4_1/amd$ allows for the possibility of enantiomorphs by its inherent symmetry. This could be a further structural feature in some of the samples. Single crystal studies would be required to identify this feature in a solid state structure.

5.4.4 Conclusions

- Theoretical modelling of the structure of defect hausmannite was undertaken together with Rietveld refinement of experimental XRD patterns. Both these analyses showed that the defect structure of hydrothermally prepared materials consists of vacancies in tetrahedral and octahedral lattice sites.

- The absolute intensities of the predominant reflections in the XRD patterns could be used for analysing different defect distributions in the hausmannite structures.

- There is a different variation of the c lattice parameter with increasing Mn^{3+}/ Mn^{2+} for hydrothermally prepared hausmannite compared to materials synthesised by high temperature processing.

- A well characterised reference material is required to resolve some of the discrepancies that have been observed between the XRD and modelling and that reported in the literature by Kazcmarek & Wolska (1993a/b).

5.5 Summary of overall conclusions

The conclusions that can be made with respect to the kinetic investigations and solid phase characterisation reported and discussed in the preceding paragraphs can be summarised specifically for the hydrothermal oxidation conditions in this reaction system as follows:

- Manganous hydroxide particles are formed by homogeneous nucleation at high levels of supersaturation.

- The rate controlling mechanism for the hydrothermal oxidation of manganous hydroxide is oxygen diffusion in films surrounding the air bubbles. A creeping flow regime exists local to individual solid particles in the hydrothermal manganous hydroxide oxidation system. The small diameter (<10μm) of these particles makes them effectively neutrally buoyant. The flow regime in the liquid phase is turbulent with a mixing intensity that is capable of fully dispersing gas bubbles throughout the reactor. The impeller used in the experiments can accommodate a higher gas flow as the operating speed is far from the critical speed for flooding.

- Thermogravimetric analysis of wet oxidation intermediates shows only single-phase decomposition of manganous hydroxide. Metastable intermediates present due to Ostwald's principle are therefore not expected.

- XRD of freeze-dried intermediates show that oxidation produces a mixture of two or possibly three crystalline phases. Crystalline $Mn(OH)_2$ typical of the mineral pyrochroite is present initially and unhydrated Mn_3O_4 predominates towards the end of oxidation. No MnOOH phases were detected which is in contrast to ambient temperature studies. A crystalline phase was identified which has an XRD pattern that does not correspond to the manganese oxyhydroxide patterns catalogued on the

JCPDS databank. Further analytical work is required to confirm the presence of this phase as a hydrothermal oxidation intermediate and to determine its structure.

- The morphological change mechanisms in this system are complex. The shrinkage of compact crystallites due to chemical reaction is accompanied by a consolidation of the $D_v(0,5)$ of the aggregated particles to about 4,0μm with an increase in $D_v(0,1)$ and a decrease in $D_v(0,9)$ with increasing extent of oxidation. This is due to the formation of a second phase of smaller particles by a dissolution and precipitation mechanism. The smallest particles grow and may agglomerate with oxidised aggregates. The largest aggregates are broken down by a combination of chemical dissolution and the hydrodynamic action of the turbulent flow conditions. Structural change processes such as bridging, sintering and pore closure occur in parallel to the interparticle processes that reduce to macro and mesoporosity of the solid phase.

- A theoretical spheres-in-spheres model for the porous products of hydrothermal oxidation of manganous hydroxide was proposed to account for some of the experimental results and observations. More sophisticated material characterisation methods and particle morphology models are required to improve the characterisation of the products of hydrothermal oxidation of manganous hydroxide and the understanding of structural change mechanisms in this reaction system.

- Hydrothermally prepared Mn_3O_4 does not contain significant quantities of bound water as found in MnOOH type materials. Approximately 30% of the contained manganese in this material can be oxidised to Mn_2O_3 by heating in air. The reactivity of this material is attributed to a valence and cation distribution that is different to that in the normal hausmannite structure prepared by high temperature synthesis.

- The tetragonal-to-cubic phase transition α-$Mn_{3-\delta}O_4 \Leftrightarrow \beta$-$Mn_{3-\delta}O_4$ was observed by TGA at a temperature higher than reported in a definitive literature study of this phase transition, though it is recognised that the non-stoichiometry influences this phase transition. Low temperature hausmannite can be prepared with much wider range of non-stoichiometry and defect concentrations. *Ab initio* calculation of the defect composition of high temperature Mn_3O_4 is possible with small deviations (<0,05%) from stoichiometry being a characteristic of this system. The phase transformation of tetragonal to cubic $Mn_{3-\delta}O_4$ is accompanied by a redistribution of cations in the tetrahedral and octahedral sites in the lattice that upon cooling yields a non-reactive Mn_3O_4.

- Solid state structural modelling showed that the defect structure of hydrothermal oxidation intermediates can be represented by cationic vacancies in the tetrahedral

and octahedral lattice positions. A well-characterised reference standard is required to completely determine the defect and valence distribution of synthetic hausmannite and to resolve some of the discrepancies that have been observed between the XRD and modelling work reported in the literature by Kazcmarek & Wolska (1993a/b).

6 DENOUEMENT

A fundamental investigation was undertaken into the equilibria, kinetics and mechanisms of the hydrothermal dissolution and oxidation of manganese metal that included characterisation of the morphology and solid state structures of the products of these reactions. The investigation included experimental testwork on a pilot scale reactor that was supported by theoretical modelling of equilibria, kinetics, morphology and solid state structures. There are a number of major contributions that this investigation makes to the field of science. These are that dissolution and oxidation reaction rate data is reported for the first time at elevated temperature and pressure conditions for manganese. Although the dissolution of manganese metal favours the formation of hydroxide precipitates at the surface of the metal, a daughter phase of aggregated crystalline manganous hydroxide particles is formed in the bulk solution. The dissolution reaction is rapid with a high activation energy that is controlled by a chemical reaction at the surface of the metal. The rate of the oxidation reaction under the experimental conditions reported was controlled by rate of oxygen mass transfer through the gas-liquid interface. The morphological transformations occurring during the oxidation of manganous hydroxide are complex and include a dissolution precipitation mechanism that again forms a daughter phase of particles. Finally, the solid products formed have unique chemical and physical characteristics.

The hydrothermal dissolution and oxidation reactions can be represented by the overall equations:

$$Mn_{(s)} + 2H_2O_{(l)} = Mn(OH)_{2(s)} + H_{2(g)}$$

$$6Mn(OH)_{2(s/aq)} + O_{2(g)} = 2Mn_3O_{4(s)} + 6H_2O_{(l)}$$

The gas phase oxidation and reduction equilibria of the oxides of manganese reported in the literature indicate that the stable phases of manganese for the conditions of the experiments are MnO_2 in the presence of oxygen and MnO in the presence of hydrogen. Other oxide phases formed under these conditions will thus be metastable and their rate of conversion will be dependent on kinetic considerations. The domains of stability of the different manganese oxides were also calculated for three phase systems. Solution equilibrium modelling was conducted using literature data for the hydrolysis equilibrium constants of Mn^{2+} which showed that this ion is sparing soluble in complexing reagent free systems. The dominant soluble species expected at ambient temperatures were shown to be the Mn^{2+} hexaquo ion, $Mn(OH)_2^0$ and $MnOH^+$. At elevated temperatures the

domain of stability for $Mn(OH)_2^0$ is reduced and Mn^{2+} and $MnOH^+$ become the predominant soluble species.

Eh-pH-type diagrams were constructed for the elevated temperatures of the hydrothermal experiments using data available in the literature. Previous work available in the literature ignored the influence of hydrolysed ions that extend the domains of stability of manganous hydroxide into lower pH regimes. This was updated using $Mn(OH)_2$ solubility information available in the literature. Equilibrium data based on MnO predicts a reduced domain of stability at low temperature for $Mn(OH)_2$ in comparison to the method proposed in this thesis. The onset of $Mn(OH)_2$ precipitation at ambient temperature therefore occurs over a wider pH range than predicted in the literature. The onset of precipitation of $Mn(OH)_2$ at elevated temperature as reported in the literature was however confirmed. The values of the $Mn(OH)_2$ saturation pH at elevated temperature as predicted by modelling were confirmed by measurements made during experiments. The domain's of stability of $Mn(OH)_2$ and Mn_3O_4 reduce significantly in low ionic strength solutions and elevated temperature. A domain of processing conditions for the production of predominantly Mn_3O_4 was however predicted and confirmed by the solid state characterisation work.

It was found from the literature survey and equilibrium modelling that active dissolution of manganese metal is theoretically possible at high pH. This process is facilitated by solubility and speciation considerations at elevated temperature. The domain of stability of the dimanganite ion increases at higher temperature and in low ionic strength solutions. This presence of this ion and the reduced solubility of $Mn(OH)_2^0$ reduces the potential for precipitation of hydroxides on the corroding metal surface that could block the dissolution reaction. Different theoretical mechanisms of manganese dissolution all predict that the highest probability for manganous hydroxide precipitation will occur on the surface of the metal particle. Complete active dissolution of manganese metal under hydrothermal conditions was however found to occur in the experiments.

The kinetics and mechanisms of dissolution of manganese metal particles in water at elevated temperature and pressure were investigated. The testwork and analysis included review of a literature study, analysis of results from isothermal testwork at normal boiling points and analysis of non-isothermal dissolution rate data obtained in the temperature range 120 to 180°C.

Non-isothermal reaction rates were extracted from gas venting rate data obtained form two differently sized reactors. A unique experimental procedure was devised so that the hydrothermal dissolution experiments could be conducted under controlled temperature and pressure conditions. This allowed for the investigation of the effect of hydrogen

partial pressure on reaction kinetics. No significant effects of hydrogen partial pressure could be found on kinetics or particle morphology. Mathematical modelling of the non-isothermal reaction kinetics with polydisperse particles using matrix methods was able to simulate gas evolution and particle shrinkage kinetics. The rate of metal dissolution was found to be controlled by chemical reaction at the surface of the metal particles with an average activation energy of 172kJ/mol. Dissolution under these conditions is accompanied by high levels of $Mn(OH)_2$ supersaturation. The hydroxide precipitate formed from under these conditions was porous and highly agglomerated or aggregated which is indicative of homogeneous nucleation and precipitation reactions occurring in series with metal dissolution.

The oxidation of precipitated $Mn(OH)_2$ by air to Mn_3O_4 was found to follow linear kinetics. Solid phase characterisation analytical methods were developed to obtain conversion rate data that was validated by oxygen measurements in the gas phase. A mathematical model was developed to estimate the parameters that define mixing, sedimentation, dispersion, hydrodynamic and mass transfer operating regimes for a three-phase mechanically agitated reactor. A conceptual slurry structure was proposed to quantify the relative interfacial areas of the three phase reacting system. This model was used to confirm that the rate controlling mechanism during the oxidation of $Mn(OH)_2$ is mass transfer of oxygen through the gas-liquid interface.

The morphological change mechanisms in the hydrothermal oxidation reaction system were found to be complex. The shrinkage of compact crystallites due to chemical reaction is accompanied by a consolidation of the $D_v(0,5)$ of the aggregated particles to about 4,0μm with an increase in $D_v(0,1)$ and a decrease in $D_v(0,9)$ with increasing extent of oxidation. This is due to the formation of a second phase of smaller particles by a dissolution and precipitation mechanism. The smallest particles grow and may agglomerate with oxidised aggregates. The largest aggregates are broken down by a combination of chemical dissolution and the hydrodynamic action of the turbulent flow conditions. Structural change processes such as bridging, sintering and pore closure occur in parallel to the interparticle processes that reduce to macro and mesoporosity of the solid phase. The variation of the specific surface area of oxidation intermediates during oxidation of manganous hydroxide showed this parameter is affected by the dissolution and precipitation mechanism. A spheres-in-spheres model was used to characterise the particle morphology of hydrothermal oxidation products and explain the results of the morphology characterisation measurements.

The hydrothermally prepared Mn_3O_4 did not contain significant quantities of bound water as found in MnOOH type materials. Approximately 30% of the contained manganese in this material could be oxidised to Mn_2O_3 by heating in air. The reactivity of this material is

attributed to a valence and cation distribution that is different to that in the normal hausmannite structure prepared by high temperature synthesis.

The tetragonal-to-cubic phase transition α-$Mn_{3-\delta}O_4 \Leftrightarrow \beta$-$Mn_{3-\delta}O_4$ was observed by TGA at a temperature higher than reported in a definitive literature study of this phase transition. This was attributed to the influence of defect structure on this phase transition. Low temperature hausmannite could be prepared with a relatively wide range of non-stoichiometry and defect concentrations using the hydrothermal synthesis techniques.

Solid state structural modelling showed that the defect structure of hydrothermal oxidation intermediates can be represented by cationic vacancies in the tetrahedral and octahedral lattice positions. Further work and a well-characterised reference standard is required to completely describe the defect and valence distribution of synthetic hausmannite and to resolve some of the discrepancies that have been observed between this work and that reported in the literature. Hausmannite structured manganese oxides prepared by hydrothermal synthesis from manganese metal are characterised by low impurity levels and therefore provide useful precursors for special applications in materials science.

6.1 RECOMMENDATIONS FOR FUTURE RESEARCH

A number of opportunities have been identified for further research. These include the following:

- Measurements are required of Mn^{2+} hydrolysis constants and solubility data for $Mn(OH)_2$ at elevated temperature.

- Equilibrium diagrams need to be drawn that map the defect domains of the lower oxides of manganese and their coprecipitated variations.

- Impedance electrochemical analysis on a Mn electrode in low conductivity solutions can be used to determine electrokinetic parameters under hydrothermal dissolution conditions.

- Specific studies are required of simultaneous mass transfer in the ventilated gas cavities on impeller turbine blades and in the jetting zone adjacent to the point of entry of high velocity spargers. Validated methods need to be developed for predicting variations in mass transfer rates in the different hydrodynamic zones of two and three phase reactors.

- The usefulness of the solution structure, cell mass transfer model and virtual mass transfer analysis concepts need to be validated in other reaction systems.

- Confirming the defect structures of hausmannite that have different reactivities towards the uptake of oxygen at elevated temperature. A well characterised reference material for synthetic high purity hausmannite needs to be prepared.

- Detailed morphological analyses and modelling is required of the aggregate structure of porous mangano-manganic oxide.

Appendix A

Point of zero charge measurements on manganese oxide particles

The pH at which zero surface charge exists on the surface of a manganese oxide was measured using a Malvern Zetasizer 2C. This instrument measures the zeta potential of a sample using an electrophoretic principle. Samples of dry manganese oxide were added directly to the sample chamber containing in dilute sodium perchlorate (0,005M) that had been deaerated with nitrogen. pH adjustments were affected by adding perchloric acid or caustic soda. Figure A1 below shows repeat measurements made on a typical Mn_3O_4 material produced by hydrothermal oxidation of manganese metal. In Figure A2 the same sample is compared to other commercially available mangano-manganic oxides.

Figure A1 Zeta potential plots for hydrothermally produced mangano-manganic oxide

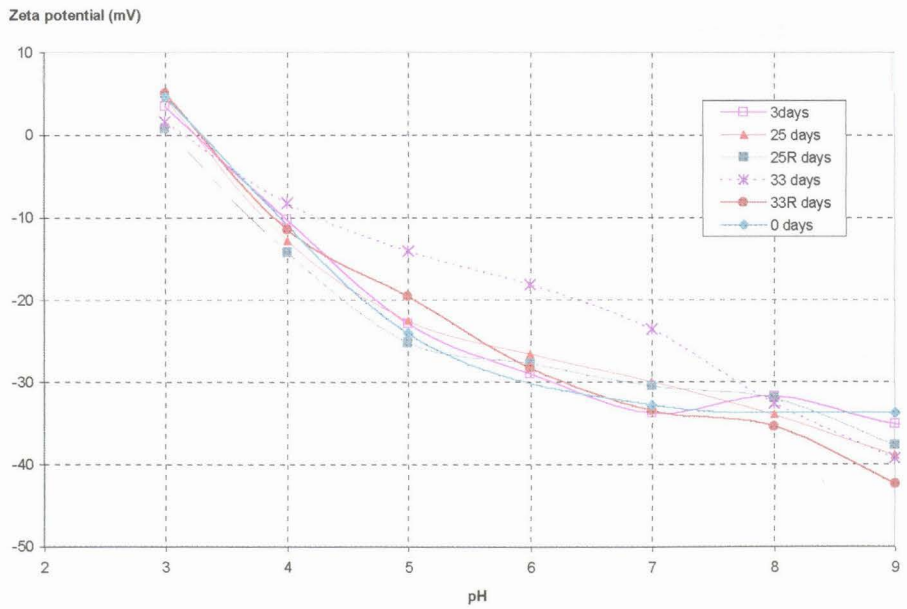

The scans show that the variability of readings generally increases in the pH range 4 to 8. The average pH of zero point charge, (pH_{pzc}) of the different readings is 3,22 with a standard deviation of 0,19. The exact cause for the variability in the higher pH ranges was not determined.

Samples of Mn_3O_4-type manganese oxides produced by different suppliers are compared to the above sample in Figure A2. The average pH_{pzc} of these is 3,25 with a standard deviation of 0,08. Samples 2 and 3 were produced by an elevated temperature process using manganese metal as a starting material. Sample 4 is produced via a chemical

precipitation process and gaseous reduction of the precipitate. The exact processing conditions for the manufacture of these samples is however not known.

Figure A2 Zeta potential plots for different mangano-manganic oxides

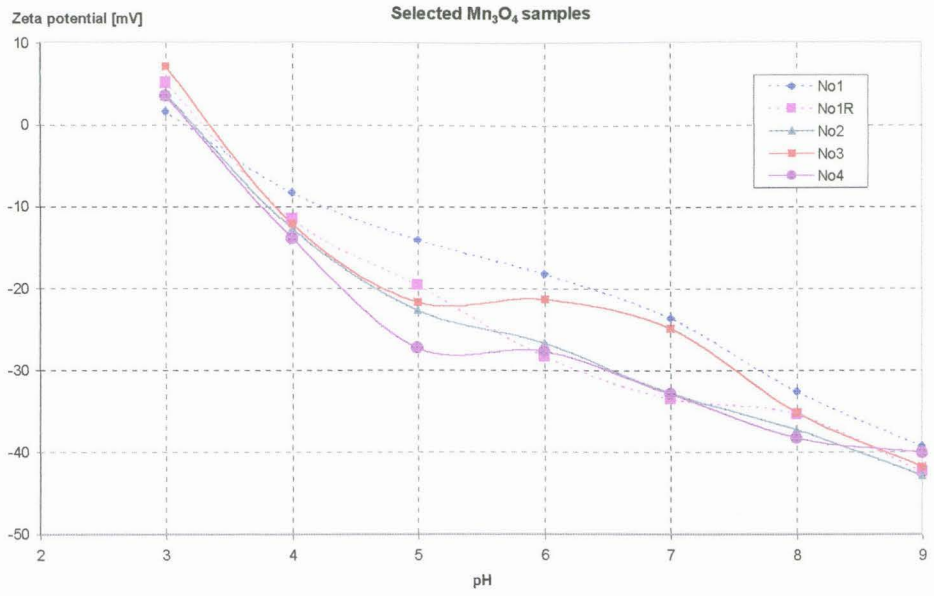

(**No1& 1R**: Hydrothermal oxidation of Mn; **No2**:Brownox; **No3**:Fermac, **No4**:SedemaHP)

Appendix B

Structural Parameters for Manganese and its Oxides

Chemical Formula	Mineral	Crystal System	Unit cell Type	Unit Cell Parameters					Unit Cell
				a Å	b Å	c Å			
α-MnO_2	Synthetic	Tetragonal		9,88		2,843	z=8		
"α-MnO_2"	Hollandite	Monoclinic		10,03	5,76	9,9	z=2	β=90°	
β-MnO_2	Pyrolusite	Tetragonal	Rutile (tP6)	4,38		2,86	z=2		Mn_2O_4
β-MnO_2	Ramsdellite	Orthorhombic	Diaspore	4,533	9,27	2,866	z=4		
"δ-MnO_2"	Birnessite	Hexagonal	Sheetlike						
γ-MnO_2	Nsutite	Hex./Ortho	Pyro+Rams	9,65		4,43	z=12		
γ-MnO_2	Nsutite	Orthorhombic	Ramsdellite	4,43	9,36	2,85			
ε-MnO_2	EMD/CMD								
ρ-MnO_2									
λ-MnO_2		Cubic	Spinel	8,029					
Mn_5O_8	Synthetic	Tetragonal	Dist. Spinel	5,823		9,55			
Mn_5O_8	Synthetic	Monoclinic		10,347	5,725	4,852		β=109	
α-MnOOH	Groutite	Orthorhombic	Diaspore	4,58	10,76	2,89	z=4		
β-MnOOH	Feitknechtite	Hexagonal	Sheetlike	3,32	4,71		z=1		
γ-MnOOH	Manganite	Monoclinic	Dist.Rutile	8,86	5,24	5,7		β=90°	$Mn_8O_8(OH)_8$
α-Mn_2O_3	c-Bixbyite Partridgeite	BCC	ThO_2 (iA3)	9,401			z=16		$Mn_{32}O_{48}$
Mn_2O_3	o-Bixbyite	Orthorhombic		9,4157	9,423	9,4047			
c-Mn_2O_3	Synthetic	Rhombohedral	Corundum	5,04		14,12			
γ-Mn_2O_3	Synthetic	Tetragonal	Dist.Spinel	5,78		9,33			
$Mn(OH)_2$	Pyrochroite	Hexagonal	Brucite (hP3)	3,34		4,68			$Mn(OH)_2$
α-Mn_3O_4	Hausmannite	Tetragonal	Dist.Spinel	5,76		9,44			$Mn_8Mn_{16}O_{32}$
β-Mn_3O_4	High temp	Cubic	Spinel	8,42			z=8		
o-Mn_3O_4	High pressure	Orthorhombic	Marokite (oP6)	5,801	6,356	9,742	z=4		
MnO	Manganosite	FCC	NaCl	4,436					Mn_4O_4
α-Mn	Manganese	BCC	Mn, chi (cI58)	8,894					58Mn
β-Mn	Manganese	Cubic	Mn (cP20)	6,289			z=20		20Mn
γ-Mn	Manganese	FC Tetragonal	Cu (cF4)	3,776		3,553			4Mn
δ-Mn	Manganese	BCC	W (cI2)	3,075					2Mn

Ref. JCPDS database

APPENDIX C

Estimation of the Variation of Mn^{2+} Hydrolysis Equilibria and Water Ionisation with Temperature

Water Ionisation Product

Data for the ionisation product of water was obtained from Weast (1982).

Temperature (°C)	- log K_w
25	13,995
50	13,725
75	12,712
100	12,265
150	11,638
200	11,289

An empirical formula fitted to the above data for the variation of the ionisation product with temperature is given by:

$$- \text{Log } K_w = 5{,}99 + 2414\ (1/T) \qquad (1)$$

where T is in Kelvin

The concentration of H^+ or OH^- ions can be obtained from the equation:

$$K_w = (H^+)\ (OH^-) \qquad (2)$$

Solubility Product of $Mn(OH)_2$

The following data was obtained from published literature,

Temperature (°C)	Log K_{sp}	Reference
18	-13,4	Weast(1982)
25	-12,7	Pourbaix(1974)

where $K_{sp}=[OH^-]^2[Mn^{2+}]$ (3)

In addition, Rodrigues (1983) presented unpublished data by Bryson,

Temperature (°C)	Ln K_s'
12	-37,07
36	-36,75
40	-36,33
44	-35,92
48	-35,51

where $K_s' = K_w^2/K_{sp}$ (4)

Converting Rodrigues' data to Ksp values using the variation in water ionisation product as defined in equation (1) gives

Temperature (°C)	K_w	Log K_{sp}
32	1,25E-14	-11,70
36	1,58E-14	-11,64
40	2,00E-14	-11,62
44	2,51E-14	-11,60
48	3,09E-14	-11,60

The above data sets were fitted to the equation:

$$- \text{Log } K_{sp} = (474/T + 1,974)^2 \quad (5)$$

Equation (5) predicts the solubility product relative to the above data within an inaccuracy of (2-3%) which serves to define the order of magnitude effect of the temperature variation of K_{sp}.

The ability of this equation to predict the solubility of the manganous hydroxide in the temperature region above 50°C needs to be verified by experimentation.

The solubility equilibrium may be represented on a plot of pH at saturation versus temperature as shown in Figure C1.

Figure C1 Variation of solubility product of $Mn(OH)_2$ with temperature

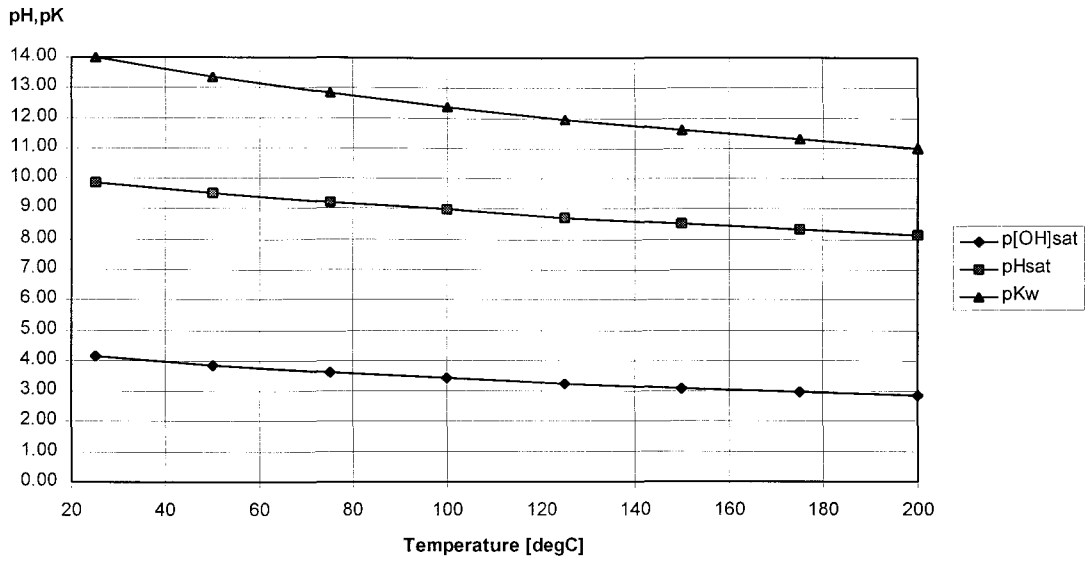

The pH measured at temperature can be seen to decrease with rising temperature from pH 10 at 20°C to pH 8 at 200°C indicating an increase in solubility of manganous hydroxide. The increase in ionisation product of water with temperature is also plotted in the above figure.

First Hydrolysis Constant of Manganous Ion

The first hydrolysis constant (K_1) of Mn^{2+} is given by the reaction:

$$Mn^{2+} + H_2O = MnOH^+ + H^+ \qquad (6)$$

with the equation for K_1 being defined by

$$K_1 = \frac{(MnOH^+)(H^+)}{(Mn^{2+})} \qquad (7)$$

Data on the variation of K_1 with temperature is given in Gmelins (1973) and is summarised in the table below.

Temperature (°C)	- log K_1
15	10,93
20	10,76
25	10,5 - 10,59
30	10,38 - 10,6
36	10,19
42	10,10
100	9,54

This data was fitted to the equation:

$$- \log K_1 = (275/T + 2{,}326)^2 \qquad (8)$$

The empirical variation of water density with temperature has a similar quadratic form over the temperature range 25 to 200°C. Water density data was taken from Naumov *et al.* (1974) for fitting empirical parameters to the equation:

$$-\log \rho = (1{,}18+0{,}121T)^2 \times 10^{-4} \qquad (9)$$

Higher Hydrolysis Constants

Baes & Mesmer (1976) have estimated the second and higher hydrolysis products for Mn^{2+}. An experimental study on the variation of these products with temperature could not be found in the literature. MacDonald (1976) uses the Criss Cobble correspondence principal for estimating the free energy of formation of relevant ions which can then be related to the equilibrium constants for the hydrolysis reactions via the equation:

$$\dot{U}G_f^\circ = -RT \ln K \qquad (10)$$

MacDonald presents a table that gives the variation of $\dot{U}G_f^\circ$ with temperature for a number of temperatures. This data can be fitted to equations of the form:

$$\dot{U}G_f^\circ = a + BT + CT^2 + dT^3 \qquad (11)$$

to ease computational effort in subsequent calculations. The solubility of the higher hydrolysis constants is expected to make a small contribution to total Mn^{2+} solubility and excluding the temperature variation from calculations therefore will not have a major influence on major solubility trends.

Appendix D

Chemical and physical analyses of manganese metal

A sample of the metal used for the reactor testwork was screened into three size fractions with the mass ratios given in Table D1. The chemical analyses were conducted on LECO CS200 (carbon & sulphur) and LECO EF400 (nitrogen & oxygen) analysers. These instruments were subject to statistical quality assurance procedures through the use of internal and reference standards.

Table D1 Screening and chemical analysis of metal

Mesh	Size	Mass %	Cum %	S%	C%	O%	N%	Total
+325	+45µm	19.9	19.9	0.06	0.011	0.75	0.014	0.84
-325+400	+37µm	11.4	31.3	0.10	0.015	1.17	0.016	1.30
-400	-37µm	68.7	100	0.10	0.009	1.17	0.017	1.30
	Total	100		0.095	0.010	1.09	0.016	

Each size fraction was examined using a Cambridge Instruments S360 digital scanning-electron microscope with an integrated Oxford Instruments ISIS energy-dispersive spectroscopy (EDS) system. Magnification ranges from 6x to approximately. 300 000x were possible. An accelerating voltage of 20kV was used. The image analyser used was a Quantimet Q570, also supplied by Cambridge Instruments.

The sample preparation consisted of preparing polished sections of each size fraction. These were prepared by mixing about 5g (obtained by rotary splitting) of each sample with an almost equivalent amount of cold-setting resin in a pill vial and allowing the mixture to cure. The result was a cylinder of resin & powder that was sectioned along its longest diameter (i.e. parallel to the direction of expected segregation of the metal particles). The sections are then mounted for diamond polishing on a semi-automatic polishing machine. The polished sections were subsequently carbon coated under vacuum for the SEM investigation.

Samples of typical images are included below. These were digitally generated using the ISIS software of the EDS system on the SEM and exported to MS PowerPoint©. The presence of oxygen in layers on the metal particles was confirmed by analysis with the EDS detector. The proportions of metal and oxide phase present were obtained using the image analyser at two different grey scale settings. Particle size distributions of the metal and oxide phases were also obtained for each phase with results given in Tables D2 and D3. The total metal and oxide proportions for each sample were also obtained on a volumetric basis and corrected to mass proportions assuming that the oxide phase consists of Mn_3O_4 (Table D4). The total oxide content of the original sample was

calculated using sample proportions given by the screening analysis results. These results are given in Table D4.

Table D2 Metal phase particle size distribution (Volume%)

SIZE RANGE (micron)	-400#	+400#	+325#
<10	33.9	9.8	0.1
10 - 25	60.6	58.2	3.1
25 - 38	5.5	30.0	7.4
38 - 53		2.0	10.5
53 - 75			14.7
75 - 106			19.6
106 - 150			17.2
150 - 212			15.2
212 - 300			9.7
300 - 425			2.5
	100.0	100.00	100.0

Table D3 Metal oxide phase particle size distribution (Volume%)

SIZE RANGE (micron)	-400#	+400#	+325#
<2	16.3	11.8	3.1
2 - 3	17.4	8.9	2.9
3- 5	25.4	15.3	5.9
5 - 7	21.8	21.9	11.2
7 - 9	9.1	19.5	14.5
9 - 13	5.7	10.3	19.2
13 - 19	4.3	10.3	19.7
19 - 26	0	0	9.8
26 - 38	0	0	13.7
	100	98	100

Table D4 Relative proportions of metal and metal oxide phases (Mass%)

Masses %	-400#	+400#	+325#	Total
Metal	79.8	78.6	90.8	82.0
Oxidised Metal	20.2	21.4	9.2	18.0
	100.0	100.0	100.0	100.0

Shape factors for the polished section images were obtained using the software supplied by the manufacturer. Frequency distributions of the shape factors for the metal and oxide phases for each sample are given in Table D5. Figure D1 is a plot of the shape factor frequency distributions for the metal and oxide phases in the –400# sample. The image analysis system was not capable of assigning particle size, shape and oxide content to individual particles simultaneously.

Table D5 Shape factor distributions for polished sections

Shape Factor	-400#		+400#		+325#	
	Metal	Oxide	Metal	Oxide	Metal	Oxide
1.0 - 1.7	38.1	17.9	34.7	6.0	40.7	8.8
1.7 - 2.4	30.7	31.2	24.0	13.5	23.3	15.8
2.4 - 3.1	13.8	18.8	14.3	14.0	11.5	22.8
3.1 - 3.8	6.9	6.4	8.2	9.5	7.6	9.6
3.8 - 4.5	4.6	7.8	5.7	13.5	4.5	7.9
4.5 - 5.2	2.4	5.0	3.8	5.5	3.7	2.6
5.2 - 5.9	1.2	4.6	2.7	7.5	1.6	8.8
5.9 - 6.6	1.0	1.8	1.6	3.5	1.7	6.1
6.6 - 7.3	0.4	2.3	1.2	5.0	1.3	2.6
7.3 - 8.0	0.3	0.0	0.7	3.5	0.9	3.5
8.0 - 8.7	0.2	0.9	0.8	3.5	0.8	1.8
8.7 - 9.4	0.1	0.9	0.5	5.0	0.7	1.8
9.4 - 10.1	0.1	0.5	0.6	1.0	0.2	1.8
10.1 - 10.8	0.1	0.5	0.0	1.5	0.3	1.8
10.8 - 11.5	0.0	0.9	0.4	1.0	0.3	1.8
11.5 - 12.2	0.0	0.0	0.1	2.5	0.2	1.8
12.2 - 12.9	0.1	0.0	0.2	0.5	0.5	0.0
12.9 - 13.6	0.1	0.5	0.3	2.5	0.1	0.0
13.6 - 14.3	0.0	0.0	0.1	1.0	0.0	0.9
14.3 - 15.0	0.0	0.0	0.2	0	0.2	0.0
Mean	2.29	3.15	2.72	5.11	2.62	4.33
Sdev	1.24	1.98	1.91	3.10	1.96	2.76
Median	1.95	2.43	2.07	4.16	1.93	3.29

Figure D1 –400# Sample shape factor frequency distributions

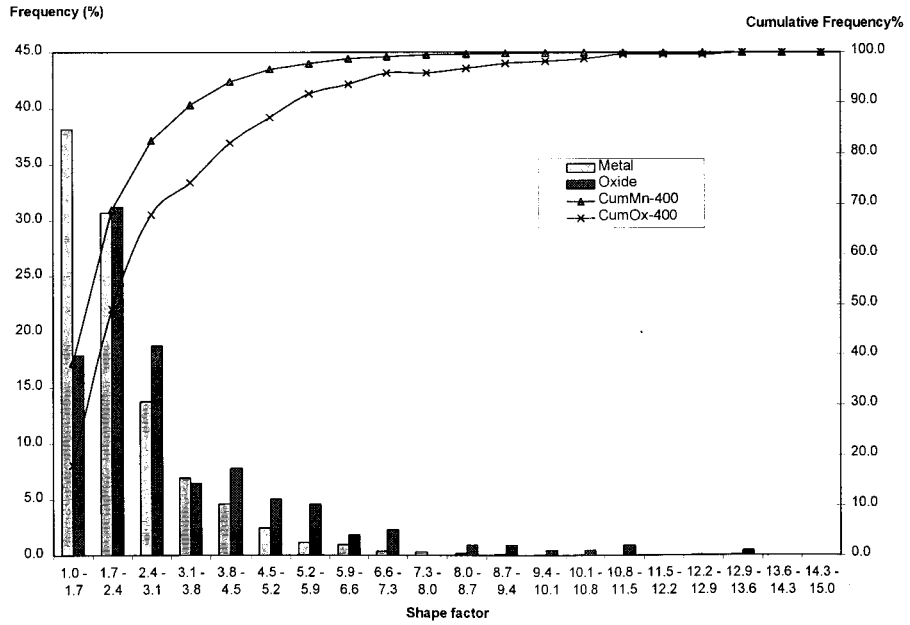

Figure D2a Digital SEM images of Mn metal.

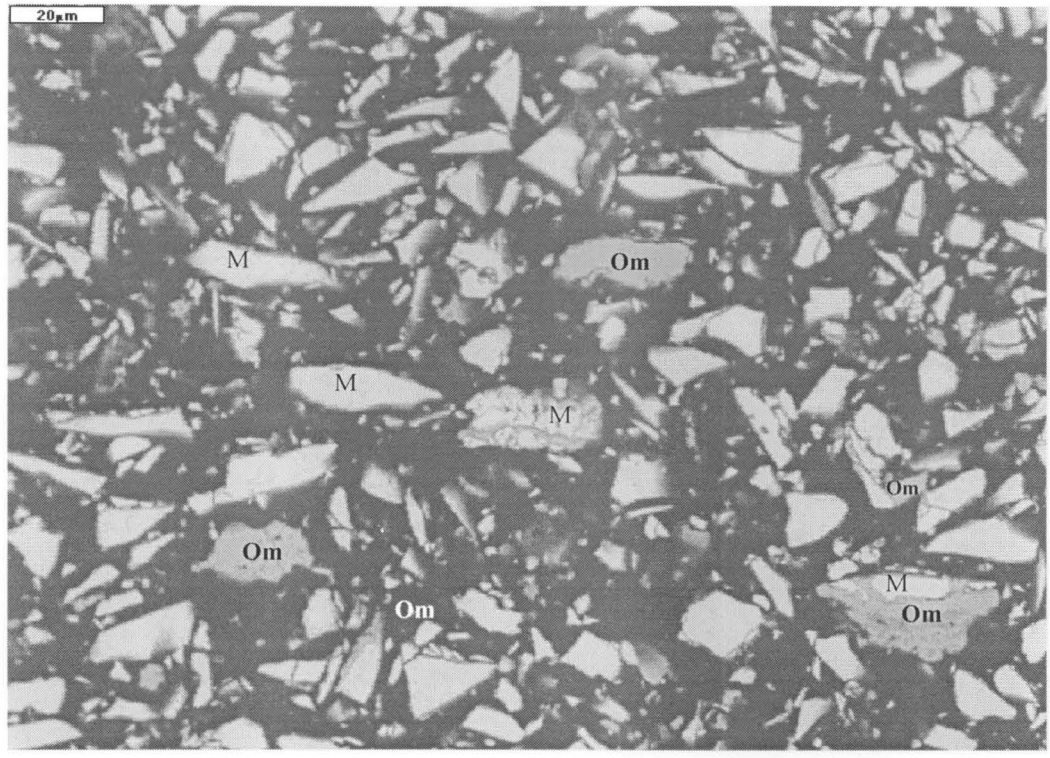

-400# (M=metal ; Om=oxidised metal)

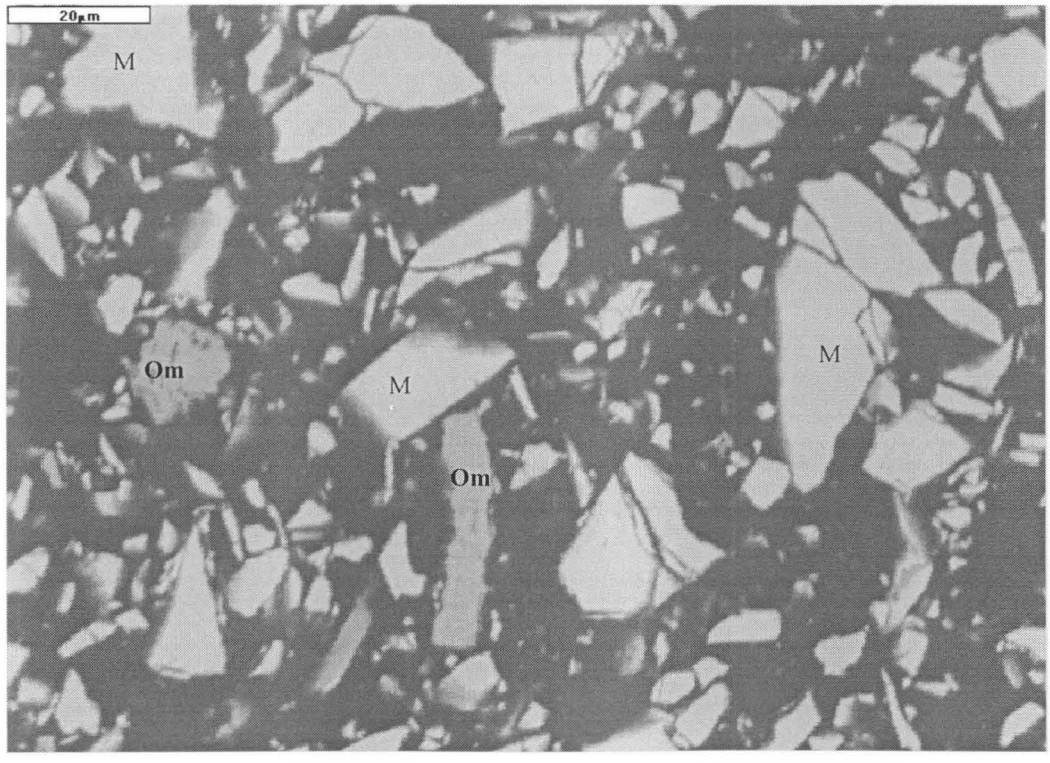

-400# (M=metal ; Om=oxidised metal)

Figure D2b Digital SEM images of Mn metal

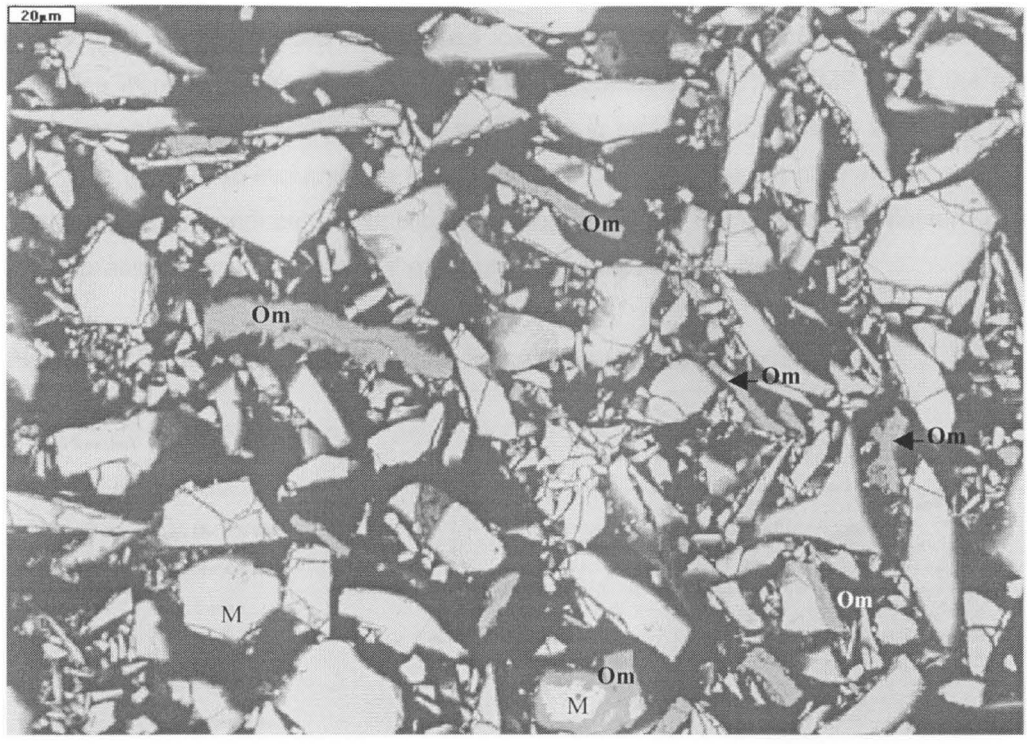

+400# (M=metal ; Om=oxidised metal)

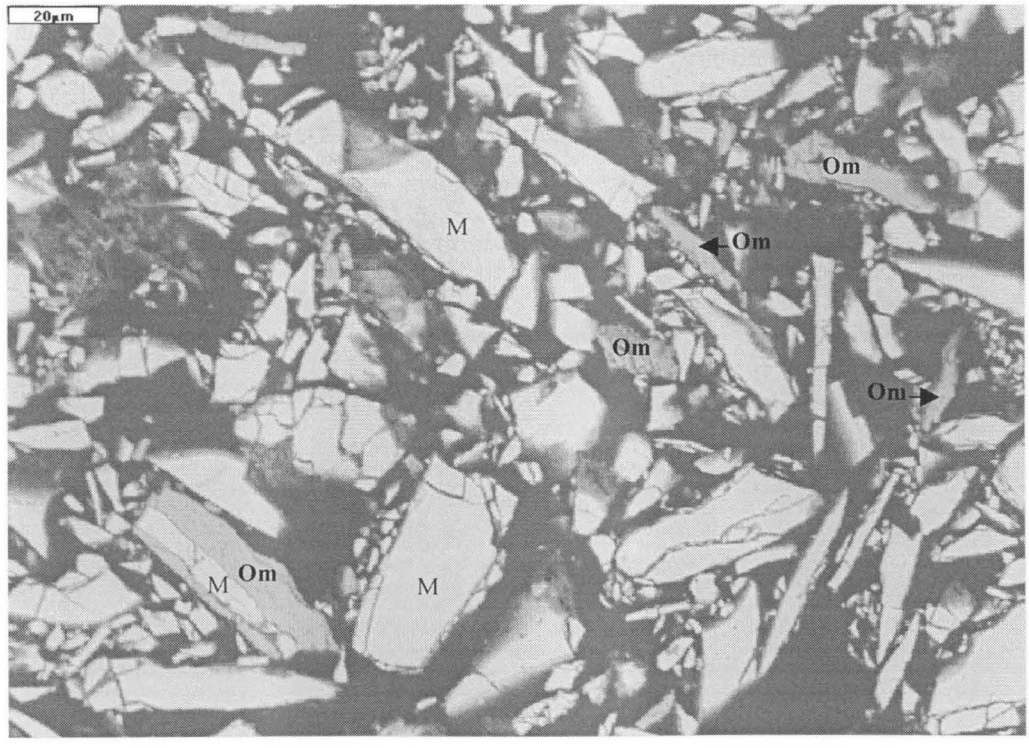

+400# (M=metal ; Om=oxidised metal)

Particle size measurements were obtained from a Malvern Mastersizer® S using procedures developed for manganese oxide samples as described in Appendix K. Samples were analysed in demineralised water containing 0,3% SHMP under the action of ultrasound. These analyses were performed in triplicate with results shown in Figure D3. This figure also includes the frequency distribution of one set of analyses and check analysis results conducted in duplicate by screening the samples. The Malvern results are expressed in volume % with the screening results in mass %.

Figure D3 Particle size distributions for metal samples

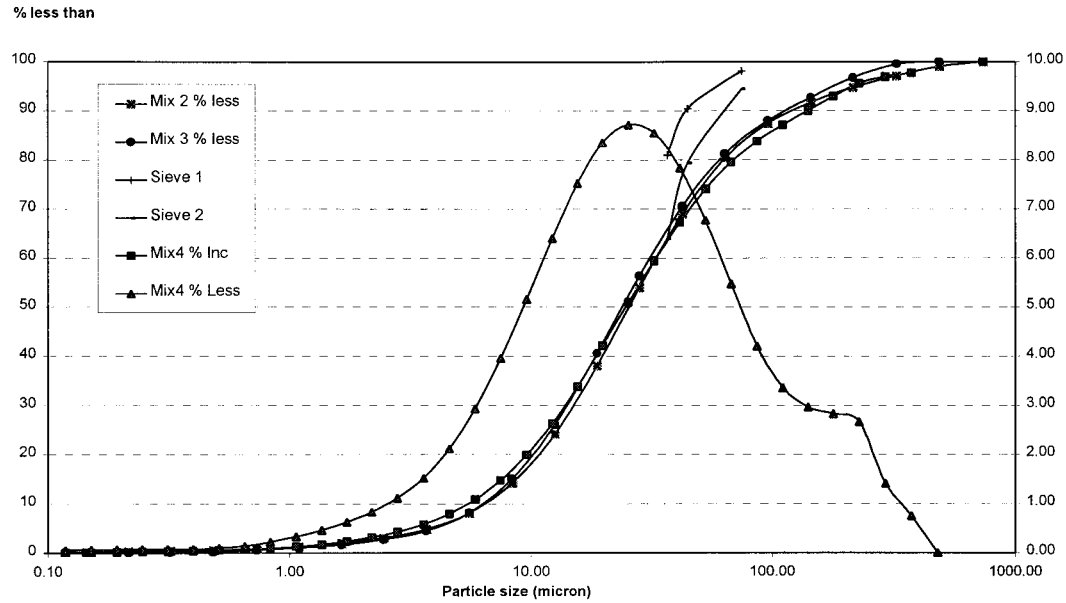

Note: Sieve results in mass%
Mix 2,3,4 in volume%

Figure D4 SEM images of sample taken during early stage of dissolution at low and high magnification

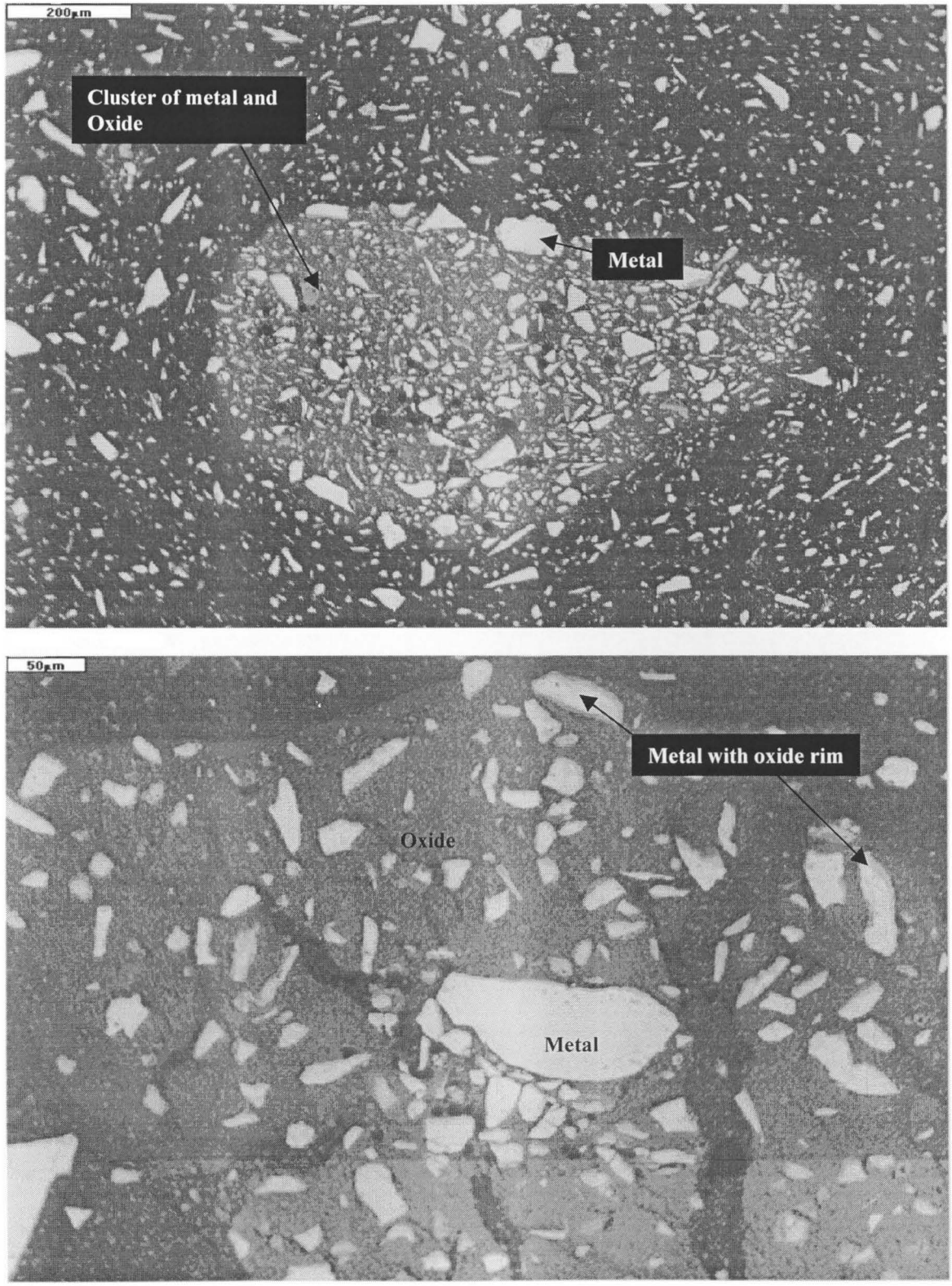

Figure D5 SEM images of sample taken during late stage of dissolution at low and high magnification

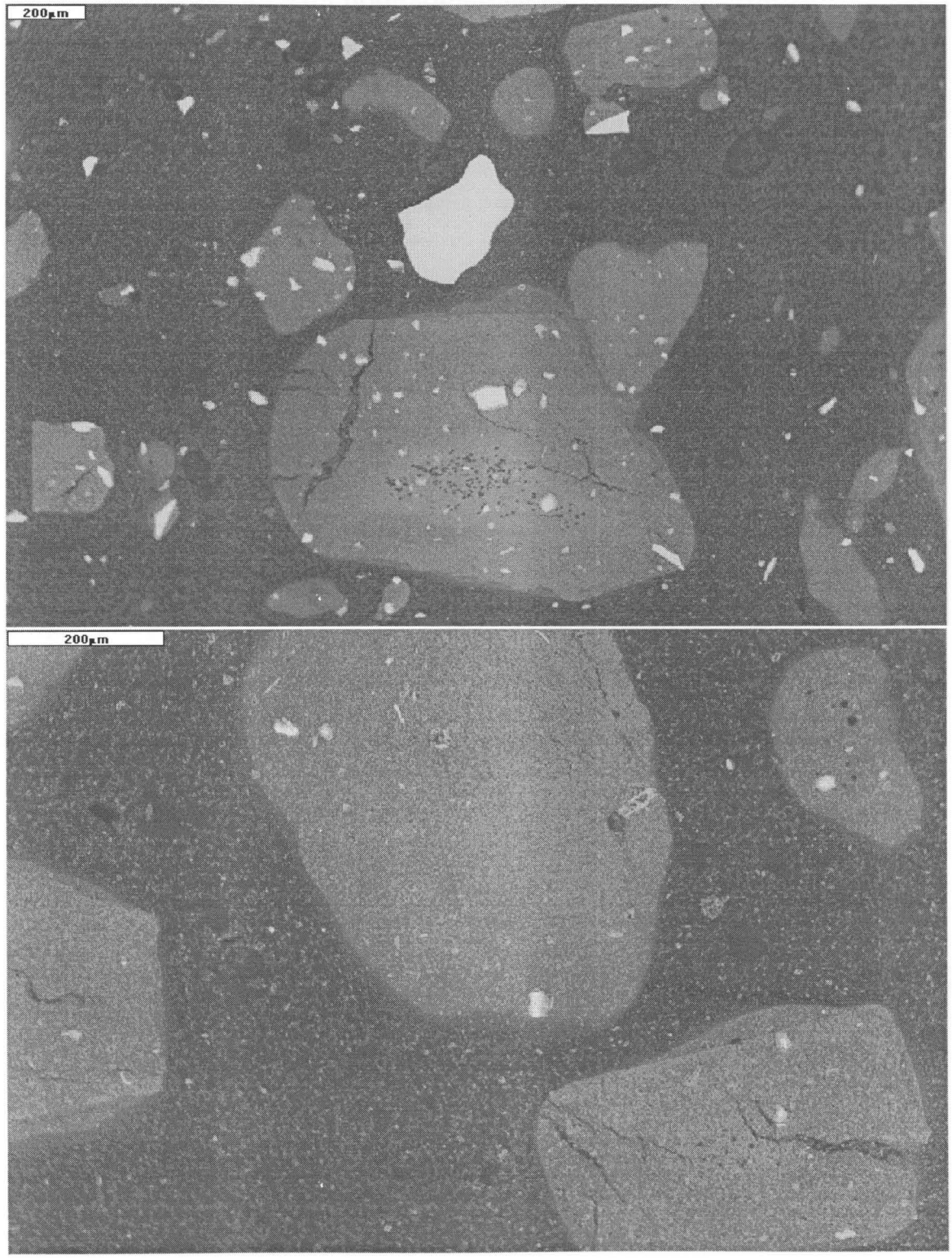

Appendix E

Results and calculations for non-isothermal dissolution experiments

Figure E1 Slurry temperature and total reactor pressure measurements pH_2*600kPa

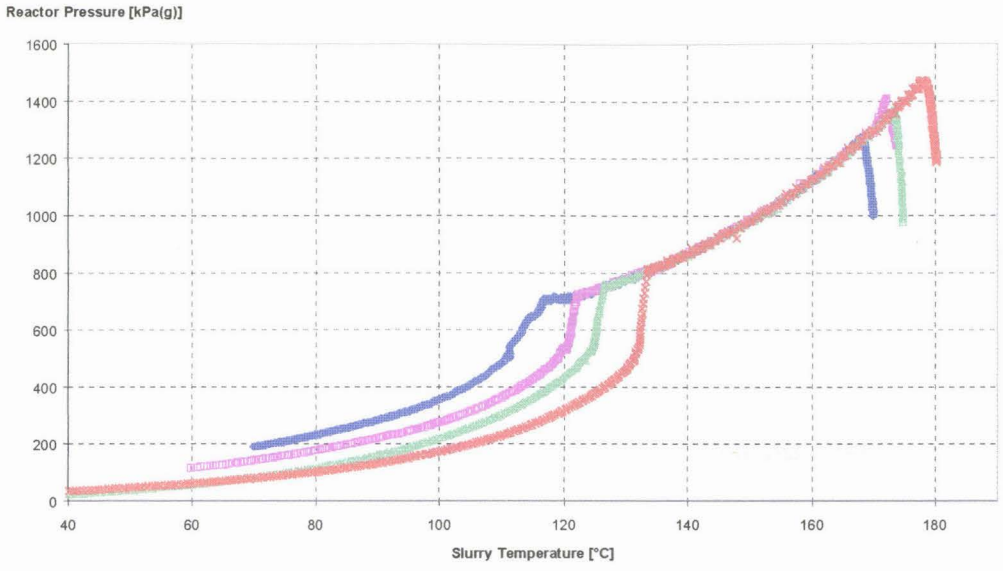

Figure E2 Slurry temperature and total reactor pressure measurements pH_2*800kPa

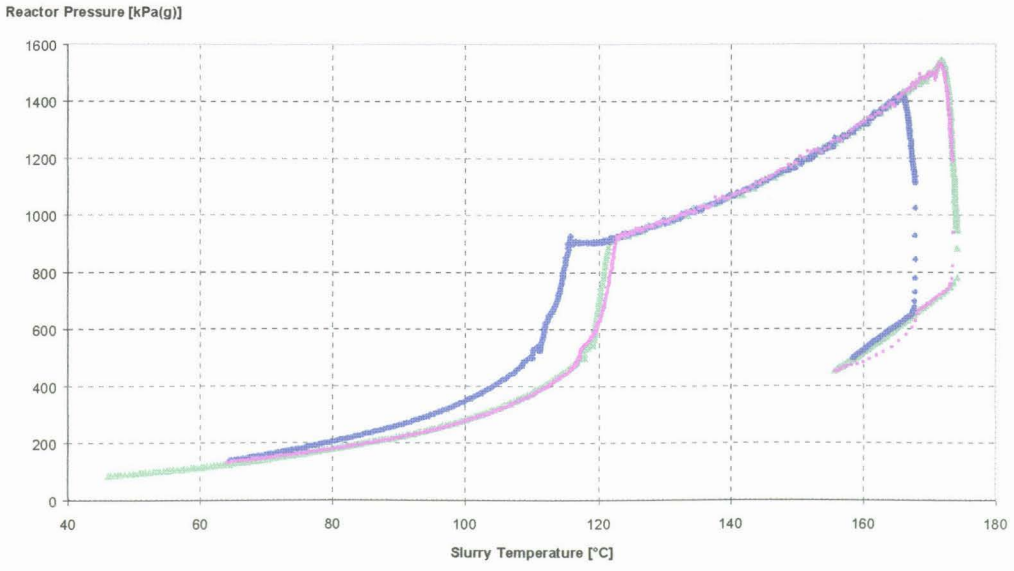

Figure E3 Slurry temperature & total reactor pressure measurements pH_2*600kPa

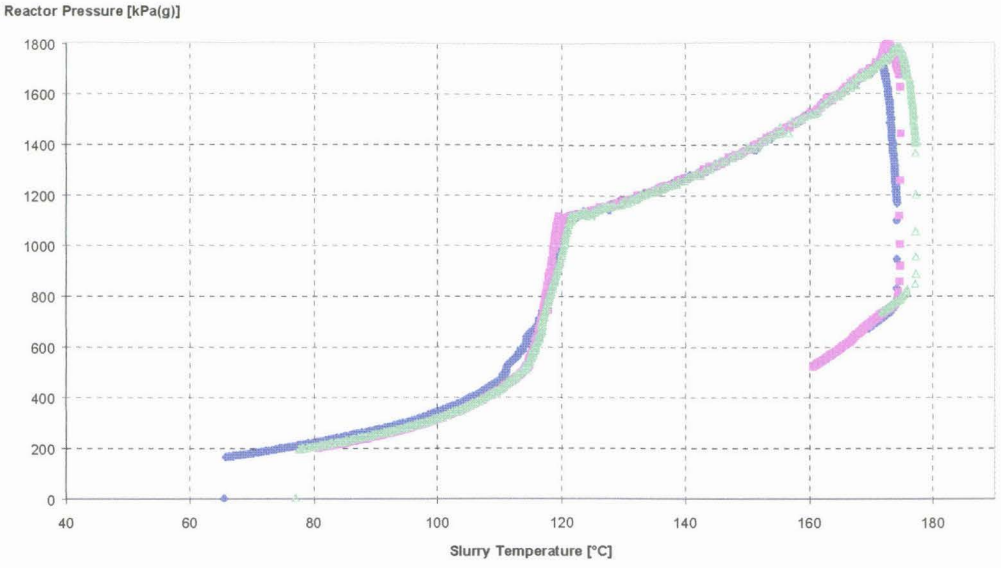

Figure E4 Conversion temperature plots for all experiments conducted at pH_2* 800kPa

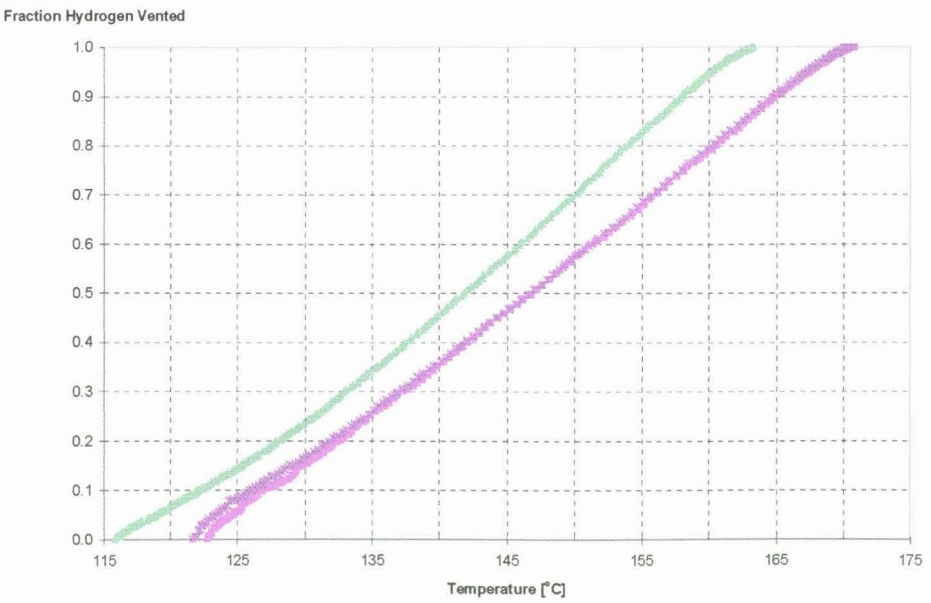

Figure E5 Conversion temperature plots for all experiments conducted at pH_2* 600kPa

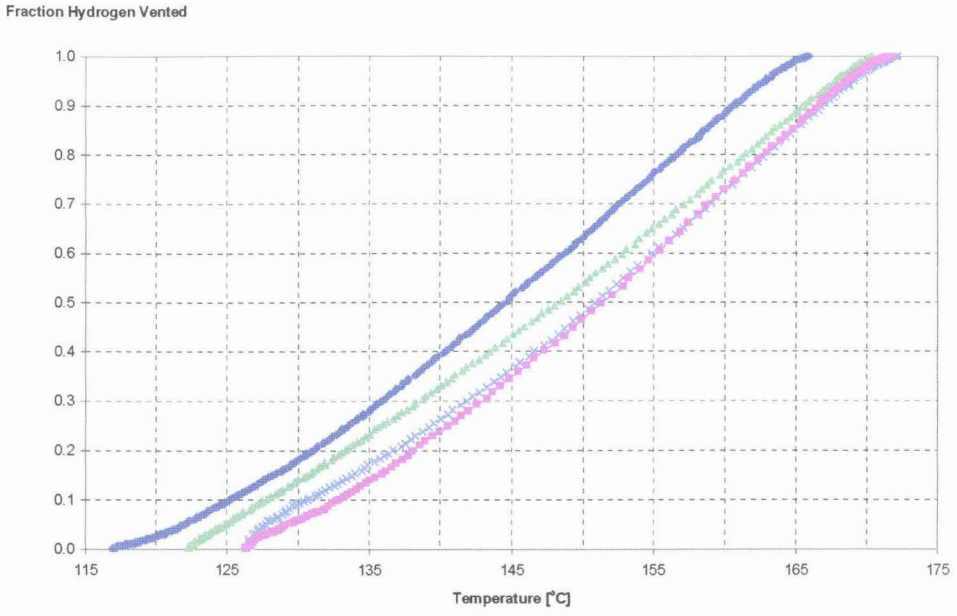

Figure E6 Contour plot of experimental PSD's made on hydrolysis samples at pH_2* 600kPa (Repeated)

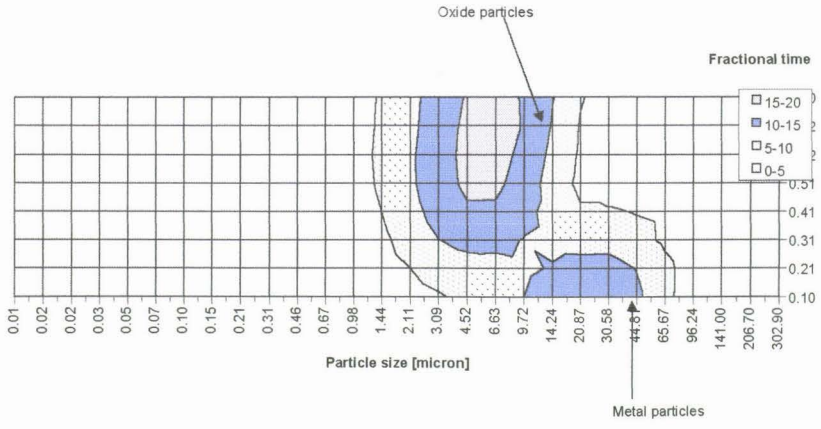

Figure E7 Contour plot of experimental PSD's made on hydrolysis samples at pH_2* 800kPa

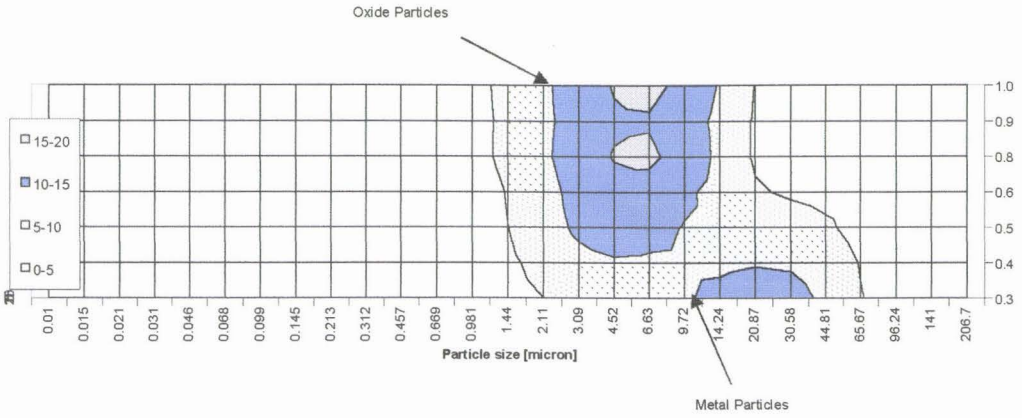

Figure E8 Arrhenius plot for three pH_2* 600kPa experiments

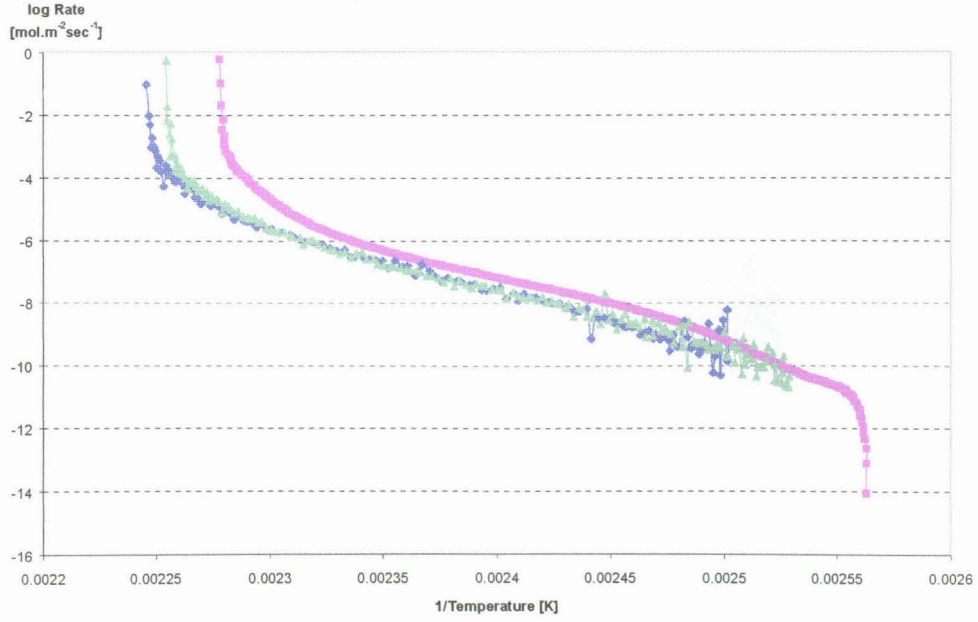

Figure E9 Arrhenius plot for three pH_2* 1000kPa experiments

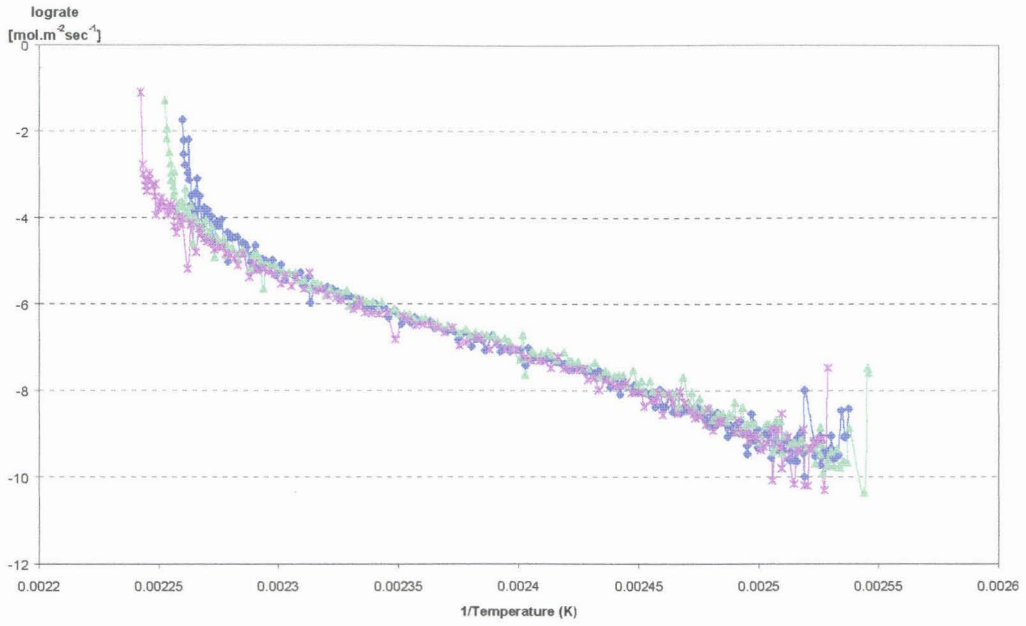

Figure E10 Arrhenius plot for data combined from all experiments

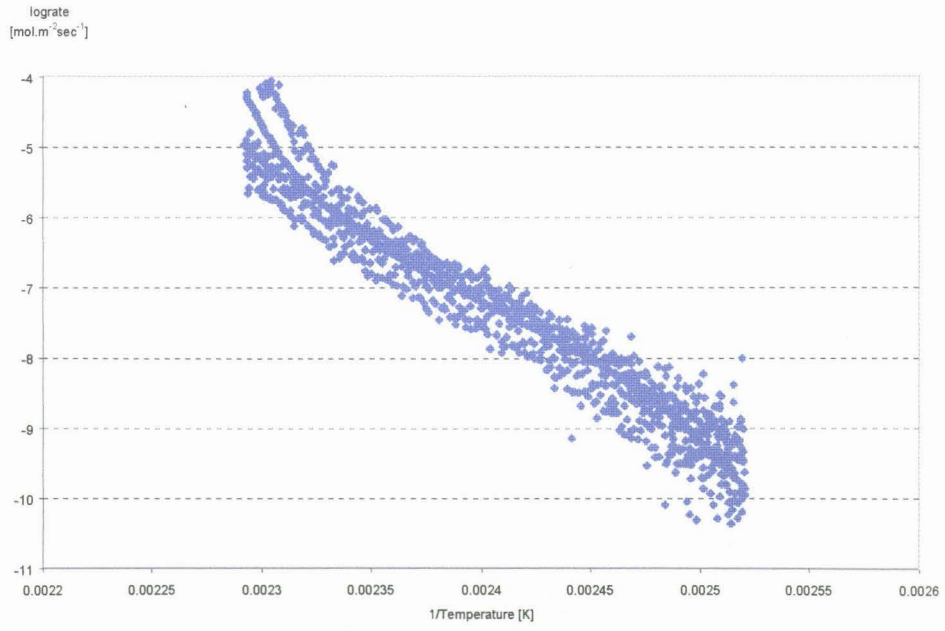

Appendix F

Spreadsheet for Calculating Oxidation and Reduction Equilibria of the Common Manganese Oxides

Manganese Oxide Dissociation Equilibria

1800 degK

	G_o	S_o	S_{abs}	H_T-H_{298}	S_t	G_t
	kcal/mol	cal/moldeg	cal/moldeg	cal/mol	cal/moldeg	kcal/mol
Temp C	25	25	25	1526.8	1526.8	1526.8
H2	0.0	31.2		11054.2	13.0	-59.1
O2	0.0	49.0		12216.5	14.2	-86.9
H20	-56.7	16.7		27077.5	32.4	-113.0
Mn	0.0	7.7		13782.1	15.1	-24.9
MnO	-86.7	14.3		19495.3	22.4	-129.0
Mn(OH)2	-143.0	23.7		46572.8	54.8	-230.7
Mn3O4	-306.7	37.2		68454.1	77.3	-433.3
Mn2O3	-210.6	26.4		49438.8	55.3	-300.3
MnO2	-111.2	12.7		27688.6	31.4	-159.0

Dissociation Equilibria

Reaction	Reactants		Products			dGt	-Log pO2 dGt / 2.3RT	pO2 [atm]	pH2O [atm]
1	4 MnO2	=	2 Mn2O3	1 O2		-51.36	-6.24	1.73E+06	
2	6 Mn2O3	=	4 Mn3O4	1 O2		-18.17	-2.21	1.61E+02	
3	2 Mn3O4	=	6 MnO	1 O2		5.69	0.69	2.03E-01	
4	2 MnO	=	1 Mn	1 O2		146.23	17.76	1.72E-18	
5	1 Mn(OH)2	=	1 MnO		1 H2O	-11.35	-1.38		4.18E-02

Allah Mahs Data

	1	2	3	4
Temp K	dGo[kcal]	dGo[kcal]	dGo[kcal]	dGo[kcal]
298.15	25.6	35.5	91.35	173.45
298.15	25.6	35.5	91.35	173.45
400	20.35	32.05	84.8	169.9
500	15.25	28.6	78.35	166.4
500	15.25	28.6	78.35	166.4
600	10.2	25.25	72	162.9
700	5.2	21.95	65.5	159.6
800	0.25	18.6	59.15	156.2
900	-4.75	15.5	52.8	152.75
1000	-9.7	12.4	46.55	149.3
1100		9.4	40.3	145.8
1200		6.6	34	142.3
1300		3.95	27.8	138.7
1400		1.15	21.6	135.2
1500		-2.25	15.85	131.55
1600			10.55	127.5
1700			5.4	123.25
1800			0.15	119.05

MacDonald data

	1	2	3	4	5		MacDonald data log pO2	
	dGo[kcal]	dGo[kcal]	dGo[kcal]	dGo[kcal]	dGo[kcal]	Temp [C]	1000/T[K] R1	R2
	23.5	36.8	93.0	173.5	-113.4	25	3.35	-17.25
	23.5	36.8	93.0	173.5	-113.4	25	3.35	-17.25
	18.3	32.7	86.8	170.7	-105.7	127	2.50	-10.01
	13.2	28.7	80.8	168.3	-98.5	227	2.00	-5.78
	13.2	28.7	80.8	168.3	-98.5	227	2.00	-5.78
	8.2	24.6	74.8	166.0	-91.6	327	1.67	-2.97
	3.1	20.7	68.8	163.8	-84.9	427	1.43	-0.98
	-1.8	16.7	62.8	161.8	-78.5	527	1.25	0.50
	-6.8	12.9	56.9	159.9	-72.2	627	1.11	1.65
	-11.7	9.2	51.0	158.1	-66.1	727	1.00	2.56
		5.5	45.1	156.4	-60.1	827	0.91	
		1.9	39.3	154.7	-54.3	927	0.83	
		-1.7	33.6	153.2	-48.5	1027	0.77	
		-5.1	27.9	151.7	-42.8	1127	0.71	
		-8.5	22.2	150.2	-37.2	1227	0.67	
			16.7	148.8	-31.7	1327	0.63	
			11.1	147.5	-26.3	1427	0.59	
			5.7	146.2	-21.0	1527	0.56	

Reduction Equilibria Temp 1526.8 degC

Reaction	Reactants			=	Products		dGo
1	2 MnO2		1 H2	=	1 Mn2O3	1 H2Ol	-36.16
2	3 Mn2O3		1 H2	=	2 Mn3O4	1 H2Ol	-19.57
3	1 Mn3O4		1 H2	=	3 MnO	1 H2Ol	-7.64
4	1 MnO		1 H2	=	1 Mn	1 H2Ol	50.17
5	1 O2		2 H2	=		2 H2Ol	-20.97

Allah Mah's Data (Gas Phase)

	1	2	3	4
Temp K	dGo[kcal]	dGo[kcal]	dGo[kcal]	dGo[kcal]
298.15	-41.85	-36.9	-8.95	32.1
298.15	-41.85	-36.9	-8.95	32.1
400	-43.35	-37.5	-11.15	31.4
500	-44.75	-38.05	-13.2	30.85
500	-44.75	-38.05	-13.2	30.85
600	-46.05	-38.55	-15.2	30.3
700	-47.35	-38.95	-17.15	29.85
800	-48.55	-39.35	-19.1	29.45
900	-49.75	-39.6	-20.95	29
1000	-50.9	-39.85	-22.8	28.6
1100		-40	-24.6	28.15

MacDonalds Data (Liquid Phase)

	1	2	3	4	5	log pH2		
	dGo[kcal]	dGo[kcal]	dGo[kcal]	dGo[kcal]	dGo[kcal]	1000/T[K] R1	R2	R3
	-44.9	-38.3	-10.2	30.1	-113.4	3.35	-30.69	-27.06
	-44.9	-38.3	-10.2	30.1	-113.4	3.35	-30.69	-27.06
	-43.7	-36.5	-9.4	32.1	-105.7	2.50	-23.70	-20.50
	-42.6	-34.9	-8.8	33.9	-98.5	2.00	-19.57	-16.64
	-42.6	-34.9	-8.8	33.9	-98.5	2.00	-19.57	-16.64
	-41.7	-33.5	-8.4	35.6	-91.6	1.67	-16.78	-14.05
	-40.9	-32.1	-8.1	37.2	-84.9	1.43	-14.79	-12.17
	-40.2	-30.9	-7.9	38.7	-78.5	1.25	-13.27	-10.76
	-39.5	-29.7	-7.7	40.2	-72.2	1.11	-12.09	-9.62
	-38.9	-28.5	-7.6	41.5	-66.1	1.00	-11.13	-8.71
		-27.3	-7.5	42.8	-60.1	0.91		-7.95

APPENDIX G

Spreadsheet for Calculating Simplified Pourbaix Diagrams

Simplified Pourbaix Diagram Plotting Working Spreadsheet

Summary of a and b Regression Formulae

	a		b	
	Intercept	Slope	Intercept	Slope
Cations	-39.57114	0.13270	1.50950	-0.00170
Anions and OH	51.70788	-0.17340	1.00000	0.00000
Oxyanions	112.51086	-0.37730	-0.96812	0.00660
Acid oxyanions	119.87640	-0.40200	-2.33984	0.01120

Quadratic Curve fit of McDonald data

	a (x2)	b (x)	c
H+	-5E-05	0.038923	-6.7312
Mn2+	-9E-05	0.082184	-70.93375
MnOH+	-7E-05	0.053867	-106.213
HMnO2=	1E-04	-0.085648	-106.1366
MnO4-	5E-05	-0.077732	-87.75747
MnO4=	1E-04	-0.094194	-102.2111
Mn3+	-1E-04	1.78E-01	-6E+01

	G_o	S_o	S_{abs}	H_t-H_{298}	S_t	G_t
	kcal/mol	cal/moldeg	cal/moldeg	cal/mol	cal/moldeg	kcal/mol
Temp C	25	25	25	125	125	125
H+	0.0	0.0	-5.0		9.1	0.1
H2	0.0	31.2		689.3	2.0	-3.2
O2	0.0	49.0		717.1	2.1	-5.0
H20	-56.7	16.7		1803.0	5.2	-58.6
Mn	0.0	7.7		656.5	1.9	-0.9
MnO	-86.7	14.3		1104.4	3.2	-88.3
Mn(OH)2	-143.0	23.7		2907.4	8.4	-145.8
Mn3O4	-306.7	37.2		3655.5	10.6	-311.0
Mn2O3	-210.6	26.4		2492.8	7.2	-213.6
MnO2	-111.2	12.7		1418.2	4.1	-112.7
Mn2+	-54.5	-27.6	-37.6		-18.0	-52.6
Mn(OH)+	-96.8	-9.0	-14.0		1.6	-96.6
HMnO2-	-121.2	15.0	10.0		-19.0	-121.6
MnO4-	-106.9	50.7	45.7		38.1	-111.5
MnO4=	-119.7	24.0	14.0		-14.5	-120.8
Mn3+	-19.6	-90.5	-105.5		-74.6	-11.9

Et

Reaction	Reactants						Products				dGt 2.3RT	-dG z
1	1 Mn2+			1 H2O		=	1 MnOH+	1 H+			8.06	
3	1 MnOH+			1 H2O		=	1 HMnO2-	2 H+			18.56	
4	1 Mn(OH)2	2 H+				=	1 Mn2+		2 H2O		-13.27	
5	1 Mn(OH)2	1 H+				=	1 MnOH+		1 H2O		-5.21	
6	1 Mn(OH)2			1 H2O		=	1 HMnO2-	1 H+	1 H2O		13.35	
7	1 Mn3O4	8 H+			2 e-	=	3 Mn2+		4 H2O			1.70
8	1 Mn3O4	5 H+			2 e-	=	3 MnOH+		1 H2O			0.74
9	1 Mn3O4	-1 H+			2 e-	=	3 HMnO2-		-2 H2O			-1.45
10	1 Mn2O3	6 H+			2 e-	=	2 Mn2+		3 H2O			1.39
13	1 MnO2	4 H+			2 e-	=	1 Mn2+		2 H2O			1.17
19	1 Mn(OH)2	2 H+			2 e-	=	1 Mn		2 H2O			-0.67
20	1 Mn3O4	2 H+			2 e-	=	3 Mn(OH)2		-2 H2O			0.13
21	3 Mn2O3	2 H+			2 e-	=	2 Mn3O4		1 H2O			0.79
23	1 Mn2+				2 e-	=	1 Mn					-1.19
25	1 HMnO2-	3 H+			2 e-	=	1 Mn		2 H2O			-0.14
a		2 H+			2 e-	=	1 H2					0.00
b	1 O2	4 H+			4 e-	=			2 H2O			1.14
Mix a,b	1 O2	6 H+			6 e-	=	1 H2		2 H2O			0.76

Activity Schedule

	1	3	4	5	6	7	8	9	10	13	19	20	21	23	25	a	
Mn2+	1.00		1.00			1.00			1.00	1.00				1.00			
MnOH+	1.00	1.00		1.00			1.00										
HMnO2-		1.00			1.00			1.00							1.00		
O2 [atm]																1.00	
H2 [atm]																	1.0

Temp	125 degC	
Temp	398.2 degK	
KW	1.09E-12	LogKw -11.96
K1	7.94E-10	LogK1 -9.10
K2	6.31E-23	LogK2 -22.20
K2sp	9.7E-11	LogK2sp -10.01
K3	1.58E-35	LogK3 -34.80

	Reaction 1	3	4	5	6	
pHt	9.10	9.28	6.96	5.21	13.35	Graph
	8.06		6.63			MacDonald
pHt	9.10		6.96			Experimental

Intersection Schedule (Error=0 Macro is CTRL i)

	pH	Eo			
R 23,4,19	6.96	-1.219			
R 19,6,25	13.35	-1.725			
R 7,4,20	6.96	-0.419			
R20,6,9	13.35	-0.924		Error	
R 10,7,21	3.84	0.488	0.488	0.00	
R 9,21	18.94	-0.704	-0.704	0.00	
R10,13	2.85	0.722	0.722	0.00	

Eo-pH pH	Reaction 1	3	4	5	6	7	8	9	10	13	19	20	21	23	25	a	b
2							0.352			0.857				-1.219		-0.158	0.969
2.85							0.184		0.722	0.722				-1.219		-0.225	0.921
3.84						0.488	-0.011		0.488				0.488	-1.219		-0.303	0.843
6.96			-1.219			-0.419	-0.626					-0.419	0.242	-1.219		-0.549	0.598
6.96			-0.419				-0.626				-1.219	-0.419	0.242			-0.549	0.598
9.10	-2.000						-1.049				-1.389	-0.588	0.073			-0.718	0.428
9.10	2.000						-1.049				-1.389	-0.588	0.073			-0.718	0.428
9.28		-2.000					-1.085				-1.403	-0.603	0.059			-0.733	0.414
9.28		2.000					-1.085				-1.403	-0.603	0.059			-0.733	0.414
13.35					-1.725		-1.888				-1.725	-0.924	-0.263		-1.725	-1.054	0.092
13.35					-0.924		-1.888	-0.924				-0.924	-0.263		-1.725	-1.054	0.092
16.00							-2.411	-0.820					-0.472		-2.038	-1.263	-0.116

Appendix H

Calculation of variation of surface potential with radius of curvature

Variation of E with curvature of surface

GibbThomson equation (Okinaka & Osaka)

Manganese water system at 25degC

Surface tension	N/m	0.072002		
Molar volume	cm3/mol	7.357	Gmelins	
Faradays constant	coul/mol	96490	Barrow	
E flat(Flat suface potential)	Volt	-1.181	MacDonald	
Number of electrons		2		

Radius of curvature		Erad(curved surface potential)	Eflat-Erad
micron	cm	Volt	dV [mV]
10000	1	-1.181	0.0
1000	0.1	-1.181	0.0
10	0.001	-1.181	0.1
1	0.0001	-1.182	0.5
0.1	0.00001	-1.186	5.5
0.01	0.000001	-1.236	54.9

degC	Barrow Surface tension N/m	Linear Regress
20	0.07275	0.072872
60	0.06618	0.065912
100	0.05885	0.058952
25		0.072002

Appendix I

Calculation Procedure for Isothermal and Non-Isothermal Xt versus t/τ Plots

Isothermal Xt versus t/τ Plots

The electronic spreadsheet matrix used for generating Figure 3.2 was structured in the following format:

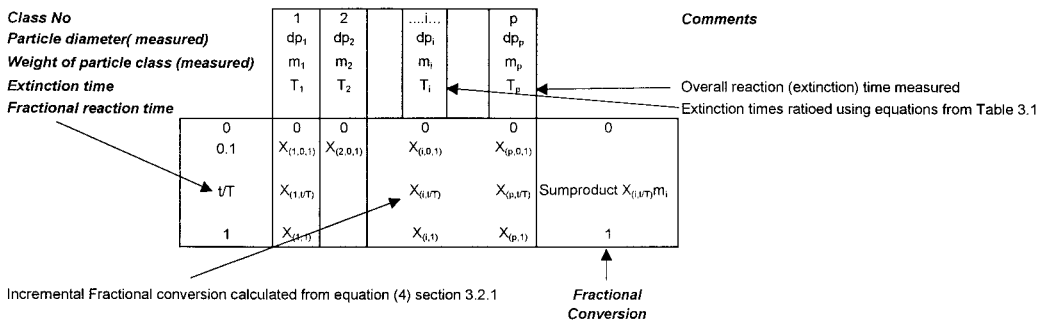

Non-isothermal Xt versus t/τ Plots

The format of the spreadsheet used for generating Figure 3.3 is as follows:

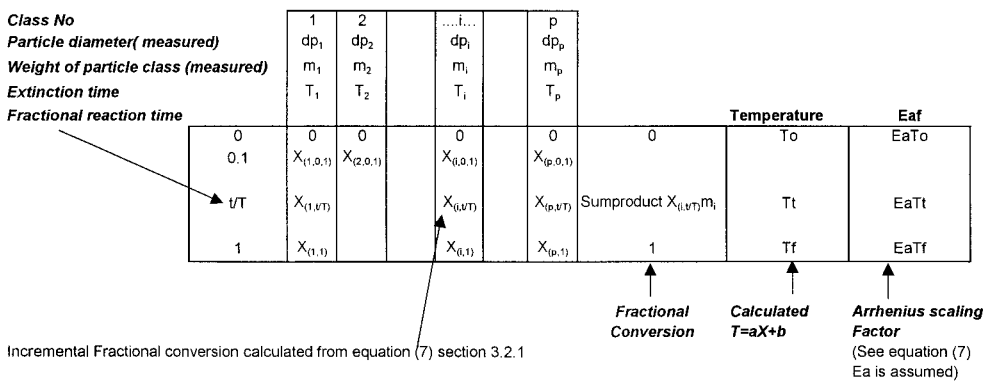

The effect of non-isothermal conditions on the extent of a reaction that is rate controlled by a surface chemical reaction with shrinking polydisperse particles is shown in Figures I1 and I2 below. These simulations are based on the measured initial metal particle size distribution. Here the influence of the proportional increase in temperature as the reaction proceeds can be seen for two assumed values of the activation energy. The reduced time required to complete the reaction with an Ea = 180 000kJ.mol^{-1} can clearly be seen in Figure I2. At this level of activation energy the rate of reaction at the end temperature (165°C) is approximately 400 times higher that at the starting temperature (119°C).

Figure I1 Simulation of non-isothermal polydisperse kinetics at Ea=18000kJ.mol^{-1}

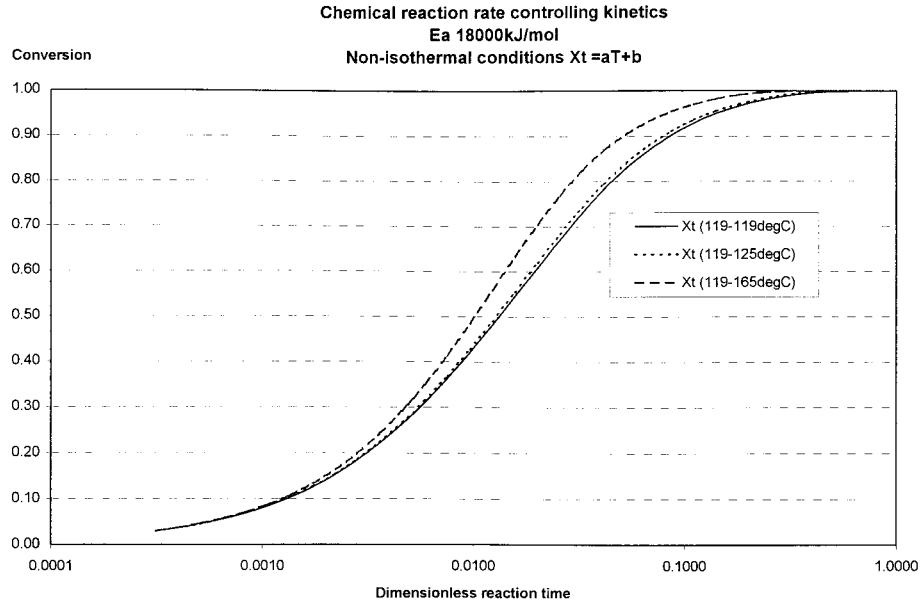

Figure I2 Simulation of non-isothermal polydisperse kinetics at Ea=180000kJ.mol^{-1}

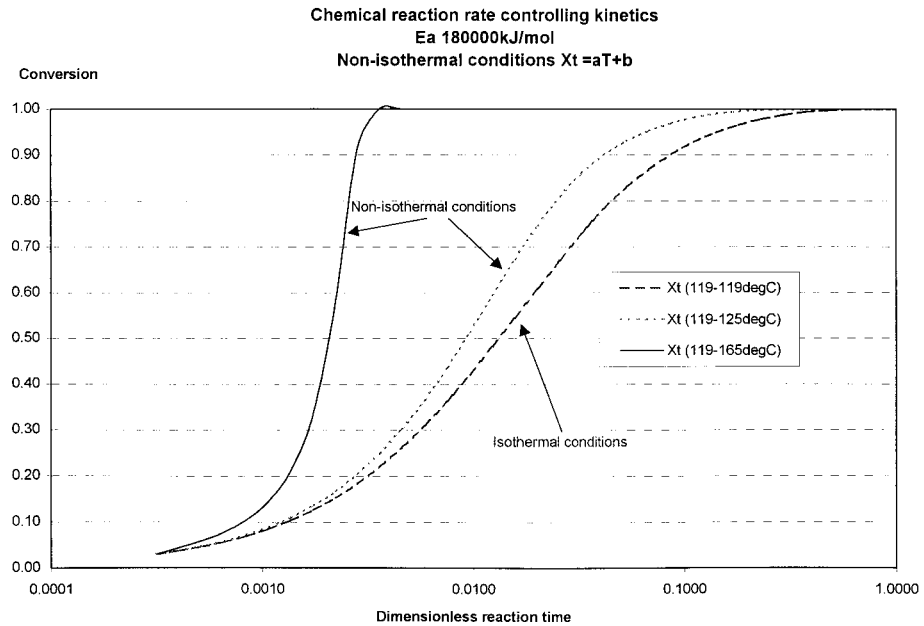

Appendix J

Experimental Conditions in Hydrothermal Reactor and Modelling of Hydrodynamic and Mass Transfer Phenomena

The derivation of models used for characterising the hydrodynamic conditions in the reactor and quantifying the mass transfer of oxygen during the hydrothermal oxidation of $Mn(OH)_2$ are described in this Appendix. Each Table J1 to J16 presented is one element of a group of parameters programmed into electronic spreadsheet format. The interdependency of the different groups is shown diagrammatically in Figure 5.2.

J.1 Physical Properties of the Reacting Phases

The description of a reaction system should include characterisation of the physical properties of the reactants and products. Physical and chemical parameters of the gas, liquid and solid phases are described in Table J.1 and Table J.2. Empirical correlations are used to predict the effect of elevated oxidation temperatures (130°C to180°C) on these parameters.

The gas condition is defined at the sparger entry point with the relevant parameters shown in Table J.1. The partial pressure of steam at the sparger inlet is estimated from the vapour pressure correlation:

$$\log_{10} p_{H2O} = 7{,}106 - \frac{3017}{1{,}8T + 413{,}3}$$

where: T: reactor temperature (°C)

p_{H2O}: water vapour partial pressure (kPa)

The solubility of oxygen in water is obtained by use of the formulae:

$$C_{O2in} = H_{O2}\, p_{O2}$$

$$H_{O2} = 0{,}145\ (3{,}418\text{x}10^{-3} - 3{,}378\text{x}10^{-5}T + 1{,}95\text{x}10^{-7}T^2)$$

where: H_{O2}: Henry type constant ($kg.m^{-3}kPa^{-1}$): Lin *et al.* (1986)

p_{O2}: oxygen partial pressure (kPa(a))

T: reactor temperature (°C)

The relatively high partial pressure of steam results in a significant increase in the gas mass flowrate. Table J1 shows that this effect decreases the molecular weight of the gas

from 29,0g.mol^{-1} to 23,9g.mol^{-1} as well as increasing the mass flowrate of gas through the reactor by approximately 50%. The superficial gas velocity within the reactor will concommitantly increase due to this effect.

Table J1 Gas phase characteristics

PARAMETER	SYMBOL	UNITS	VALUE
Gas			AIR
Compressibility	K_{gas} c_p/c_v		1,4
Total gas inlet flowrate	$m°_{gas}$	kg.hr^{-1}	14,8
O_2 Concentration		%m/m	23,3
Gas viscosity	μ_{gas}	cp	0,01182
Pressure in	P_{gasin}	kPa	530
Gas mole weight	mwt_{in}	g.mol^{-1}	28,96
Bottom pressure	P_{bottom}	kPa	500
H_2O vapour pressure	p_{H2O}	kPa	231
H_2O vapour mole fraction	x_{H2O}		0,46
H_2O vapour entrained	$m°_{H2O}$	kg.hr^{-1}	7,92
Total internal gas flowrate	m_{gin}	kg.hr^{-1}	22,72
Oxygen partial pressure	p_{O2}	kPa	56,6
Henry's constant	H_{O2}	kg.m^{-3}kPa^{-1}	0,00026
Saturated DO at inlet	c_{O2in}	kg.m^{-3}	0,015
Dissolved oxygen @ inlet	DO_{sat}	ppm	14,7
Gas mix molecular weight	mwt_{mix}	g.mol^{-1}	23,9

Note #1:All physical data from Perry (1973) & Weast (1982) unless where described in the text

#2: Pressures are absolute

The stoichiometry of the oxidation reaction:

$$6Mn(OH)_{2(s)} + O_{2(g)} \rightarrow 2Mn_3O_{4(s)} + 6H_2O_{(aq)}$$

has been described from a solid phase perspective in the chapter 4. At stoichiometric conditions, 1 gram of $Mn(OH)_2$ reacts with 0,06 grams of O_2. In a typical experiment, 260kg.m^{-3} of solid $Mn(OH)_2$ suspended in water will consume 15,6kg.m^{-3} of oxygen. Dissolved oxygen concentrations of 15g.m^{-3} are expected at saturation conditions in the reactor (*vide supra* Table J1). An approximate thousand-fold turnover of dissolved oxygen at saturated concentrations is therefore required to complete the oxidation reaction. If the dissolved oxygen concentration does not reach saturation, i.e. gas to liquid phase rate control, then the turnover rate that is required to complete the reaction

would increase for the same gas flowrate. A shortcoming of most studies of mass transfer in three phase systems is the inability to measure the extent of dissolved oxygen saturation in the bulk liquid phase. This is also the case for this study. The reaction would be complete in 1,2 hours with oxygen sparging rates of $13kg.hr^{-1}m^{-3}$ if dispersion was ideal and no oxygen was lost in the gas stream leaving the reactor. Actual conversion times obtained from experiments were found typically to be in excess of 3 hours suggesting that approximately 30% utilisation of gas was obtained. This was confirmed by the utilisation calculations in Figure 4.8.

The liquid phase used in the testwork consisted of demineralised water ($<10\mu S.cm^{-1}$). Physical parameters are given in Table J.2.

Table J.2 Liquid phase characteristics

PARAMETER	SYMBOL	UNITS	VALUE
Liquid			Water
Volume used	V_{liq}	m^3	0,220
Temperature	T	°C	125
Viscosity	μ_{liq}	cp	0,22
Surface tension	σ_l	$N.m^{-1}$	0,058
Liquid density	ρ_l	$kg.dm^{-3}$	0,967

The temperature dependencies of water viscosity, surface tension and specific gravity are given respectively by the following formulae:

- $\mu_{liq} = 1{,}002 * 10^{\frac{1{,}3272(T-20)-0{,}001053*(T-20)^2}{T+105}}$

  (Weast (1982) based on data from Hardy & Cottington for the temperature range 20 to 100°C.)

- $\sigma_l = (-0.16644*T+75.97768)/1000$

  (This correlation was derived by least squares regression (R^2=0,9968) using data from Weast (1982) in the temperature range 0 to 100°C.)

- $\rho_l = 999{,}7 - 0{,}105128(T-10) - 0{,}005121(T-10)^2 + 0{,}00001329(T-10)^3$

  (Shook & Roco (1991) for the temperature range 5 to 100°C.)

Extrapolation to the experimental temperature (125°C) was therefore required. A median value of the beginning and end liquid temperature was taken for these calculations.

Table J.3 Solid and slurry phase properties

PARAMETERS	SYMBOL	UNITS	VALUES
Solid			$Mn(OH)_2$
Molecular weight	mw_{sol}	$g.mol^{-1}$	88,95
Surface area	BET	m^2g^{-1}	12,0
Crystallite size	d_{cry}	μm	0,1
Aggregate size	d_{agg}	μm	3,5
Skeletal density	ρ_{sol}	$kg.dm^{-3}$	4,5
Solid porosity	ε_s	$m^3.m^{-3}$	0,769
Particle density	ρ_{part}	$kg.dm^{-3}$	1,039
Liquid-solid ratio		%v/v	6,1
Liquid-solid ratio		%m/m	23,2
Suspension viscosity	μ_{slurry}	cp	5,0
Suspension density	ρ_{slurry}	$kg.dm^{-3}$	1,189

Section 5.4 provides a detailed account of the morphological changes of the solid phase during the oxidation process. The relevant parameters that characterise the solid are summarised in the Table J3 above and are calculated assuming average particle dimensions for the beginning of the oxidation reaction. Variations in solid and slurry properties due to different experimental conditions are taken into account as well as variations in parameters due to experimental design conditions. The viscosity of the suspension was measured by using a rotating cup viscometer.

J.2 Reactor Geometry and Geometric Ratios

The description of mass transfer requires that a co-ordinate system is defined in which mass flux vectors may be related, Bird *et al.* (1960). In the case of mechanically agitated stirred tank reactors, a standard geometry has been determined which results in an optimised configuration for most processes, Garrison (1983). General operating conditions and physical dimensions are given in Table J4 and Table J5.

Table J4 Reactor dimensions and operating conditions

PARAMETERS	SYMBOL	UNITS	VALUES
Ambient Temperature	T_{amb}	^{o}C	26
Ambient Pressure	P_{amb}	kPa	93
Reactor Temperature	T_r	^{o}C	125
Head Space Pressure	P_2	kPa	493
Gravity	g	$m.s^{-2}$	9,81
Tan to Tan Height	TT	m	0,876
Tank ID	T	m	0,600
Top Dish Height 2:1 Semi-ellipse	TDH	m	0,190
Bottom Dish Height 2:1 Semi-ellipse	BDH	m	0,190
Cylinder Volume	V_c	m^3	0,248
Dish End Volume	V_d	m^3	0,004
Total Liquid Height	Z_t	m	1,01
Total Volume	V_t	m^3	0,255

Table J5 Impeller and sparger geometrical detail

PARAMETER	SYMBOL	UNITS	VALUES
Baffle width	B	m	0.07
Bottom impeller type			4B Flat
Impeller diameter	D_{impb}	m	0,29
Blade width	W_{impb}	m	0,05
Top impeller type			4B-45deg
Impeller diameter	D_{impt}	m	0,22
Blade width	W_{impt}	m	0,05
Mixer speed	N	rpm	340
Impeller clearance	C	m	0,60
No of spargers			2
Sparger to impeller	S	m	0,15
Sparger diameter	D_{sp}	m	0,02

The geometrical ratios of this vessel are compared to recommended optimum ratios for standard reactor geometry in Table J6.

Table J6 Dimensionless geometric ratios of the experimental reactor

Parameters	Symbol	Actual	Optimum
Liquid Length to Diameter	Z_t/T	1,67	1,4
Tank T-T to Diameter	TT/T	1,46	1,4
Impeller to Tank Diameter	D/T	0,48	0,2-0,4
Impeller Width to Diameter	W/D	0,18	0,15-0,5
Impeller Clearance to Diameter	C/T	1,00	0,25-1,5
Baffle to Diameter	B/T	0,11	0,083-0,1
Impeller Liquid Coverage	Z_g-C/D	1,78	
Impeller Bottom Clearance	C/D	0,789	

J.3 Suspension Characteristics

One of the functions of an agitator in a stirred reactor is to prevent the settling of particles. Musil et al. (1984), Wichterle (1988), Ditl & Rieger (1985), Ditl (1985), Coetzee & Cloete (1989) and Shaw (1992) have investigated the identification of the hydrodynamic factors that affect the suspension of particles in ungassed mechanically agitated reactors. The classic parameters that measure a mixer's ability to suspend particles are based on Zweitering's just-suspended concept - Wichterle (1988). When this condition is satisfied, sufficient flow exists across the reactor bottom to ensure that no settling of particles occurs. Shaw (1992) showed that particle behaviour could further be classified as shown in Table J.7. The just-suspended condition corresponds to off-bottom suspension that does not necessarily ensure a uniform solid concentration throughout the liquid phase.

Table J.7 Degrees of solids suspension

Type of suspension	Particle behaviour
In-motion	Stationary fillets form in corners. No stationary particles on tank bottom.
Off-bottom	No corner fillets but a solid concentration profile exists between top & bottom of tank.
Uniform	Uniform solids concentration throughout vessel

Ref. Shaw(1992), Corpstein et al (1994)

The mixing speed required to obtain off-bottom suspension can be estimated from empirical correlations which need to be specific for different impeller configurations. It is

generally accepted that axial flow impellers suspend particles more efficiently than radial flow turbines, Corpstein *et al.* (1994). The minimum suspension speed determines the speed at which the impeller effectively suspends particles in the reactor. Table J.8 summarises the parameters required to estimate this critical suspension speed. The calculation procedure for these is based on the procedure proposed by Wichterle (1988).

Table J.8 Suspension characteristics of solid particles

PARAMETER	SYMBOL	UNITS	VALUE
Archimedes number	Ar		0,0066
Particle terminal settling velocity	v_{part}	$mm.s^{-1}$	0,0243
Amin factor	A_{min}		2,5
Bottom shearrate	y_b	s^{-1}	1019
Bottom velocity	v_{bot}	$mm.s^{-1}$	3,565
B factor	B_{act}	v_{bot}/v_{part}	147
Critical suspension speed	N_{crit}	rpm	3,95
Critical suspension power	P_{js}/V_{slurry}	$kW.m^{-3}$	0,000009

The flow regime around the solid particles can be characterised by the Archimedes number which is the ratio of the gravitational to viscous forces on a solid body in a fluid medium:

$$Ar = \frac{d_p{}^3 \rho_l (\rho_{part} - \rho_l) g}{\mu_l}$$

The effective density of the particle ρ_{part} and the viscosity of water are used in these calculations, as conditions local to individual particles determine settling behaviour. The low value of the Archimedes number (Ar=0,0066) means that a creeping flow condition exists for which the terminal settling velocity can be determined from the Stokes equation. Under these conditions the flow field around a spherical body would not give significant wake eddy formation. Wichterle (1988) gives a correlation for the terminal settling velocity in terms of the Ar that reduces to the Stokes equation for small values of Ar:

$$v_{part} = \frac{\mu_l Ar}{d_p \rho_l (18 + 0{,}6Ar^{0{,}5})}$$

The shear rate and flow velocity across the tank bottom is then estimated using an agitator type dependent factor A_{min}. The condition of settling is determined by the B factor, which is the ratio of free settling velocity to across the bottom flow. Values of B

below 10±2 indicate settling conditions. Thereafter the impeller speed and agitator power consumption to maintain just-suspended conditions (N_{crit}) of all particles are calculated using empirical correlations. The results of these calculations are given in Table J.8.

The actual rotational speed of the impeller is two orders of magnitude larger than the critical suspension speed. Settling of particles thus does not occur in this system.

The literature studies mentioned above are confined to liquid-solid systems. The introduction of a gas phase into a stirred reactor will generally lower the power drawn by the agitator and can result in particle sedimentation under certain operating conditions. Frijlink *et al.* (1990) and Rewatkar & Joshi (1991a,b) investigated suspension phenomena in gassed reactors. Frijlink *et al.* (1990) investigated the influence of energy dissipation on solid suspension phenomena. The importance of across the bottom flow for suspension was confirmed in this work. The shape of the tank bottom has a strong influence on settling behaviour with round bottoms requiring half the power consumption of a flat bottomed vessel. The influence of gas cavities attached to impeller blades was used as a reference point for the explanation of suspension behaviour. Rewatkar & Joshi (1991a,b) showed that sparger design and location influenced suspension. Brucato *et al.* (1991) applied a network-of-zones approach for predicting solid suspension variations in a high aspect ratio vessel with multiple impellers. These studies are useful for complicated mixing geometry's, when the power required for suspension is large (i.e. large particle systems) or careful optimisation of suspension and dispersion is essential. These conditions do not apply to the manganous hydroxide oxidation process.

J.4 Impeller Flow Conditions

The main function of the agitator in a stirred reactor is to create a flow field in the liquid phase. This flow field may have laminar (creeping flow) or turbulent flow characteristics - Patterson (1991). Turbulent flow agitators may be grouped into two broad categories, viz. stirrers with radial or axial pumping impellers. The flat bladed Rushton turbine is the best example of a radial flow impeller, while flat pitch bladed turbines and high efficiency flow turbines such as the Lightnin® A315 are examples of axial flow impellers. The turbulent flow patterns produced by these impeller systems are shown in simplified format in Figure J.1.

Figure J.1 Flow patterns in stirred tanks with single impellers

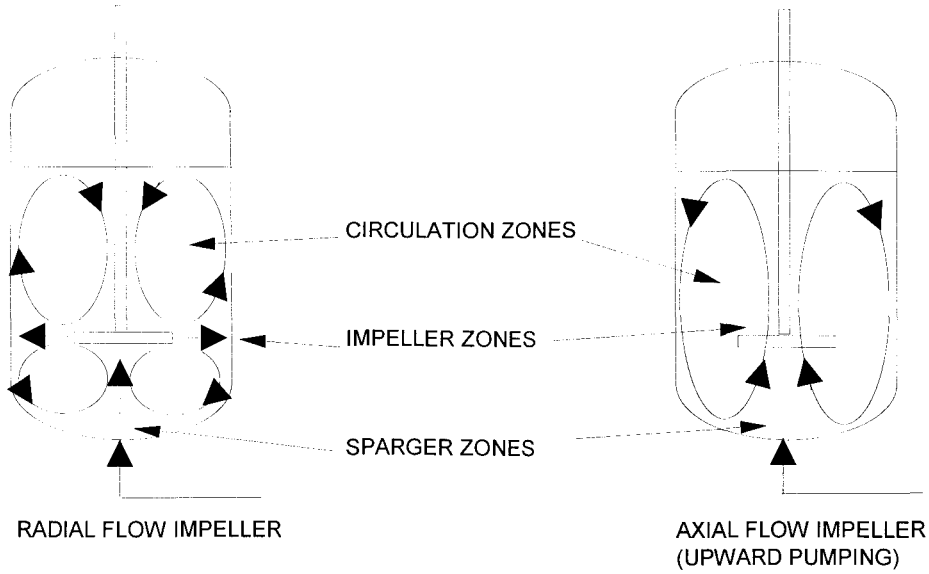

Zones with specific hydrodynamic characteristics are produced with steady state operation at different locations within the flow field. Patterson (1991) lists some of the flow structures that can occur in a mechanically agitated reactor. The region close to the impellers consists of complex flow structures which include high velocity discharge flows, blade wake regions, trailing and blade bound vortex systems. Jet flow from the impeller impinges on the wall and vortex flow can result on baffles. The bulk region is characterised by the formation of one or more toroidal structures within the circulating flow field. Depending on the local gas velocity, jet structures with a conical geometry may form at the spargers. These structures may entrain significant quantities of liquid. The gas phase interacts with the turbulent flow field and may create new flow structures (e.g. cavities on trailing edges of impeller blades). In addition, processes of bubble disintegration and coalescence may accompany the dispersion of gas. The impeller zone is very effective in reducing the size of gas bubbles, while coalescence to form larger bubbles occurs in the circulation zones. Due to the unavailability of measurement techniques to characterise these structures, a gross-scale or overall analysis was made of these mixing patterns as described by Patterson (1991).

Kuboi & Nienow (1982) studied the behaviour of mixing vessels with combinations of impellers. Careful selection of impeller type and pumping orientation is necessary in dual impeller systems. Hysteresis effects are found in flow pattern development for certain radial (Rushton) and axial (45°-pitch blade) impeller combinations. Downward pumping systems, particularly pitched blade impellers create unstable flow patterns. This is similar to single impeller behaviour. An upward and downward axial impeller combination was found to be surprisingly effective at dispersing gas due to the formation of a stable

toroidal vortex cavity between the two impellers. The power draw of the radial-axial combination was the least affected to the amount of gas introduced to the reactor. Accurate prediction of power draw by summation of individual impeller contributions for matched impellers was shown to be suitable for ungassed systems only. The total ungassed power draw for the experimental agitator is estimated by summation as the upper impeller draws only approximately 7% of the total power. A correction for the decrease in power due to gassing is made on the combined contributions.

Computational Fluid Dynamics (CFD), statistical turbulence and structural turbulence theory are popular methods to determine streamlines and power dissipation in mechanically agitated vessels. A more recent approach (Chem. Eng. (p23, Dec., 1996)) is to use lattice gas theory as an alternative to solving the Navier-Stokes equation. Tavlarides & Bapat (1983), Wen (1987), Pericleous & Patel (1987), Ju *et al.* (1990), Kresta & Wood (1991/1993) are examples of three dimensional flow modelling studies using the CFD approach which generally only deal with a single phase. Non-invasive Laser Doppler Anemometry (Calabrese & Stoots (1989)) has also been developed to provide more accurate experimental measurements of flow patterns. Kresta & Wood (1991) successfully predicted flow from a Rushton turbine using a turbulent swirling radial jet model. These techniques have been used successfully to model two and three phase flow systems but are not within the scope of this thesis.

The general characteristics of the flow field and the two-impeller mixer used for the oxidation experiments are quantified in Table J.9. The total flow (Q) and the power (P) required to maintain the rotational speed can be estimated from knowledge of the flow (N_q) and power (N_p) numbers by the following formulae:

$$Q=N_q\, N\, D^3$$
$$P=N_p\, N^3\, D^5\, \rho_{slurry}$$

where: N: rotational speed (rpm)
D: impeller diameter (m)
ρ_{slurry} : slurry density ($kg.m^{-3}$)

Table J.9 Flow conditions at impellers

PARAMETER	SYMBOL	UNITS	VALUE
FLOW CONDITIONS BOTTOM IMPELLER			
Tip Speed	v_{tip}	$m.min^{-1}$	304
Flow Number	N_q		0,66
Total Flow	Q_{lbot}	m^3hr^{-1}	312
Turnover Rate	$Q_{lb}/V_{slurryg}$	min^{-1}	20,7
Gassed Imp Reynolds Number	Re_{imp}		102221
Power Number	N_p		3,31
Mixer Power Ungassed	P_{mbot}	kW	1,3
Power to Volume Ratio	$P_{mbot}/V_{slurryg}$	$kW.m^{-3}$	5,74
Torque	T_{qbot}	N.m	38
Bulk Velocity	v_{Qbot}	$m.s^{-1}$	0,31
Mix Intensity	I		5
FLOW CONDITIONS TOP IMPELLER			
Tip Speed	v_{tip}	$m.min^{-1}$	230
Flow Number	N_q		0,78
Total Flow	Q_{ltop}	m^3hr^{-1}	158
Turnover Rate	$Q_{ltop}/V_{slurryg}$	min^{-1}	10,5
Impeller Reynolds Number	Re_{imp}		58174
Power Number	N_p		1,36
Mixer Power Ungassed	P_{mtop}	kW	0,1
Power to Volume Ratio	$P_{mtop}/V_{slurryg}$	$kW.m^{-3}$	0,58
Torque	T_{qtop}	N.m	4
Bulk Velocity	v_{Qtop}	$m.s^{-1}$	0,16
Mix Intensity	I		3
COMBINATION IMPELLERS			
Ungassed Power	P_{mtot}	kW	1,5
Power to Volume Ratio(Ungassed)	P_{mtot}/V_{slurry}	$kW.m^{-3}$	6,32
Total Flow	Q_{tot}	m^3hr^{-1}	470
Total Turnover	$Q_{tot}/V_{slurryg}$	min^{-1}	31

Ref. Np, Nq and background theory -Oldshue (1983)

Mixing intensity - Hicks & Gates (1976)

The magnitude of the impeller Reynolds number ($\rho_{slurry}ND^2/\mu_{slurry}$) places the flow in the turbulent regime (Re_{imp} >10000). In addition, the tip speeds of both impellers make these capable of fine dispersion (300< v_{tip} <1500 $m.min^{-1}$). The level of mixing intensity calculated from the bulk circulation superficial velocity (I = $v_Q/6$) according to the method

proposed by Hicks & Gates (1976), classifies the mixing regime as typical of reactors with high rates of mass transfer.

Fine bubbles would be driven completely to the vessel wall and recirculation of dispersed bubbles back to the impeller occurs under these conditions. This intensity of agitation should be sufficient to suspend particles with a terminal settling velocity of 600-1200mm.s^{-1}. A relatively high power to volume ratio (5,7 kW.m^{-3}) is required to achieve these flow conditions.

J.5 Mixing Analysis

Statistical turbulence theory characterises motions within a flow field in terms of scale parameters - Patterson (1991). These parameters can be defined in terms of concentration, length, time and velocity variables. Parameters such as energy dissipation and mixing can assume a continuous spectrum of values according to these scales. For example, the energy spectrum at any point in the reactor can be divided into large eddy, inertial-convective and viscous-dissipative subranges. The smallest scales dissipate most of the turbulence by molecular (kinematic) viscosity. The eddy viscosity and mechanical flow properties govern the intermediate and large scales. Transfer mechanisms for energy dissipation exist from the large to small scales. Mixing analysis can be classified into macromixing or micromixing categories as shown in Table J.10.

Table J.10 Macro and micromixing parameters

PARAMETER	SYMBOL	UNITS	VALUE
Kinematic viscosity	ν_l	mm^2s^{-1}	0,232
Liquid power dissipation rate	ε_l	$W.kg^{-1}$	5,0
Kolmogoroff length scale	η_l	micron	7,1
Kolmogoroff velocity scale	v_e	$mm.s^{-1}$	32,9
Mean recirculation velocity	v_{cavg}	$m.min^{-1}$	42,2
Mixing time	θ_m	s^{-1}	1,10

Ref. Kawase & Moo-Young (1988)

The Kolmogoroff microscale length determines the lower limit of the viscous-dissipative subrange of the flow field:

$$\eta_l = \left(\frac{\nu^3}{\varepsilon}\right)^{1/4}$$

The analysis in section 5.3 has shown that the effective particle size of precipitated manganous hydroxide is dependent on this parameter. Molecular diffusion is required to eliminate concentration gradients in the microscale-mixing regime. It is therefore expected that as the size of an average $Mn(OH)_2$ particle is similar to the Kolmogoroff length, the flow regime within the porous structure of this particle is laminar. It is feasible for large porous particles to have an intraparticle flow that has some turbulent characteristic.

Macromixing is the process of distributing and homogenising large elements of fluid throughout the reactor to the extent that turbulence disappears. The macroscale mixing time is the time required for these processes. Kawase & Moo-Young (1988) give a correlation for estimating this time in standard geometry reactors:

$$\theta_m = 4{,}3\left(\frac{T}{D}\right)^2 N^{-1}$$

The numeric value of the mixing time according to this correlation (1,1 seconds) agrees with that of Geisler *et al.* (1992) who give a correlation which estimates this time as 1,8 seconds. It is useful to compare this time to the average retention of the gas in the reactor. This is estimated at approximately 16 seconds in Table J.12. The mixing time is therefore significant relative to the gas retention time (ca.10%) and perfect utilisation of the gas cannot be expected.

J.6 Gas Dispersion Characteristics

In addition to creating flow and preventing suspension of solid particles, the impeller/s of an agitator in a three-phase reactor must adequately disperse the gas phase throughout the liquid phase for optimal gas utilisation at minimal power consumption. The effect of the gas phase on the flow structures in the experimental reactor is analysed in the following paragraphs. The inlet flowrate of the gas is expressed in different terms in Table J.11. Both the free-air-delivered (FAD) and actual flowing conditions are estimated using the ideal gas assumption.

Table J.11 Gas flowrates and velocities

PARAMETER	SYMBOL	UNITS	VALUE
Gas mix addition rate	M	$kg.hr^{-1}m^{-3}$	90,5
Gas volume addition rate (FAD)	Q_g	$m^3.hr^{-1}$	13,5
Mix volume addition rate @ bottom	Q_{gbot}	$m^3.hr^{-1}$	6,2
Gas density @ bottom	ρ_g	$kg.m^{-3}$	3,66
Volumetric sparge rate (FAD)	vvm	min^{-1}	0,9
Superficial gas velocity(FAD)	υ_{go}	$m.min^{-1}$	0,80
Superficial gas velocity (actual)	υ_g	$m.min^{-1}$	0,37

Agitator and bulk zone gas dynamics

Introducing a gas that is not fully absorbed into a reactor will result in formation of a dispersed phase that has a characteristic hold-up volume. Mann (1983) summarised correlations for the estimation of gas hold-up from a number of authors. An estimation of the gas hold-up expressed as a fraction of total reactor volume is given in Table J12. Once an estimate has been made of this quantity, the gas retention time and gas rise velocity are calculated assuming the volume of gas passing through the reactor is not changed significantly (<6% change) due to absorption.

Table J.12 Gas dispersion and bubble characteristics

PARAMETER	SYMBOL	UNITS	VALUE
Mean shear rate @ impeller	dv/dz_a	s^{-1}	108,5
Maximum shear rate @ impeller	dv/dz_m	s^{-1}	250,7
Maximum shear stress	S_{max}	Pa	1,3
Aeration number	A (Q/ND^3)		0,013
Gas hold-up (Hassan Robin)	ε_{g1}		0,110
Gas hold-up (Yung)	ε_{g2}		0,105
Mean gas hold-up	ε_g		0,108
Dispersion speed	N_{dis}	rpm	111
Gas retention time	t_g	s	16
Mean gas rise velocity	v_{bub}	$mm.s^{-1}$	56
Bubble free rise velocity	v_{bf}	$m.s^{-1}$	0,20
Bubble diameter (Sauter)	d_b	mm	7
Bubble diameter free rise	d_{bfree}	mm	8
Bubble Reynolds number	Re_{bub}		92
Free Rise Reynolds Number	Re_{bfr}		409

Ref. Mann (1983), Nienow *et al.* (1986), Bailey & Ollis (1977)

Van't Riet & Smith (1973) studied flow in the impeller region of a dispersing Rushton turbine. Bubble coalescence and dispersion through the trailing vortices on the agitator blades were found to be the main mechanisms of gas phase mixing. A steady flow of gas to the impeller will result in stable cavities that rotate with the blade and cause a nett decrease in power consumption of the agitator. Bubbles captured in the cavity region become distorted at higher tip speeds and the vortex structure develops a cylindrical form. The addition of more gas results in extension of the cavity into the tip of the trailing vortex region where random closure of the cavity tip results in the escape of small bubbles. This behaviour is similar to a jetting sparger with a stable cavity releasing bubbles at random, Geary & Rice (1991).

Warmoeskerken *et al.* (1984) found similar behaviour for pitched blade turbines and classified different types of cavities. These were given as:

- Vortex cavities with dispersed small bubbles.
- Clinging cavities.
- Growing cavities with small vortex tails.
- Large cavities.

Two distinct gas-loading regimes were identified:

- Indirect loading occurs at low gassing rates when the primary gas flow stream reaches the impeller by recirculation flow.
- Direct loading occurs at higher gassing rates with the gas from the sparger reaching the impeller directly.

Indirect loading of gas corresponds to the formation of the dispersed and clinging type cavity conditions. At sufficiently high gassing rates the impeller is unable to disperse the gas. This is the flooding condition and is accompanied by significant bypassing of gas around the impeller blades. A critical speed for dispersion without flooding therefore exists for each gassing rate.

The flooding impeller speed is estimated at approximately 30% of the operating speed using the correlation of Nienow *et al.* (1986). Higher gas flowrates can therefore be accommodated in this reactor. The magnitude of the aeration number (A) also indicates that the lower impeller is far from the point of flooding (A_f=0,03). Growing or large type cavities are therefore expected on the blades of the impeller.

The gas phase spends approximately 16 seconds in the reactor based on gas hold-up. Gas bubbles will tend to rise in the liquid due to the density difference between these phases. The free rise velocity of air bubbles in water and bubble diameter is calculated using correlations given by Bailey & Ollis (1977). These parameters are both three

orders of magnitude larger than those corresponding to the settling particles of solid $Mn(OH)_2$. The significance of this is discussed below.

Koetsier & Thoenes (1972) measured bubble size distributions in a stirred tank with liquids of different ionic concentrations. Coalescence of bubbles was found in low ionic strength solutions. The mean bubble size measured in the radial flow stream leaving the impeller was approximately half the mean size in the recirculation zone. The distribution of bubble sizes expected in the reactor is narrow and is not quantified further here.

Sparger zone dynamics

The points at which sparged gas is introduced into a reactor can form different types of hydrodynamic conditions. The jetting conditions at the sparger are determined by the magnitude of the Mach and Weber numbers - Irons (1993). The classification of bubbling and jetting flow regimes is based on the Mach number. The intermediate flow regime $0.03<Ma<0.5$ usually results in constant frequency bubbling flow. The onset of stable jets is predicted at Mach numbers greater than one. The low values of the sparger exit velocity, Weber number and Mach number indicate that the sparger is characterised by a bubbling regime with no well-defined jet. Table J.13 summarises the values of these parameters.

Table J.13 Sparging characteristics

PARAMETER	SYMBOL	UNITS	VALUE
Sparger velocity	υ_{sparg}	$m.s^{-1}$	4,89
Sparger gas Reynolds number	Re_g		22661
Sparger Weber number	We		23
Jetting Weber number	$We_{critjet}$		183
Sparger local sonic speed	υ_{sonic}	$m.s^{-1}$	445
Sparger Mach number	Ma_s		0,01099
Sparger expansion power	P_s	kW	0,067
Static head gas power dissipation	ε_{sparg}	$kW.m^{-3}$	0,081
Gas input kinetic power	ε_{kinet}	$W.kg^{-1}$	0,0002
Total gas input power	P_{stot}	kW	0,15
Gassed agitator power	P_{gtot}	kW	1,02
Total power input	P_{tg}	kW	1,17
Total power to volume ratio	$P_{tg}/V_{slurryg}$	$kW.m^{-3}$	4,65
Impeller to gas power ratio	P_{gbot}/P_{tg}		6,89

Ref. Bailey & Ollis (1977), Marrone & Kirwan (1986), Asai *et al.* (1989)

The reduction in impeller power consumption due to the introduction of gas is estimated by the Michel Miller correlation given in Mann (1983):

$$P_{gtot} = 0,72\left(\frac{P_{mtot}^2 ND^3}{Q^{0,56}}\right)^{0,45}$$

Although gassing lowers the power draw of an agitator, the direct interaction of the gas stream with the liquid phase will result in the transfer and dissipation of energy. This energy has an influence on processes such as mixing, dispersion and mass transfer and is usually included with the total energy dissipated in the reactor. The contribution of the energy associated with the gas stream to the total energy that is dissipated in the reactor is estimated by a number of different methods:

- Isentropic and isothermal expansion, Marrone & Kirwan (1986).
- Static head energy, Asai *et al.* (1989).

The gas phase provides an input of 0,148kW of energy that is about 1/7th of the energy provided by the impeller. Therefore the agitator makes the primary energy input.

J.7 Suspension Structure

The relative volumes of gas, liquid and solid are used to determine a hypothetical geometrical structure for the suspension in the reactor. The large difference in bubble and particle diameter suggests that this structure may be visualised as a "unit" cell comprising a spherical gas bubble with a surrounding liquid film containing dispersed solid particles. The structure is derived by making the following assumptions:

- The dispersed phases of gas and solid are made up of spheres with uniform diameter.

- The dispersion of both phases is uniform throughout the liquid phase. This assumption is not strictly correct for the gas as is it known that the impeller cavities hold relatively high volumes of gas.

- The bubbles and particles do not interact with another in processes such as bubble coalescence and solid particle agglomeration.

- The porosity of the solid particles is an additional surface beyond the projected diameter of the particle.

Hypothetical interfacial areas for mass transfer may be calculated from the above assumptions using the following formulae:

$$\frac{a_b}{a_p} = \frac{d_p}{d_b}\left(\frac{\varepsilon_g}{1-\varepsilon_g}\right)\frac{1}{\varepsilon_p}$$

where: a_b and a_p are the total surface areas of the gas and solid phase respectively

$$\varepsilon_g = \frac{V_{gas}}{V_{part} + V_{gas} + V_{liq}}$$

where: V_i : total volume of an individual phase i

ε_g : gas hold-up volume

$$\varepsilon_p = \frac{V_{part}}{V_{part} + V_{liq}}$$

where: ε_p is the mass fraction of solids in unaerated liquid

Numerical values for these quantities are shown in Table J.14. The surface area presented to the bubbles by the particles is approximately 3 orders of magnitude larger than the surface area of the bubbles. The total interfacial area of the aggregated crystallites within the particles is approximately 5 orders of magnitude larger than the bubble area. These observations and the fact that oxygen is sparingly soluble in water suggests that the controlling mass transfer resistance is most likely in the liquid film surrounding individual gas bubbles.

Calculating inter-bubble and inter-particle distances can be used to extend the hypothetical suspension structure further. In this way, a spatial representation of a " mass transfer unit cell" may be obtained. This unit cell can be defined as one gas bubble with surrounding liquid and dispersed particles in the volume proportions of these phases in the reactor. Karve & Juvekar (1990) used the concept of a cell model mass transfer for a reacting slurry of small particles. This model was able to predict the enhancement of mass transfer rate for a number of experimental studies evaluated. Further assumptions are required to determine how the individual particles and bubbles are arranged in the structure. It is assumed that the liquid and solid phase can be represented in terms of

close packed spheres with a certain packing efficiency. This assumption will be reasonable if the dispersion is uniform.

Table J.14 Suspension structure and mass transfer cell

PARAMETER	SYMBOL	UNITS	VALUE
Liquid volume	V_l	m^3	0,22
Solid volume	V_s	m^3	0,014
Gas volume	V_g	m^3	0,028
Total volume	$V_{slurryg}$	m^3	0,263
Bubble diameter	d_b	mm	6,7
Number of bubbles	n_b		176689
Bubble area	a_b	m^2m^{-3}	96
Bubble packing efficiency	χ_{pf}		0,70
Bubble space diameter	d_{beq}	mm	12,6
Particle diameter	d_p	mm	0,0035
Number of particles	n_p		$6,41*10^{14}$
Particle external area	a_p	m^2m^{-3}	93946
Total particle interfacial area	a_{ptot}	m^2m^{-3}	2959237
Particle packing factor	χ_{pf}		0,7
Particle space diameter	d_{peq}	mm	0,0079
Mass transfer cell diameter	d_{mt}	mm	14,2
Ratio of particle to bubble area	a_p/a_b		981

- An equivalent particle with liquid diameter can then be calculated from the relationships:

$$(V_l + V_s)\chi = n_p(4/3\Pi\, r_p^3)$$

$$d_{peq} = d_p \sqrt[3]{\chi\left(\frac{V_l}{V_s} + 1\right)}$$

where: χ : packing efficiency of a close packed structure

d_{peq} : equivalent diameter of a sphere containing particles and water

- A similar assumption is made for the gas bubbles in the liquid-solid suspension:

$$d_{beq} = d_b \sqrt[3]{\chi\left(\frac{V_s}{V_g} + \frac{V_l}{V_g} + 1\right)}$$

- The equivalent diameter of a mass transfer unit cell is obtained from:

$$d_{mt} = 2 * \sqrt[3]{r_{beq}^3 + \frac{n_p}{n_b}\frac{r_{peq}}{\chi}}$$

Calculation of these quantities is included in Table J.14. Each gas bubble is located at the centre of a liquid sphere that has approximately double the diameter of the bubble. The liquid phase of this sphere contains approximately 3 million solid particles. These calculations confirm that the solids are well dispersed and that the gas bubbles have a strong influence on the geometrical properties of the slurry.

J.8 Mass Transfer Coefficients

This has been discussed in section 3.3. Numerous studies have been made of the effect of solid particles on mass transfer processes in mechanically agitated vessels e.g. Harriott (1962), Nikolaishvili *et al.* (1980), Miyachi *et al.* (1981), Alper & Deckwer (1983), Ledakowicz *et al.* (1985), Marrone & Kirwan (1986) and Nagy *et al.* (1986a,b & 1989). The effect of the presence of solid particles on mass transfer rate becomes important at high levels of solids concentrations (typically 20% by mass). Large and small particles can penetrate or accumulate in hydrodynamic liquid films and enhance the rate of mass transfer from the bubble. The aforementioned authors make extensive use of the Frössling (or Ranz & Marschall) equation to predict the mass transfer coefficient for suspended spheres:

$$Sh_p = 2 + a\, Re_p^{\,b}.\, Sc_p^{\,c}$$

where: $0{,}36 < a < 0{,}6$

$0{,}3 < b < 0{,}79$

$0{,}3 < c < 0{,}39$

These coefficients are dependent on the configuration and type of reactor. The values proposed by Ditl (1985), a=0,49, b=0,6 and c=0,39 for a gassed stirred reactor were used to estimate the liquid-solid film mass transfer coefficient. Table J.15 summarises the results of these calculations. The particle Reynolds number is calculated from the expression as suggested by Marrone & Kirwan (1986):

$$Re_p = \frac{d_p^{4/3}\varepsilon^{1/3}}{\nu}$$

The diffusivity of oxygen in water at 25°C is taken as $2,5x10^{-5}$ $cm^2.sec^{-1}$ and is corrected for temperature using the Stokes Einstein equation:

$$D_{ab} \sim \frac{kT}{\mu_l}$$

Table J.15 Liquid solid mass transfer coefficient

PARAMETER	SYMBOL	UNITS	VALUE
Schmidt number of particle	Sc_p		284
Reynolds number of particle	Re_p		0,40
Sherwood number of particle	Sh_p		4,14
O_2 Diffusivity @125°C	D_{ab}	cm^2sec^{-1}	$1,49*10^{-4}$
Mass transfer coefficient	k_{ls}	$cm.sec^{-1}$	1,76

Ref. Sherwood number from Ditl (1985)

Gas-liquid mass transfer coefficients calculated according to the Calderbank correlation (Bailey & Ollis (1977)) yield values of $0,024cm.s^{-1}$. The orders-of-magnitude difference between the mass transfer coefficients and the interfacial areas for the gas and solid interfaces therefore confirm that mass transfer from the gas to liquid phase is rate controlling.

J.9 Mass Transfer Virtual Analysis

The use of the virtual reaction or mass transfer rate principle of Wagner is advocated by Riekert (1990) for the analysis of a complex multistep process. The virtual rate is the hypothetical rate that would prevail in a network, or sequence of coupled processes, under the condition that all the driving forces of distinct steps except the rate controlling step are strictly zero. The actual rate of a sequence of steps having linear kinetics can be shown to be exactly equal to the reciprocal of the sum of all reciprocal virtual rates. The exact rate of a process including a step with non-linear kinetics (e.g. a second order reaction) cannot be determined from the set of virtual rates. In practise though, the errors in performing a similar reciprocal calculation are minimal. The virtual rates are useful instruments of comparison for steady state processes. Transient or dynamic processes require comparisons with respect to relaxation times. The virtual rate-controlling step can further be used for the classification of complex systems.

Virtual mass transfer rates correspond to mass transfer under a maximised concentration gradient. For gas absorption into a reactor, the upper limit of concentration is the saturated gas solubility while the lower limit is zero.

The general formula used in the calculations is:

$$m_{vi} = k_i a (C_g^*)$$

Estimates must be made of the mass transfer coefficients that generally cannot be calculated exactly. The results of a virtual rate analysis are shown in Table J.16.

Table J. 16 Experimental and virtual oxidation rates

PARAMETER	SYMBOL	UNITS	VALUE
O_2 addition rate	m_{O2}	$kg.hr^{-1}m^{-3}$	13,1
Oxidation time	T	min	210
Oxidation rate	m_{O2reac}	$kg.hr^{-1}m^{-3}$	4,2
Gas utilisation	e		0,32
Virtual controlling rate	m_{vo2r}	$kg.hr^{-1}m^{-3}$	2,5
Virtual experimental MTC	$(ka)_{vexpt}$	hr^{-1}	287

MTC: Mass transfer coefficient

The virtual controlling rate is approximately 60% of the actual reaction rate. This indicates that the interfacial areas or mass transfer coefficients have not been estimated accurately. The virtual controlling rate should be equal to or greater than the experimental reaction rate. The virtual rate can exceed the actual rate if mixed rate control is present. The magnitude of overall mass transfer coefficient for these calculations is $65hr^{-1}$, which needs to be compared to a value of $287hr^{-1}$ for the overall actual mass transfer coefficient assuming virtual conditions. The calculated overall mass transfer coefficients are within the range typically found in stirred reactors i.e. 10 to $1000hr^{-1}$ -Patterson (1991). The simplifying assumptions made in the interfacial area model would be responsible for the underestimation of this parameter. The model assumes that the suspension can be characterised as uniform and fully dispersed, similar to the bulk or solid dispersion, gas hold-up and mass transfer in different zones of the reactor. The conclusion that the oxidation rate is controlled by the mass transfer rate from the gas to the liquid will however not be altered by more accurate estimation of these quantities.

Appendix K

Analyses of Particle Morphology of Manganese Oxide/Hydroxide Intermediates taken during Oxidation of Manganous Hydroxide Produced by Hydrothermal Dissolution of Manganese Metal

Particle Size Analysis using Laser Light Scattering

Equipment

A Malvern Mastersizer S was used to measure the particle size distributions of wet and dry samples of manganese oxides and oxyhydroxides. This instrument uses the so-called "Low Angle Laser Light (He-Ne:λ=0,63μm) Scattering" technique to measure particles in the size range 0,05 to 3000μm. Both the Fraunhofer and Mie theory light scattering approximations can be used in the experimental set-up. The Fraunhofer approximation is generally used for measuring large opaque particles with a minimum particle size of 3μm. The Mie theory approximation is used when measuring non-opaque particles that transmit and absorb light. Generally, most particles with a size below 25μm are subject to this phenomenon, Rawle (1999). The use of the Mie theory approximation therefore requires an estimation of the refractive index of the material.

Setup and Calibration

A 300RF lens was used for the analyses using the Mie theory detection mode. This arrangement made the instrument capable of measuring particles in the size range 0,05 to 880μm. The active laser beam length was 2,4mm on a sample suspended in demineralised water. The sample presentation used assumed a real refractive index of 2,46 (Malvern Dispersion & Refactive Index Guide) and imaginary refractive index (absorption) of 0,1 for the particles. A refractive index of 1,33 was used for the dispersing water medium. The mathematical transformation of the light diffraction pattern into a particle size distribution by the Malvern software used the 'Polydisperse Distribution' option that accommodates polymodal particle size distributions.

The optical performance of the instrument was verified by measuring a reticule (MSX65 No.816) using a procedure that is traceable to a NIST standard. The calibration measurements are compared to the certified measurements in the following table:

Table K1 Calibration data

	$D_v(0,1)$	$D_v(0,5)$	$D_v(0,9)$
Reticule measured on instrument (μm)	31,72	39,48	50,47
Reticule certified measurement (μm)	31,46	38,98	50,88
Measured variance (%)	0,83	1,28	-0,81
Certified specification variance (%)	±5	±2	±5

Measurement Procedure

It became clear during the analysis procedure that the samples introduced into the Mastersizer's dispersion receptacle were subject to aggregation and deaggregation phenomena. An experimental procedure was thus developed which made it possible to obtain relatively stable repeatable measurements of the particle size distribution of a sample. The procedure consisted of the following:

- The sample bath of the dispersion unit was flushed with tap water and drained.

- Approximately 1litre of demineralised water (4,0μS/cm) containing 0,3%m/m sodium hexametaphosphate (SHMP) was used to fill the sample bath. Pumping and stirring speeds were set at 60% of maximum settings. The SHMP acted as an effective stabiliser of the suspension preventing reagglomeration of particles.

- After instrument initialisation or cell window cleaning the detectors were aligned.

- The background was measured prior to each sample being introduced in the sample bath.

- The samples were then introduced into the sample bath in a slurry form to obtain an obscuration reading of between 10 and 30%. Reactor slurry samples were added directly from well-shaken sample bottles. Dry powder samples were mixed into a paste before being introduced to the sample bath.

- Five measurements were made lasting 5 seconds each during which time the sample was subjected to 2500 sweeps to determine the initial dispersion of the sample.

- The ultrasound (70W @40kHz) was switched onto a 100% setting for 2 minutes and 15 measurements were made. Note that the ultrasound power input into the sample holding chamber at this setting is estimated at 62,5kW/m^3.

- After switching the ultrasound off, five further measurements were made. The last of these measurements was regarded as the particle size distribution of the sample. The full suite of measurements gave qualitative and quantitative information on reproducibility and the stability of the suspension.

The above procedure was adopted as an optimum after assessing the effect of variables such as type of water, ultrasound intensity and duration, stabiliser addition and pumping speed on the measurements obtained. Measurements were generally not sensitive to the pumping and stirring speeds of the dispersion unit. However, ultrasound was required to obtain deaggregation of the manganese oxide/hydroxide particles and SHMP was required to prevent coalescence of the deaggregated particles. The effect of the ultrasound was more pronounced on dry samples that had been reslurried than on slurry samples taken directly from the reactor. A second application of ultrasound was tested during method development and was found to have no affect on dispersion, though with extended application (90 minutes) of ultrasound did reduce the measured particle size distributions. Details are presented in the following tables.

Repeatability

The repeatability of the method was determined by six repeat measurements of one sample each of slurry and dry solids. The mean and standard deviation of 5 measurements made on each of the 6 repeats (i.e. total of 30 readings) are shown in Table K2.

Table K2 Repeatability results

Slurry sample	$D_V(0,1)$	$D_V(0,5)$	$D_V(0,9)$	Solid sample	$D_V(0,1)$	$D_V(0,5)$	$D_V(0,9)$
Mean (μm)	1,50	3,06	5,26	Mean (μm)	0,39	1,64	4,28
Stdev (μm)	0,057	0,019	0,144	Stdev (μm)	0,02	0,02	0,06
Stdev/Mean	0,038	0,006	0,027	Stdev/Mean	0,062	0,011	0,014

Reproducibility

The reproducibility of the technique was tested by running the 6 repeat analyses on the same sample as above on a identical instrument from another laboratory. The mean and standard deviations of the instruments are compared below

Table K3 Reproducibility results

Machine A	$D_V(0,1)$	$D_V(0,5)$	$D_V(0,9)$	Machine B	$D_V(0,1)$	$D_V(0,5)$	$D_V(0,9)$
Mean (μm)	1,50	3,06	5,26	Mean(μm)	1,45	2,99	5,09
Stdev (μm)	0,06	0,02	0,14	Stdev (μm)	0,09	0,04	0,09
Stdev/Mean	0,038	0,006	0,027	Stdev/Mean	0,059	0,012	0,017

The repeatability of the second instrument is less than the first. The measurements are however all within the certified specifications of these machines.

The effect of extended treatment of a slurry sample with ultrasound can be seen in the following table.

Table K4 Effect of ultrasound on particle size measurements

Time (min)	$D_V(0,1)$ (μm)	$D_V(0,5)$ (μm)	$D_V(0,9)$ (μm)
0	1,51	3,03	5,1
20	1,03	2,57	4,71
60	0,54	1,55	3,64
85	0,31	0,94	6,91
90	0,36	1,13	4,14

These results clearly show that the slurries are unstable to extended treatment of ultrasound confirming the aggregated nature of these materials. The results therefore indicate that repeatable results can be obtained for relative comparison purposes if the analytical procedure is followed consistently. Results for measurements made on slurries drawn from the reactor during hydrothermal oxidation of manganous hydroxide are shown in the Table K5 with distributions plotted in Figures K1 to K9.

Table K5 $D_v(0,1)$, $D_v(0,5)$, $D_v(0,9)$ moments of Malvern particle size distributions for oxidation samples

pH_2	600			600			600		
Sample	$D_v(0,1)$	$D_v(0,5)$	$D_v(0,9)$	$D_v(0,1)$	$D_v(0,5)$	$D_v(0,9)$	$D_v(0,1)$	$D_v(0,5)$	$D_v(0,9)$
1	0.91	4.00	15.4	0.88	2.87	9.88	0.89	2.85	9.3
2	0.37	1.34	6.42	0.63	2.32	11.5	0.47	1.91	12.9
3	1.47	3.38	5.71	0.93	2.26	4.51	0.83	2.35	4.63
4	1.8	3.72	6.11	1.54	3.55	6.06	1.69	3.58	5.91
5	1.79	3.72	6.15	1.84	3.73	6.09	1.78	3.67	5.98
pH_2	800			800			800		
Sample	D_{10}	D_{50}	D_{90}	D_{10}	D_{50}	D_{90}	D_{10}	D_{50}	D_{90}
1	0.94	3.28	11.2	0.88	2.76	8.62	0.90	2.97	9.35
2	0.37	1.28	5.66	0.42	1.6	12.1	0.55	1.87	9.56
3	0.75	2.51	4.85	0.88	2.41	4.73	0.73	2.54	4.75
4	1.83	3.73	6.10	1.66	3.61	5.94	1.78	3.61	5.80
5	1.78	3.67	5.98	1.93	3.81	6.06	1.71	3.62	5.97
pH_2	1000			1000			1000		
Sample	D_{10}	D_{50}	D_{90}	D_{10}	D_{50}	D_{90}	D_{10}	D_{50}	D_{90}
1	0.89	2.85	9.65	0.88	2.73	10.7	0.87	2.78	11.6
2	0.50	1.50	4.82	0.55	1.83	9.93	0.52	2.18	22.7
3	0.79	2.56	4.74	0.71	2.47	4.61	0.83	2.34	4.62
4	1.88	3.75	6.07	1.82	3.71	6.03	1.69	3.61	5.92
5	1.87	3.72	6.00	1.99	3.84	6.15	1.80	3.68	5.95

Figure K1 Particle Size Frequency Distributions for pH_2*600 Experiment 1

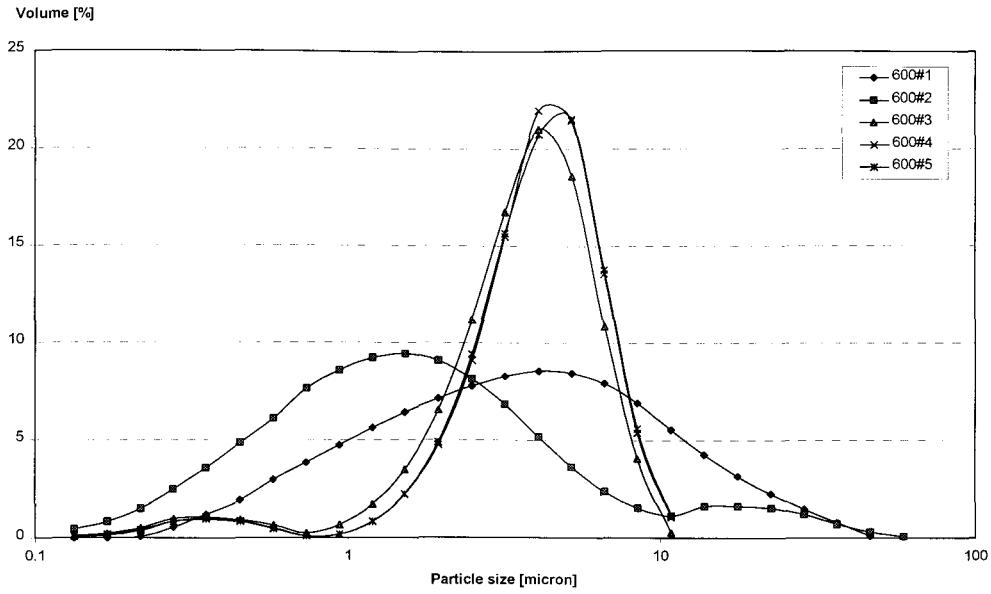

Figure K2 Particle Size Frequency Distributions for pH_2*600 Experiment 2

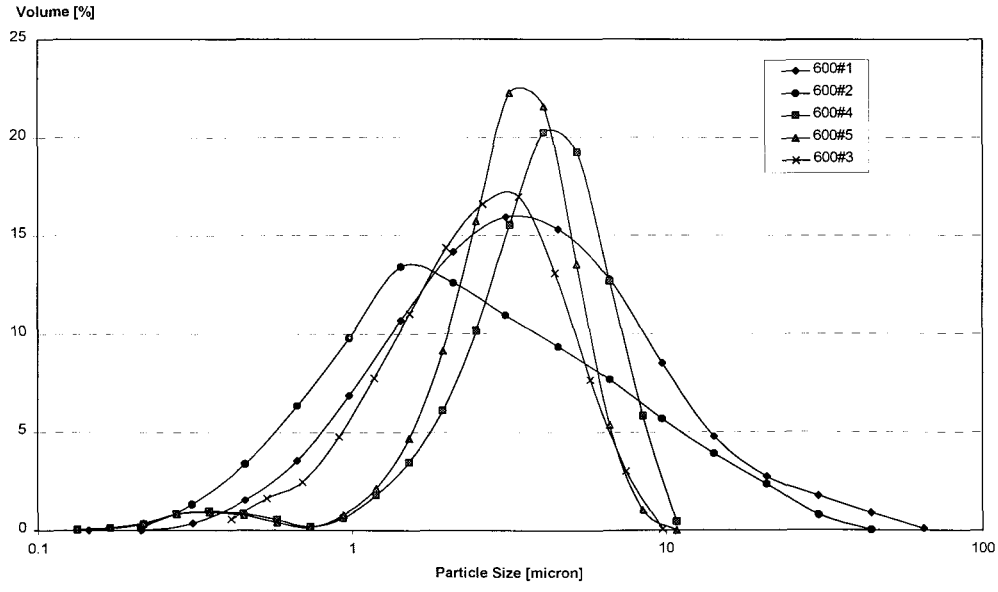

Figure K3 Particle Size Frequency Distributions for pH_2*600 Experiment 3

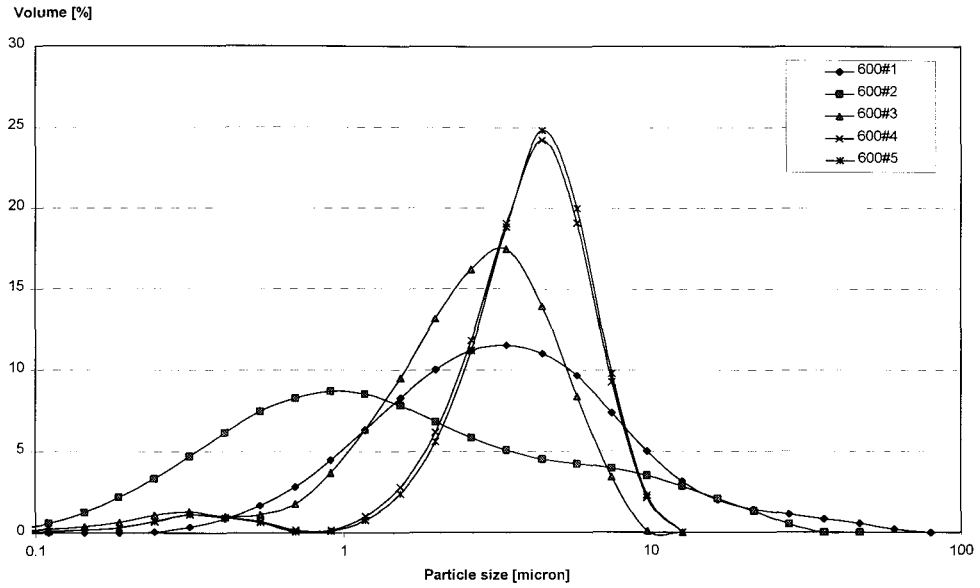

Figure K4 Particle Size Frequency Distributions for pH_2*800 Experiment 1

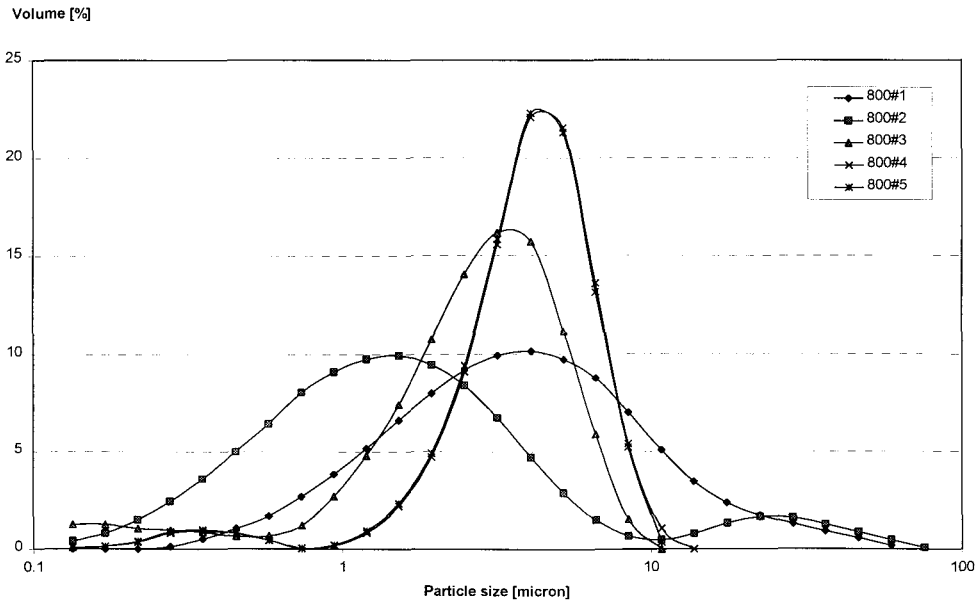

Figure K5 Particle Size Frequency Distributions for pH_2*800 Experiment 2

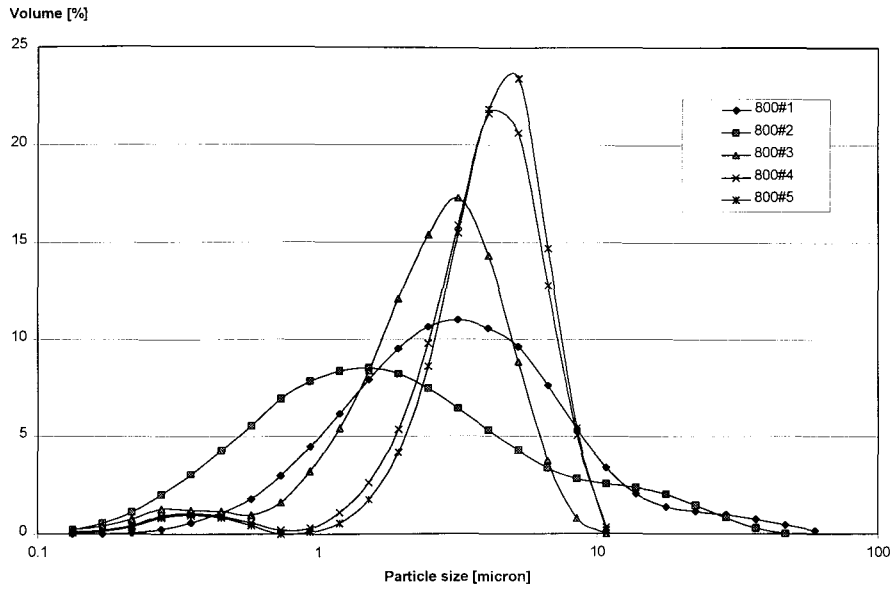

Figure K6 Particle Size Frequency Distributions for pH_2*800 Experiment 3

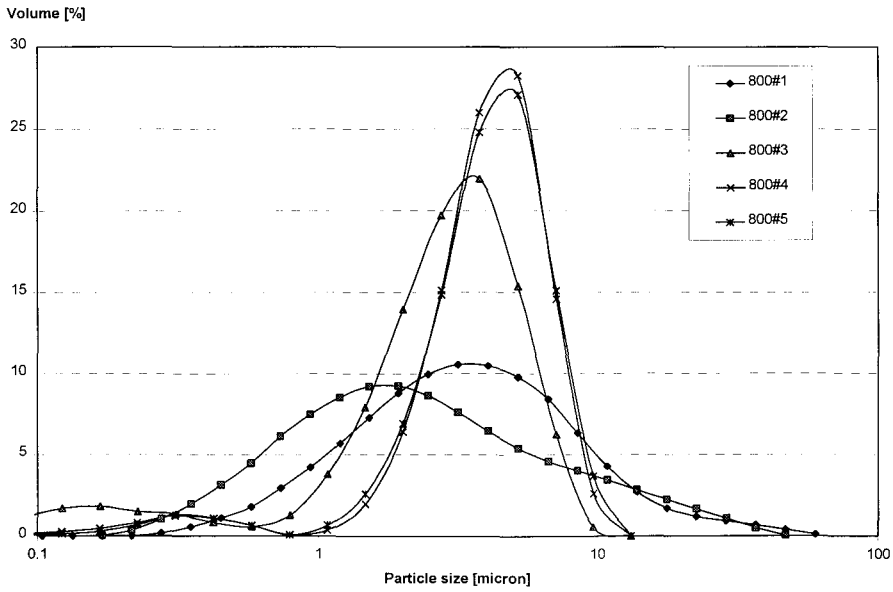

Figure K7 Particle Size Frequency Distributions for pH_2*1000 Experiment 1

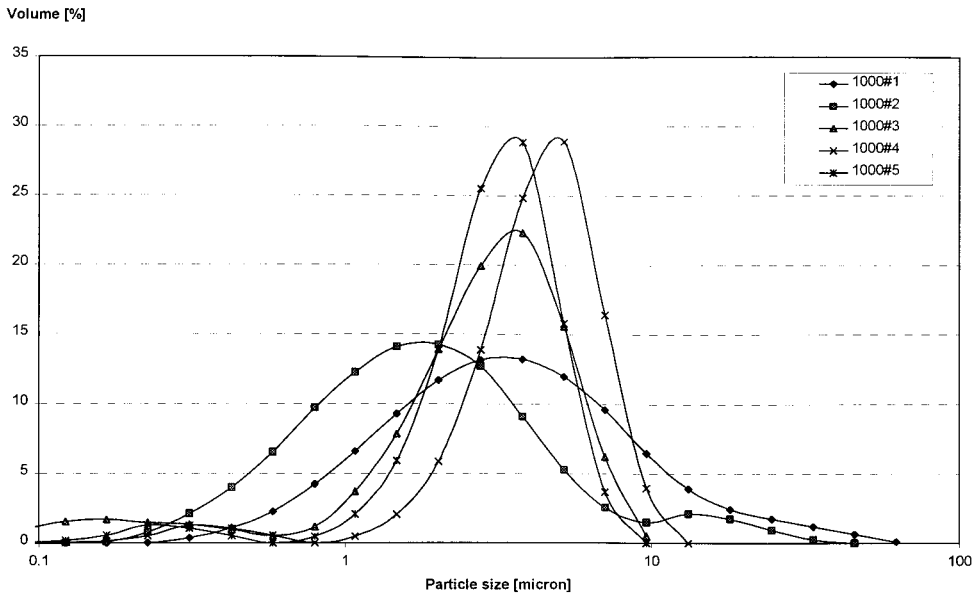

Figure K8 Particle Size Frequency Distributions for pH_2*1000 Experiment 2

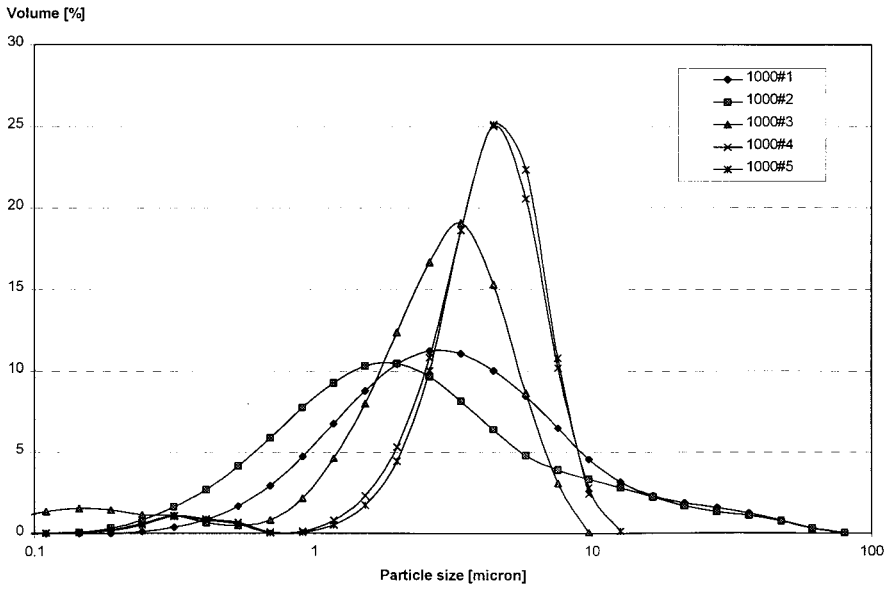

Figure K9 Particle Size Frequency Distributions for pH_2*1000 Experiment 3

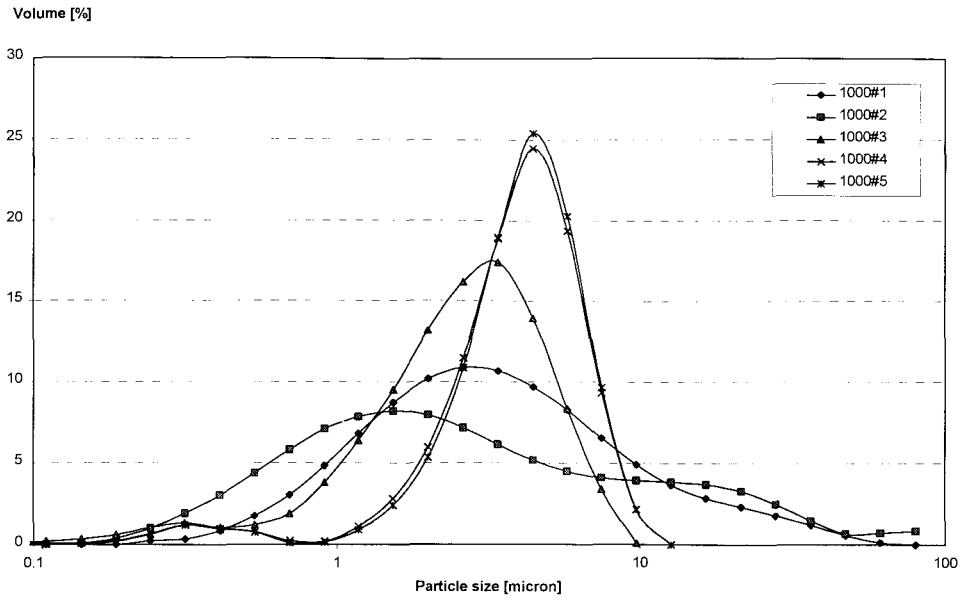

Particle size analysis of dried manganese oxide

The particle size distributions measured on samples that had been taken from the reactor and dried before being redispersed in the Malvern dispersing system for analysis were found to be different to the slurry samples measured directly for particle size distribution. These differences also depended on the extent of oxidation that the hydroxide underwent in the reactor and on the drying procedure employed.

In Figure 4.3 it can be seen that when a hydroxide sample not exposed to oxidation in the reactor is filtered, dried and redispersed, a particle size distribution that is coarser than the original slurry is obtained. A separate experiment was conducted where the slurry sampled at different oxidation time intervals was split, one half was filtered, dried and crushed by hand to a powder while the other was analysed directly. Both the slurry and the dry material were analysed with the comparative results for the small size fractions being shown in Table K6.

Table K6 Comparison of fine fractions for slurry and dried samples

Oxidation time [hrs]	Dry & redispersed solids [Cum %<1,0μm]	Slurry sample [Cum %<1,0μm]
0	15	8
1	22	38
2	31	16
3	17	5
4	15	3

The table shows that the small size distributions follow a similar trend, first increasing and then decreasing, although in the case of the dry sample significantly more fines were obtained in the dry sample at the end of oxidation than in the case of the slurry sample (15% c.f. 3%). This suggests that the sample drying process affects the state of aggregation of particles.

Typically 40-45%<1,0μm was obtained for samples that had been pressed wet into a pellet, dried, crushed and screened at 45μm. Subjecting dried oxide to milling resulted in further deaggregation and larger proportions of the <1,0μm sized particle fraction. The formation of higher proportions of fines became more pronounced when the material had been subjected to milling.

Two methods were used for measuring the particle size distribution of milled material as further verification of the particle size analytical procedure and to assess the extent of change in aggregation. The results of these measurements are shown in Figure K10.

Figure K10 Comparison of different methods of particle size analysis

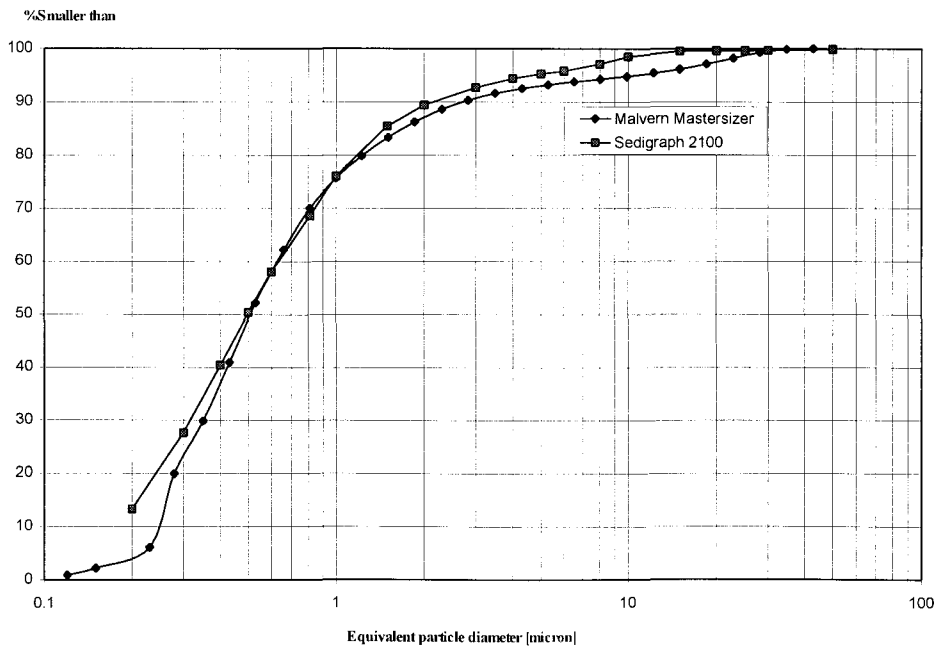

The Malvern Mastersizer® relies on Rayleigh laser light scattering from particles and is capable of wet and dry measurements. The Sedigraph® 2100 measures the Stokes sedimentation rate of particles using a pulsed X-ray source. The pycnometric density of the material was measured separately and was entered at the data processing stage to produce a particle size distribution based on the masses of particles present. For these

measurements a fully oxidised sample from the reactor was filtered, dried at 120°C in air and milled in a high energy pinmill.

A comparison is made in Figure K11 of the particle size distributions obtained by analysing a reactor sample as a slurry directly with the dried redispersed sample. The Sedigraph and Malvern readings give similar particle size distributions which can be expected for materials that have no variation of solid density with respect to particle size. Non-porous materials generally conform to this requirement. The variation of density with particle size in submicron sized porous materials can however be significant.

Figure K11 Comparison of wet and dry analysis of mangano-manganic oxide particles

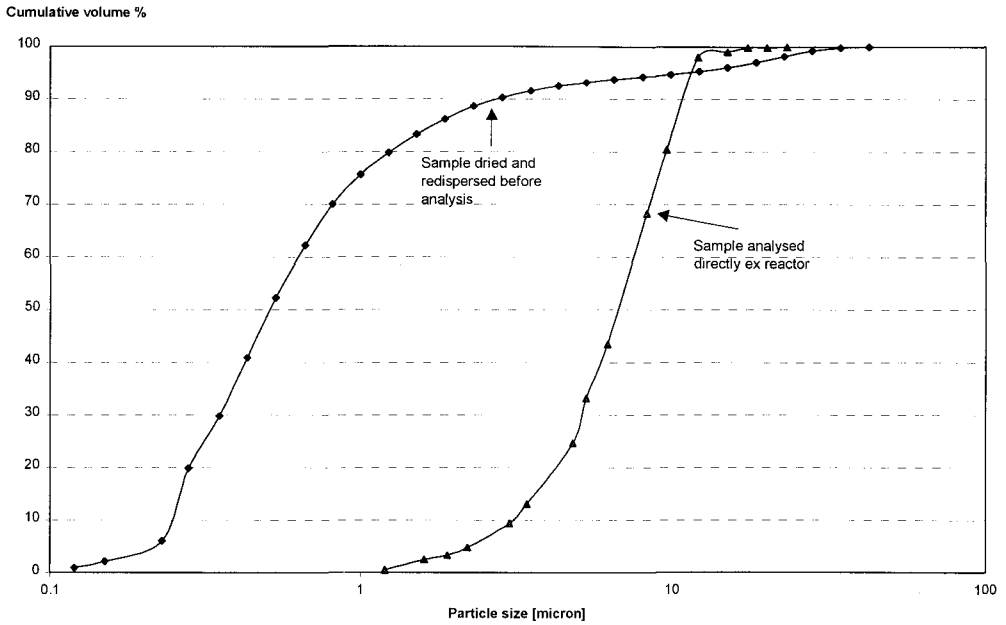

The presence of a small fraction (1-2%) of particles larger than 20μm in Figure K11 indicates that limited aggregation occurs after the material has been discharged from the reactor. Dewatering and drying occurs under relatively high compressive loads that could result in limited aggregation of particles. This effect is thus not indicative of any process occurring within the reactor. The dried material shows a wider distribution of particle sizes and significantly more small particles (~75%<1,0μm) present than in slurry samples (~<1%<1,0μm).

The above measurements show that the extent of dispersion of the dried oxide is dependent on the extent of oxidation and the sample preparation procedure used before particle size analysis. In addition, substantially higher proportions of fully oxidised fine fractions are present in comparison to slurry samples. This is due to the combination of

milling the product and the postulate that the crystallites are not substantially bonded by solid bridges between the aggregates. The binding forces in these particles may consist of the interfacial tension of water, van der Waals and electrostatic forces. The interfacial tension forces generally are larger than the van der Waals or electrostatic forces. Collapse of the aggregate occurs upon removal of the interfacial tension with dewatering. The desegregated particles from this process are dispersed relatively easily when the particles are resuspended for the particle size measurement.

In conclusion, the method of particle size analysis by laser light diffraction can quantitatively measure the extent of dispersion of aggregated powders that have been subjected to a range of different processing conditions and provide qualitative assessment of the strength of the aggregates. Reproducible measurements of particle size distribution could be obtained on slurries analysed directly. These quantitative results can be used for relative comparisons of changes in particle morphology. It is essential that the results of particle size analyses of these types of material should always be reported together with some quantification of the mechanical strength of the material.

Scanning Electron Microscopy

A LEO S440 scanning electron microscope was used to examine samples of Mn_3O_4 material. The images obtained are shown below. All samples were mounted onto an aluminium stub and coated with a thin-layer of gold-palladium alloy to provide a conductive surface. Different sample mounting procedures were used. A sample of unfiltered slurry was mounted by smearing onto an aluminium stub. Dried powder was applied directly for the second mount.

Figure K12 SEM Image of slurry sample at low magnification

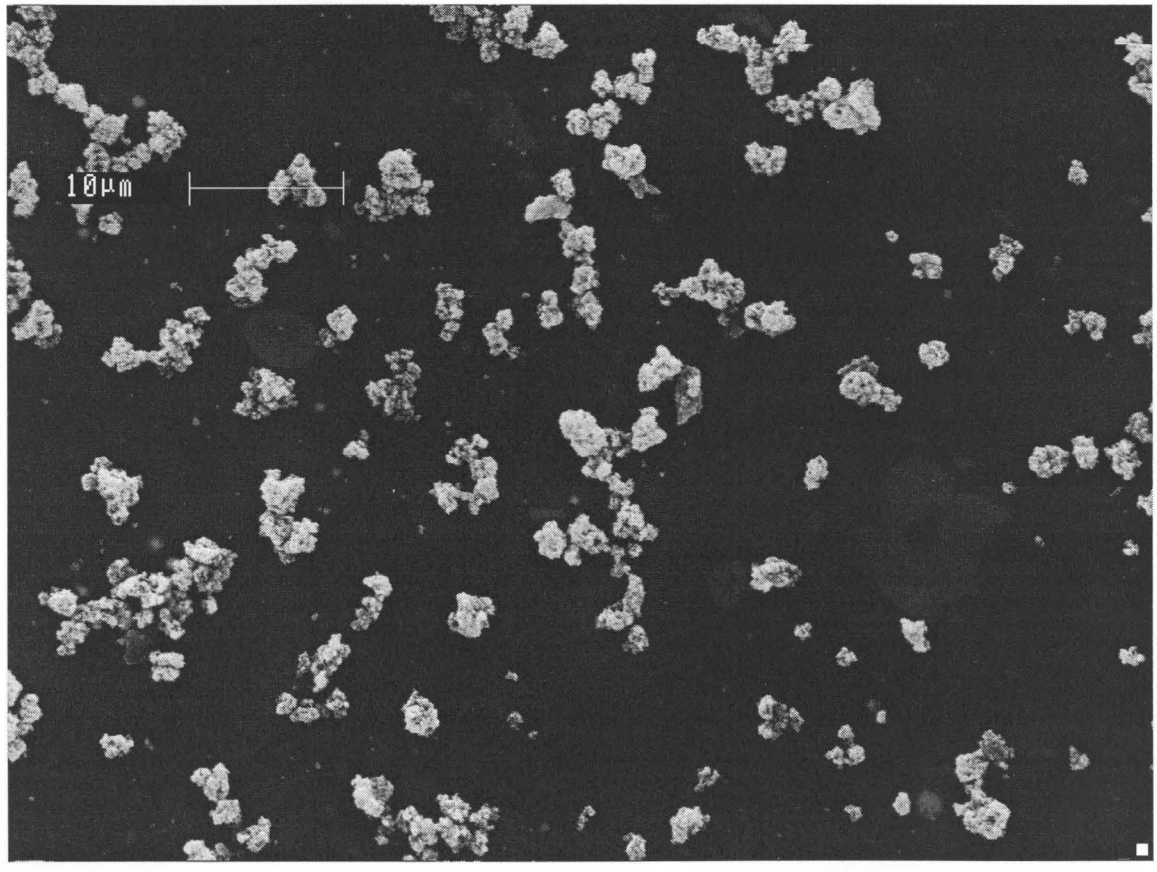

Figure K13 SEM image of slurry sample at high magnification

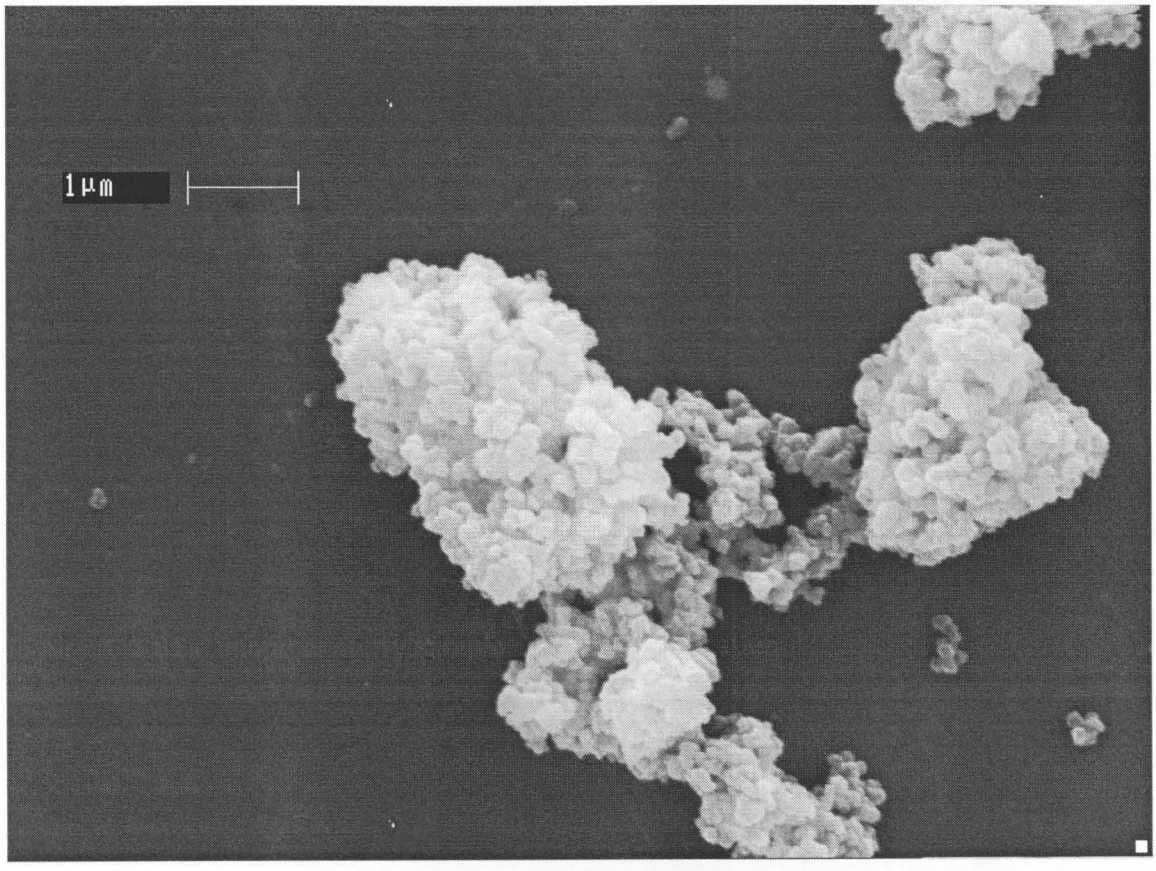

Figure K14 SEM images of dried material at high magnification

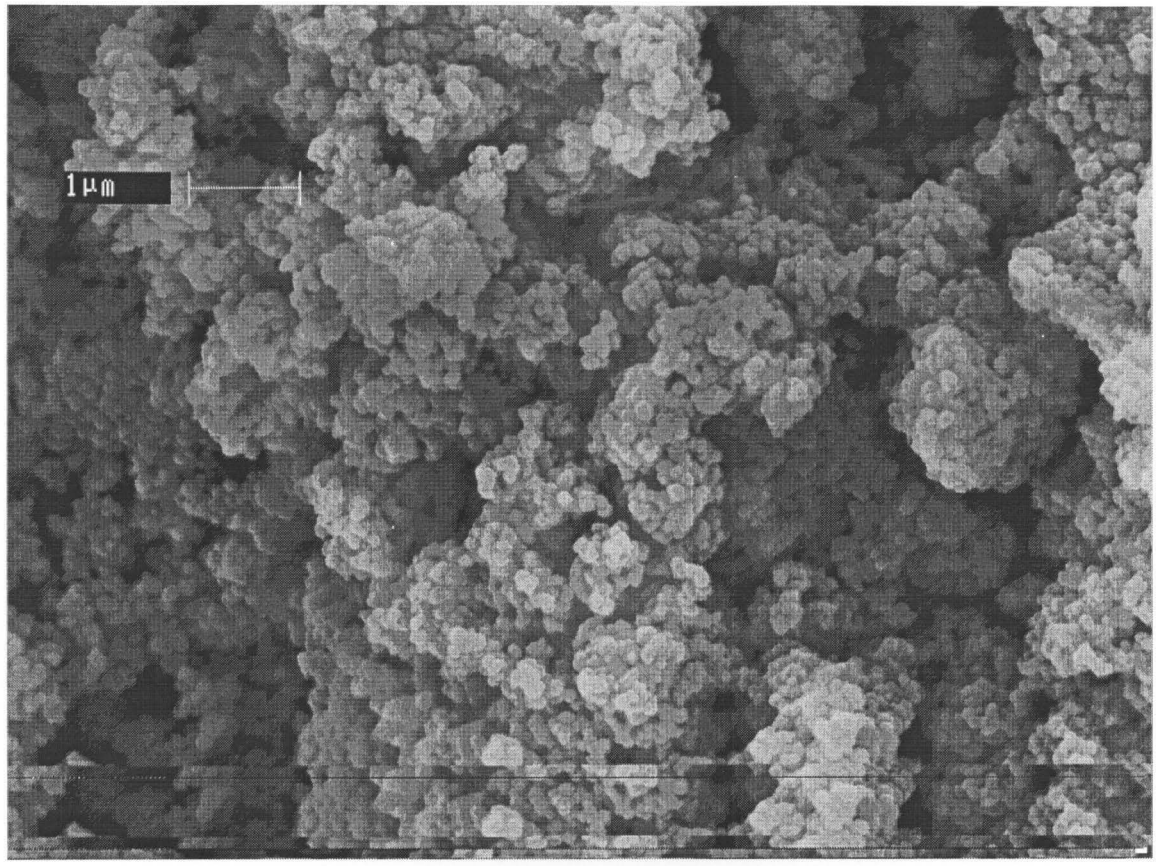

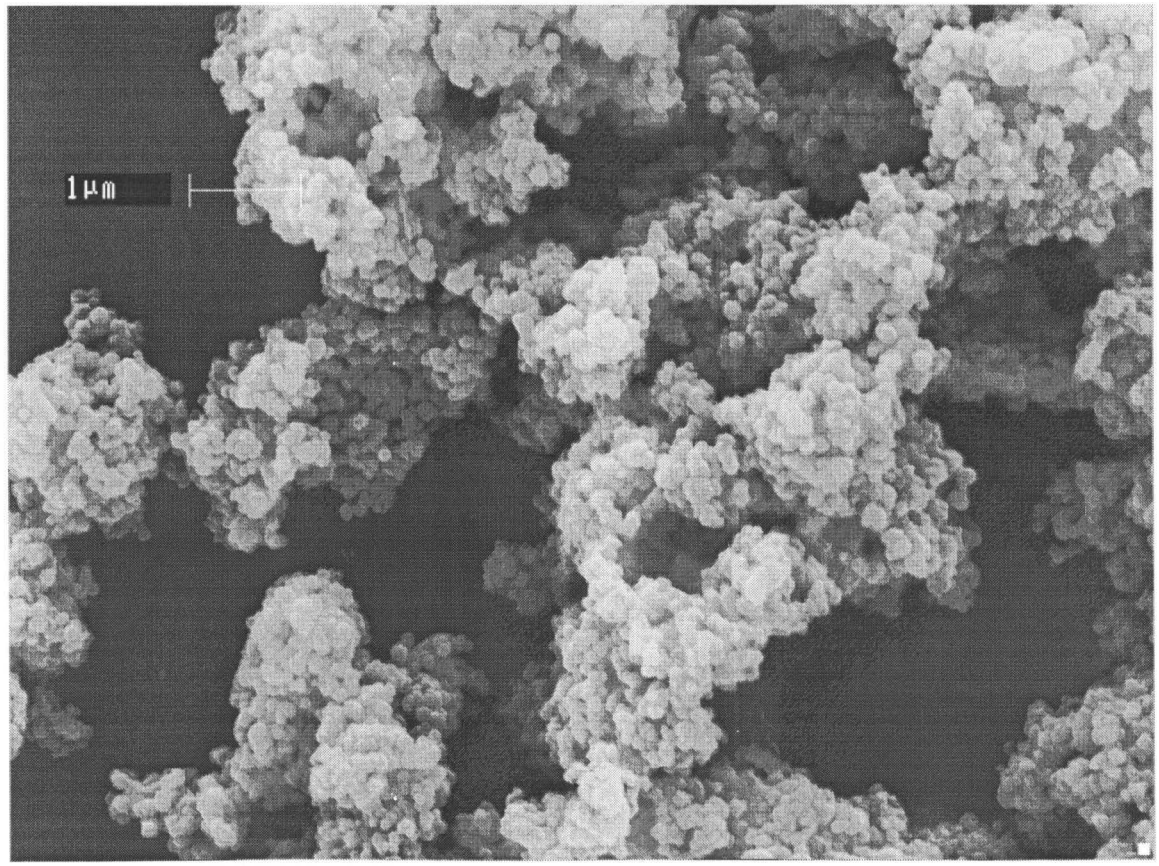

Appendix L

X-ray Diffraction Traces for Freeze Dried Oxidation Intermediate Samples

Sample 1 (0 minutes)

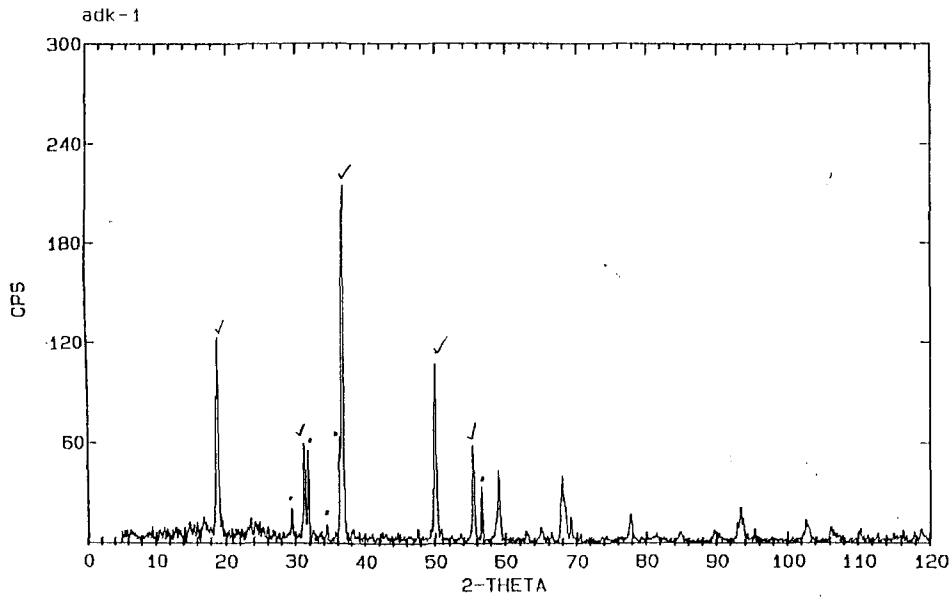

Sample 2 (30 minutes)

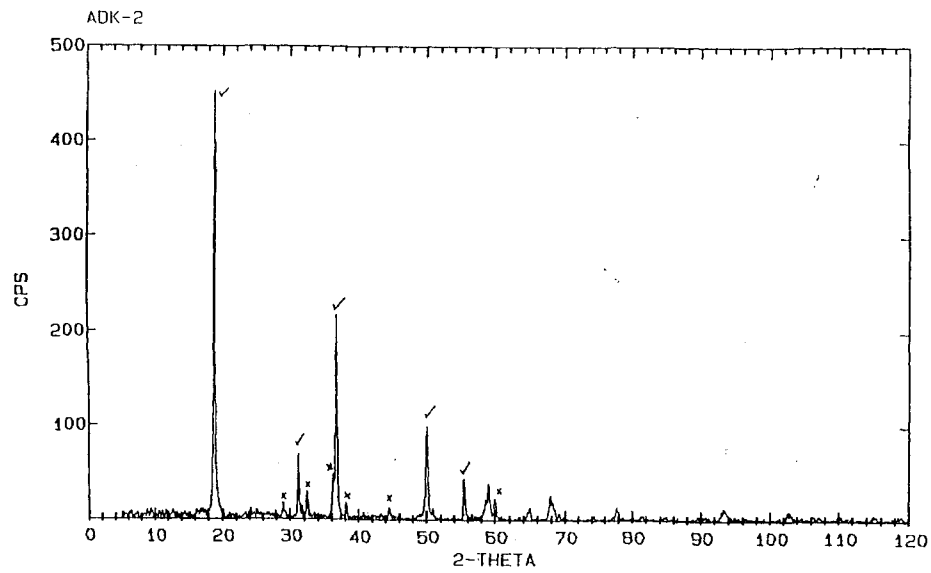

Appendix L

X-ray Diffraction Traces for Freeze Dried Oxidation Intermediate Samples

Sample 3 (60 minutes)

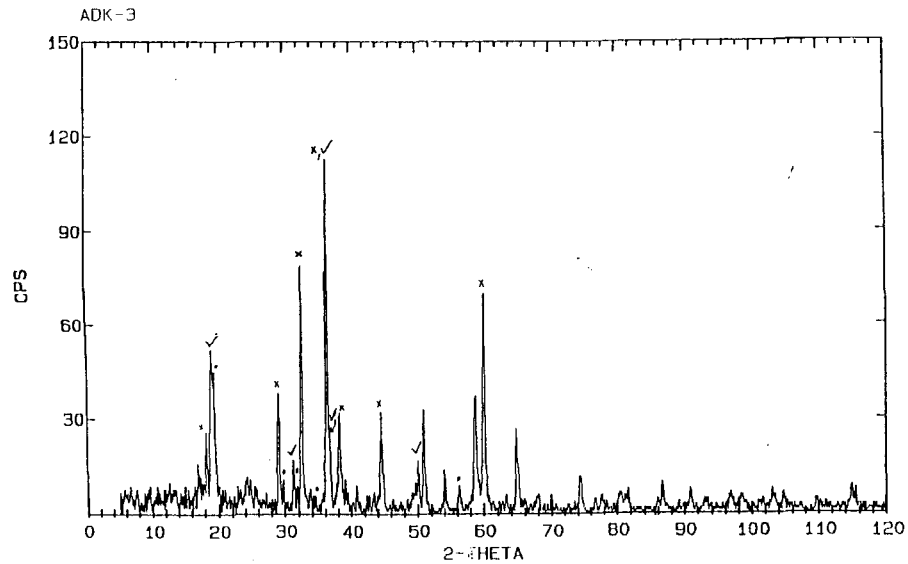

Sample 4 (90 minutes)

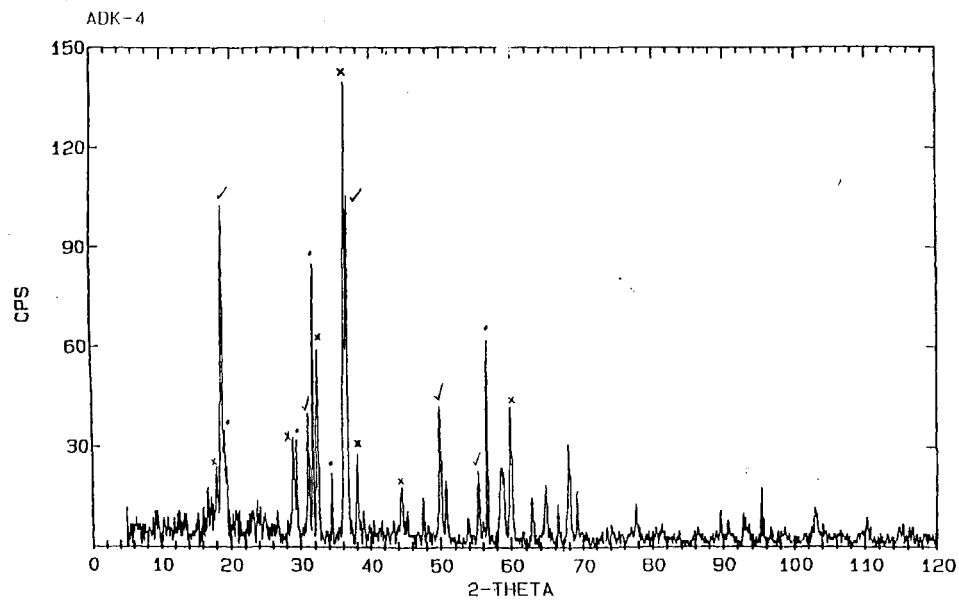

Appendix L

X-ray Diffraction Traces for Freeze Dried Oxidation Intermediate Samples

Sample 5 (120 minutes)

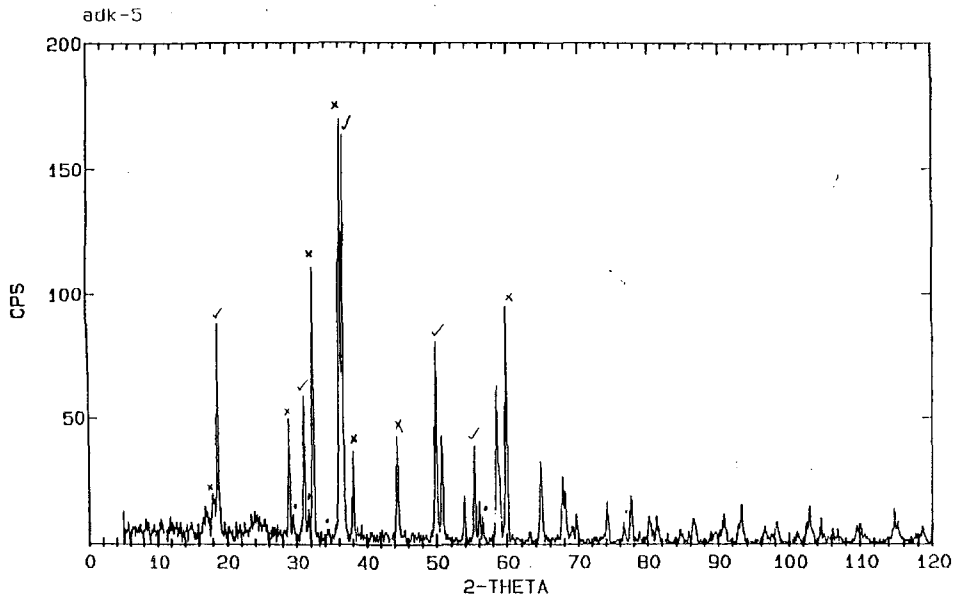

Sample 6 (150 minutes)

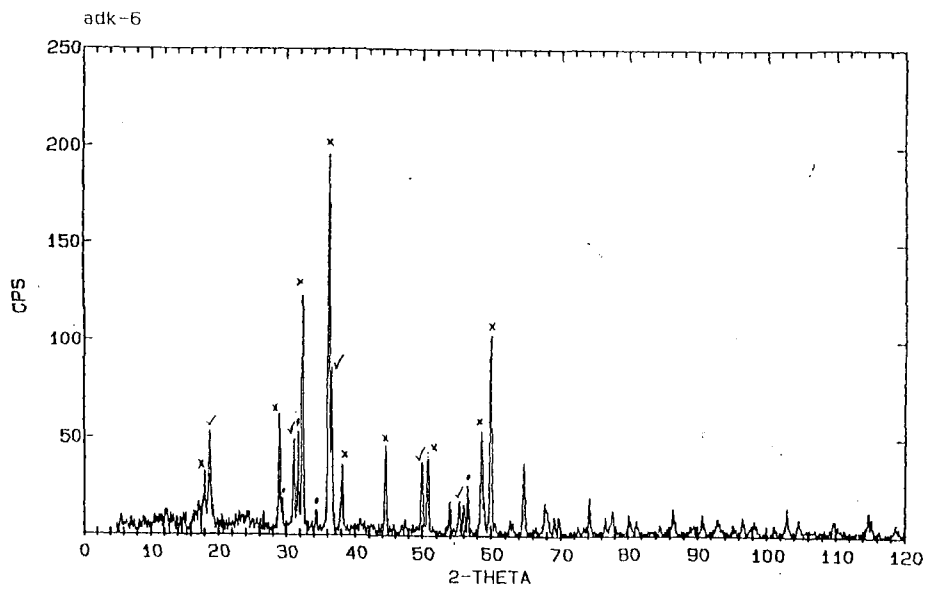

Appendix L

X-ray Diffraction Traces for Freeze Dried Oxidation Intermediate Samples

Sample 7 (170 minutes)

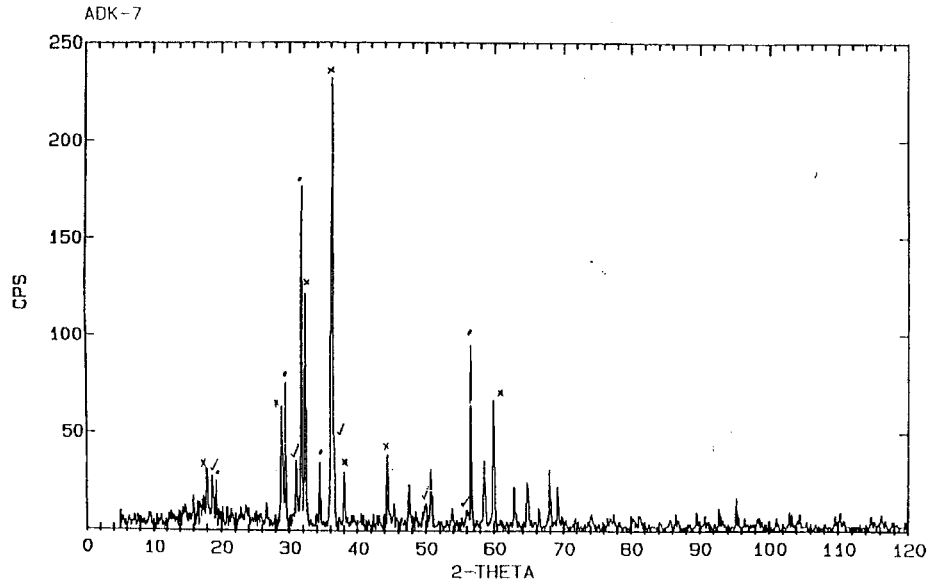

Unidentified Phase
Obtained from Sample 7-Sample 2 $Mn(OH)_2$-Single phase Mn_3O_4

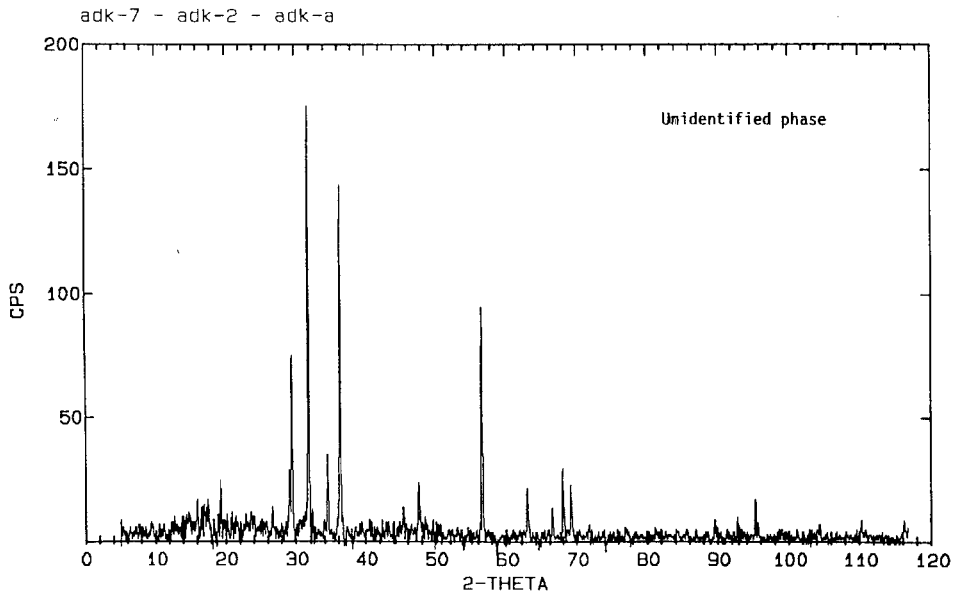

Appendix M

X-ray Diffraction Traces for Oxidation Intermediates Dried in Air

0 minute sample

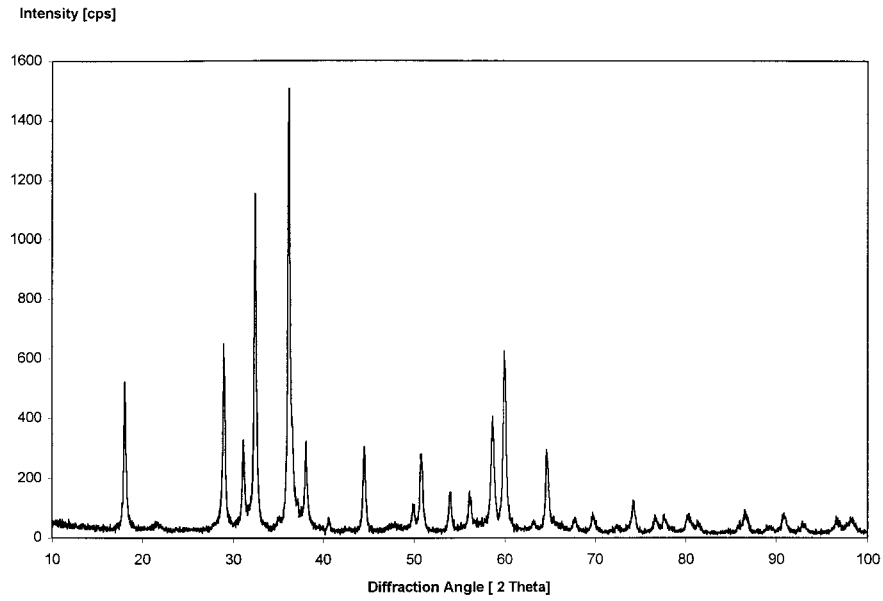

30 minute sample

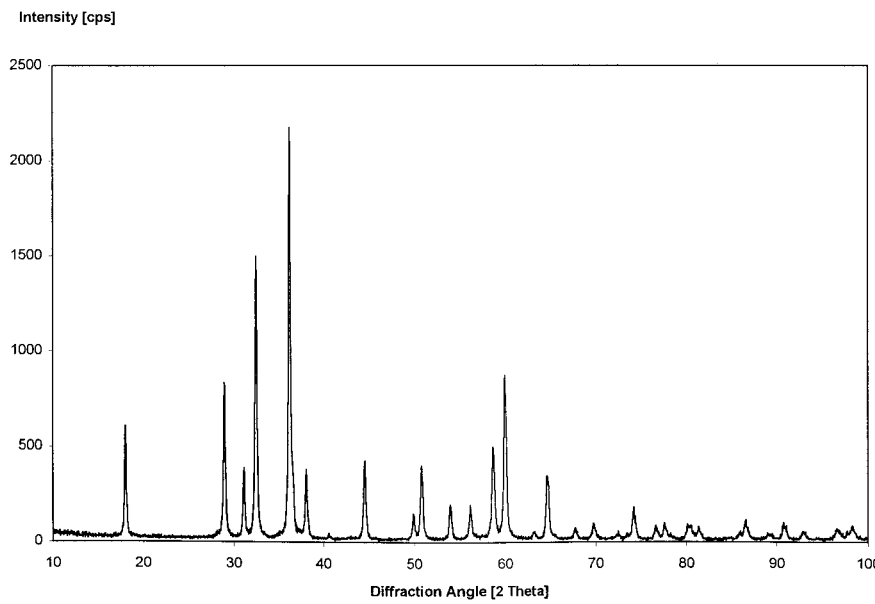

Appendix M

X-ray Diffraction Traces for Oxidation Intermediates Dried in Air

60 minute sample

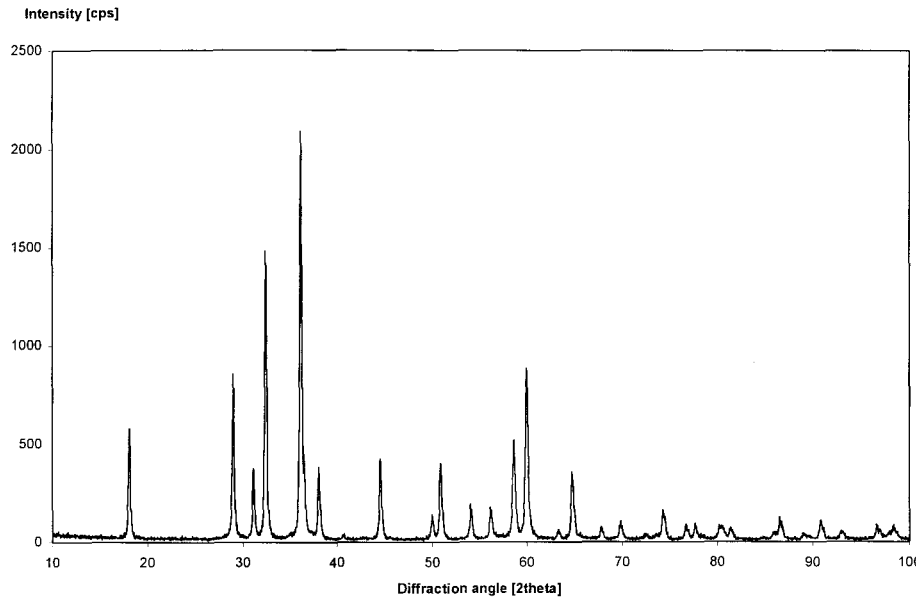

90 minute sample

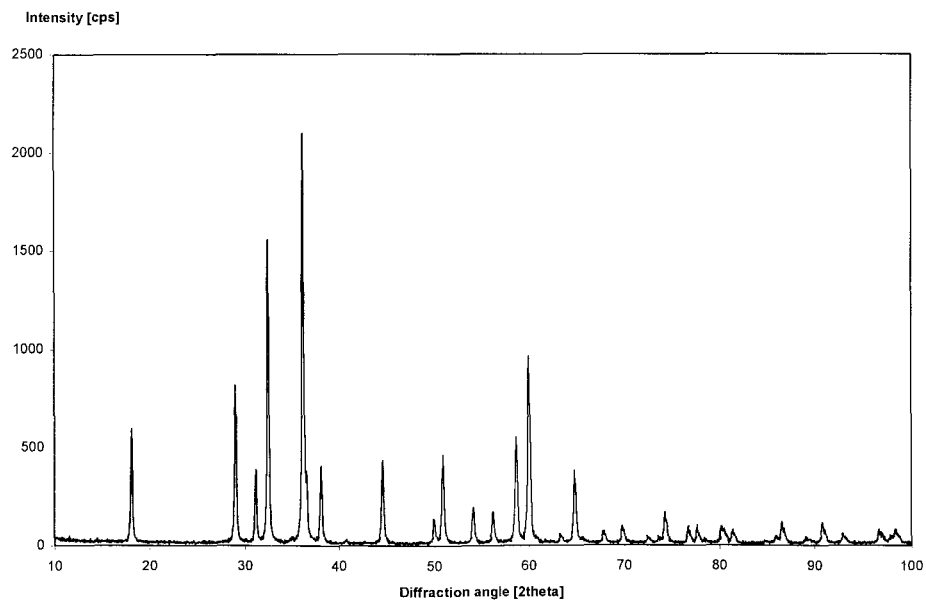

Appendix M

X-ray Diffraction Traces for Oxidation Intermediates Dried in Air

120 minute sample

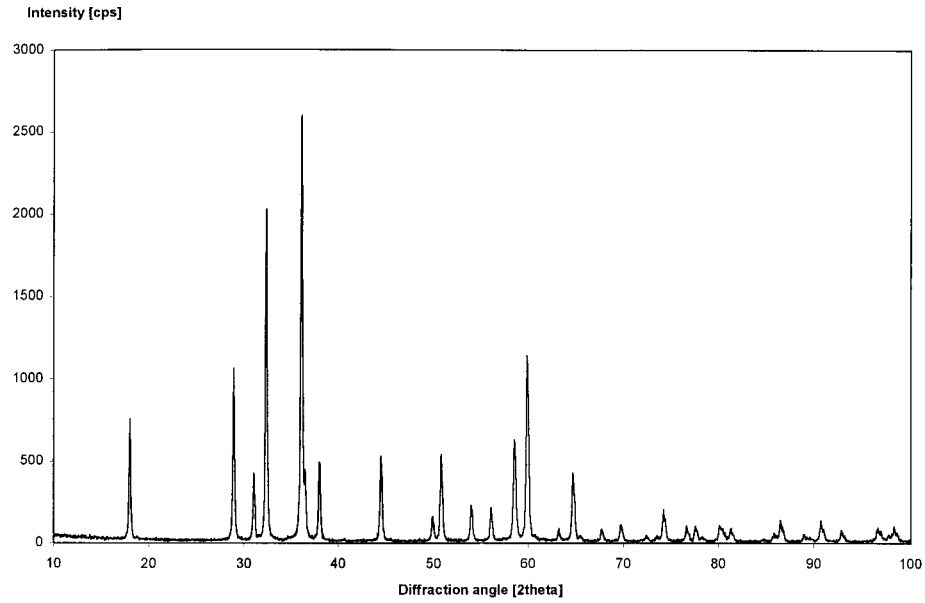

150 minute sample

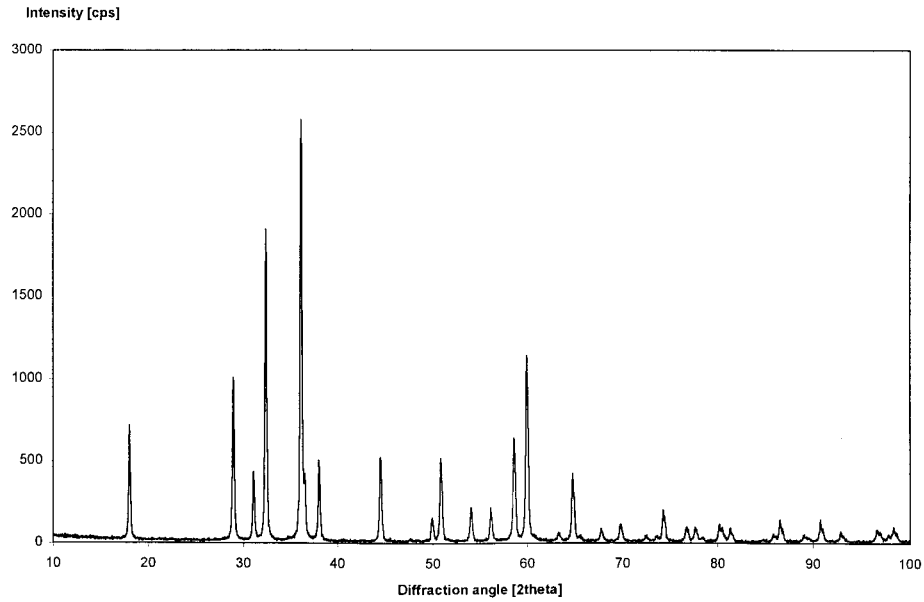

Appendix M

X-ray Diffraction Traces for Oxidation Intermediates Dried in Air

165 minute sample

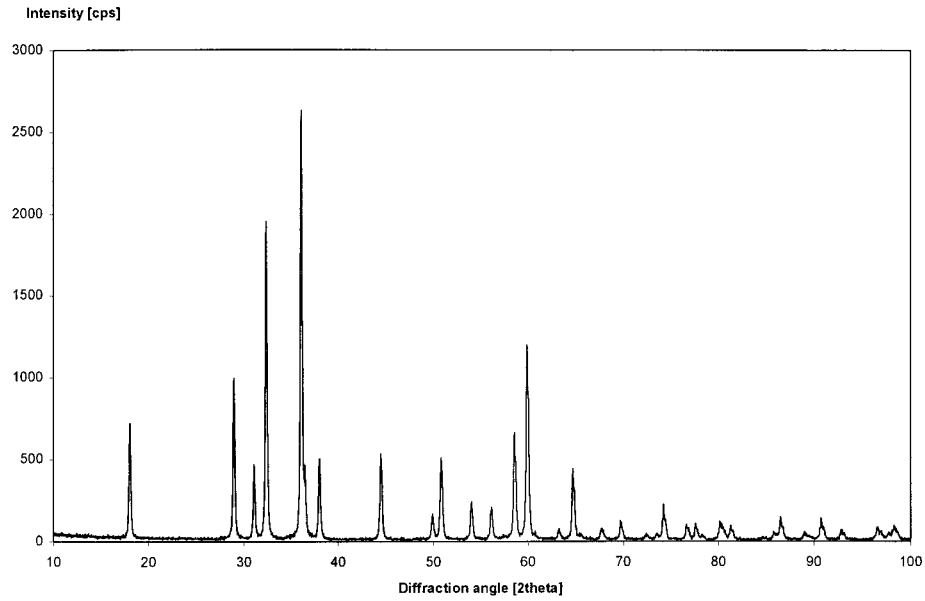

Discharge sample

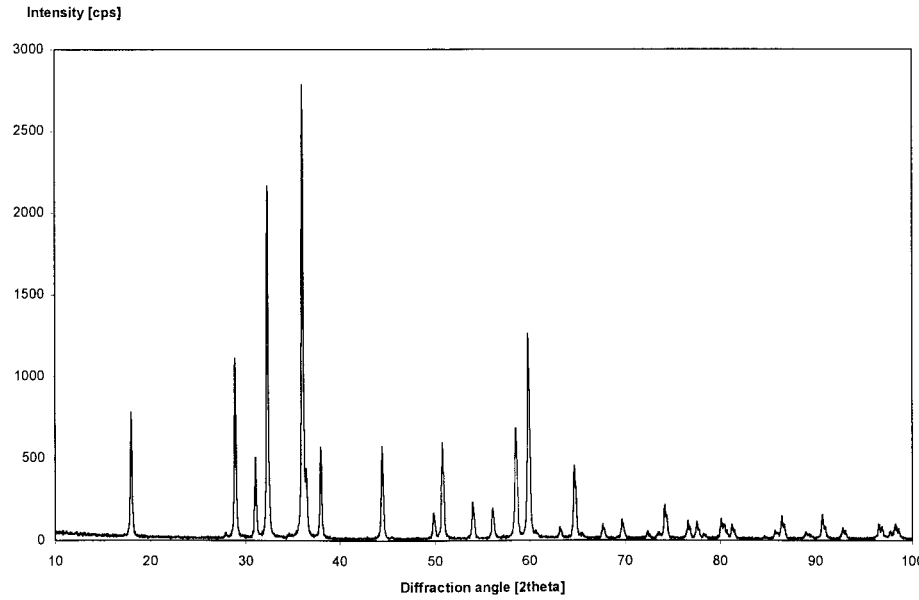

Appendix M

X-ray Diffraction Traces for Oxidation Intermediates Dried in Air

Calcined sample

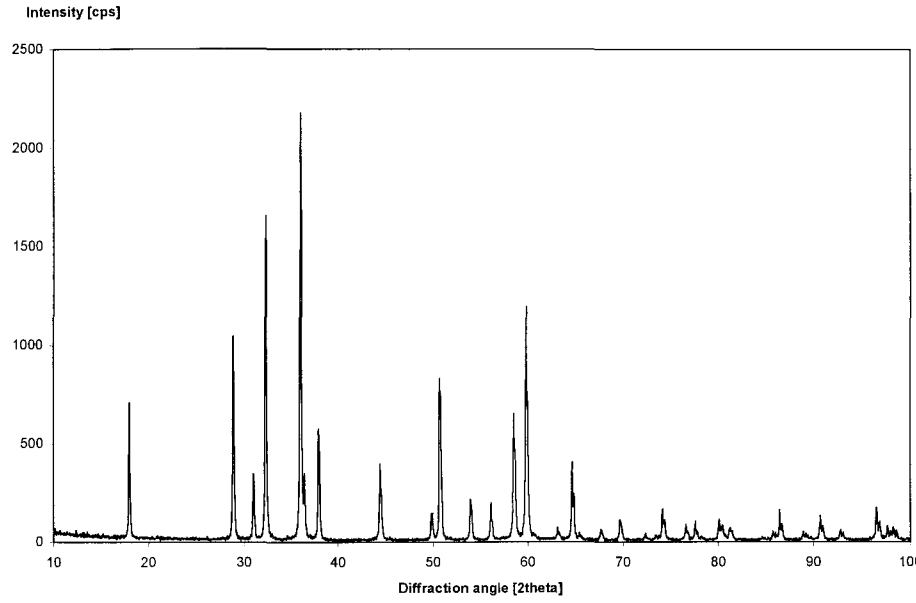

Appendix M

Table M1 Relative intensity patterns of air dried oxidation intermediates

Intermediate oxidation samples							Completely oxidised samples				
Oxidation time (minutes)											
0	30	60	90	120	150	165	Disch	Calcd	JCPDS 24-734		
I/I_o	I/I_o	I/I_o	I/I_o	I/I_o	I/I_o	I/I_o	I/I_o	I/I_o	d Å	I/I_o	[hkl]
35,2	27,5	28,0	26,9	26,6	24,7	25,1	25,8	28,7	4,9240	30	101
43,8	39,0	40,8	36,4	41,1	35,6	37,3	41,6	47,4	3,0890	40	112
22,8	16,5	19,0	17	16,8	16,0	18,5	16,5	16,3	2,8810	17	200
79,0	68,7	74,3	72,9	77,2	68,3	75,9	77,9	76,2	2,7680	85	103
100,0	100,0	100,0	100	100,0	100,0	100,0	100,0	100,0	2,4870	100	211
26,5	16,9	22,1	17,5	17,4	14,5	17,1	14,8	15,6	2,4630	20	202
22,4	17,3	20,1	19,6	19,6	21,0	19,0	21,7	28,0	2,3670	20	004
5,2	2,2	1,8	1,6	1,1				0,9			
21,6	20,7	23,4	21,6	22,5	21,0	21,0	22,0	20,1	2,0369	20	220
								1,7	1,9962	1	213
7,5	7,7	7,6	7,8	6,9	6,2	6,6	7,0	7,4	1,8288	7	204
22,0	20,8	20,7	23,3	22,5	21,2	20,8	24,6	43,0	1,7988	25	105
2,6	1,9		1,6			0,9					
12,4	10,1	10,6	9,7	10,3	9,1	10,2	9,1	11,2	1,7008	10	312
4,6				2,2	1,7	0,8		0,9			
12,8	9,6	9,3	9,1	9,6	9,6	8,7	8,2	10,4	1,6405	8	303
29,2	25,9	27,6	28,1	27,1	27,5	28,4	28,3	33,8	1,5762	25	321
46,6	47,3	48,3	51,7	51,8	48,4	52,0	52,0	61,5	1,5443	50	224
3,8		3,2	2,9	1,7		2,3	2,4	2,5	1,5260	2	215
4,2	2,7	3,2	2,9	3,7	2,9	3,0	3,5	3,7	1,4721	3	116
23,3	18,6	20,8	21,7	19,2	18,5	19,6	18,7	21,5	1,4405	20	400
5,1	2,4	2,4	1,7	1,8	1,6		1,6	2,7	1,4260	3	323
4,3		1,5			0,9		0,9				
							3,6	2,4	1,3841	4	206

Appendix M

TableM2 Simulated and experimental powder diffraction patterns for defect Mn_3O_4

	Simulated powder diffraction peak intensities							Experimental patterns		
hkl	Mod.1	Mod.2	Mod.3	Mod.4	Mod.5	Mod.6	Mod.7	Disch	Calcd	JCPDS 24-734
101	1	34	11	4	17	9	7	26	29	30
112	40	20	29	36	26	31	33	42	47	40
200	17	8	12	15	11	13	14	17	16	17
103	68	68	68	68	68	68	68	78	76	85
211	100	100	100	100	100	100	100	100	100	100
202	4	13	8	7	11	9	10	15	16	20
004	16	32	23	17	24	20	18	22	28	20
220	18	37	27	19	28	23	21	22	20	20
204	8	4	6	7	5	6	6	7	7	7
105	17	17	17	17	17	17	17	25	43	25
312	12	6	9	11	8	9	10	9	11	10
303	12	12	12	12	12	12	12	8	10	8
321	21	21	21	21	21	21	21	28	34	25
224	55	61	58	54	57	55	53	52	62	50
400	21	23	22	20	21	21	20	19	22	20

hkl	Miller indices
Model 1: $Mn_{2,67}O_4$	octahedral vacancies only
Model 2: $Mn_{2,67}O_4$	tetrahedral vacancies only
Model 3: $Mn_{2,67}O_4$	tetra. + octa. vacancies
Model 4: $Mn_{2,83}O_4$	octahedral vacancies only
Model 5: $Mn_{2,83}O_4$	tetrahedral vacancies only
Model 6: $Mn_{2,83}O_4$	tetra. + octa. vacancies only
Model 7: Mn_3O_4	no vacancies

APPENDIX N

Structural Models For Compact And Porous Particle Size Distributions Base Model

Spherical Dense Model				as $Mn(OH)_2$
BET	m^2/gm	18	1.236	22.248
Skeletal density	kg/m^3	4720		3258
Specific volume	m^3/kg	2.119E-04		3.07E-04
Equivalent diamet	micron	0.071		0.083
Corrected diamete	micron	0.071	as Mn_3O_4	
		0.041	as $Mn(OH)_2$	

Packing efficiencies-infinite lattices

	k	*e*
Random loose		0.445
Random close packed	6	0.364
Primitive cubic	6	0.4764
Orthorhombic	8	0.3954
Tetragonal spheroid	10	0.3019
Rhombohedral (hexag	12	0.2595
Tetragonal	12	0.2595

Particle size [um]	Volume Distn.%	Number Distn.%	ensity [kg/m³]	Mass Dist.%	Area Distn.%	Number of part	Mass of part	Area of part
20.70	0.00	0.0	3258	0.0	0.0	0.00000	0	0
15.65	0.20	0.0	3258	0.2	0.0	0.00010	1401	0.2
12.05	1.00	0.0	3258	1.0	0.3	0.00109	7007	1.1
9.35	3.10	0.0	3258	3.1	1.0	0.00724	21722	4.3
7.30	10.90	0.1	3258	10.9	4.6	0.05351	76376	19.3
5.70	18.70	0.4	3258	18.7	10.0	0.19285	131031	42.3
4.45	20.00	0.9	3258	20.0	13.8	0.43346	140140	58.0
3.45	18.60	1.9	3258	18.6	16.5	0.86508	130330	69.6
2.70	14.30	3.0	3258	14.3	16.2	1.38754	100200	68.3
2.15	5.30	2.2	3258	5.3	7.5	1.01850	37137	31.8
1.70	1.80	1.5	3258	1.8	3.2	0.69972	12613	13.7
1.35	1.50	2.5	3258	1.5	3.4	1.16437	10510	14.3
0.6	4.6	87.5	3258	4.6	23.5	40.67293	32232	98.9
	100.0	100.0		100.0	100.0	46.49641	700699	421.8

Filling of sphere by sphere (Heintz et al 1988)

Crystallite diamete	0.074	***dc***		Correlation equation constants			
Aggregate diamet	10	***da***					
R = ***da/dc***	135	No sph/sph	Poroty	A	B	C	D
Cubic (4)		1273491	0.4840	0.529	-1.8209	5.1533	-13.145
Cubic (5)		1290379	0.4771	0.539	-2.2752	10.3609	-27.8031
Body centered cubic		1645340	0.3333	0.682	-2.1466	3.8011	-7.8396
Face centered cubic		1799265	0.2709	0.748	-2.5743	7.0472	-16.1001

Aggregate of Crystallites Model

BET	m^2/gm	18
Skeletal density	kg/m^3	4720
Equivalent diamet	micron	0.071

Particle size [um]	Volume Distn.%	Number Distn.%	ensity [kg/m³]	Mass istn.	Area Distn.%	Pore Volume Distn.%
20.70	0.00	0.0	2582	0.0	0.0	0.0
15.65	0.20	0.2	2575	0.2	0.2	0.2
12.05	1.00	1.1	2566	1.0	1.1	0.9
9.35	3.10	3.3	2555	3.2	3.3	2.9
7.30	10.90	11.4	2542	11.2	11.4	10.3
5.70	18.70	19.4	2525	19.1	19.4	18.0
4.45	20.00	20.4	2505	20.3	20.4	19.5
3.45	18.60	18.7	2478	18.6	18.7	18.5
2.70	14.30	14.0	2447	14.1	14.0	14.5
2.15	5.30	5.1	2413	5.2	5.1	5.5
1.70	1.80	1.7	2371	1.7	1.7	1.9
1.35	1.50	1.3	2323	1.4	1.3	1.7
0.6	4.6	3.4	2100	3.9	3.4	6.1
	100.0	100.0		100.0	100.0	100.0

Particle size [um]	R	Cubic (4) packing N sp/sp	orosity	Eff De in H2	Eff Density in Air	No of aggl	No of cryst	Mass	Area	Inc PV cm^3/gm	Total PV
20.70	293.1	13385321	0.575	2582	2008	0.0E+00	0	0	0	0.286	0.0000
15.65	221.6	5758143	0.577	2575	1999	1.0E+14	5.738E+20	515	9E+18	0.289	0.0006
12.05	170.6	2613922	0.579	2566	1987	1.1E+15	2.853E+21	2566	4E+19	0.291	0.0030
9.35	132.4	1212738	0.582	2555	1974	7.2E+15	8.784E+21	7921	1E+20	0.295	0.0094
7.30	103.4	572239	0.586	2542	1957	5.4E+16	3.062E+22	27707	5E+20	0.299	0.0335
5.70	80.7	269480	0.590	2525	1936	1.9E+17	5.197E+22	47222	8E+20	0.305	0.0582
4.45	63.0	126487	0.596	2505	1910	4.3E+17	5.483E+22	50091	9E+20	0.312	0.0632
3.45	48.9	57909	0.603	2478	1876	8.7E+17	5.01E+22	46094	8E+20	0.321	0.0599
2.70	38.2	27173	0.611	2447	1837	1.4E+18	3.77E+22	34993	6E+20	0.333	0.0471
2.15	30.4	13393	0.620	2413	1793	1.0E+18	1.364E+22	12786	2E+20	0.346	0.0179
1.70	24.1	6424	0.632	2371	1740	7.0E+17	4.495E+21	4267	7E+19	0.363	0.0063
1.35	19.1	3105	0.644	2323	1679	1.2E+18	3.616E+21	3484	6E+19	0.384	0.0054
0.6	8.5	227	0.704	2100	1396	4.1E+19	9.218E+21	9659	1E+20	0.504	0.0197
							2.684E+23	247307	4E+21		0.3241

Appendix N

Calculations for Wet Particle Size Distribution

BET	m^2/gm	13.5
Pycnometric de	kg/m^3	4823
Equivalent diam	micron	0.104

article size [um]	Volume Distn.%	Number Distn.%	ff. Density [kg/m^3]	Mass istn.%	urface Area Distn.%	Pore Volume Distn.%
38.75	0.10	0.2	3038	0.1	0.2	0.1
31.40	0.60	1.0	3033	0.5	1.0	0.6
25.45	1.10	1.8	3027	1.0	1.8	1.2
20.65	1.10	1.8	3019	1.0	1.8	1.2
16.75	1.00	1.6	3009	0.9	1.6	1.1
13.60	0.70	1.1	2997	0.6	1.1	0.8
11.10	0.60	0.9	2983	0.5	0.9	0.7
9.60	0.50	0.8	2972	0.4	0.8	0.6
5.90	0.50	0.8	2920	0.4	0.8	0.6
4.80	0.60	0.9	2891	0.5	0.9	0.7
3.90	0.90	1.3	2856	0.8	1.3	1.1
3.20	1.30	1.9	2818	1.1	1.9	1.6
2.60	1.70	2.4	2771	1.4	2.4	2.2
2.10	2.40	3.3	2716	1.9	3.3	3.2
1.70	2.90	3.8	2654	2.3	3.8	4.0
1.40	3.50	4.4	2592	2.7	4.4	5.1
1.10	4.20	5.0	2505	3.1	5.0	6.5
0.90	5.60	6.3	2423	4.0	6.3	9.2
0.74	7.80	8.2	2329	5.3	8.2	13.7
0.60	10.00	9.4	2194	6.4	9.4	19.4
0.48	11.30	8.6	1961	6.5	8.6	26.4
0.39	11.10	4.9	4823	15.7	4.9	0.0
0.32	9.90	1.0	4823	14.0	1.0	0.0
0.26	13.80	2.6	4823	19.5	2.6	0.0
0.19	3.90	1.9	4823	5.5	1.9	0.0
0.13	1.30	2.2	4823	1.8	2.2	0.0
0.0625	1.6	22.0	4823	2.3	22.0	0.0
	100.0	100.0		100.0	100.0	100.0

	R	N sp/sp	Porosity	Eff De in H2O	Eff Density in Air	No of aggl	No of cryst	Mass	Area	Pore Vol Size Frac cm^3/gm	Total Pore Volume
38.75	374.3	27964741	0.467	3038	2572	3.28E+12	9.2E+19	304	3.09E+18	0.182	0.0002
31.40	303.3	14840733	0.468	3033	2565	3.70E+13	5.5E+20	1820	1.85E+19	0.183	0.0010
25.45	245.8	7876671	0.470	3027	2557	1.27E+14	1E+21	3329	3.38E+19	0.184	0.0018
20.65	199.5	4191267	0.472	3019	2547	2.39E+14	1E+21	3321	3.37E+19	0.186	0.0018
16.75	161.8	2226123	0.474	3009	2535	4.06E+14	9E+20	3009	3.05E+19	0.187	0.0017
13.60	131.4	1184641	0.478	2997	2520	5.31E+14	6.3E+20	2098	2.12E+19	0.190	0.0012
11.10	107.2	639628	0.481	2983	2503	8.38E+14	5.4E+20	1790	1.8E+19	0.193	0.0010
9.60	92.7	411371	0.484	2972	2488	1.08E+15	4.4E+20	1486	1.49E+19	0.195	0.0008
5.90	57.0	92992	0.498	2920	2423	4.65E+15	4.3E+20	1460	1.46E+19	0.206	0.0009
4.80	46.4	49312	0.505	2891	2386	1.04E+16	5.1E+20	1735	1.72E+19	0.212	0.0011
3.90	37.7	25964	0.514	2856	2342	2.90E+16	7.5E+20	2571	2.53E+19	0.220	0.0017
3.20	30.9	14045	0.525	2818	2294	7.58E+16	1.1E+21	3663	3.58E+19	0.229	0.0025
2.60	25.1	7340	0.537	2771	2235	1.85E+17	1.4E+21	4711	4.56E+19	0.240	0.0033
2.10	20.3	3747	0.551	2716	2165	4.95E+17	1.9E+21	6518	6.24E+19	0.255	0.0049
1.70	16.4	1917	0.567	2654	2088	1.13E+18	2.2E+21	7698	7.27E+19	0.272	0.0061
1.40	13.5	1030	0.584	2592	2009	2.44E+18	2.5E+21	9071	8.45E+19	0.291	0.0077
1.10	10.6	472	0.606	2505	1899	6.03E+18	2.8E+21	10521	9.58E+19	0.320	0.0098
0.90	8.7	245	0.628	2423	1796	1.47E+19	3.6E+21	13569	1.21E+20	0.350	0.0139
0.74	7.1	127	0.652	2329	1677	3.68E+19	4.7E+21	18163	1.57E+20	0.389	0.0207
0.60	5.8	61	0.688	2194	1507	8.84E+19	5.4E+21	21937	1.81E+20	0.457	0.0293
0.48	4.6	25	0.748	1961	1214	1.95E+20	4.9E+21	22165	1.65E+20	0.617	0.0400
0.39	3.8	8	0.000	4823	4823	3.57E+20	2.8E+21	53535	9.35E+19	0.000	0.0000
0.32	3.1	1	0.000	4823	4823	5.77E+20	5.8E+20	47748	1.94E+19	0.000	0.0000
0.26	2.5	1	0.000	4823	4823	1.50E+21	1.5E+21	66557	5.05E+19	0.000	0.0001
0.19	1.8	1	0.000	4823	4823	1.09E+21	1.1E+21	18810	3.66E+19	0.000	0.0000
0.13	1.2	1	0.000	4823	4823	1.27E+21	1.3E+21	6270	4.28E+19	0.000	0.0000
0.0625	0.6	1	0.000	4823	4823	1.25E+22	1.3E+22	7717	4.21E+20	0.000	0.0000
							5.7E+22	341575	1.92E+21		0.1515

Bibliography

Agrawal, R.D., (1981), Simultaneous TG, DTG and DTA Studies on Manganese Oxides. *Trans. Jap. Inst. Metals,* vol. 22, no. 4, pp. 253-257.

Alper, E., Deckwer, W.D., (1983), Some Aspects of the Gas Absorption Mechanism in Slurry Reactors. *NATO ASI. Ser.*, vol. 873, pp. 199-224.

Ambrose, J., Briggs, G.W.D., (1971), The Manganous Hydroxide Electrode. *Electrochim. Acta*, vol. 6, pp. 11-119.

Anderson, J.R., (1971), *Chemisorption and Reactions on Metallic Films.* Academic Press, London and New York, vol. 1 & vol. 2.

Ardizzone, S., Bianchi, C.L., Tirelli, D., (1998), Mn_3O_4 and γ-MnOOH Powders, Preparation, Phase Composition and XPS Characterisation. *Colloids Surfaces A: Physicochem. Eng. Aspects,* vol. 134, pp. 305-312.

Asai, S., Konishi, Y., Kajiwara, T., (1989), Effect of Sparger Gas on Mass Transfer between Fine Particles and Liquids in an Agitated vessel. *J. Chem. Eng. Japan*, vol. 22, no. 1, pp. 96-98.

Ayazi Shamlou, P., Stavrinides, S., Titchener-Hooker, N., Hoare, M., (1994), Growth-Independent Breakage Frequency of Protein Precipitates in Turbulently Agitated Bioreactors. *Chem. Eng. Sci.,* vol. 49, no. 16, pp. 2647-2656.

Bauer, J., Buss, D.H., Glemser, O., (1985), The Electrochemical Behaviour of Manganese(II)-Hydroxide and Manganese(II)-Hydroxide/Aluminium Hydroxide. *Ber. Bunsenges. Phys. Chem.,* vol. 89, no. 10, pp. 1070-1074.

Baes, C.F., Mesmer, R.E., (1976), *Hydrolysis of Cations.* J. Wiley & Son, New York, pp. 219-227.

Bailey, J.E., Ollis, D.F., (1977), *Biochemical Engineering Fundamentals.* McGraw Hill, Tokyo.

Basolo, F., Pearson, R.G., (1967), *Mechanisms of Inorganic Reactions.* 2nd Ed. J. Wiley & Son, New York.

Berg, L.G., Kovyrzina, V.P., (1963), *Zh. Neorgan. Khim.,* vol. 8, pp. 2041-2045. *Russian J. Inorgan. Chem.,* vol. 8, (1963), pp. 1065-1068.

Bertaut, E.F., (1951), On Recent Progress in Crystallography of Spinels and, in Particular, Ferrites. *Phys. Rad. J.,* vol. 12, pp. 252-255.

Bhandage, G.T., Tareen, J.A.K., Basavalinga, B., (1987), Retrieval of Thermodynamic Properties of Metal Hydroxide ($M(OH)_2$) (M = Ni, Mn) Phases from Hydrothermal Phase Equilibria of Metal Monoxide - Water Systems. *J. Thermal Anal.*, vol. 32, no. 6, pp. 1823-1831.

Bird, R.B., Stewart, W.E., Lightfoot, E.N., (1960), *Transport Phenomena.* J. Wiley & Sons, New York.

Birks, N., Meier, G.H., (1983), *Introduction to High Temperature Oxidation of Metals.* E. Arnold, London.

Borges-Soares, M., Menes, F., Fontaine, R., Caillat, R. (1983), Etude Par Spectroscopie De Photoelectrons Des Reactions du Manganese Avec L'Oxygene Et La Vapeur D'Eau (Translated: A Study of the Reactions of Manganese with Oxygen and Water Vapour.). *J. Microsc. Spectrosc. Electron.,* vol. 8, pp. 93-107.

Brenet, J.P., Gabano, J.P., Reynaud, J., (1963), Additional Information pertaining to the Eh - pH Diagram for Manganese. *Electrochim. Acta*, vol. 8, pp. 207-216.

Brenet, J.P., Pavlovic´, Z., Popovic´, R., (1968), Zur Thermodynamik des Systems Mangan/wäßrige Lösung in der Abwesenheit und Anwesenhiet von gelöstem Sauerstoff. (Translated: The Thermodynamics of Manganese/Water Systems in the Absence and Presence of Dissolved Oxygen.) *Werkstoffe Korrosion,* vol. 10, pp. 393-405.

Brenet, J.P., Picquet, P.C., (1984), A New View on the Equilibrium Diagram Potential-pH of the System Mn-H_2O. *Proc. Symp. MnO2 Elect. Theo. Prac. Electr. Appl., New Orleans, The Electrochem. Soc.*, vol. 85-4, pp. 3-20.

Brennan, D., Hayward, D.O., Trapnell, B.M.W., (1960), The Calorimetric Determination of the Heats of Adsorption of Oxygen on Evaporated Metal Films. *Proc. Royal Soc.*, London, vol. 256, pp. 81-105.

Bricker, O., (1965), Some Stability Relations in the System Mn-O_2-H_2O at 25°C and One Atmosphere Total Pressure. *Am. Mineral.*, vol. 50, pp. 1296-1354.

Briggs, G.W.D., Davies, D.F., (1979), The Electrochemical Oxidation of Manganous Hydroxide. *Electrochim. Acta*, vol. 24, pp. 439-444.

Brucato, A., Magelli, F., Nocentini, M., Rizzuti, L., (1991), Application of the Network-of-Zones Model to Solids Suspension in Multiple Impellor Mixers. *Chem. Eng. Res. Des.*, vol. 69, no. 1, pp. 43-52.

Budevski, E., Staikov, G., Lorenz, N.J. (1996), *Electrochemical Phase Formation and Growth,* VCH Weinham New York.

Burton, W.K., Cabrera, N., Frank, F.C., (1951), The Growth of Crystals and the Equilibrium Structure of Their Surfaces. *Philo. Trans. Royal Soc.*, London A, vol. 243, pp. 299-358.

Calabrese, R.V., Stoots, C.M., (1989), Flow in the Impellor Region of a Stirred Tank. *Chem. Eng. Prog.*, vol. 85, no. 5, pp.43-50.

Cavollotti, P., Colombo, P., Ducati, V., Piotti, A., (1987), Electrochemical Kinetics and Structure of Electrodeposits. *Proc. Electrochem. Soc.*, vol. 87-17, pp. 429-448.

Chiswell, B., Mokhtar, M.B., (1986), The Speciation of Manganese in Freshwaters. *Talanta*, vol. 33, no. 8, pp. 669-677.

Chouaib, F., Picard, G., (1989), Elaboration of Metal Oxide Compounds in Concentrated Water + Alkaline Hydroxide Mixtures. Preparation and Study of New Manganese Oxides. *J.Chem.Res (M),* pp. 0128-0136.

Coetzee, M.C., Cloete, F.L.D., (1989), A Comparison of Axial-flow Impellors with Inclined-blade Turbines in a Baffled Mixer. *J. S. Afr. Inst. Min. Metall.*, vol. 89, no. 4, pp. 99-109.

Cohen, S.L., Russak, M.A., Baker, J.M., McQuire, T.R., Scilla, G.J., Rossnagel, S.M., (1988), Characterisation of the Surface Oxidation and Magnetic Properties of MnFe Thin Films. *J. Vac. Sci. Tech.*, vol. 6, no. 3, pt. 1, pp. 918-923.

Corpstein, R.R., Fasano, J.B., Myers, K.J. (1994), The High Efficiency Road to Liquid-Solid Agitation, *Chem. Eng*, vol.101, no.10, pp. 138-144

Cotton, F.A., Wilkinson, G., (1976), *Basic Inorganic Chemistry.* J. Wiley & Sons, New York.

Couderc, J.J., Fritsch, S., Brieu, M., Vanderschaeve, G., Fagot, M., Rousset, A., (1994), A Transmission Electron Microscopy Study of Lattice Defects in Mn_3O_4 Hausmannite. *Philos. Mag. B.,* vol. 70, no. 5., pp. 1077-1094.

Criss, C.M., Cobble, J.W., (1964), The Thermodynamic Properties of High Temperature Aqueous Solutions. IV. Entropies of the Ions up to 200°C and the Correspondance Principle. *J. Am. Chem. Soc.,* vol. 86, pp. 5385-5390.

Davies, S.H.R., Morgan, J.J., (1989), Manganese (II) Oxidation Kinetics on Metal Oxide Surfaces. *J. Coll. Inter. Sci.*, vol. 129, no. 1, pp. 63-77.

Delahaye-Vidal, A., Sac-Pee, N., Portemer, F., Beaudoin, B., Figlarz, M., Jamin, T., (1995), Dissolution-Recrystallisation Processes of Nickel Hydroxide, The Active Material of the Ni/Cd and Ni/H_2 Cells. *Mat. Res. Soc. Symp. Proc.,* vol. 369, pp.107-117.

Dessouki, H.A., Abdel Fattah, A.A., El Sayed, G.E., El Haleem, Abd, S.M., (1990), Cyclic Voltammograms of Manganese Electrodes in NaOH. *Corros. Prev. Control*, vol. 37, no. 3, pp. 69-72.

Ditl, P., (1985), Hydromechanics and Mass Transfer in Agitated Suspensions. *Proc. 5th European Conf. Mixing*, pp. 78-103.

Ditl, P., Rieger, F., (1985), Suspension of Solid Particles - Relative Velocity of Particles in Turbulent Mixing. *Proc. 5th European Conf. Mixing*, pp. 53-61.

Dollimore, D., Tonge, K.H., (1971), The Thermo-Analytical Behaviour of Some Synthetic Manganese Oxides. *Proc.Third ICTA, Davos, Therm. Anal.* vol. 2, pp. 91-103.

Doraiswamy, L.K., Sharma, M.M., (1984), *Heterogeneous Reactions: Analysis, Examples, and Reactor Design, Volume.1: Gas-Solid and Solid-Solid Reactions.* J. Wiley & Sons, New York.

Dressel, W.M., Kenworthy, H., (1961), Thermal Behaviour of Manganese Minerals in Controlled Atmospheres. *RI 5761, US Dept. of the Interior, Bureau of Mines,* Washington.

Driessens, F.C.M., (1967), Place and Valence of the Cations in Mn_3O_4 and Some Related Manganates. *Inorg. Chim. Acta,* vol. 1:1, pp. 193-201.

Echeverria, A., Paidassi, J., (1959), Sur l'oxydation du manganèse dans l'air aux température élevées. (Translated:The Oxidation of Manganese in Air at High Temperature). *Acta Metal.,* vol. 7, pp. 298-295.

Engel, H.J., (1956), Über die Auflösung von Oxygen in Verdünnten Sauren.(Translated: On the Solubility of Oxygen in Dilute Acids.). *Zeit. Phys. Chem. N. F.*, vol. 7, pp.158-181.

Fallab, S., (1967), Reactions with Molecular Oxygen. *Angew. Chem. Int. Ed.,* vol. 16, no. 6, pp. 496-507.

Feitknecht, W., Brunner, P., Oswald, H.R., (1962), Über den Einfluß der Feuchtigkeit auf die Oxydation von Manganhydroxid durch Molekularen Sauerstoff. (Translated: On the Influence of Moisture on the Oxidation of Manganese Hydroxide by Molecular Oxygen). *Zeit. Anorg. Chem.,* vol. 316, pp. 154-160.

Franck,U.F., Fitzhugh,R., (1961), Periodise Elektrodenporsozesse und Ihre Beschreibung durch ein Mathematisches Modell. (Translated: Periodic Electrode Processes and their Description by a Mathematical Model). *Zeit. Fur Elektrochem.,* vol. 62, no. 617, pp. 649-655.

Foord, J.S., Jackman, R.B., Allen G.C., (1984), An X-ray Photoelectron Spectroscopic Investigation of the Oxidation of Manganese. *Philo. Mag. A.*, vol. 49, no. 5, pp. 657-663.

Frijlink, J.J., Bakker, A., Smith, J.M., (1990), Suspension of Solid Particles with Gassed Impellors. *Chem. Eng. Sci.*, vol. 45, no. 7, pp. 1703-1718.

Fritsch, S., Navrotsky, A., (1996), Thermodynamic Properties of Manganese Oxides. *J.Am.Ceram. Soc.,* vol. 79, no. 7, pp. 1761-1768.

Frondel, C., (1953), New Manganese Oxides: Hydrohausmannite and Woodruffite,. *Amer. Mineral.* vol. 38, pp. 761-769.

Fuecki, K., Wagner, J.B., (1965), Oxidation of Manganese in CO_2-CO Mixtures. *J. Electrochem. Soc.,* vol. 112, no.10, pp. 970-974.

Garrison, C.M., (1983), How to Design and Scale Mixing Pilot-Plants. *Chem.Eng.*, vol. 90, no. 2, pp. 63-70.

Geary, N.W., Rice, R.G., (1991), Bubble Size Prediction for Rigid and Flexible Spargers. *A.I.Ch.E.J.*, vol. 37, no. 2, pp. 161-168.

Gesmundo, F., Nanni, P., Viani, F., (1975), Low Pressure Oxidation of Manganese in Pure Oxygen at 550°C and 650°C. *Werkstoffe und Korro.,* vol. 26, no. 11, pp. 831-835.

Geisler, R., Mersmann, A., Voit, H., (1992), Macro- and Micromixing in Stirred Tanks. *Int. Chem. Eng.,* vol. 31, no. 4, pp. 642-653.

Glück, T., (1994), Mechanisms of Nitriding Electrolytic Manganese Metal. *Chem. Eng. J.*, vol. 54, pp. 167-173.

Gmelins Handbuch der Anorganischen Chemie, Manganese B. (1973), Ed., Kugler, K. Verlag Chemie, Weinheim.

Golikov, Yu.V., Barkhatov, V.P., Balakirev, V.F., Avdukov, V.I., (1989), High-Temperature and Quenched States in Manganese-Containing Systems in Air. *High Temp.-High Press.,* vol. 21, pp. 685-700.

Gosztola, D., Weaver, M.J., (1989), Electro-Induced Structural Changes in Manganese Dioxide and Manganese Hydroxide Films as Characterised by Real Time Surface Enhanced Raman Spectroscopy. *J. Electroanal. Chem. Interfac. Electrochem.*, vol. 271, no. 1-2, pp. 141-154.

Gray, M.J., (1978), Surface-Chemical Studies of Manganese Dioxide with Special Reference to Water Chemistry. *PhD Thesis, Medway and Maidstone College of Technology.*

Groth, P., (1987), Enteisenung und Entmanganung. (Translated: Iron and Manganese removal). *DVGW-Schriften. Wass. Nr.406, Eschborn,* Chap. 13.

Harriott, P., (1962), Mass Transfer to Particles: Part 1. Suspended in Agitated Tanks. *A.I.Ch.E.J.,* vol. 8, no. 1,.pp.93-102.

Hauffe, K., (1965), *Oxidation of Metals.* Plenum Press, New York.

Healy, T.W., Herring, A.P., Fuerstenau, D.W., (1966), *J.Coll. Inter. Sci.,* vol. 21, pp. 435-440.

Heintz, J.M., Weill, F., Bernier, J.C., (1989), Characterisation of Agglomerates by Ceramic Powder Compaction. *Mater. Sci. Eng. A Struct. Mater. Prop. Micro. ,* vol. A109, no. 1-2, pp. 271-277.

Hem, J.D., (1981), Rates of Manganese Oxidation in Aqueous Systems. *Geochim. Cosmochim. Acta.,* vol. 45, pp. 1369-1374.

Hem, J.D., Lind, C.J. (1983), Nonequilibrium Models for Predicting Forms of Precipitated Manganese Oxides. *Geochim. Cosmochim. Acta,* vol. 47, pp. 2037-2046.

Hernandez Ubeda, M., Mishima, H.T., López de Mishima, B.A., (1991), The Electrochemical Response of Manganese Hydroxide-Oxide Films in Slightly Alkaline Films-1. The Redox Couple. *Electrochim. Acta,* vol. 36, no. 5-6, pp. 1013-1018.

Heusler, K.E., (1963), On the Passivity of Manganese in Acid Solution. *J. Electrochem. Soc.*, vol. 110, no. 6, pp. 703-708.

Heusler, K.E., Bergmann, M., (1970), Der Kinetik der Aktiven Manganelektrode. (Translated: The Kinetics of the Active Manganese Electrode). *Electrochim. Acta*, vol. 15, pp. 1887-1898.

Heusler, K.E., Grzegorzewski, A. (1990), The Mechanism of the Manganese Dioxide Electrode. *Electrochim. Acta,* vol. 35, no. 2, pp. 539-544.

Heusler, K.E., Kusian, B., McPhail, D., (1990), Kinetics of the Corrosion of Iron in Aqueous Electrolytes at Temperatures up to 300°C. *Ber. Bunsenges. Phys. Chem.,* vol. 94, pp. 1443-1449.

Hicks, R.W., Gates, L.E., (1976), How to Select Turbine Agitators for Dispersing Gas into Liquids. *Chem. Eng.* vol. 83, no. 7, pp. 141-148

Hougen, O.A., Watson, K.M., (1966), *Chemical Process Principles II.* J Wiley & Sons, 2nd Ed.

House, C.I., (1987), Potential-pH Diagrams and Applications to Hydrometallurgical Systems. *Separation Processes in Hydrometallurgy*, G.A. Davies Ed, Ellis Horwood, pp.3-19.

Hurlbut, C.S., (1971), *Dana's Manual of Mineralogy*. J. Wiley & Sons, New York.

Hurlen, T., (1962), Kinetics of Metal/Metal Ion Electrodes - Iron, Copper, Zinc. *Electrochim. Acta*, vol. 7, pp. 653-668.

Hurlen, T., Valand, T., (1964a) Dissolution of Manganese in Acids. *Corr. Sci.*, vol. 4, pp. 253-259.

Hurlen, T., Valand, T., (1964b), Electrochemical Behaviour of Manganese: Dissolution, Deposition, Hydrogen Evolution. *Electrochim. Acta,* vol. 9, pp. 1077-1085.

Hurlen, T., Valand, T., (1964c), Activiation energy of the Mn/Mn^{2+} Electrode. *Electrochimica Acta,* vol. 9, pp. 1087-1092.

Hu, H.K., Rabalais, J.W., (1981), Chemisorption and the Initial Stage of Oxidation on Mn. *Surf. Sci.*, vol. 107, pp. 376-390.

Ilea, P., Tissot, P., Oniciu, L., (1997), Kinetic Mechanism of the Hydrogen Evolution Reaction (HER) for Several Materials in Ammonium Sulfate Solution, *Chem. Bull. "Politehnica" Univ. (Timisoara),* vol.42, no. 56, pp. 5-11.

Irons, G.A., (1993), Fundamental Design Issues for Gas and Solids Injection into Molten Metals, *Proc. Int. Symp. Ext. Met. Cu Co & Ni*, vol. 1, pp. 261-273. Ed. Reddy and Weizenbach, MMM Soc.

Jarosch, D., (1987), Crystal Structure Refinement and Reflectance Measurements of Hausmannite, Mn_3O_4. *Mineral. Petro.* vol. 37, pp. 15-23.

Jenne, E.A., (1967), Controls on Mn, Fe, Co, Ni, Cu, and Zn Concentrations in Soils and Water: The Significant Role of Hydrous Mn and Fe Oxides. *Adv. Chem. Ser. 73, Amer. Chem. Soc., Trace Inorganics in Water, Symp. 153rd Meet. of Am. Chem. Soc.*, pp. 337-387.

Jones, C.F., Segall, R.L., Smart, R.St.C., Turner, P.S., (1977), Semiconducting Oxides : The Effect of Prior Annealling on Dissolution Kinetics of Nickel Oxide. *J. Chem. Soc. Farad. Trans.*, vol. 73, pp. 1710-1720.

Jones, C.F., Segall, R.L., Smart, R.St.C., Turner, P.S., (1978a), Semiconducting Oxides: Infrared and Rate Studies of the Effects of Surface Blocking by Surfactants in Dissolution Kinetics. *J. Chem. Soc. Fara. Trans.*, vol. 74, pp. 1624-1633.

Jones, C.F., Segall, R.L., Smart, R.St.C., Turner, P.S., (1978b), Semiconducting Oxides: Effects of Electronic and Surface Structure on Dissolution Kinetics of Nickel Oxide. *J. Chem. Soc., Farad. Trans.*, vol. 74, pp. 1615-1624.

Jones, C.F., Smart, R.St.C., Turner, P.S., (1990), Dissolution Kinetics of Manganese Oxides. *J. Chem. Soc., Farad. Trans.*, vol. 86, no. 6, pp. 947-953.

Ju, S.Y., Mulvahill, T.M., Pike, R.W., (1990), Three-dimensional Turbulent flow in Agitated Vessels with a Nonisotropic Viscosity Turbulence Model. *Can. J. Chem. Eng.*, vol. 68, pp. 3-16.

Kaczmarek, J., Wolska, E., (1993a), Cation and Vacancy Distribution in Nonstoichiometric Hausmannite. *J. Sol. State Chem.*, vol. 103, pp. 387-393.

Kaczmarek, J., Wolska, E., (1993b), The Defect Structure and Vacancy Distribution in Low-Temperature Hausmannite. *Sol. State Ionics.*, vol. 63-65, pp. 663-638.

Kaczmarek, J., Wolska, E., (1994), Structural Study on the Thermal Evolution of $Mn_{3-\delta}(O,OH)_4$ in the Oxidising and Reducing Atmosphere. *Sol. State Phenom.*, vol. 39-40, pp. 153-156.

Kao, W.H., Weibel, V.J., (1992), Electrochemical Oxidation of Manganese (II) at a Platinum Electrode. *J. Appl. Electrochem.*, vol. 22, no. 1, pp. 21-27.

Karve, S., Juvekar, V.A., (1990), Gas Absorption into Slurries Containing Fine Catalyst Particles.*Chem. Eng. Sci.*, vol. 45, no. 3, pp. 587-594.

Kawase, Y., Moo-Young, M., (1988), Volumetric Mass Transfer Coefficients in Aerated Stored Tank Reactors with Newtonian and Non-Newtonian Media. *Chem. Eng. Res. Des.*, vol. 66, no. 3, pp. 284-288.

Keller, H., Dieckmann, R., (1985), Defect Structure and Transport Properties of Manganese Oxides: (II) The Nonstoichiometry of Hausmannite ($Mn_{3-\delta}O_4$). *Ber. Bunsenges. Phys. Chem.* vol. 89, no. 10, pp. 1095-1104.

Keller, M., Xue, J., Dieckmann, R., (1991), Electrochemical Investigation of the Oxygen Activity at the Manganosite-Hausmannite Equilibrium. *J. Electrochem. Soc.*, vol. 138, no. 11, pp. 3398-3401.

Kessick, M.A., Morgan, J.J., (1975), Mechanism of Autoxidation of Manganese in Aqueous Solution. *Envir. Sci. Tech*, vol. 9, no. 2, pp. 157-159.

Kiyama, M., (1978), The Formation of Manganese and Cobalt Ferrites by the Air Oxidation of Aqueous Suspenson and Their Properties. *Bull. Chem. Soc. Jap.,*vol. 51, no. 1, pp.134-138.

Klingsberg, C., Roy, R., (1959), Stability and Interconvertibility of Phases in the System Mn-O-OH*. *Am. Miner.,* vol. 44, pp. 819-838.

Koertsier, W.T., Thoenes, D., (1972), Coalescence of Bubbles in a Stirred Tank. *Proc. 5th Europ./ 2nd Int. Symp. Chem. Reac. Eng.*, Amsterdam, pp.B3-15 – B3-24.

Kohlenbrander, M., Zaspalis, V.T., Mauczok, R., Essing, A., Rusch, A. (2000) Relation between Morpholgy and Reactivity for High Purity Ruthner Iron Oxides. *Digest of 8th International Conference on Ferrites,* Kyoto, p200.

Kresta, S.M., Wood, P.E., (1991), Prediction of the 3 Dimensional Turbulent Flow in Stirred Tanks. *A.I.Ch.E.J.*, vol. 37, no. 3, pp. 448-460.

Kresta, S.M., Wood, P.E., (1993), The Flow Field Produced by a Pitched Blade Turbine: Characterisation of the Turbulence and Estimation of the Dissipation Rate. *Chem. Eng. Sci.*, vol. 48, no. 10, pp. 1761-1774.

Kshirsagar, S.T., Biswas, A.B., (1966), Crystallographic Studies of Some Mixed Manganite Spinels. *J. Phys. Chem. Solids,* vol. 28, pp. 1493-1499.

Kuboi, R, Nienow, A.W., (1982), The Power Drawn by Dual Impellor Systems under Gassed and Ungassed Conditions. *Proc. 4th European Conf. Mixing* (BHRA Fluid Eng.), G2, pp. 247-261.

Kulp, J.L., Perfetti, J.N., (1950), Thermal Study of Some Manganese Oxide Minerals. *Mineral. Mag.* vol. 210, no. 210, pp. 239-251.

Laxen, P.A., (1972), *A Fundamental Study of the Dissolution in Acid Solutions of Uranium Minerals from South African ores.* PhD Thesis, University of the Witwatersrand.

Ledakowicz, S., Brehm, A., Ogus, M., (1985), Effect of Suspended Inert Particles on Gas Liquid Mass Transfer in Mechanically Agitated Contactors. *Hung. J. Ind. Chem.*, vol. 13, no. 4, pp. 489-501.

Lee, J.A., Newnham, C.E., Stone, F.S.,Tye, F.L., (1980), Thermal Decomposition of Manganese Oxyhydroxide. *J. Sol. Stat. Chem.* vol. 31, pp. 81-93.

Levenspiel, O., (1972), *Chemical Reaction Engineering. 2nd Ed.* J. Wiley & Sons, New York.

Liang, C.C., (1973), Manganese. *Encyclopedia of Electrochemistry of Elements.* Ed. A.J. Bard, M. Dekker Inc., New York., vol. 1, pp. 349-403.

Lin, H.K., Sohn, H.Y., Wadsworth, M.E., (1986), The Kinetics of Leaching of Chalcopyrite Ore under Simulated Solution Mining Conditions. *Hydrometallurgical Reactor Design and Kinetics,* Ed. Bautista, R.G., Wesely, R.J. Warren, G.W. The Metalurgical Society, Inc., pp. 149-168.

L'Homme, G.A., (1981), *Proceedings of the NATO Advance Study Institute on Mass Transfer with Chemical Reaction in Multiphase Systems*, Cesme-Izmir, Turkey.

Lussiez, P., Osseo-Asare, K., Sinkovich, G., (1981), Effect of Solid State Impurities on the Dissolution of Nickel Oxide. *Met. Trans. B*, vol. 12B, pp. 651-657.

MacDonald, D.D., (1976), The Thermodynamics and Theoretical Corrosion Behaviour of Manganese in Aqueous Systems at Elevated Temperatures. *Corr. Sci.*, vol. 16, pp. 461-482.

Mah, Allah D., (1960), Thermodynamic Properties of Manganese and Its Compounds, *U.S. Dept of the Interior, Bureau of Mines Report of Investigations 5600,* Washington.

Mann, R., (1983), Gas-Liquid Contacting in Mixing Vessels,. *I. ChemE. Industrial Research Fellowship Report*, I. ChemE., Rugby, England.

Marrone, G.M., Kirwan, D.J., (1986), Mass Transfer to Suspended Particles in Gas-Liquid Agitated System. *AIChEJ.*, vol. 32, no. 3, pp. 523-525.

Mayhew, Y.R., Rogers, G.F.C., (1977), *Thermodynamic and Transport Properties of Fluids SI Units*,2nd Ed., Basil Blackwell, Oxford,

Meenakshisundaram, A., Gunasekaran, N., Srinivasan, V.,(1982), Distribution of Metal Ions in Transition Metal Manganites AMn_2O_4. *Phys. Stat. Sol. (a)*, vol. 69, pp. K15-K19.

Melendez, M., Brenet, J., (1971), Electrochemical Behaviour of a Manganese Electrode in a Phosphoric Medium. *Electrochim. Acta*, vol. 16, pp. 61-77.

Mendelovici, E., Sagarzuzu, A., (1988), Thermal Synthesis of Hausmannite via Manganese Alkoxide. *Thermochim.Acta,* vol. 133, pp. 93-100.

Miyachi, M., Iguchi, A., Uchida, S., Koide, K., (1981), Effect of Solid Particles in Liquid Phase on Liquid Side Mass Transfer Coefficient. *Can. J. Chem. Eng.*, vol. 59, no. 5, pp. 640-641.

Morgan, D.J., Milodowski, A.E., Warne, S.StJ., Warrington, S.B. Atmospheric Dependance of the Thermal Decomposition of Manganite, γ-MnO.OH. *Thermochim. Acta,* vol.135, pp. 273-277.

Mullin, J.W., (1993), *Crystallisation.* Buttersworth-Heinemann, Oxford.

Murray, J.M., Dillard, J.G., Giovanoli, R., Moers, H., Stumm, W., (1985), Oxidation of Mn(II): Initial Mineralogy, Oxidation State and Ageing. *Geochimica Cosmochim. Acta*, vol. 49, pp. 463-470.

Musil, L., Vlk, J., Jiroudkova, H., (1984), Suspending Solid Particles in an Agitated Tank with Axial-Type Impellors. *Chem. Eng. Sci.,* vol. 39, no. 4, pp. 621-628.

Nagy, E., Blickle, T., Ujhidy, A., (1986a), Enhancement of Gas Absorption Rate as a Function of the Particle Size in Slurry Reactors. *Chem. Eng. Sci.*, vol. 41, no. 8, pp. 2193-2195.

Nagy, E., Blickle, T., Ujhidy, A., (1986b), Mass Transfer through Spherical Surface Accompanied by Chemical Reaction. *Hung. J. Ind. Chem.*, vol. 14, no. 2, pp. 163-179.

Nagy, E., Blickle, T., Ujhidy, A., (1989), Spherical Effect on Mass Transfer between Fine Solid Particles and Liquid Accompanied by Chemical Reaction. *Chem. Eng. Sci.*, vol. 44, no. 1, pp. 198-201.

Narbutt, K.I., (1988), X-Ray Spectral Determination of Manganese Valence in Minerals. Translated from the Russian. *Zavodskaya Laboratoriya*, vol. 54, no. 8, pp. 39-42.

Naumov, G.B., Ryzhenko, B.N., Khodakovsky, I.L., (1974), *Handbook of Thermodynamic Data (*Moskow: Atomizdat, 1971). Translated from the Russian by the U.S. Geological Survey. *NTIS PB-226* 722, 328p.

Nicol, M.J., Needes, C.R.S., Finkelstein, N.P., (1975), Electrochemical Model for the Leaching of Uranium Oxide. *Ext. Leach. and Reduct. in Hydromet. Inst. Min. & Met.*, pp. 1-19.

Nienow, A.W., Konno, M., Bujalski, W., (1986), Studies on Three Phase Mixing. A Review and Recent Results. *Chem. Eng. Res. Des.*, vol. 64, pp. 443-450.

Nikolaishvili, E.K., Barabash, V.M., Braginskii, L.N., Kulov, N.N., Malyusov, V.A., (1980), Rate of Dissolution of Solid Particles in Stirred Vessels. *Theor. Found. Chem. Eng.*, vol. 14, no. 3, pp. 230-237.

Nohan, A.K.H., Zaki, M.I., Mansour, R.B., Fahim, R.B., Kappenstein, C., (1992), Characterisation of the Thermal Genesis of Manganese Oxides from Inorganic Precursors. *Thermchim. Acta,* vol. 210, pp. 103-121.

Nolan, G.T., Kavanagh, P.E., (1992), Computer Simulation of Random Packing of Hard Spheres. *Powd. Tech.,* vol. 72, pp. 149-155.

Nørlund-Christensen, A., (1965), A Single Crystal X-Ray Diffraction Study of $Mn(OH)_2$. *Acta. Chem. Scand.,* vol. 19, pp. 1765-1766.

Nørlund-Christensen, A., Ollivier, G., (1972), Hydrothermal Preparation and Low Temperature Properties of $Mn(OH)_2$. *Solid State Comm.*, vol. 10, pp. 609-614.

Ohta, M., Wakao, S., Ohzeki, K., (1990), New Synthesis Method of Pure Mn_3O_4 and Its Reaction Mechanism. (Translated) *J. Adv. Sci.*, vol. 2, no. 3, pp. 141-144.

Oku, M., Hirokawa, K., Ikeda, S., (1975), X-Ray Photoelectron Spectroscopy of Manganese-Oxygen Systems. *J. Elec. Spec. Rel. Phen.*, vol. 7, pp. 465-473.

Oldshue, J.Y., (1983), *Fluid Mixing Technology*. McGraw-Hill, New York.

Olowe, A.A., Génin, J.M.R., (1991), The Mechanism of Oxidation of Ferrous Hydroxide in Sulphated Aqueous Media: Importance of the Initial Ratio of The Reactants. *Corro. Sci.,* vol. 32, no. 9, pp. 965-984.

Osseo-Asare, K., (1981), Application of Activity-Activity Diagrams to Ammonia Hydrometallurgy:3-Mn-NH_3--H_2O, Mn-NH_3--H_2O-CO_3 and Mn-NH_3--H_2O-CO_3-SO_4 Systems at 25°C. *Trans. Instn. Min. Metall. (Sect. C: Mineral. Process. Extr. Metall.),* vol. 90, pp. C152-C158.

Osseo-Asare, K., (1984), Interfacial Phenomena in Leaching Systems. *Hydrometallurgical Process Fundamentals.* Ed. R.G. Bautista, Plenum Press, NewYork, pp. 227-268

Pankow, J.F., Morgan, J.J., (1981), Kinetics for the Aquatic Environment. *Environ. Sci. Tech.,* vol. 15, no. 11, pp. 1306-1313.

Pattanayak, J., Sitakara Rao, V., (1989), Preparation and Thermal Stability of Manganese Oxides Obtained by Precipitation from Aqueous Manganese Sulphate Solution. *Thermochim.Acta,* vol.153, pp.193-204.

Patterson, G.B., (1991), *Fluid Mixing and Gas Dispersion in Agitated Tanks.* McGraw-Hill, New York.

Pericleous, K.A., Patel, M.K., (1987), Modelling of Tangential and Axial Agitators in Chemical Reactors. *Physiochem. Hydrodyn.*, vol. 8, no. 2, pp. 105-123.

Perrin, D.D., (1962), The Hydrolysis of Manganese (II) Ion. *J.Chem.Soc.*, pp. 2197-2200.

Perry, R.H., Ed., (1973), *Chemical Engineers Handbook.* 5th Ed. McGraw-Hill, Tokyo.

Popplewell, L.M., Campanella, O.H., Peleg, M., (1989), Simulation of Bimodal Size Distributions in Aggregation and Disintegration Processes. *Chem. Eng. Prog.*, vol. 85, no. 8, pp. 56-62.

Pourbaix, M., Moussard, A., Brenet, J., Jolas, F., Van Muylder, J., (1974), *Atlas of Electrochemical Equilibria in Aqueous Solutions.* 2nd Ed., NACE, Houston, pp. 283-293.

Proult, A., Donnadieu, P., (1995), A Simple Description of the αMn (A12) Structure Derived from Defect Studies. *Philos. Mag. Lett.,* vol. 72, no. 5, pp. 337-344.

Ramanane, E.T., (1987), The Kinetics of the Reaction of Manganese with Distilled Water at Temperatures Below Boiling Point. *Unpublished results, University of the Witwatersrand.*

Rawle, A., (1999) Malvern Instrument Company. Private Communication

Rewatkar, V.B., Raghava Rao, K.S.M.S., Joshi, J.B., (1991a), Critical Impeller Speed for Solid Suspension in Mechanically Agitated Three Phase Reactors. 1. Experimental Part. *Ind. Eng. Chem. Res.,* vol. 30, no. 8, pp. 1770-1784.

Rewatkar, V.B., Joshi, J.B., (1991b), Critical Impeller Speed for Solid Suspension in Mechanically Agitated Three Phase Reactors. 2. Mathematical Model. *Ind. Eng. Chem. Res.,* vol. 30, no. 8, pp. 1784-1791.

Riekert, L., (1990), On the Concept of a Rate-Determining Process in Compound Kinetics. *Chem. Eng. Proc.*, vol. 27, no. 2, pp. 95-106.

Robins, R.G., (1968), The Application of Potential-pH Diagrams to the Prediction of Reactions in Pressure Hydrothermal Processes. *LR 80 (MST) Warren Spring Laboratories,* England.

Rode, E.Y., (1955), *Tr.1-goSoveshd.Temograf.(1953),* pp. 218-238,223,231-232.

Rodriguez, J.C.P., (1983), Modelling the Performance of Electrowinning Cells. *MSc. Dissertation, University of the Witwatersrand*, Johannesburg.

Rousset, A., (1993), Reactivity of Solids and New Metastable Phases: Examples of Mixed Valence Defect Spinel Ferrites and Manganites. *Solid State Ionics,* vol. 63-65, pp. 236-242.

Sánchez, L., Perriera-Ramos, J.P., (1997), Electrochemical Properties of a New Non-Stoichiometric Spinel Oxide ($Mn_{2.5}O_4$) as Li Insertion Compound. *Electrochim. Acta,* vol. 42, no. 4, pp. 531-535.

Sarma, D.D., Sen, P., (1983), XPS and Auger Studies of the Surface Oxidation of Manganese. *Proc. Indian Natl. Sci. Acad.,* Part A, vol. 49, no. 3, pp. 424-430.

Schaefer, S.C., (1982), Electrochemical Determination of the Thermodynamic Properties of Manganomanganic Oxide and Manganese Sesquioxide. *R18704, USBM.*

Segal, M.G., Sellers, R.M., (1984), Redox Reactions at Solid Liquid Interfaces. *Adv. Inorg. Bioinorg. Mech.*, vol. 3, pp. 97-129.

Shaw, J.A., (1992), Succeed at Solids Suspension. *Chem. Eng. Prog. (May Issue)*, pp. 34-41.

Sherman, D.M., (1984), Electronic Structures of Manganese Oxide Minerals. *Am. Mineral.,* vol. 69, no. 6-8, pp. 788-799.

Shook, C.A., Roco, M.C. (1991), *Slurry Flow Principles and Practise.* Butterworth-Heinemann, Boston, p. 283.

Simon, A., (1943), Über das System Manganooxyd/Wasser (Translated: Concerning the System Manganooxide/Water). *Zeit. Anorgan. Allgem. Chem.*, vol. 232, pp. 969-981.

Smallman, R.E., Bishop, R.J. (1995), *Metals and Materials: Science, Processes and Applications,* Butterworth-Heinemann Ltd, Oxford, pp. 395-413.

Smeltzer, W.W., (1986), Oxidation Mechanisms of Metals and Alloys. *Proceedings of the Norman L. Peterson Symposium on Oxidation of Metal and Associated Mass Transport*, Ed. M.A. Dayananda, S.J. Rothman, W.E. King, Am. Inst. Metals, pp. 109-129.

Söhnel, O., Garside, J., (1992), *Precipitation: Basic Principles and Industrial Applications.* Butterworth-Heinemann Ltd, Oxford.

Sully, A.H., (1955), *Metallurgy of the Rarer Metals.No. 3. Manganese.* Buttersworth, London.

Tailhades, P., Gillot, B., Rousset, A, (1997), Mixed Valence Defect Ferrites: A New Family of Thin Powders and Thin Films of Spinel Ferrites. *J. Phys.IV France 7 Colloq. C1, Supplement au Journal de Physique III*, pp. C1-249 to C1-252.

Tamura, H., Oda, T., Nagayana, M., Furuichi, R., (1969), Acid Base Dissociation of Surface Hydroxyl Groups on Manganese Dioxide in Aqueous Solutions. *J. Electrochem. Soc.*, vol. 135, no. 10, pp. 2782-2786.

Tang, Z.X., Sorensen, C.M., Klabunde, K.J., Hadjipanayis, G.C., (1991), Preparation of Manganese Ferrite Fine Particles from Aqueous Solution. *J. Coll. Int. Sci.*, vol. 146, no. 1, pp. 38-51.

Tareen, J.A.K., Basavalingu, B.,Kutty, T.R.N.,Bhandge, G.T.,Yoshimura, M.,Somiya, S., (1982), Hydrothermal Synthesis of Oxides of Manganese Single Crystals. *Proc.Int. Symp.Hydrotherm. Reac.* pp. 649-657.

Tavlarides, L.L., Bapat, P.L., (1983), Models for Scaleup of Dispersed Phase Liquid Reactors. *A.I.Ch.E. Symp. Ser.*, vol. 238, no. 80, pp. 12-46.

Tompkins, F.C., (1978), *Chemisorption of Gases on Metals.* Academic Press, London.

Treybal, R.E., (1968), *Mass Transfer Operations* McGraw-Hill, Kogakusha, Japan.

Tsumara, T., Shimizu, A., Inagaki, M., (1996), Lithium Extraction/Insertion from $LiMn_2O_4$ - Effect of Crystallinity. *Sol. State Ionics*, vol. 90, pp. 197-200.

Valverde, N., (1976), Investigations on the Rate of Dissolution of Metal Oxides in Acidic Solutions with Additions of Redox Couples and Complexing Agents. *Ber. Buns. Gesel.*, vol. 80, no. 4, pp. 333-340.

Valverde, N., Wagner, C., (1976), Considerations on the Kinetics and the Mechanism of the Dissolution of Metal Oxides in Acidic Solutions. *Ber. Buns. Gesel.*, vol. 80, no. 4, pp. 330-333.

Van't Riet, K., Smith, J.M., (1973), The Behaviour of Gas-liquid Mixtures near Rushton Turbine Blades. *Chem. Eng. Sci.*, vol. 28, pp. 1031-1037.

Vermilyea, P.A., (1966), The Dissolution of Ionic Compounds in Aqueous Media. *J. Electrochem. Soc.*, vol. 113, no. 10, pp. 1067-1070.

Vijh, A.K., Randin, J. P., (1975), Correlation between Rate Constants for Water Substitution in Inner Coordination Spheres of Metal Ions and Their Electrochemical Activities in Metal Deposition Reactions. *J. Phys. Chem.*, vol. 79, no. 13, pp. 1252-1254.

Vila, E., Rojas, R.M., Martín de Vidales, J.L., García-Martínez, O., (1996), Structural and Thermal Properties of the Tetragonal Cobalt Manganese Spinels $Mn_xCo_{3-x}O_4(1.4<x<2.0)$. *Chem. Mater.*, vol. 8, pp. 1078-1083.

Von Bogdandy, L., Engel, H.J., (1970), *The Reduction of Iron Ores.* Verlag Stahleisen, Düsseldorf.

Wachi, S., Jones, A.G., (1992), Dynamic Modelling of Particle Size Distribution and Degree of Agglomeration During Precipitation. *Chem. Eng. Sci.*, vol. 47, no. 12, pp. 3145-3148.

Wakao, S., Hashimoto, T., (1990), A Method of Manufacturing Manganese Oxide. *Japan Patent Office,* Hei 2-296732.

Warmoeskerken, M.M.C.J., Speur, J., Smith, J.M., (1984), Gas Liquid Dispersion with Pitched Blade Turbines. *Chem. Eng. Comm.*, vol. 25, pp. 11-29.

Warren, I.H., Devuyst, E., (1973), Leaching of Metal Oxides. *Int. Symp. Hydromet.* Ed. D.J.I. Evans & R.S. Schoemaker, chap. 11, pp. 230-264.

Weast, R.C. *Ed.*, (1982), *Handbook of Chemistry and Physics.* Chemical Rubber Publishing Company, 63rd Ed., Cleveland.

Welsch, J.Y., (1967), The Role of Manganic Ion in the Production of Electrolytic Mn Dioxide. *Electrochem. Tech.,* vol.5, no. 11-12, pp. 504-507.

Wen, L., (1987), Radial Flow Impellors. *Proc. Heat Trans. Fluid Mech. Inst.*, vol.30, pp. 25-48.

Wichterle, K., (1988), Conditions for Suspension of Solids in Agitated Vessels. *Chem. Eng. Sci.*, vol. 43, no. 3, pp. 467-471.

Young R.A., (1995), DBWS-9411-An Upgrade of the DBWS Programs for Rietveld Refinement with PC and Mainframe Computers, *J. Appl. Cryst.*, vol. 28, pp. 366-367.

Xu, C.N., Miyazaki, K., (1994), Thermal Incorporation of External Oxygen into EMD-Derived Manganese Oxides. *J. Electrochem. Soc.*, vol. 141, no. 12, pp. 3343-3346.

Zhang, H., Park, S., (1994), Electrochemical Oxidation of Manganese (II) in $HClO_4$ Solutions. *J. Electrochem. Soc.,* vol. 141, no. 9, pp. 2422-2429.